Spin Waves in Confined Nanostructures

Syed Adnan Raza
Supervisor: Rubem Luis Sommer
Centro Brasileiro de Pesquisas Físicas

Thesis

Doctor of Philosophy

Rio de Janeiro, May of 2020

CENTRO BRASILEIRO DE PESQUISAS FÍSICAS, RIO DE JANEIRO
DEPARTMENTO: MATÉRIA CONDENSADA FŚICA APLICADA
NANOCIÊNCIAS (COMAN)

Spin Waves in Confined Nanostructures

Syed Adnan Raza

Tese de Doutorado apresentada ao Programa de Pós-Graduação em Física do Centro Brasileiro de Pesquisas Físicas Rio de Janeiro - CBPF, como parte dos requisitos necessários á obtenção do título de Doutor em Ciências (Física).

Orientador: Rubem Luís Sommer

Rio de Janeiro
May, 2020

Resumo

Ondas de Spin em Nanoestruturas Confinadas

Syed Adnan Raza

Orientador: Rubem Luís Sommer

Resumo da Tese de Doutorado apresentada ao Programa de Pós-Graduação em Física do Centro Brasileiro de Pesquisas Físicas Rio de Janeiro - CBPF, como parte dos requisitos necessários á obtenção do título de Doutor em Ciências (Física).

O objetivo principal da presente tese é investigar os ondas de spin em nanoestruturas confinadas em filmes contínuos de Co_2FeAl (CFA), sistema de tricamadas de Co/NiFe/Co e arranjos periódicos com elementos com dimensões submicrométricas baseados em $Ni_{81}Fe_{19}$ em forma de antidots e elipses. Os filmes contínuos foram produzidos usando o sistema de deposição magnetron sputtering, enquanto as arranjos periódicos foram fabricados através da combinação das técnicas de litografia por feixe de elétrons, deposição por magnetron sputtering, plasma etching e/ou lift-off.

A caracterização magnética estática das amostras foi realizada usando um magnetômetro de gradiente de campo alternado (AGFM) e as propriedades dinâmicas foram analisadas fazendo uso de ressonância ferromagnética (FMR) de banda larga, baseada na utilização de uma guia de onda coplanar e um analisador vectorial de rede (VNA).

No caso de sistemas de filmes contínuos baseados em ligas de Heusler Co_2FeAl estudamos a evolução do campo coercitivo, anisotropias, constante de amortecimento e alargamento da largura da linha em função da espessura do filme CFA na faixa de 5 nm a 200 nm. As curvas de magnetização estática mostram a existência de anisotropia magnética no plano e campos coercitivos baixos. A partir dos ajustes das relações de dispersão, obtivemos os valores das anisotropias no plano, fora do plano e da anisotropia rodável.

No sistema de tricamadas baseados em camadas de cobalto e NiFe investigamos o modo uniforme de FMR e os modos excitação de ondas de spins perpendicular

(PSSW). Os modos observados foram ajustados numericamente usando a equação da relação de dispersão de ondas de spin. Conseguimos controlar as anisotropias e a magnetização efetiva em sistemas de camadas sintética. Também fomos capazes de manipular o amortecimento efetivo e o alargamento não homogêneo da largura de linha ($\mathit{\Delta H_0}$) manipulando os componentes da camada sintética.

Elementos baseados em $\mathrm{Ni}_{81}\mathrm{Fe}_{19}$ com geometria com confinamento lateral, tais como antidots e elipses também foram estudados nessa tese. A caracterização magnética estática dos arranjos periódicos foi realizada usando um AGFM e o estado magnético remanente foi analisado em função da direção do campo magnético aplicado por medidas de Microscopia de Força Magnética (MFM).

Investigamos os modos de ressonância ferromagnética em estruturas de antidots (poros no filme de $\mathrm{Ni}_{81}\mathrm{Fe}_{19}$) usando medições de ressonância ferromagnética de banda larga. As amostras de arranjos periódicos de antidots foram fabricadas por meio do processo top-down usando um plasma etching. Estruturas tipo antidots mostram um efeito de endurecimento magnético com incremento dos campos coercitivos. Nesse trabalho, analisamos a resposta dinâmica em função de diferentes ângulos de excitação dos modos de onda de spin em relação ao campo externo. Os resultados experimentais mostram uma estrutura rica de modos nos espectros de absorção de ressonância, com amplitudes de pico de absorção dependentes da direção do campo magnético externo.

Nas amostras em formato de elipses investigamos a resposta dinâmica da magnetização com configuração magnética do tipo vórtice com campo de excitação de rádio frequência aplicado perpendicular a direção do campo magnético externo. Além de manipular as propriedades magnéticas dos sistemas variando o tamanho das elipses, enquanto a razão entre as suas dimensões laterais é mantida, investigamos os diferentes modos de FMR de estados de vórtices magnéticos obtidos por meio de medidas de FMR e simulação micromagnética.

Nessa tese os resultados experimentais dos sistemas com confinamento lateral foram analisados por meio de simulação micromagnética realizadas com o código Mumax3. Os dados simulados são analisados por meio de algoritmos que permitem extrair a potência absorvida em função do campo e da frequência aplicada. Além dos detalhes sobre a energia absorvida analisamos também o perfil dos modos de ressonância excitados em cada sistema.

Palavras-chave: Ressonância ferromagnética, dinâmica da magnetização, ondas de spin, amortecimento de Gilbert, nanoestruturas magnéticas, filmes ferromagnéticos.

Abstract

Spin waves in confined nanostructures

Syed Adnan Raza

Orientador: Rubem Luís Sommer

Resumo da Tese de Doutorado apresentada ao Programa de Pós-Graduação em Física do Centro Brasileiro de Pesquisas Físicas Rio de Janeiro - CBPF, como parte dos requisitos necessários á obtenção do título de Doutor em Ciências (Física).

The general scope of the present thesis is to study the spin waves in confined magnetic nanostructures of single layered Co_2FeAl (CFA), trilayered $Co/Ni_{81}Fe_{19}/Co$ and periodic arrays of $Ni_{81}Fe_{19}$ patterned elements in the form of antidots and ellipses. Continuous films were produced using magnetron sputtering, while the periodic arrays were fabricated by combining electron beam lithography, magnetron sputtering, plasma etching and / or lift-off techniques.

The static magnetic characterization of all samples was performed using an alternating field gradient magnetometer (AGFM) and the dynamic properties were analyzed using broadband ferromagnetic resonance (FMR), based on the use of a coplanar waveguide and a network vector analyzer (VNA).

In the case of continuous film systems based on Heusler alloys Co_2FeAl we study the evolution of the coercive field, anisotropies, damping constant and linewidth broadening as a function of the thickness of the CFA film in the range from 5 nm to 200 nm. The static magnetization curves show the existence of in-plane magnetic anisotropy and low coercive fields. From the fittings of the dispersion relations we obtained the values of the in-plane, out-of-plane and rotatable anisotropy constants.

In trilayered systems, based on cobalt and NiFe layers, we investigated the uniform FMR mode and the perpendicular standing spin wave (PSSW) excitation modes. From the dispersion relation fittings we obtained the effective magnetization and in-plane uniaxial anisotropy. We were able to control the anisotropies and effective magnetization in synthetic layer system. We were also able to manipulate the effective damping and inhomogeneous line width broadening (ΔH_0) by playing with the synthetic layer component.

The patterned elements of $Ni_{81}Fe_{19}$ with lateral confinement, such as antidots and ellipses, were also studied in this thesis. The static magnetic characterization of the periodic arrays were performed using AGFM and the remanence magnetic state was analyzed as a function of the direction of the applied magnetic field with Magnetic Force Microscopy (MFM) measurements.

We investigated ferromagnetic resonance modes in antidots nanostructures (pores in the $Ni_{81}Fe_{19}$ film) using broadband ferromagnetic resonance measurements. Samples of periodic arrays of antidots were fabricated using a top-down process using plasma etching. The presence of the antidots generally leads to a magnetic hardening effect with enhancements of the coercive fields. A noticeable change in the excitation of spin wave modes was observed when measured at different angles of applied DC field. The dynamic properties results shows a rich structure of modes in the resonance absorption spectra, with absorption peak amplitudes dependent on the direction of the external magnetic field in respect to the array axis.

In the case of magnetic ellipses samples, we investigated the dynamic response of magnetization with a magnetic configuration of the vortex with a radio frequency (RF) excitation field applied perpendicular to the external magnetic field. In addition to manipulating the magnetic properties of the systems by varying the size of the ellipses, while maintaining the ratio between the lateral dimensions, we investigated the different FMR modes of magnetic vortex states obtained through FMR measurements.

In this thesis, the experimental results of patterned elements were analyzed by the means of micromagnetic simulation performed with the Mumax3 code. The simulated data were analyzed by means of algorithms developed by the Applied Magnetism Laboratory group, which allow to extract the spectral power absorbed as a function of applied field and frequency. In addition to the details about the power absorbed, we were able to analyze the excited resonant modes within each system.

Keywords: Ferromagnetic resonance, magnetization dynamics, magnetic nanostructures, spin waves, Gilbert damping, ferromagnetic films.

Acknowledgment

(All praises to ALLAH ALMIGHTY, The Creator and Sustainer of The Universe, The most gracious, The invincible and the all-wise. All esteem to His Holy Prophet Muhammad (Peace be upon Him) for eternal source of guidance and knowledge for mankind.)

This work would not have been possible without the help and support of many people, and I hereby would like to take the opportunity to thank them. First of all, my supervisor Professor Rubem Luís Sommer. His enthusiasm for my project and his constant belief in my abilities have been an invaluable support. He always encouraged my ideas, and gave me the freedom and financial framework to realize them.

My colleagues at the campus and Post doctoral fellows, most notably Diego González, Roberta Dutra and B. G. Silva. I really enjoyed my discussions with Diego González, and highly appreciate that he always found time for them, also his help with simulation work, practical stuff or repairing lab equipment's.

Thank you my friends out of campus who made my stay in Rio de Janeiro more enjoyable without them it was difficult. I would like to mention my Brazilian family members Thatiana Vitorino and Odlorah Oiapmas, and also Luana Vitorino, Felipe Barbosa, Ronaldo Santiago and Simone Alcantra.

Thank you my Pakistani friends who give me the backup all the time, not a single moment I felt that I am away from my family, namely Rafqat Ali, Asmat Pervez, Quaid Zaman, Tahir Jan and Syed Hamza Safeer.

And most of all, my family and friends. I cannot express in words how grateful I am for your understanding and encouragement, and the constant love and support you have given me during all these years. Especially, I would like to thank my elder brother Syed Summer Raza (Baraa Bhai), who gives me continuous attention and motivation during this period always wants to know if I need something.

Also, I am very grateful to Post Graduate Office (COEDU) and their administrative staff for their technical support and the Brazilian funding agencies CNPq and CAPES for providing the scholarship which supported my research assistantship for my years in CBPF.

List of Publications

- Low damping and small inhomogeneous linewidth broadening in Co_2FeAl films

  S. A. Raza, B. G. Silva, Cilene Labre, D. E. Gonzalez-Chavez, M. A. Correa, R. L. Sommer
  J. Magn. Magn. Mater., 513 (2020) 167081

- Magnetic damping and perpendicular standing spin waves in $Co/Ni_{81}Fe_{19}/Co$ synthetic magnetic layers

  S. A. Raza, D. E. Gonzalez-Chavez, R. L. Sommer
  (In manuscript).

- Dipole-exchange modes in elliptical magnetic nanostructures

  S. A. Raza, R. Dutra, D. E. Gonzalez-Chavez, R. L. Sommer
  (In manuscript).

- Spin Wave Dynamics in Magnetic Antidots lattice

  S. A. Raza, R. Dutra, D. E. Gonzalez-Chavez, R. L. Sommer
  (In manuscript).

Related Publications by the author

- Filtering Magnetic Relaxation Mechanisms of YIG(001) Thin Films Using Ferromagnetic Resonance

  A. Oliveira, R. R. Suarez, M. A. Correa, F. Bohn, **S. A. Raza**, R. L. Sommer, C. Chesman
  J. Magn. Magn. Mater., 507 (2020) 166851

- Exploring the magnetization dynamics, damping and anisotropy in engineered CoFeB/(Ag, Pt) multilayer films grown onto amorphous substrate

  M. A. Correa, J. G. S. Santos, B. G. Silva, **S. A. Raza**, R. D. Della Pace, C. Chesman, R. L. Sommer, F. Bohn
  J. Magn. Magn. Mater., 485 (2019), pp. 75-81

Contents

List of Figures

Chapter 1

Introduction

1.1 Historical background

The early magnetic phenomena observations were made back in the ancient times. Historically, this can be seen not only in Greek and Chinese writings but also in the archaeological remains of pre-Columbian civilizations [24]. These civilizations reported that, they found some stones (magnetite, an iron oxide naturally magnetized) which have property to attract iron. Centuries later, the first remarkable application of magnetism has appeared: the sea-navigation compasses. Therefore, the magnetism has an important role in the expansion of the "known world" in the fifteenth century by European navigators.

After three centuries of scientific research with many theoretical proposals and empirical observations, the research of magnetism comes to the nineteenth century, where the electromagnetism was discovered and its interaction with the light, in the experimental works of Hans-Christian Oersted (the magnetic field produced by an electric current), André-Marie Ampère (equivalence between an electric coil and a magnet) and Michael Faraday (electromagnetic induction). Besides, the most important development of the nineteenth century was made in 1864, by James Clerk Maxwell, with the formulations of the laws of electrodynamics. All this scientific research in magnetism gave birth to the new technologies: electric motors and generators, telephones, telegraphs etc.

In the 20th century, the quantum mechanics revealed the concept of spin of electron. Many famous names came, e.g Pauli, Dirac, Fermi, Heisenberg, Bloch and Néel for the significant contributions to the theory of metals and magnetism. Besides that, the first recordings in magnetic media appeared in the 1930's. The recording technology evolves to the magnetic tapes, floppy-disks and the first hard disk drive (HDD).

However, the new breakthrough in terms of technology had come by the end of the twentieth century, with the discovery of the giant magnetoresistance effect (GMR) in 1988 [25, 26] and the birth of spintronics. This make possible the development of faster devices for data storage and processing. This called the efforts of the scientific community to find new materials and solutions for magnetic storage. Now, the challenge is to stabilize bits with the fewest possible number of atoms and optimization of processing, associated with the lower energy consumption. The studies show that despite all the advances made, the understanding of magnetism in matter from the basic knowledge to the applications of high density magnetic storage and spintronic/magnonic devices is a daily challenge for scientists.

In view of these perspectives and high scientific interest in the field of nanomagnetism, in this thesis we presents experimental studies of the spin waves in confined nanostructures, which is done by the means of broadband ferromagnetic resonance by vector analyzer (VNA-FMR) [27, 28].

1.2 State of the art and objectives

The study of spin waves in confined systems is fundamentally importance to understand the basic physical properties of these systems as well as to provide new roads to applications. The discovery of novel materials and the exploration of the dynamic magnetic response in diverse systems have provided the development and optimization of a wide range of technological devices in recent decades [29, 30, 31]. This is especially true for ferromagnetic films, which are employed in a variety of magnetic sensors [32, 33] and also giant magneto resistance devices (GMR's). In particular, spintronics devices and data storage applications such as magnetic reading and random magnetic access memories (MRAM) [34] are increasingly being used at frequencies comparable to the natural ferromagnetic resonance frequency. The response in these systems depends strongly on the experimental conditions used to excite the magnetization dynamics, as well as the intrinsic and extrinsic properties of the material. Furthermore, there is a growing interest in understanding the propagation of spin wave in magnonic crystals nanostructures [35, 36], with potential for use as a means of transmitting information in spintronic applications and beyond [37].

The later developments in experimental techniques have a remarkable role for the research on magnetic materials. From last few decades the practical implementation of these devices got a lots of interest, because of the advances in the fabrication techniques (advanced lithography) which allow us to fabricate the complex magnetic structures ranging from nano to millimeters scale. The use of these devices requires the control of excitation and detectors that operate in the microwave frequency range. This excitation and detection can be easily performed by electrical means due to the large amount of technology available in traditional electronics.

When the dimensions of the magnetic structures are reduced to the point of being comparable to the exchange length, the reversal of the magnetization is drastically modified [38]. In the same way, the propagation of spin waves in these structures is also affected by the presence of direction and magnitude of RF (radio frequency) fields, resulting in significant changes in the frequency dependent magnetization response [9].

The study of a single magnetic element is challenging, since it requires a great sensitivity in the experiment. To avoid this problem, we arranged the magnetic elements in arrays or in periodic structures where, depending on the distance between the elements we can study the interaction between them. The interaction between the elements of an array affect the properties of the spin waves in the system [39]. Experiments as well as theory show that a number of factors such as geometry, anisotropy, interaction between the elements, and the formation of single or multiple domains, influence the magnetic behavior of these systems [40, 41].

In this thesis, we study the spin waves in confined nanostructures, based on the the knowledge acquired by the Applied Magnetism Group and the viability of the production at LABNANO/CBPF. The samples were produced with different degrees of confinement, starting with single layers of Co_2FeAl (CFA), followed by trilayers of $Co/Ni_{81}Fe_{19}/Co$ with vertical confinement and, finally, periodic arrays of $Ni_{81}Fe_{19}$ patterned elements in form of antidots and ellipses with lateral and vortex state confinements respectively. It is expected that the confinement, symmetries and periodicity of the systems will enrich the spectrum of resonant frequencies measured by broadband FMR, therefore providing new insights on the magnetization dynamics and spin waves in this kind of samples. The spin wave control over these systems can be of great help in designing devices with tailored responses.

This thesis is composed of seven chapters; the theoretical basis to explain the obtained results is presented in the second and third chapters. In the fourth and fifth chapters we describe the experimental techniques and the details about the micromagnetic simulations formalism, which were used to reproduce the experimental data . Chapter 6 is dedicated to the results and discussions. Finally, in chapter 7 we discuss the conclusions of this thesis and future perspectives.

Chapter 2

Magnetic Free Energy

In this chapter we present the basic physics and relevant concepts to the magnetic free energy. The literature review has been done with the motivation to get into the basic and brief theoretical understanding of the magnetic free energy. Many theoretical models and formalism have been used by different authors for the understanding of the different parameters of magnetic free energy.

2.1 Magnetic Interactions

This section explains the origin of magnetic interactions by using ferromagnetic ordering, although ferromagnets are the subject of this thesis.

2.1.1 Magnetic Dipolar Interaction

Classically, the dipole-dipole interaction energy depends on the relative orientation of the magnetic moments (consider two bar magnets). To get insight to the dipolar interaction consider two magnetic dipoles $\vec{\mu}_1$ and $\vec{\mu}_1$, each put into magnetic field from the other dipole in this case the corresponding magnetic energy can be given as [42]:

$$E_{dipole} = \frac{\mu_o}{4\pi r^3}\left[\vec{\mu}_1 \cdot \vec{\mu}_2 - \frac{3}{r^2}(\vec{\mu}_1 \cdot \vec{r})(\vec{\mu}_2 \cdot \vec{r})\right], \tag{2.1}$$

where μ_o is the permeability. Since $\vec{r}$ is the vector connecting the two dipoles, the energy decreases with the 3^{rd} order of their distance. In general, the strength of the interaction depends on several factors: (i) the magnitudes of the individual interacting dipoles; (ii) the distance separating the interacting dipoles; (ii) the orientation of the dipoles relative to one another; and (iv) the ”spectral overlap” of resonances that satisfy the conservation of angular momentum and energy. The dipolar interaction is accountable for effects such as demagnetizing field and spin waves in the long wave length regime (as it is discussed later in the subsection of demagnetization energy).

2.1.2 Spin-Orbit Interaction

Generally, electrons have an orbital magnetic moment ($g_l m_l \mu_B$) associated with their angular momentum, and a spin magnetic moment ($g_s m_s \mu_B$), where μ_B is the Bohr magneton, $g = 2$ is the g-factor of the electron spin and $m_s = \pm\frac{1}{2}$ is the the spin quantum number. The spin magnetic moment of the electron indeed interacts with its own orbital magnetic moment. This coupling is known as spin-orbit interaction and causes a splitting of the electronic states. For hydrogen-like atoms the energy splitting due to spin-orbit interaction given as [43]:

$$E_{so} = \beta \frac{< \vec{S} \cdot \vec{L} >}{n^3 l(l + 1/2)(l + 1)} \tag{2.2}$$

so,

$$E_{so} \propto < \vec{S} \cdot \vec{L} > \tag{2.3}$$

where, n and l being the principle and angular momentum quantum numbers, respectively. The angular and the spin moment are given by $\vec{L}\hbar$ and $\vec{S}\hbar$, respectively. The pre-factor β is:

$$\beta = \frac{z^4 e^2 \hbar^2}{4\pi\epsilon_o q_o^3}, \tag{2.4}$$

where z is the atomic number and a_o is the Bohr radius. For atoms in a crystal lattice the magnitude of the splitting is of the order of 10^{-4} to 10^{-3} eV. The origin of magnetic anisotropies is related with the spin-orbit interaction, where the crystal symmetry mediated to the spin of the system. Moreover, by linking the spin system to the crystal lattice, spin-orbit coupling represents a path for energy transfer between the two degrees of freedom, which is important for intrinsic magnetic damping.

2.2 Energy Contributions

The total effective field $\vec{H}_{eff}$ acting on the magnetic moments $\vec{\mu}$ inside a solid could by found by taking the functional derivative of the total energy density $\varepsilon_{tot} = E_{tot}/V$ with respect to the reduced magnetization $\vec{m} = \vec{\mathrm{M}}/M_s$ [43, 44].

$$\vec{H}_{eff} = -\frac{1}{\mu_0} \frac{\partial \varepsilon_{tot}}{\partial \vec{m}} \tag{2.5}$$

where, V is the sample volume and ε_{tot} is the free energy density of the system. The total magnetic free energy density of a ferromagnetic sample in the applied magnetic field can be described as the sum of various energy density contributions, which could be given as:

$$\varepsilon_{tot} = \varepsilon_{zee} + \varepsilon_{ani} + \varepsilon_{dem} + \varepsilon_{ex} + ... \tag{2.6}$$

where, ε_{zee} is the Zeeman energy density, ε_{ani} is the effective anisotropy energy density, ε_{dem} is the demagnetization energy density and ε_{ex} is the exchange energy density. In the following subsection, we will discuss and explain the most relevant energies to our work.

2.2.1 Zeeman Energy

The Zeeman term arises from interaction of the magnetization $\vec{M}$ with an external field H_0

$$E_{zee} = \frac{1}{V} \int dV \vec{M}.\vec{H}_0. \tag{2.7}$$

Moreover, the Zeeman energy always favors the parallel alignment of the magnetization along the external field direction [45].

2.2.2 Exchange Energy

The exchange energy corresponds to an electrostatic interaction, which has a quantum-mechanical nature, and is responsible for the long-range magnetic order in ferromagnetic materials [46]. Apart from ferromagnets, this interaction is also present in antiferromagnets (AFM) and ferrimagnet, where the exchange interaction between the neighboring magnetic ions forces the individual moments into parallel or antiparallel alignment with their neighbors. It a consequence of the Coulomb interaction energy and Pauli exclusion principle, it can be described by the Heisenberg exchange Hamiltonian [47, 45], given by

$$H_{ex} = -2J \sum_{i \neq j} \vec{S}_i \cdot \vec{S}_j, \tag{2.8}$$

where $\vec{S}_i$ and $\vec{S}_j$ corresponds to the spin operator of the i-th and j-th atoms, and J denotes the exchange integral. In the perpetuation to the model, if we consider the exchange interaction only between nearest neighbors in the cubic lattice, the above equation can be written as [13]:

$$E_{ex} = A_{ex} \int (\bigtriangledown \vec{m})^2 dV, \tag{2.9}$$

where $\vec{m}$ is a continuous vector of the reduced magnetization $\vec{m} = \vec{M}/M_s$ and A_{ex} is the exchange stiffness constant, which could be written, for the simple cubic lattice of spins,

$$A_{ex} = \frac{2JS^2}{a}, \tag{2.10}$$

where a is the lattice constant.

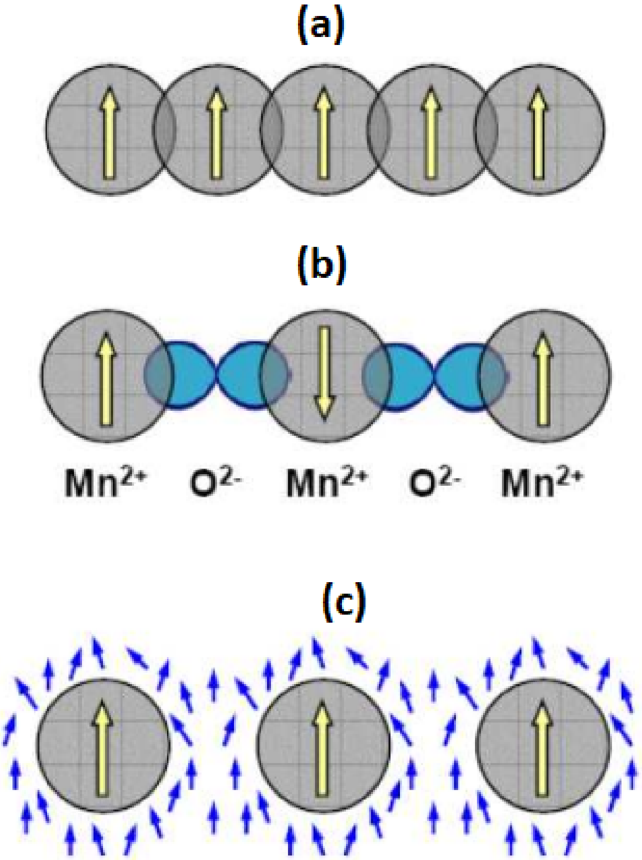

Figure 2.1: Schematic illustration of the main types of exchange interactions: (a) Direct exchange interaction, from direct overlap; (b) Superexchange, mediated by paramagnetic atoms; (c) RKKY interaction, indirect exchange interaction mediated by polarized conduction electrons [1].

Furthermore, the above-mentioned exchange coupling is also known as direct exchange interaction, where the electrons of magnetic atoms interact with their nearest neighbors (as shown in the Fig. 2.1). Besides that, the exchange interaction can also take place in indirect ways, which couples moments over relatively larger distances. For example, the Ruderman–Kittel– Kasuya–Yosida (RKKY) interaction, where the metallic ions are coupled via conduction electrons, super-exchange, where the exchange is conciliates via different nonmagnetic ions. The expression of RKKY interaction is given as:

$$J_{RKKY}(r) = \frac{\sin x - x\cos x}{x^4} \rightarrow \frac{1}{x^3}(x \rightarrow \infty) \tag{2.11}$$

where $x = 2k_F r$ and k_F being the Fermi wave vector.

Here in Fig. 2.2 we show an example of RKKY interaction by changing the spacer thickness: the interlayer coupling can be chosen to be ferromagnetic, antiferromagnetic or zero, e.g. in CoFe–Ru–CoFe [43, 46, 47].

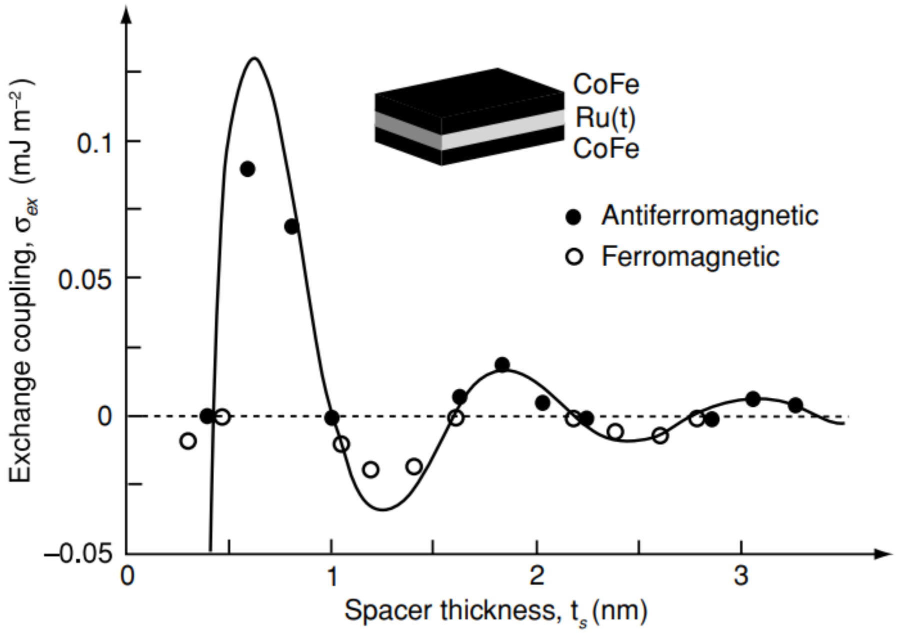

Figure 2.2: Oscillating exchange coupling in a CoFe–Ru–CoFe trilayer [2].

An important anisotropic exchange interaction, is the Dzyaloshinskii-Moriya interaction (DMI), where the spin-orbit coupling (SOC) plays an important role and often leads to tilting of adjacent spins by a small angle [48, 49]. DMI is a contribution to the total magnetic exchange interaction between two neighboring magnetic spins, S_1 and S_2, the Hamiltonian for this system is given as:

$$H_{DM} = D_{12} \cdot (S_1 \times S_2) \tag{2.12}$$

where, D_{12} is the resulting DMI vector, which is perpendicular to the plane of the triangle (as shown in the Fig. 2.3).

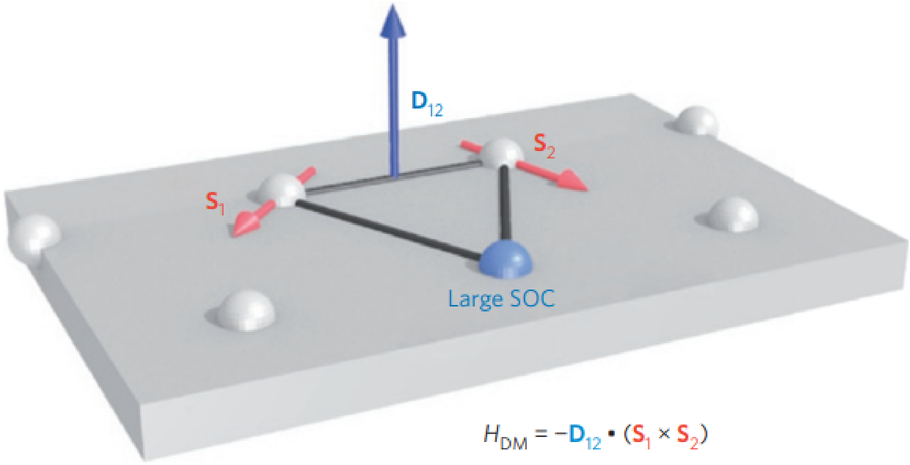

Figure 2.3: Schematic of a DMI generated by indirect exchange for the triangle composed of two atomic spins and an atom with a strong SOC [3].

2.2.3 Magnetostatic Energy

The magnetostatic energy, also known as demagnetizing energy E_{dem}, is related to the field generated by sample magnetization, such as demagnetizing field H_d. In the case of ferromagnets, the magnetostatic energy plays an important role in a number of phenomena such as formation of domains, demagnetizing field, and spin waves in the long wavelength regime. A magnetic system with finite boundaries exhibits poles at its surfaces which lead to a stray field outside the sample. This effect also gives rise to the demagnetizing field inside the sample [50]. The energy corresponding to the stray field is given by

$$E_{dem} = -\frac{1}{2} \int \mu_0 \vec{M} \cdot \vec{H}_{dem} dV. \tag{2.13}$$

$\vec{H}_{dem}$ is associated with the sample geometry (see Fig. 2.4), for example in case of a homogeneously magnetized ellipsoid, $\vec{H}_{dem}$ is uniform and can be expressed as:

$$\vec{H_{dem}} = -\overleftrightarrow{N} \vec{M}. \tag{2.14}$$

where $\overleftrightarrow{N}$ is called the demagnetizing tensor, which can be written as

$$\overleftrightarrow{N} = \begin{pmatrix} N_x & 0 & 0 \\ 0 & N_y & 0 \\ 0 & 0 & N_z \end{pmatrix} \tag{2.15}$$

which depends on the dimensions and coordinates of the elements major axes. The trace of tensor $\overleftrightarrow{N}$ satisfies,

$$N_x + N_y + N_z = 1 \ S \cdot I \tag{2.16}$$

$$N_x + N_y + N_z = 4\pi \ (CGS) \tag{2.17}$$

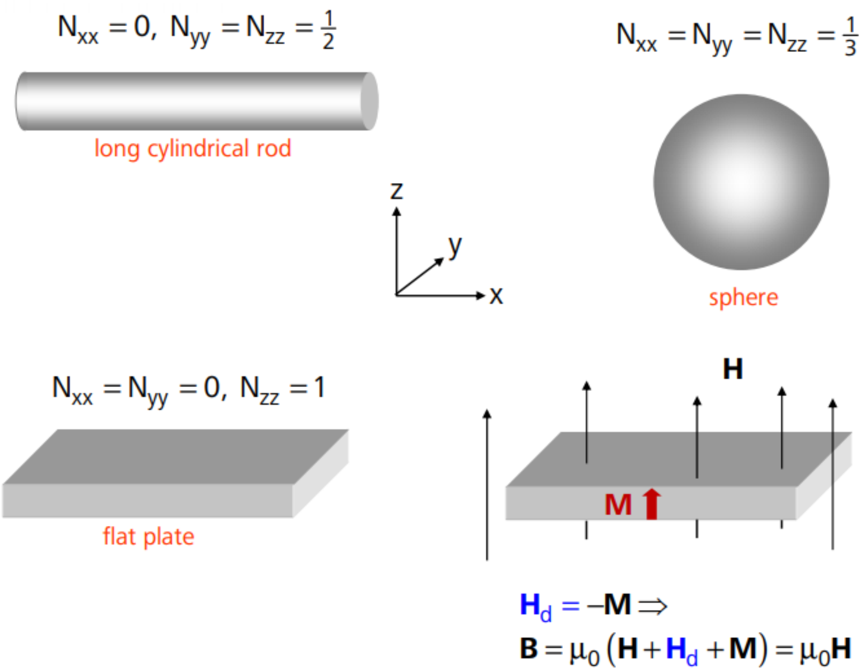

Figure 2.4: Demagnetizing tensor N for different geometries, the demagnetizing field H_{dem} pointing opposite to the magnetization $\vec{M}$

.

Note that, in the case of ellipsoid, thin film as shown in Fig. 2.5 represents a good approximation of a flat ellipsoid. When the film is magnetized in-plane, the stray field can be neglected on account of infinitely separated boundaries (see Fig. 2.5(a)). In contrast, when the magnetization points out of the film plane, the magnetic poles at the surfaces give rise to a field of H_{dem}, given as:

$$\vec{H_{dem}} = -\hat{z} M_s. \tag{2.18}$$

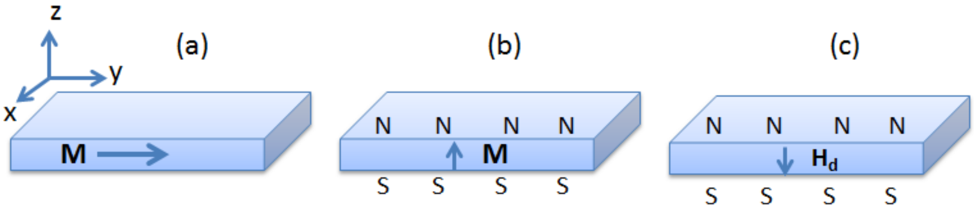

Figure 2.5: A thin film magnetized parallel (a) and perpendicular ((b) and (c)) to its plane. Film surfaces generate a strong demagnetizing field H_{dem} orientated opposite to the magnetization $\vec{M}$ (c).

pointing opposite to the magnetization $\vec{M}$ (see Fig. 2.5(c)). Hence, the in-plane demagnetizing factors vanish ($N_x = N_y = 0$). On the other hand the perpendicular component is maximum ($N_z = 1$). As a consequence of energy minimization, the demagnetizing field tends to prevent the magnetic moments from aligning perpendicular to the sample surface. [51, 45].

2.2.4 Magnetic Anisotropy Energy

In magnetic crystals the magnetic anisotropy is usually dependent on the orientation of the magnetization with respect to preferential directions (known as magnetization axes) inside the crystal. Variation from the easy axes requires an additional energy penalty on the system, the so-called anisotropy energy. Magnetic anisotropy could be arising from different sources, such as:

(i) **Magnetocrystalline anisotropy:** Magnetic anisotropy originating from crystalline symmetries is referred to as magnetocrystalline anisotropy. It is caused by spin-orbit interaction of the electrons, which is an intrinsic property of magnetic crystals. For example, in the case of cubic systems, the energy density due to crystal anisotropy reads [52]

$$\varepsilon_{ani} = K_1 \left(\alpha_x^2\alpha_y^2 + \alpha_y^2\alpha_z^2 + \alpha_z^2\alpha_x^2\right) + K_2\alpha_x^2\alpha_y^2\alpha_z^2\,, \tag{2.19}$$

where α_i are the directional cosines of the normalized magnetization $\mathbf{m}$ with respect to the Cartesian axes of the lattice. K_i's are the magnetocrystalline anisotropy constants, i.e., K_1 and K_2 are the crystalline anisotropy constants of first and second order, respectively. Besides, for crystals having uniaxial anisotropy, the energy density can be written as:

$$\varepsilon_{ani} = K_U\alpha_x^2\,, \tag{2.20}$$

where K_U is the uniaxial anisotropy constant.

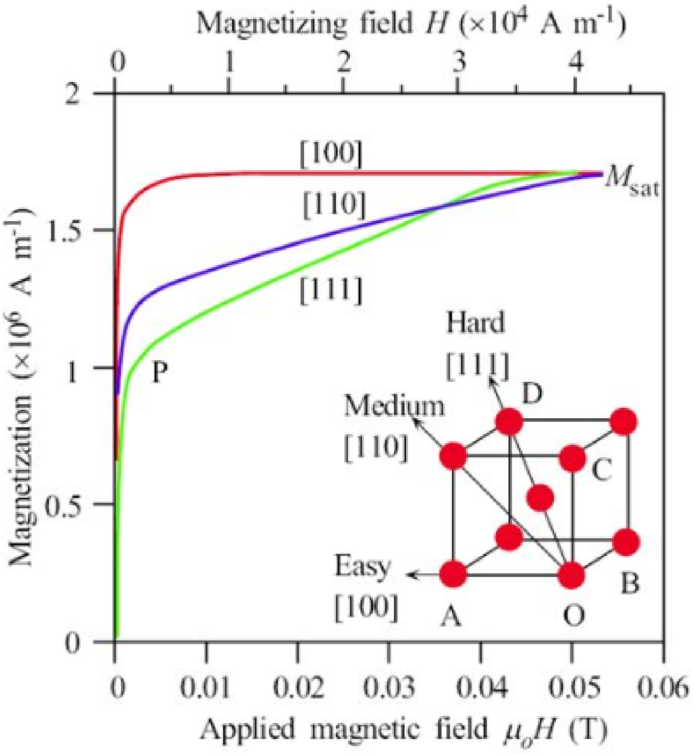

Figure 2.6: Magnetocrystalline anisotropy in a single iron (Fe) crystal. $\vec{M}$ vs. $\vec{H}$ depends on the crystal directions and is easiest, along [100] and hardest, along [111] directions [4].

(ii) Shape anisotropy: Shape of the magnetic crystal is another common origin of magnetic anisotropy, know as shape anisotropy. It basically originates from anisotropic dipolar interaction of free magnetic poles (demagnetization and stray fields) that tries to magnetize magnetic elements with magnetic moments directed parallel to the surfaces (to minimize magnetostatic energy). The shape anisotropy plays an important role for preferable magnetization in sample with different shapes e.g., vortex state of magnetic disk or ellipses, and preferable magnetization of magnetic stripes along their axis. For instance, the shape anisotropy for the case of Fig. 2.5 a thin film can be written as $K^V_{Shape} = \frac{\mu_0 M_s^2}{2}$.

(iii) Surface and interface anisotropy: Surface anisotropy was first discussed by Neel in 1956. This energy comes from the coupling of the surface atoms to the crystal field produced by their anisotropic surroundings. Mostly it originates from the broken symmetry at surfaces and interfaces of magnetic thin films and multilayers. The surface first few monolayers experience structural relaxation normal to the surface. The total anisotropy of a thin film is therefore sum of terms that scale with volume and surface area, given as:

$$E_a = K_{eff} \sin^2 \theta \,, \tag{2.21}$$

where K_{eff} is the effective anisotropy constant is divided into two parts:

$$K^{eff} = K^v + \frac{2K^s}{t} \,, \tag{2.22}$$

where K^v and K^s are volume and surface anisotropy constants, respectively, and t is the thickness of the film. The competition between volume and surface anisotropy gives rise to a dependence of the magnetization on the film thickness. With increasing thickness, magnetocrystalline anisotropy term dominates and the magnetization switches to perpendicular direction at a critical thickness (given by $t_c = -\frac{2K^S}{K^V}$). For thick films, the shape anisotropy is the dominating contribution, that determines the easy axes of the films [53, 43, 54].

Moreover, one could deduce both K^v and K^s by plotting the anisotropy energy per unit area versus t for a series of films of different thickness, provided they have a common easy axis (Fig. 2.7).

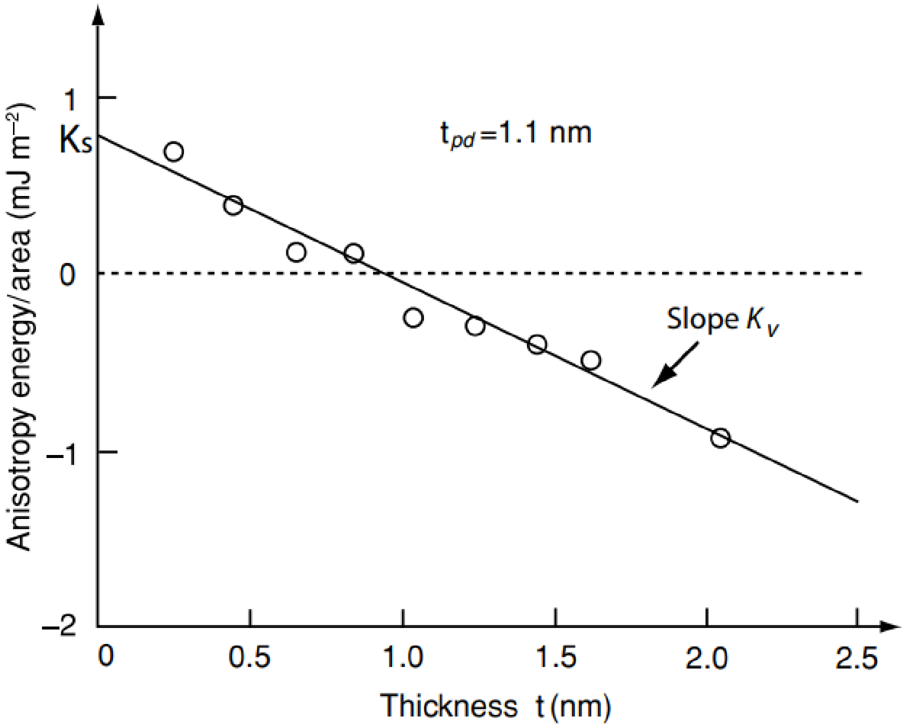

Figure 2.7: Plot to determine the surface and volume anisotropy terms for a Co–Pd multilayer [5].

2.2.5 Rotatable Anisotropy

The rotatable anisotropy causes the anisotropy axis to follow the direction of magnetization [55]. This type of anisotropy is generally observed both in static measurements ($\vec{M}$ vs. $\vec{H}$) and dynamic measurements, shown in the isotropy of the magnetization curve in relation to the angle of application of the magnetic field ($\vec{H}$). In dynamic measurements rotatable anisotropy causes a frequency shift in the dispersion relations [56], which is the signature of the so-called rotatable anisotropy (RA), which refers to the reorientation of the easy axis of an uniaxial anisotropy towards the direction of the applied magnetic field [57, 58].

The source of rotatable anisotropy may be related to film substrate interfaces, the presence (coupling) of a native oxide layer or can be related to the degree of magnetic disorder. The RA effect was first observed in ferromagnetic films and has been attributed to the ferromagnetic–antiferromagnetic exchange interaction with the expected NiO surface-oxide layer formed during the film deposition [59, 60]. It has been also observed in Ni–Fe films [61, 62] and Heusler alloy films [63]. RA is attributed to the magnetic disorder, micro domains and the negative magnetostriction for films above a critical thickness [64]. We used the Kittel formula with rotatable anisotropy contibution to simulate the experimental data of the ferromagnetic resonance dynamic measurements in Heusler alloys film samples studied in this thesis.

2.2.6 Magnetoelastic Energy and Magnetostriction

Mechanical stress applied on a magnetic material, it may change the domain structure and create a new source of magnetic anisotropy, which is known as magnetostriction energy (a schematic diagram is given in Fig. 2.8). This phenomenon can have a significant effect on the low-field magnetic properties, such as permeability and remanence. On the other hand, the magnetostriction is an effect in which a sample of magnetic material undergoes changes in its dimensions as it is magnetized. In a broader sense, magnetostriction is the occurrence of mechanical deformation of a magnetic sample due to changes in the degree of magnetization, or in the direction of magnetization. In the case of cubic crystalline structures, the magnetostatic energy density can be written as:

$$\begin{aligned}\varepsilon_{mc} = -\frac{3}{2}\lambda_{100}\sigma\left(\alpha_1^2\gamma_1^2 + \alpha_2^2\gamma_2^2 + \alpha_3^2\gamma_3^2\right) \\ -3\lambda_{111}\sigma\left(\alpha_1\gamma_1\alpha_2\gamma_2 + \alpha_2\gamma_2\alpha_3\gamma_3 + \alpha_3\gamma_3\alpha_1\gamma_1\right),\end{aligned} \tag{2.23}$$

where γ_1, γ_2, γ_3 are the direction cosines of applied stress σ and α_1, α_2, α_3 are the direction cosines of M_s. The first and second terms of Equation 2.23 corresponds to the magnetostrictive strains and the stress, respectively. It is usually called magnetoelastic energy E_{me}. When the magnetostriction is isotropic, $\lambda_{100} = \lambda_{111} = \lambda_s$ and

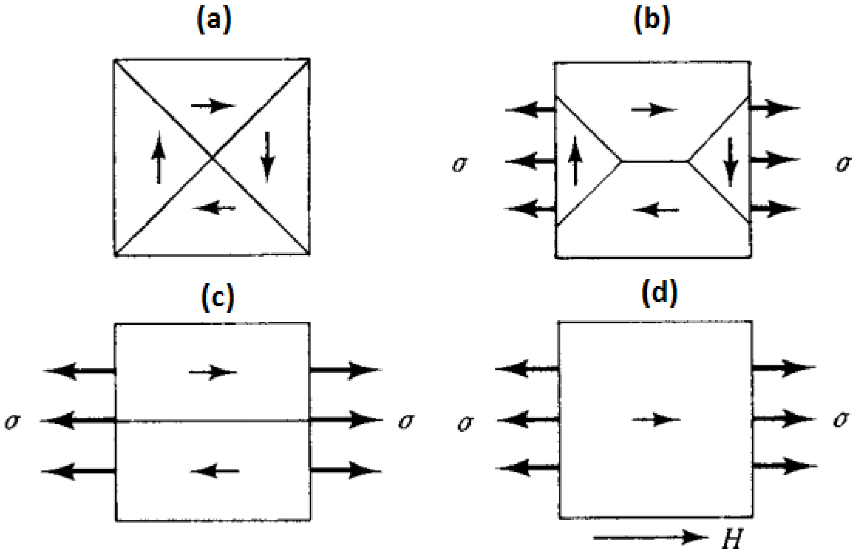

Figure 2.8: Magnetization of a material with positive magnetostriction under tensile stress (schematic) (a) no stress; (b), (c) & (d) with increasing stress.

the last two terms of Equation 2.23 become very simple:

$$\varepsilon_{mc} = -\frac{3}{2}\lambda_s \sigma \cos^2\theta, \tag{2.24}$$

where λ_s is the magnetostriction constant and θ is the angle between M_s and σ. Alternatively, we can substitute $(1 - \sin^2\theta)$ by $\cos^2\theta$, drop a constant term, and write the energy as:

$$\varepsilon_{mc} = -\frac{3}{2}\lambda_s \sigma \sin^2\theta. \tag{2.25}$$

The two forms are equivalent with respect to the angular dependence of E_{me} and differ only in what is taken as the zero of energy. In one form or the other these relations are often used to determine the effect of stress on magnetic behavior.

Usually the magnetostrictive strain is small in most magnetic materials, for example permalloy is consider as near zero magnetostriction material, where the magnetostriction energy is neglected. However, in amorphous materials such as glass-covered magnetic wires and amorphous tapes, this term is the most important due to the high stresses induced during the manufacturing process [52].

Chapter 3

Magnetization Dynamics

This chapter is dedicated to the presentation of dynamic aspects of magnetization first we briefly recall the terms related to the magnetization dynamics, the equation of motion. The equilibrium and metastable magnetic states correspond to global respective local minima of the total energy. The transition from one stable state to another or the relaxation from an out-of-equilibrium state towards the nearest minimum is given by the Landau-Lifshitz-Gilbert equation, which describes the magnetization dynamics. Its solution, for given boundary conditions will yield the magnetization trajectory (evolution of $\vec{M}$ in time). In the last section we discuss the spin waves and different types of spin waves modes and confined spin wave modes in patterned magnetic structures.

3.1 Introduction

If the magnetization is not in equilibrium, i.e., if $\vec{M}$ is not parallel to the internal magnetic field, the magnetic moments of a magnetic material experience a torque which induces a precessional motion about the direction of the external field. In addition, the moments try to align themselves along the external field to minimize the energy. Effectively, they execute a damped spiral motion about the field direction which is referred to as magnetization dynamics (see Fig.3.1). The net behavior of dynamic magnetization is phenomenologically illustrated by the Landau-Lifshitz and Gilbert (LLG) equation of motion. The LLG equation is a torque equation, which was first introduced by Lev Landau and Evgeny Lifshitz in 1935 as the Landau-Lifshitz (LL) equation [65]. Later, Gilbert modified it by inserting a Gilbert damping term [66].

Magnetization dynamics, where one investigates the time-dependent motion of the magnetization rather than its equilibrium behavior, is an important access to the magnetism of materials. In simple case, the magnetization dynamics (basically the precessional motion of the magnetization) can be accounted for by a frequency-dependent permeability tensor. An incident electromagnetic wave then interacts with the magnetic system through the permeability, and can have its wavelength, phase, transmission, reflection, and absorption all influenced by the properties of the magnetic material or by an external magnetic field that acts on the material.

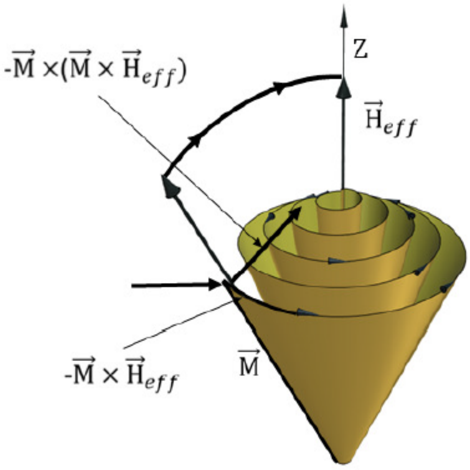

Figure 3.1: Precession of magnetization vector [6]

3.1.1 The Landau-Lifshitz-Gilbert Equation

The magnetic moment is also known as magnetic dipole $\vec{m}$ on the atomic scale. When an effective magnetic field $\vec{H}_{eff}$ is applied, it experiences a torque $\vec{\tau}$ given as:

$$\vec{\tau} = \frac{\mathrm{d}\vec{L}}{\mathrm{d}t} = \vec{m} \times \vec{H}_{eff}\,, \tag{3.1}$$

where $\vec{L}$ is the classical angular momentum, which is proportional to $\vec{m}$ ($\vec{m} = \gamma\vec{L}$, where γ is the gyromagnetic ratio. Substitute this in Eqn. 3.1 and consider the magnetization of a single-domain particle in its effective magnetic field as:

$$\frac{\mathrm{d}\vec{m}}{\mathrm{d}t} = -\gamma\left(\vec{m} \times \vec{H}_{eff}\right), \tag{3.2}$$

where $\gamma = g\mu_B/\hbar$ is the gyromagnetic ratio, g is the Lande-factor ($g \approx 2$), μ_B is the Bohr magnetron and $\hbar$ is the reduced Planck constant. Here, the effective magnetic field H_{eff} is a sum of all external and internal magnetic fields:

$$\vec{H}_{eff} = \vec{H}_0 + \vec{h}(t) + \vec{H}_{ex} + \vec{H}_{dem} + \vec{H}_{ani}\,, \tag{3.3}$$

where $\vec{H}_0$ is the applied bias magnetic field, $\vec{h}(t)$ is the dynamic component, $\vec{H}_{ex}$ is the exchange field and $\vec{H}_{dem}$ represents the demagnetization field created by the dipolar interaction of magnetic surface and volume charges. $\vec{H}_{ani}$ includes all kinds of anisotropic fields described in the chapter 2. All these magnetic fields can be calculated as the first derivatives of the corresponding energies with respect to the magnetization vector[67].

Physically, the above equation 3.2 features a continuum precession which means that the system is non-dissipative. To avoid this impractical situation, Landau and Lifshitz proposed the damping term proportional to: $-\vec{M} \times \left(\vec{M} \times \vec{H}_{eff}\right)$. Later, Gilbert introduced another damping term into the LL equation resulting in the so-called Landau-Lifshitz-Gilbert (LLG) equation. The magnetization dynamics $\vec{M}$ of a magnetic system under the effect of a external magnetic field is described as [67, 68]:

$$\frac{\mathrm{d}\vec{M}}{\mathrm{d}t} = \underbrace{-\gamma\left(\vec{M} \times \vec{H}_{eff}\right)}_{\text{precessional term}} - \underbrace{\frac{\alpha}{M_s}\left(\vec{M} \times \frac{\mathrm{d}\vec{M}}{\mathrm{d}t}\right)}_{\text{damping term}}, \tag{3.4}$$

where α is the phenomenological and dimensionless damping parameter. The equation 3.4 consist of a precessional and a damping term. As a result of the damping term, the motion of the magnetization follows a helical trajectory as shown in Fig. 3.1 for the magnetization relaxation toward the equilibrium state (or the closest minimum). In absence of damping ($\alpha = 0$) the magnetization $\vec{M}$ processes indefinitely around the effective field H_{eff} and will never align to the effective field in this case the LL and the LLG equations are equivalent. The damping mechanism is associated to the coupling between the magnetic spins and other degrees of freedom (phonons, electrons) as well as impurities and defects) [69]. On the other hand, when ($\alpha \neq 0$) the magnetization executes precessions around the effective field, which are explained by an angle that is exponentially decaying as shown in Fig. 3.2. Regarding the damping parameter as phenomenological implies that the microscopic origin of the magnetic damping is not completely understood in detail and constitutes a very active area of research. Possible relaxation mechanisms can be divided into intrinsic and extrinsic processes. Unavoidable processes, like direct coupling of the magnons to the lattice via spin-orbit interaction and eddy currents mediated by free electrons present in conducting materials are refereed to as intrinsic processes. Scattering processes due to sample imperfections leading to magnon-magnon scattering [70, 71, 72, 73] are extrinsic contributions to damping. An experimental access to purely intrinsic damping is given by conventional FMR, as described in chapter 4. However, in

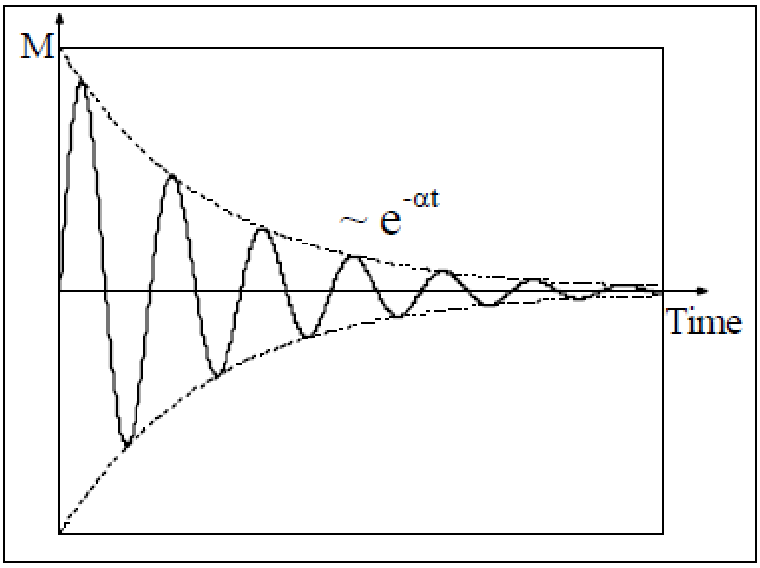

Figure 3.2: Attenuated magnetization processions around the effective field, for $\alpha > 0$.

general, nonuniform excitation and a small bias field range prevent the separation of extrinsic and intrinsic contributions to damping. The mixture of the two contributions are accounted for in this work by introducing an effective damping constant α_{eff}.

3.2 Ferromagnetic Resonance FMR

When a ferromagnetic material is subjected to an alternating field, the magnetization vector may precess around its equilibrium direction. The ferromagnetic resonance (FMR) occurs when the oscillation frequency of the applied field is equal to the magnetization resonance frequency [74].

The simplest case of FMR occurs when the field is strong enough to remove the domain structure, i.e. the sample is magnetically saturated. In this case the precession could be uniform, where all the spins are parallel and developing an oscillation in phase (as shown in the Fig. 3.4(a)). However, FMR can also occur in unsaturated states and the resonance modes may be non-uniform, indicating areas of different magnetizations. In the case of non-uniform precession the propagation of phase shift across the spin system (as shown in the Fig. 3.4(b)) and hence the mutual interactions between the moments play a crucial role in determining the wavelength, frequency and overall dispersion behavior of the spin wave. In the long-wavelength regime, the phase difference between consecutive spins is rather small, the spin wave energy is

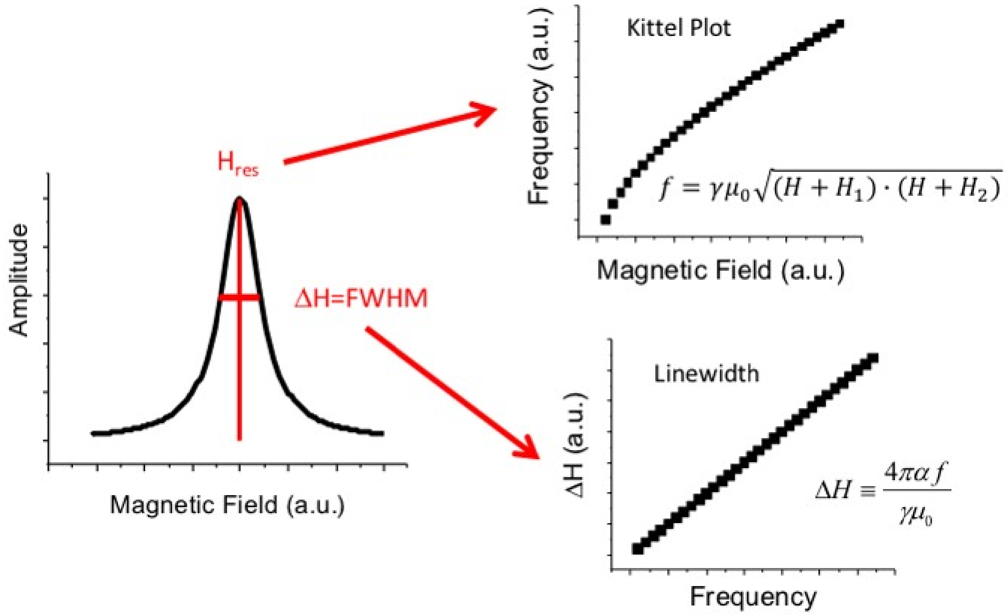

Figure 3.3: Fitting of FMR spectra to the Landau-Lifshitz equation allows us to extract the magnetic anisotropy field and damping constant. The FMR linewidth is decomposed into damping (slope) and inhomogeneous broadening ΔH_0 (intercept) [7].

primarily dominated by dipolar energy and the spin waves are referred to as dipolar-dominated or magnetostatic spin waves. On the other hand, the short-wavelength spin waves are governed by exchange interaction and known as exchange spin waves [52, 67].

The dispersion relation can be obtained as a function of the resonance frequency for each applied external field ($f_r \times H$). This allows us to describe property such as damping constant, inhomogeneous broadening ΔH_0 (as shown in Fig. 3.3). Moreover, one can also calculate the anisotropy and coupling field. The dependence of the field with the resonance frequency can be obtained from the Smit-Beljers relation [75, 76].

$$\frac{\omega^2}{\gamma_o} = \frac{1}{M_s^2 \sin^2(\theta)} \left[\frac{\partial^2 F}{\partial \theta^2} \frac{\partial^2 F}{\partial \phi^2} - \left(\frac{\partial^2 F}{\partial \theta \partial \phi} \right)^2 \right], \tag{3.5}$$

where F is the magnetic energy of the system,M_s is the saturation magnetization, γ_o is the gyromagnetic ratio, θ and ϕ are the polar and azimuthal angles of the magnetization vector, respectively. By minimizing the free energy of the system, the dispersion relation can be obtained in terms of second order derivative of the energy relation to the magnetization equilibrium angles of the magnetic layer. In continuous media, which behave as a single spin, there is only one mode of oscillation.

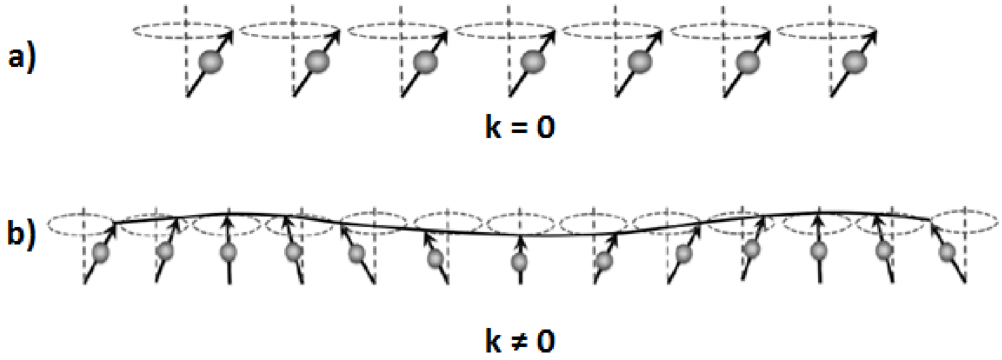

Figure 3.4: Illustration of the uniform precession mode (a) Illustration of a of spin wave in a ferromagnetic system in one dimension (b).

In the case of structured materials such as magnonic crystal there are different modes of oscillation. For this, it is necessary to study the systems with confinement in nanoscales that will influence the homogeneity of the magnetization with the presence of demagnetizing fields that can be controlled by the geometry of the system [38, 77, 69, 78]. In the last two sections of this chapter we will discuss these systems in details.

3.3 Spin Waves

In 1930, the idea of spin waves was introduced by Bloch [79]. The higher order excitations in ferromagnetic film may cause the magnetic moments to precess with the same frequency but at different phases, which is known as spin waves (as shown in Fig. 3.4(b)). The spin wave carries information about system energy such as the anisotropy energy, the external magnetic field or the saturation magnetization (M_s). Therefore, measurements of spin wave frequencies are an important tool to characterize any magnetic systems. There are different types of experiments that are commonly used to study spin waves e.g. neutron-scattering [80], Spin-Polarized Electron Energy Loss Spectroscopy (SPEELS) [81], Brillouin Light Scattering (BLS) [82, 83], Ferromagnetic Resonance (FMR) [84, 85] and broadband Ferromagnetic Resonance (VNA-FMR). In this work the VNA-FMR techinque is used, where a coplanar wave-guide is connected with the vector network analyzer (VNA), which allows one to determine the natural precession frequency from the damped oscillations measured in the frequency domain (more details are given in Chapter 4).

Spin waves can be classified into different types depending on their wavelength, such as, dipole or exchange dominated spin waves. In the following subsection a general description of the different spin waves modes is discussed.

3.4 Magnetostatic Modes

The characteristics of magnetostatic spin waves propagating in thin ferromagnetic films were first reported by Damon and Eshbach [86] in 1961. The dipolar interaction being anisotropic, the frequency, amplitude and propagation properties of magnetostatic modes strongly depend on the geometry of their propagation direction with respect to the applied field and the film plane. Let us briefly consider three main spin wave configurations and the corresponding dispersion relations for a wave propagating in a thin film with a thickness d [87].

Here, for all three configurations, the external magnetic field $\vec{H}_0$ is along the z direction, the precession axis of the magnetization vector $\vec{M}$ is also along the z direction, and the wavenumber vector $\vec{k}$ is along the film strip length and points to the right. In each dispersion diagram, the curve shows the change of spin-wave frequency ω with wavenumber $\vec{k}$.

In each dispersion diagram, the curve shows the change of spin-wave frequency ω with wavenumber k. The three horizontal dashed lines indicate the characteristic frequencies $\omega_H = \gamma\vec{H}$, $\omega_B = \gamma[\vec{H}(\vec{H} + 4\pi M_s)]^{1/2}$, and $\omega_S = \gamma(\vec{H} + 4\pi M_s/2)$, where γ is the absolute gyromagnetic ratio, $\vec{H}$ is the net internal static magnetic field, and $4\pi M_s$ is the saturation induction of the magnetic film. The field $\vec{H}$ usually consists of the external field $\vec{H}_0$, the effective anisotropy field $\vec{H}_a$, and the demagnetization field $\vec{H}_d$.

Moreover, the dispersion relations for three different types of the magnetostatic spin waves modes in Fig. 3.5 were calculated for $4\pi M_s$= 1750 G, γ = 2.8 MHz/Oe, $\vec{H}$= 1500 Oe and d = 5 nm.

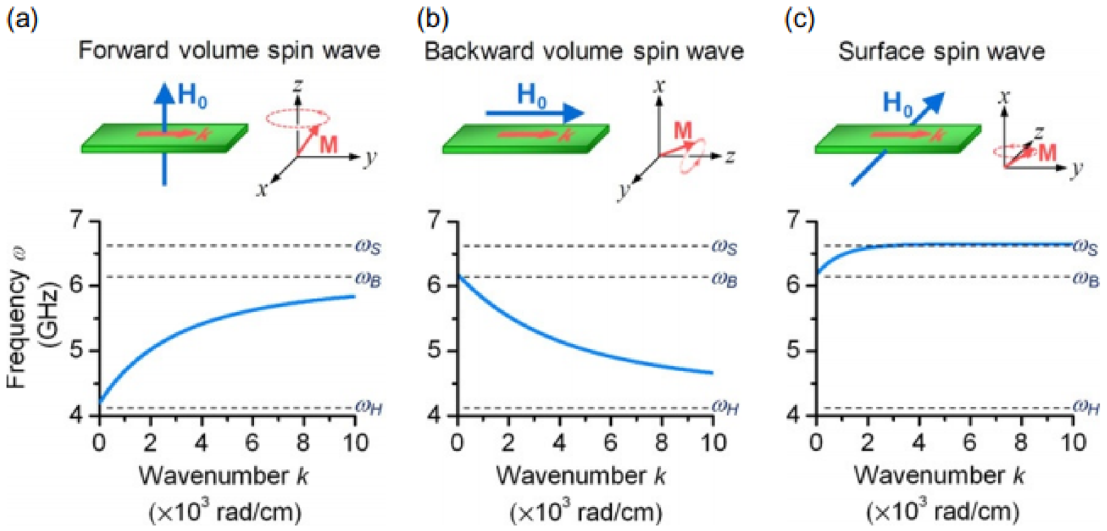

Figure 3.5: Field/film configurations, magnetization precessions, and dispersion diagrams for three classes of spin waves in a long and narrow magnetic thin film strip. In each dispersion diagram, the curve shows the spin-wave frequency as a function of wavenumber, and the horizontal dashed lines show three characteristic frequencies, as indicated [8].

3.4.1 Magnetostatic Forward Volume Wave (MSFV)

A magnetostatic wave, which propagates in the film plane ($\vec{M} \parallel \hat{n}$) with the magnetization perpendicular to the plane ($\vec{M} \perp \hat{n}$), is called Magnetostatic Forward Volume Wave (MSFV) Fig. 3.5 (a). The dispersion relation for the MSFV mode, which writes as [88].

$$\omega^2{}_{MSFV} = \omega_H \left[\omega_H + \omega_M \left(1 - \frac{1 - e^{-2k_\parallel d}}{k_\parallel d}\right)\right], \tag{3.6}$$

depends on the magnitude of the wave vector and does not depend on its direction. Following equation 3.6, the resonance frequency increases with $\vec{k}$ increasing Fig. 3.5 (a) indicating a forward wave character.

3.4.2 Magnetostatic Backward Volume Wave (MSBV)

The MSBV are the waves in which the wave vector in the plane is colinear with the magnetization that is also in the plane Fig.3.5 (b). While these modes are located on the surfaces of the sample, the amplitude of the MSBV is evenly distributed over the entire thickness of the film.

An approximate dispersion relation for the volume backward spins wave was determined by Kalinikos [89]

$$\omega^2{}_{MSBV} = \omega_H(\omega_H + \omega_M) + (\frac{1 - e^{-2k_\| d}}{k_\| \quad d}). \tag{3.7}$$

At the limit $k_\| \rightarrow 0$ one can also find the frequency of uniform precession in the plane. The quantification of MSBV modes has been observed in laterally confined systems such as transverse magnetized nanowires due to inhomogeneity of the internal generated fields.

3.4.3 Magnetostatic Surface Wave (MSSW)

The magnetostatic surface wave modes (MSSW) Fig. 3.5 (c), also called Damon-Eshbach (DE), are observed when both the applied field and the spin wave wavevector $\vec{k}$ lie in the film plane and are perpendicular to each other. The dispersion relation of a magnetostatic surface wave is described as below [86]

$$\omega^2{}_{\mathrm{MSSW}} = \omega_H(\omega_H + \omega_M) + \frac{\omega_M^2}{4}(1 - e^{-2k_\| d}). \tag{3.8}$$

For the limiting case $k_\| \rightarrow 0$ we find the frequency of the in plane uniform precession. Typically the quantization of DE modes has been observed in laterally confined systems, for example in the case of disks in saturated state and magnetized nano lines along their length due to the spatial confinement on the side of the structure.

3.5 Spin Waves in confined systems

In the discussion above, we considered the general properties of spin waves in an infinite thin film. When the is structure is confined, the spectrum of spin wave modes is modified by the boundary conditions imposed by the lateral dimensions [90]. In particular, the spin waves may find a propagation channel [91] or form standing waves [92] in the distribution of "potential wells" defined by the geometry of the structure. The standing wave often leads to a localized mode or quantized mode (with multiple quantization numbers) when the sample dimensions are of the order of the wavelength of the spin wave. Overall, the number of spin wave modes within a given frequency range increases with increasing size of the structure, whose properties are strongly dependent on the system geometry as well as on the direction of the magnetic field.

3.5.1 Perpendicular Standing Spin Waves (PSSW)

The excitation of magnetostatic modes occurs especially in dipole−dipole interaction dominated systems where the wavevector ($\vec{q}$) lies in the film plane. The modes with wavevector ($\vec{q}$) component perpendicular to the film surface are termed perpendicular standing spin wave (PSSW) modes and the quantization of these modes is due to the geometrical confinement (as shown in the Fig. 3.6) [93]. In FMR, the external microwave field couples with uniform and non uniform spin wave modes. In previous section we explained about the uniform mode excitation. Besides the uniform mode, we can also explored the higher order modes in ferromagnetics with FMR.

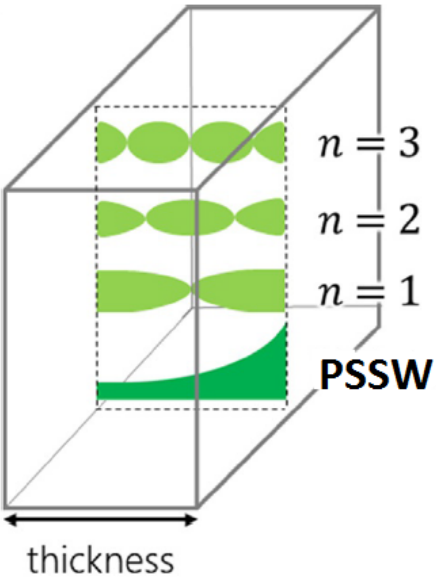

Figure 3.6: The profile of the fundamental mode ($n = 0$) and perpendicular standing spin wave modes (n = 1, 2, 3) are sketched across the film thickness [9].

3.5.1.1 Theoretical Background of PSSW

In the following section, we discuss the formalism of the dispersion relation for uniform and PSSW. The free energy density of a single magnetic thin film can be written as,

$$\begin{aligned} F = & -M_sH\left[\sin\theta_H \sin\theta_M \cos(\phi_H - \phi_M) + \cos\theta_H \cos\theta_M\right] \\ & - 2\pi {M_s}^2 \sin^2\theta_M - K_u \sin^2\theta_M \cos\phi_M \cos^2\phi_u \\ & + sin^2\theta_M \sin\phi_M \sin^2\phi_u + K_\perp \sin^2\theta_M. \end{aligned} \tag{3.9}$$

In the above expression, ϕ_H and ϕ_M are azimuthal angles corresponding to H and M directions, respectively. θ_H and θ_M are polar angles (as shown in the Fig. 3.7). The

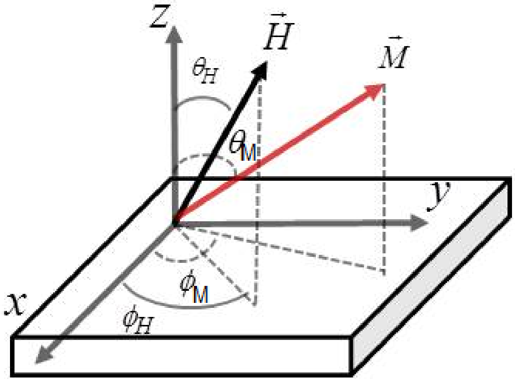

Figure 3.7: Schematic diagram of magnetization (M) and external magnetic field (H) vectors in spherical polar coordinate system [10].

first term in the above expression corresponds to the Zeeman energy, and the second term is dipolar demagnetization energy. The third and fourth terms represent the uniaxial planar and perpendicular magnetic anisotropy energies, respectively. M_s is the saturation magnetization, K_u and $K_\perp$ are the in-plane and out of-plane uniaxial magnetic anisotropy constants, respectively. The resonance frequency (f_r) of the uniform precession mode is deduced from the energy density by using the equation number 3.5 [76]. The resonance equations for planar configuration are solved at the equilibrium position of $\vec{H}$ under the applied magnetic field ($\vec{M}$) by enforcing the condition

$$\frac{\partial F}{\partial \phi} = 0.$$

The solution of H from the energy minimization condition is;

$$H = \frac{2K_u \cos\phi_M \sin\phi_M}{M_s \sin(\phi_H - \phi_M)}. \tag{3.10}$$

The in-plane ($\theta_H = \theta_M = \frac{\pi}{2}$) dispersion relation of the uniform and PSSW modes can be modeled in a combined way from the total magnetic energy density, which arises from the exchange and dipolar interactions and the corresponding resonance frequency is given by [94, 95].

$$\begin{aligned} f_r = &\left(H\cos(\phi_M - \phi_H) + \frac{2K_u}{M_s}\cos 2(\phi_M - \phi_u) + \frac{2A_{\text{ex}}}{M_s}(\frac{n\pi}{t})^2 \right)^{\frac{1}{2}} \\ &+ \left(H\cos(\phi_M - \phi_H) + 4\pi M_{\text{eff}} + \frac{2K_u}{M_s}\cos^2(\phi_M - \phi_u) + \frac{2A_{\text{ex}}}{M_s}(\frac{n\pi}{t})^2 \right)^{\frac{1}{2}}, \end{aligned} \tag{3.11}$$

where t is the thickness of film and γ is the gyromagnetic ratio, A_{ex} is the exchange stiffness constant and n is the quantized number for the PSSW along the thickness direction. $n = 0$ represents the uniform precession mode and the higher order modes ($n = 1, 2, 3, ...$) represent PSSW mode.

3.6 Elliptical Nanostructures

Nanomagnets can display a variety of magnetic states due to confinement, such as single vortex and double vortex. It is therefore instructive to explore dynamics aspects and interaction in these systems.

We start describing a single vortex structure in restricted geometry, also known as a nonlocalized soliton, that exhibits a curling spin structure in the XY plane around its equilibrium position. This two dimensional topological defect is characterized by three "topological charges":

- The *Vorticity* q: This is a very general quantity related to the topology of the magnetic moments curling in the XY plane. The vorticity quantity q is an integer multiple of 2π, generally known as the winding number. As can be seen in Fig.3.8, positive q is related to vortex structures and negative q to anti-vortices. In this thesis, only vortices with vorticity equal to ± 1 will be considered.
- The *Polarity* p: It defines the relative orientation of the magnetic moments inside the vortex core with respect to the plane of the ferromagnet. This quantity p can only take values $\pm$ 1.
- The *Chirality* C: This quantity completes the vorticity by giving information about the rotation of the spin vector in a circular contour around the vortex. It can be clockwise or counterclockwise, so $C = \pm$ 1.

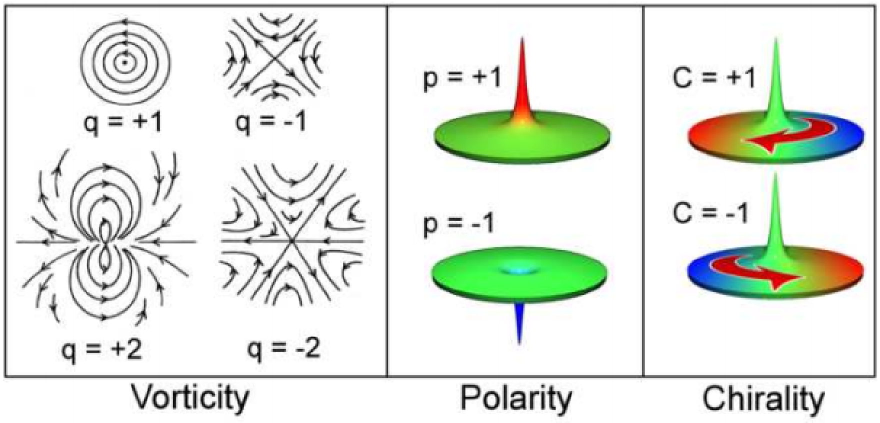

Figure 3.8: Topological "charges" of a ferromagnetic vortex: Vorticity (or winding number, from Mermin [11]), Polarity and Chirality.

For nanomagnets with ellipitical cross section, depending upon the size and thickness of the ellipses, there could be different magnetic statesand some examples are illustrated in Fig. 3.9. Here, the letters label regions with different spin configurations: (A) in-plane quasi-uniform magnetization; (B) perpendicular quasi-uniform magnetization; (C) in-plane vortex; (D) double In-plane vortex; (E) lateral vortex. Here, all the ellipses have semiaxes ratio $a/b = 2$.

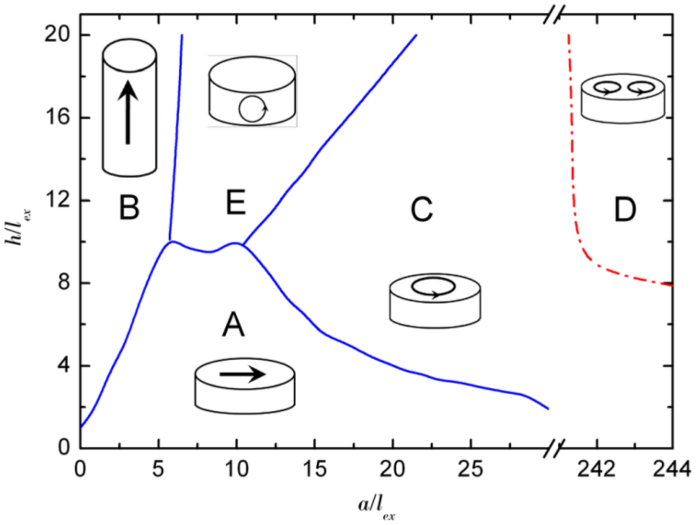

Figure 3.9: Phase diagram for elliptical nanodot of permalloy, as a function of the reduced height h/l_{ex} and reduced semiaxis axis of the ellipses a/l_{ex} ($l_{ex}$is the material exchange length). Note the break in the horizontal scale, to reveal the appearance of two-vortex structures obtained for larger ellipses, from Guimaraes [12]).

The magnetization reversal in this kind of samples can occur through the nucleation of one or more vortices depending on their geometry. This case is typical for ellipses with the major axis above 2 μm. For a double vortex, the magnetization circulation has opposite directions of rotation, that is, one core rotates clockwise and the other core counterclockwise in the same ellipse (see Fig. 3.10 D). However, the polarities of the vortexes can be the same ($p1 \cdot p2$ = +1), or opposite ($p1 \cdot p2$ = -1) [96].

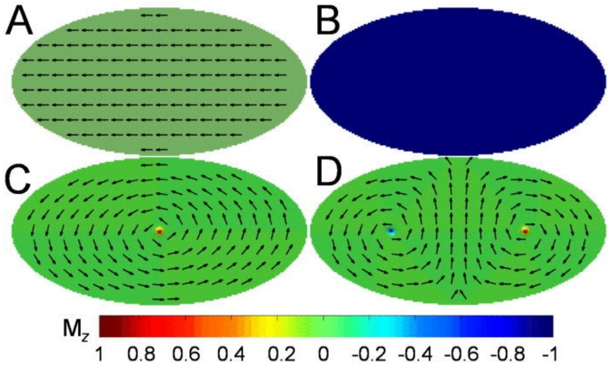

Figure 3.10: Magnetic configurations of elliptic nanodots that appear in the phase diagram of Fig. 3.9.

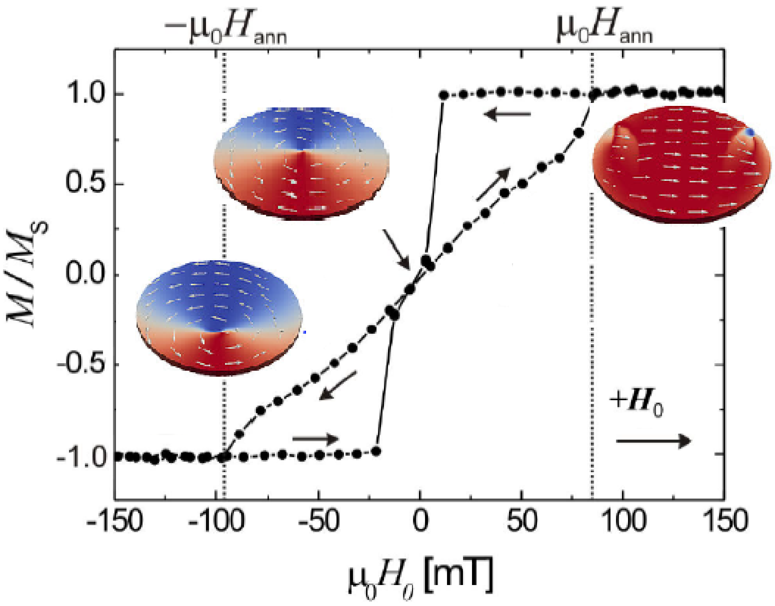

Figure 3.11: Typical hysteresis loop of magnetic vortex state [13].

In Fig. 3.11 we have a hysteresis curve for a permalloy elliptical sample. Depending on the Zeeman energy, the magnetic moments are energetically aligned parallel to the external magnetic field. For a vortex configuration, the static magnetic field in the plane increases the size of the domain with parallel orientation. This effect in turn causes a displacement of the core of the vortex perpendicular to the applied field, as illustrated by micro-magnetic simulation in the inset of Fig. 3.11.

3.6.1 Vortex state oscillation modes

In this thesis, we will study the spin waves in vortex state for an elliptical magnetic nanostructures with different sizes and same aspect ratios with broadband VNA-FMR and micromagnetic simulations.

Here in the following section, we will discuss the simulated oscillation modes at vortex state, as an example to understand the results in the Ch.6. Moreover, the red areas shows the excitation amplitude within the individual ellipse.

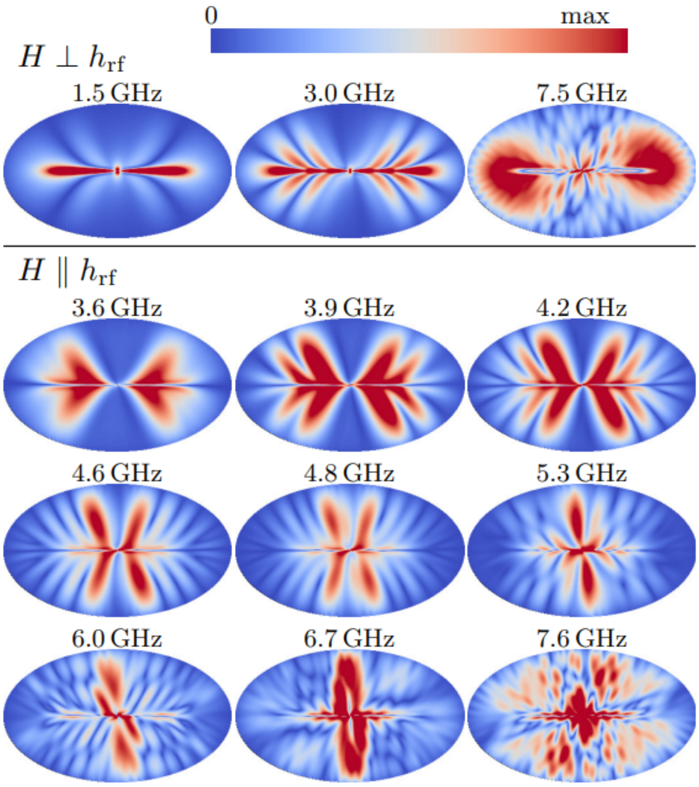

Figure 3.12: Main modes in-plane component of the magnetization oscillations at H = 0 Oe [14].

The vortex state oscillation modes were studied in our group by Dutra et. al. [14]. The numerical simulations for oscillating magnetization M_{osc} amplitude is presented in 3.12. For all modes, the in-plane component of M_{osc} is mostly in quadrature ($\pm\pi/2$ phase difference) with h_{rf} at f_r, and there is no continuous change in the phase with respect to the position. They observed standing spin waves modes with remarkable contrast, where spin waves circulate around the vortex core. For frequencies below 4.8 GHz, standing spin waves with wave vector locally parallel to the static magnetization were observed. The wave length decreases with increasing frequency, and consequently the observed number of nodes gradually increases. The simplest mode observed corresponds to the absorption peak at 1.5 GHz, where only two large intensity anti-nodes are observed. For frequencies higher than 4.8 GHz the mixed oscillation modes were observed, with wave vectors parallel and perpendicular to the static magnetization (as shown in the Fig. 3.12).

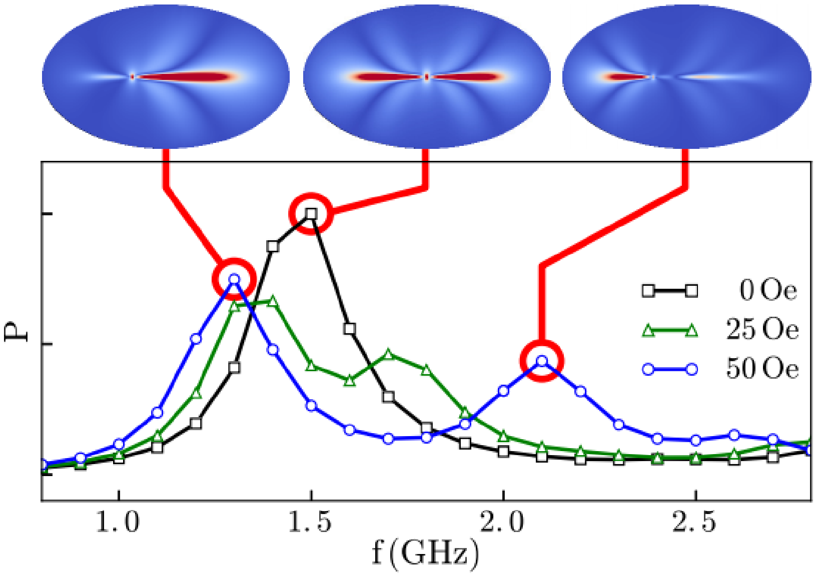

Figure 3.13: Vortex core motion and frequency splitting of the 1.5 GHz mode due to applied external magnetic field [14].

The numerical simulations for the frequency splitting due in-plane field is shown in the Fig. 3.13. In the case of $H = 0$ a single absorption peak with $f_r = 1.5$ GHz is observed. The corresponding oscillation mode is symmetric with respect to the vortex core and shows two anti-nodes with equal amplitudes, along the major ellipse axis. When a field is applied perpendicular to the major axis the vortex core is displaced, breaking the symmetry in the ellipse magnetic configuration. In this case, the two regions at each side of the vortex are different. The resonant frequency of the shrinking region (top right mode in Fig. 3.13) rapidly increases with H as the contributions to exchange, dipolar and Zeeman energies increase. On the other hand, in the growing region (top left mode in Fig. 3.13), the exchange and dipolar energies decrease with H. This leads to an initial frequency drop, but with larger H the frequency rises as the Zeeman energy becomes dominant.

The magnetization curling changes and the associated exchange energy depend, both, on the ellipse aspect ratio. In this thesis, we studied the ellipses with different sizes, where the mode at 1.5 GHz is intrinsically related to the exchange energy as the frequency and amplitude increase for smaller ellipses. On the other hand, the mode observed at 7.5 GHz the dipolar energy seems to be dominant as, both, the oscillation amplitude and frequency are almost not changed for different ellipse sizes (the details are given in Ch. 6).

3.7 Antidot Nanostructures

Magnetic antidot lattices are exciting objects composed of a periodic array of pores (antidots) within the continuous magnetic film [97, 98, 99]. The magnetization is distributed periodically in its ground state along the array of antidot lattice, which is altered by the application of external magnetic fields. Antidot lattices (ADL) are therefore ideal candidates to study the combined behaviour of non-trivial periodic distributions under the influence of external disturbances. To achieve the stable magnetization configurations in antidot lattices, and to realize the occurrence of reliable field driven switching between these states, it is essential to understand magnetization reversal processes in antidot lattices. Many research efforts have been made to study the magnetization reversal in antidots, several of them are focussed on the macroscopic aspects of the reversal mechanisms, for example the effects of lattice geometry and spacing on the coercivity and magneto-resistive properties [99, 100, 101] also on the magnetization dynamics [102]. The magnetization reversal behaviour of ADL can be tuned using a number of geometric parameters viz., the antidot shape (square, elliptical or circular), the lattice geometry (square or hexagonal), the antidot diameter and inter-antidot spacing, and the thickness of the antidot lattice(some examples are shown in the Fig. 3.14). In this thesis the magnetization dynamics of ADLs, with circular shape and square lattice geometry are studied.

The continuous film displays an intrinsic uniaxial anisotropy which could be modified by the presence of hole arrays. In the case of antidot array with a square lattice, a fourfold magnetic anisotropy with alternating hard axis (HA) and easy axis (EA) every 45° is observed. Both the honeycomb and rhomboid antidot lattices, however, show a sixfold anisotropy, which conforms well to the symmetry of their respective lattices. The micromagnetic simulation results of the spin states at remanence show that the magnetization reversal process is very sensitive to the lattice arrangement of the holes (as shown in Fig. 3.14).

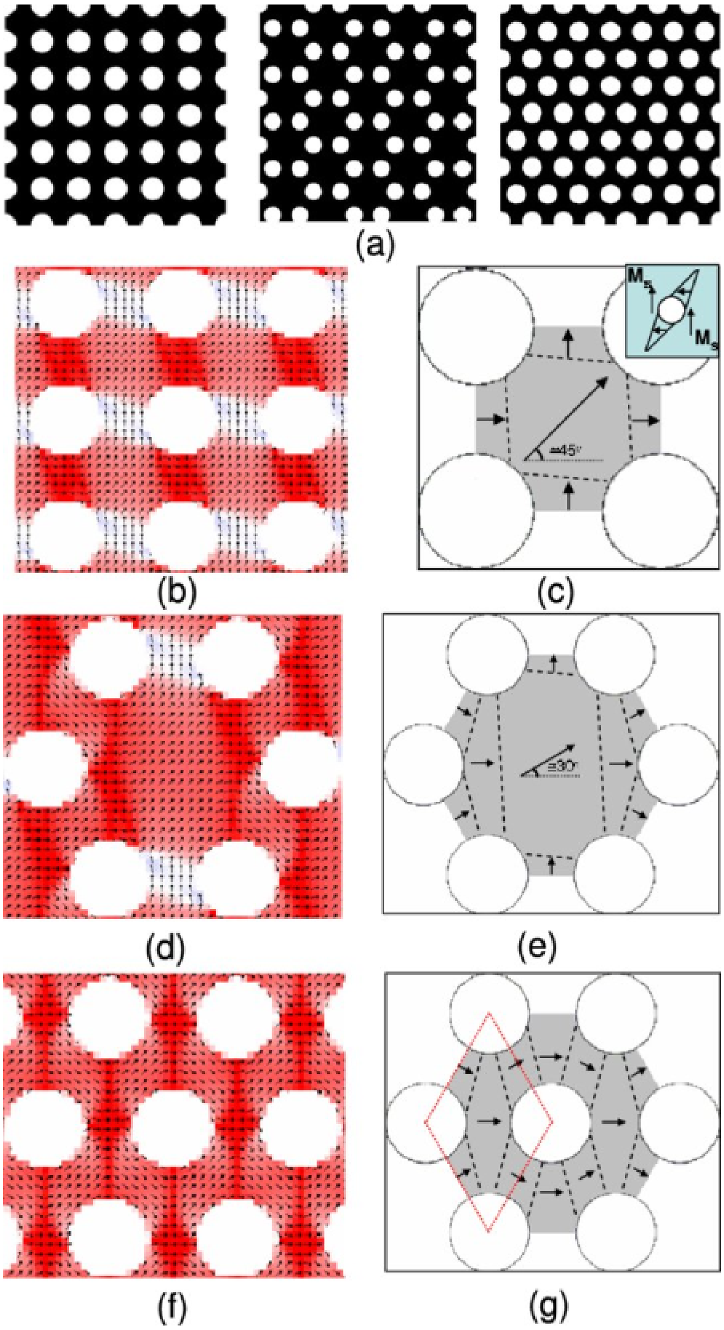

Figure 3.14: (a) The simulation models for the three geometries studied. The remanent spin states in a unit cell captured from the micromagnetic simulation and the sketch of the domain distributions are shown for (b), (c) the square lattice, (d), (e) the honeycomb lattice, and (f), (g) the rhomboid lattice arrays. Note: drawings are not to proportion for the clarity of presentation [15].

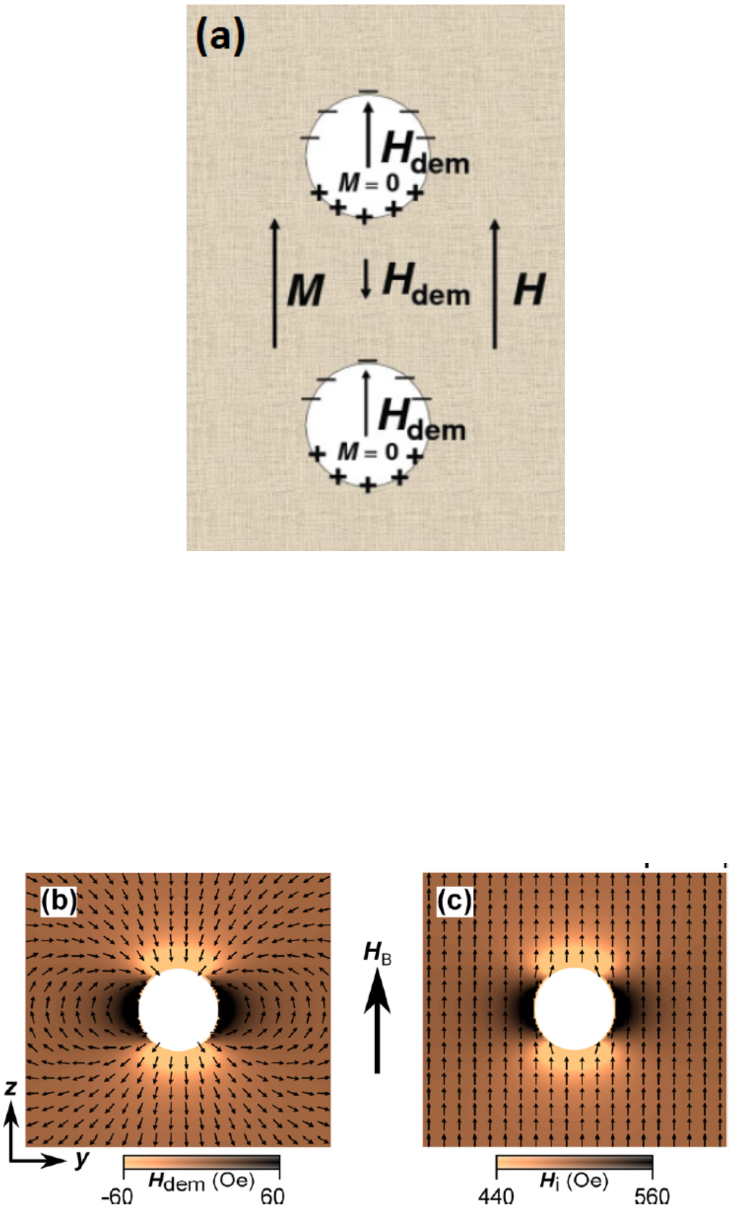

Figure 3.15: (a)Sketch of the antidot lattice with two holes (white) embedded in the ferromagnetic film (dark). The orientations of H_{dem}, H, and M together with the induced surface "magnetic charges" are shown.(b) The calculated distribution of the demagnetizing field in the vicinity of the antidot. (c) The calculated distribution of the total internal field is shown in the vicinity of the antidot [16].

3.7.1 Oscillation modes in Antidots

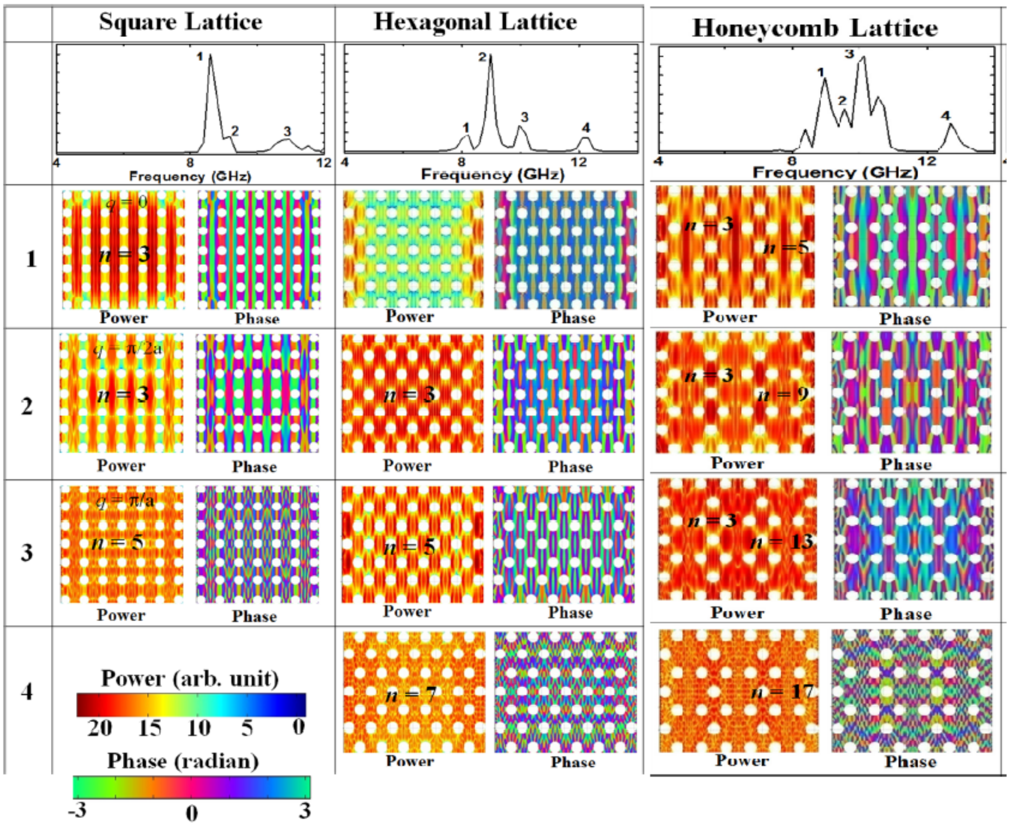

Figure 3.16: Simulated spin wave spectra for the square, hexagonal and honeycomb lattices are shown in the top panel. Simulated spin wave mode profiles (power and phase maps) for the $Ni_{80}Fe_{20}$ antidot lattices with square, hexagonal and honeycomb lattice symmetry are shown in the lower panels. The color scales for the power and phase maps are shown at the bottom of the figure [17].

To understand the magnetization dynamics in ADL, here we discuss simulated spin wave mode profiles for the three different lattices. Fig. 3.16 shows the power and phase maps for all modes, while the color scales for both power and phase are shown at the bottom of the figure. In the case of square lattice when the bias field is applied along the x-direction, and the modes are extended along y-direction giving rise to modes with different wave vectors $\vec{q}$. Moreover, the modes along x-direction form standing waves due to confining potentials produced by the demagnetizing fields around the antidots. Here, n is the quantization numbers (number of antinodes for the standing waves in the backward volume (BV) geometry) for these standing waves. For a square lattice, modes 1, 2, and 3 correspond to Damon Eshbach (DE) modes at the centre $\vec{q} = 0$, middle $\pi/2a$, and the boundary of the first Brillouin zone π/a

(BZ), respectively, where a is the lattice constant of the square lattice. Moreover, along x-direction, these modes correspond to standing spin wave modes in the BV geometry with $n = 3$, 3 and 5.

In the case of hexagonal lattice, no extended modes in the DE geometry are observed as the positions of the antidots along the y-direction cause unavailability of continuous channels of materials along y-direction unlike the square lattice. Hence, no $\vec{q}$ vector corresponding to DE-mode is assigned in this case, and only BV-like standing spin wave modes and localized modes are observed. Mode 1 is a localized mode confined in the potential around the edges of the antidots, while modes 2–4 correspond to BV-like standing spin waves with $n = 3$, 5 and 7. Finally, in case of honeycomb lattice, the BV-like standing wave modes inside the honeycomb unit for modes 1, 2, 3 and 4 are found to have $n = 5$, 9, 13 and 17, while the modes confined between two honeycomb units have $n = 3$ for modes 1, 2 and 3.

Chapter 4

Experimental Techniques

In this chapter we present the details about the experimental techniques and the major steps used during the sample preparation. We used fabrication techniques such as: magnetron sputtering, e-beam lithography (EBL), plasma etching/reactive-ion etching (RIE), techniques used in the clean room and focused ion beam (FIB). The characterization of the intermediate steps were done using the X-ray diffraction (XRD), atomic force microscopy (AFM), the magnetic force microscopy (MFM) and scanning electron microscopy (SEM). These provide us information on the structural, topographic and magnetic structure of the nanostructures samples. Moreover, other characterizations were done with an Alternative Gradient Field Magnetometer (AGFM), Vibrating Sample Magnetometer (VSM), Broadband VNA-FMR and High Resolution Transmission Electron Microscopy (HR-TEM).

4.1 Sample Preparation Techniques

4.1.1 Sputtering Technique

There are different techniques used for deposition of materials such as metals, ceramics, and plastics onto a surface (substrate) to form a thin film. Among these, there is a technique which is known as "sputtering" that has become one of the most common ways to fabricate thin films. Sputtering is a physical vapor deposition (PVD) process used for depositing materials onto a substrate, by ejecting atoms from such materials and condensing the ejected atoms onto a substrate in a high vacuum environment [103].

The main advantages of using a sputtering system are:

- Versatility; since the sputter process is based on the momentum transfer and not on a chemical or thermal reaction, virtually any kind of material can be sputtered;

- Film uniformity over large areas;
- Surface smoothness and thickness control;
- High deposition rates.

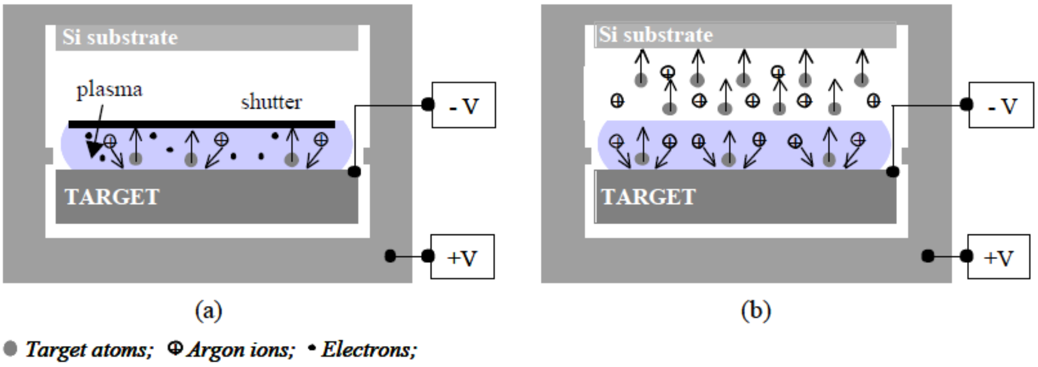

Figure 4.1: Sputtering system: (a) plasma is switched near the target surface; the argon ions are strikes the target and creates the ejection of target atoms, shutter position is closed; (b) the shutter opens, the target atoms are sputtered on the substrate.

The basic process is as follows, consists of ionizing an inert gas (e.g argon) between two electrodes, generating a plasma and the ions of this gas accelerate and collide with the target atoms and pulverize the surface of the substrate. These small particles are deposited on a substrate (as shown in the Fig. 4.1). This is a basic technique for the production of single layers and multilayers samples, which studied in this thesis.

Most deposition processes of magnetic layers, oxide layers, metallic non-magnetic layers, have been realized in the sputtering machines AJA (as shown in Fig. 4.2), that is part of the equipment of the multi-user laboratory LABNANO/CBPF.

This system has capacity of six targets installed at the same time. The targets are connected to DC and RF sources to power the plasma. In both cases, a voltage is applied between the cathode and the anode, a breakdown occurs and plasma is formed and sustained. RF power, though, allows the use of insulating materials as sputtering targets and it increases the level of ionization in the plasma. The main vacuum pump is a turbo pump that allows a pressure of up to 10^{-8} Torr in the main chamber of the system.

An secondary load-lock chamber allows the exchange of samples without breaking the vacuum in the main chamber. The samples are placed in a rotating turret that allows you to take them to the position of each target and control the distance between the target and the substrate. A shutter over the each target allows the control of exposure on the substrate and the precise control of the deposition time via software.

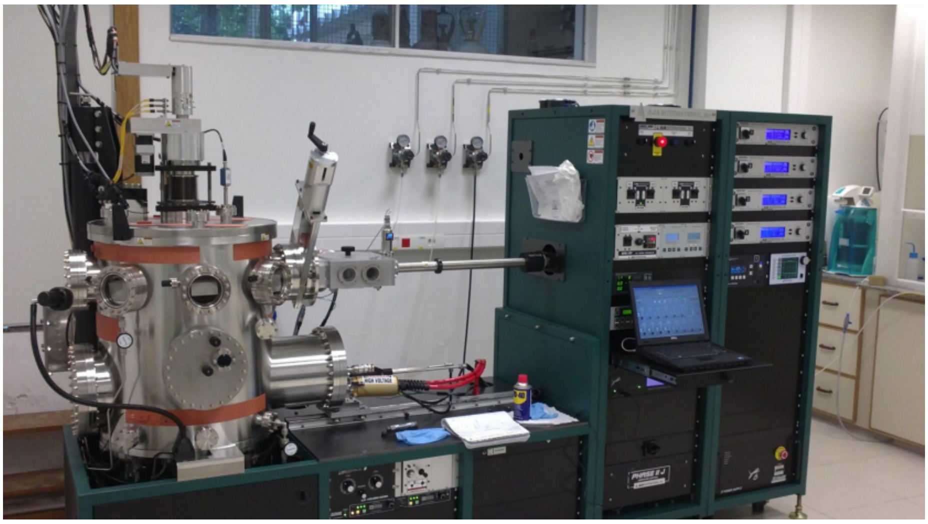

Figure 4.2: Photograph of the LABNANO/CBPF Magnetron sputtering system.

Different substrate holders allow the application of a magnetic field over the substrates during deposition. The entire system is automated and controlled by a computer, allowing automated production of multilayers and other complex structures. The deposition times of each layer, the pressure of argon gas during deposition, and the powers of the DC and RF sources can be automated.

4.1.1.1 Calibration of deposition rates

The deposition rates were calibrated with X-ray reflectometry (XRR), which is an analytical technique for investigating thin layered structures, surfaces and interfaces using the effect of total external reflection of X-rays. Reflectometry is used to characterize single and multi-layer structures and coatings in magnetic, semiconducting and metals among others. X-Ray Diffraction (XRD) is a basic technique for structural characterization of deposited films. It allows the calibration of the deposition rate, crystal crack analysis (high angle diffraction), film thickness and roughness (low angle diffraction). XRD measurements were performed in the crystallography and X-ray laboratory using a Panalytical X Pert PRO (Philips, Panalytical) diffractometer. The source of this diffractometer emits Cu-K$_\alpha$ radiation with waveform of 1.54045 Å. The film thickness is calculated by analyzing the Bragg interference peaks obtained experimentally. For each peak found at angle θ_n, the scattering vector q$_n$ is found given by

$$q_n = \frac{4\pi \sin\theta_n}{\lambda}. \tag{4.1}$$

The linear fitting of ($q = an + b$) of these values vs. the peak number found n the thickness is obtained $t = 2\pi/a$ that of the measured film. When dividing this thickness between the deposition time is found to deposition rate (τ).

$$\tau = \frac{thickness}{deposition\ time}. \tag{4.2}$$

The X-ray spectrum at grazing angles for $Ni_{81}Fe_{19}$ thin film deposited on Si (100) is shown in Fig. 4.3, along with the graph of the scattering vector q vs. index n and the linear fitting ($q = an + b$) of each measured value. The type of gun source and the power chosen for the deposition of each target in the deposition of the films used in this thesis are shown in Table 4.1.

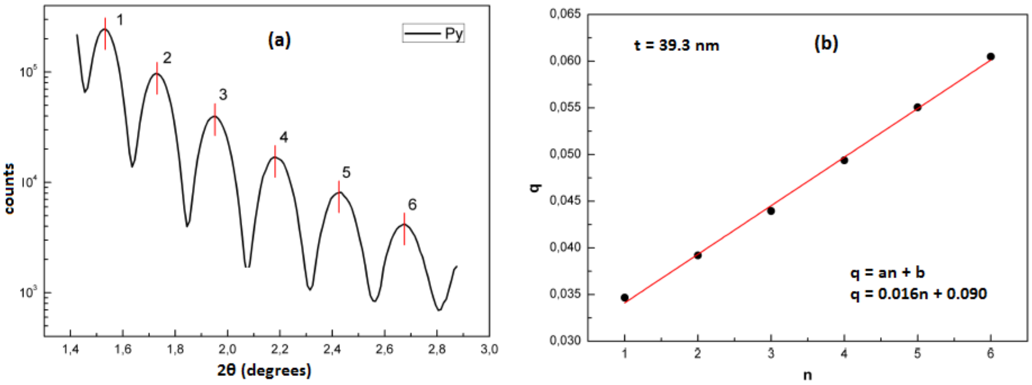

Figure 4.3: (a) X-ray spectra at grazing angles of a $Ni_{81}Fe_{19}$ film. (b) Shows the linear fitting ($q = an + b$) of each measured value. The black dots indicate the n indices and the red line is the linear fitting [18].

Table 4.1: Type of gun source and power chosen for the deposition of each target and deposition rates.

Target	Source	Potencial	Deposition Rate (nm/s)	Method
Ti	DC	150 mA	1.120	XRR
$Ni_{81}Fe_{19}$	DC	150 mA	1.250	XRR
Co	DC	100 mA	0.679	XRR
Ru	DC	100 mA	0.731	XRR
Co_2FeAl	DC	150 mA	0.998	XRR
Cu	DC	150 mA	4.901	XRR
IrMn	DC	200 mA	4.650	XRR
SiO_2	RF	250 W	1.380	FEG-SEM
NiO_2	DC	75 W	0.750	AFM

4.1.2 Electron beam lithography

Electron-beam lithography (EBL) is a field emission gun (FEG) type lithography for construction of nanostructures with high resolution. In this work we developed a method based on EBL for writing nanostructures on SiO_2 substrate using the Raith 150 electron-beam lithography system. The Raith 150 system is capable for control and place patterns with a resolution better than 50 nm.

The EBL setup uses a hardware like a scanning electron microscope (SEM). First, the sample surface is coated with a thin layer of polymer an electron-sensitive resist, which is nothing more than a thin material sensitive to the radiation. The focused electron beam is guided on the surface to form patterns in the resist. The result of this exposure is to provide the resist either soluble (called a positive resist) or insoluble (negative resist) in an appropriate developer solution. The steps used in the e-beam lithography are shown in the Figure 4.4.

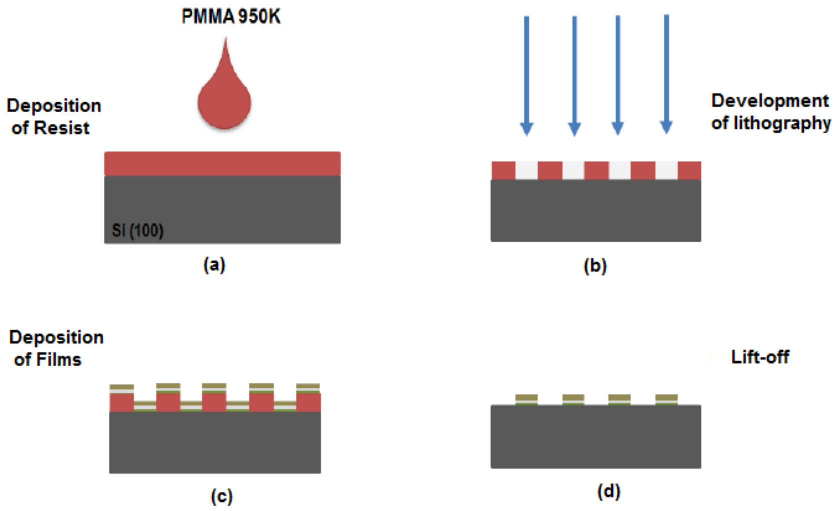

Figure 4.4: Electron beam lithography process: coating of the sample surface with resists (a); exposure of the electron beam resist and revelation of resists (b); deposition of thin film (c) and lift-off process (d).

However, there are limitations to its use in manufacturing large areas of nanostructures because the writing process in EBL is time consuming, thus making the areas greater than 10 mm^2 are extremely difficult [104]. In these cases it is more convenient to use other techniques, such as optical lithography, if not too much resolution is required.

A schematic representation of electron beam lithography system is shown in figure 4.5. It consists of an electron gun, an electron optical column, and a vacuum chamber containing an x/y stage for positioning the substrate under the e-beam.

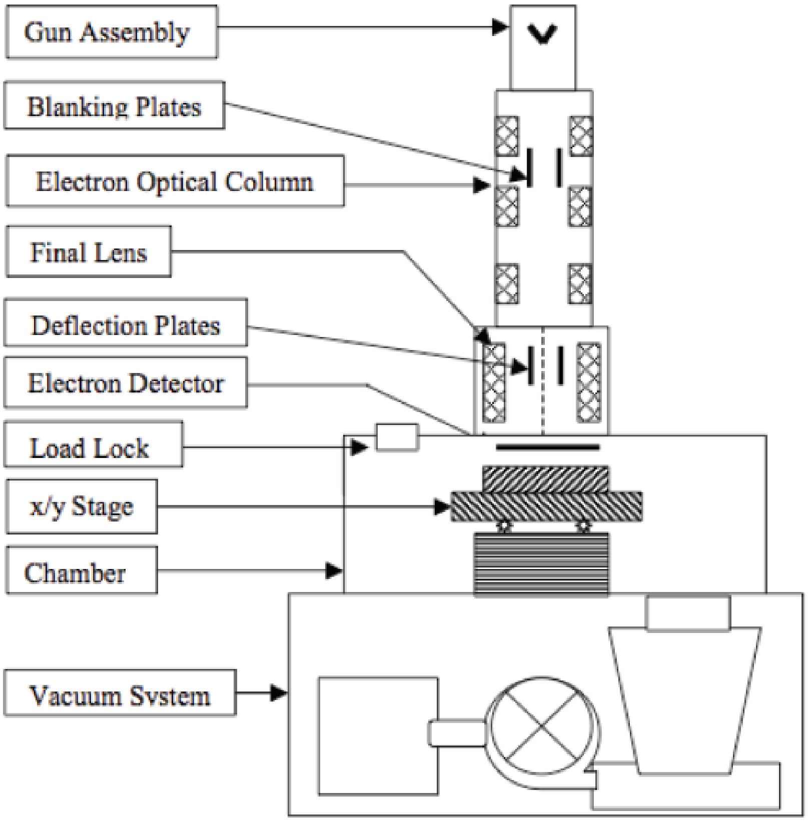

Figure 4.5: Block diagram of a typical electron beam lithography system [19].

The electron beam is focused on the substrate using the optical column, the electrons are produced in the upper section of column, which is called electron source or gun. After the generation of electron beam it passes through several other processes for beam modification for specific beam current and spot size, finally it is correctly focused onto the substrate. The interaction of forward-scatter and back-scatter electrons is illustrated in Fig. 4.6.

Before starting lithography process, the substrate are cleaned with acetone, isopropanol and deionized (DI) water.

i) Clean Room: The first step corresponds to coating the substrate surface with a layer of positive resists PMMA (poly(meth)acrylates) using spin coating.

ii) Dose calibration: The dose must be calibrated accurately before performing lithography. The initial dose could be estimated from the resist data sheet in the

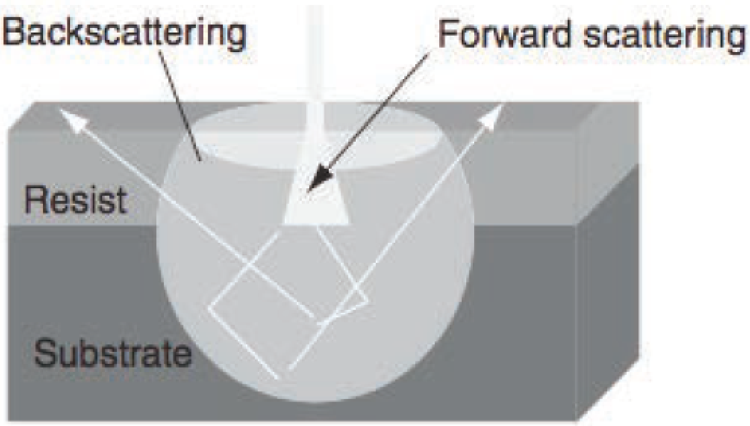

Figure 4.6: Illustration of the short-range (forward-scatter) and long-range (backscatter) interaction of electrons with resist-coated substrate.

case of PMMA 950k, the inital dose was selected 120 μC/cm^2. First we did the rough calibration in which the dose was changed with 10 μC/cm^2 per step. After we selected the best dose and then did the fine calibration, in which each step was changed with 2 μC/cm^2 per step. The dose design consist of the required nanostructure for example ellipse or circle with desired dimensions. SEM observation after metallization and lift-off allows then for finding the optimal dose.

iii) Lithography: The lithography step corresponds to exposure of the PMMA resist to the electron beam with calibrated dose, which modify its chemical characteristics, in such a way that a selective removal of the exposed material thus creating the desired pattern. The exposure of the substrate to the electron beam is made in a high-resolution scanning electron microscope. The LABNANO/CBPF electron beam nanolithography is a system of nano-engineering work from e-line RAITH Gmbh.

iv) Development: After the resist is exposed to the electrons, it was developed in the solution. The developer used is a mixture of 70 % of isopropyl alcohol (IPA) and 30 % distilled water and the sample was agitated until 60 seconds in the solution.

v) Lift-off: The lift-off process removes the excess metal. The metal film on the PMMA resist is detached from the sample when the (PMMA) is dissolved in acetone. A thick layer of deposited metal can lead to difficulties in the lift-off process by forming a continuous metal layer across the developed area. Therefore, the metal thickness should be less then one third of the resist thickness to avoid a lift-off problem. To check that all the excess metal has been lifted-off, the chip can be controlled under an optical microscope. This has to be done while the sample is still wet, otherwise the excess metal will stick to the chip and won't come off. If all the excess metal has not been lifted-off, the chip can be soaked in acetone for longer time, rinsed with a syringe or put in an ultrasonication bath. However, in the case of ellipse nanostructures we used the ultrasonication for 5 to 10 seconds only. When the lift-off of excess metal is completed, the sample is rinsed with isopropyl alcohol and blown dry with a nitrogen gun.

PMMA Resist: The Polymethyl methacrylate PMMA is a transparent polymer, which is electron-beam sensitive. When exposed to the electron beam, these complex macromolecules get broken down into simpler compounds, which can be easily dissolved in a chemical developer. We use a recipe resulting in a 250 nm thick layer of PMMA to allow for a lift-off process of metal deposition. The actual spin coating recipe is the following: Multiple drops of AR-P 672.045 PMMA 950k solution are deposited on the surface until covering entirely the whole sample. The spinning rate is then set up to 4000 rpm, which is maintained for 60 seconds to uniformly coat the chip. After spinning, the sample is baked on a hot plate at 150° C for 3 minutes to harden the PMMA layer.

Fabrication of Antidots:

The steps used for the fabrication of antidots are shown in the Fig. 4.7. The antidots of 1 μm diameter and with 2 μm center to center distance were fabricated with hard mask and Plasma etching techniques.

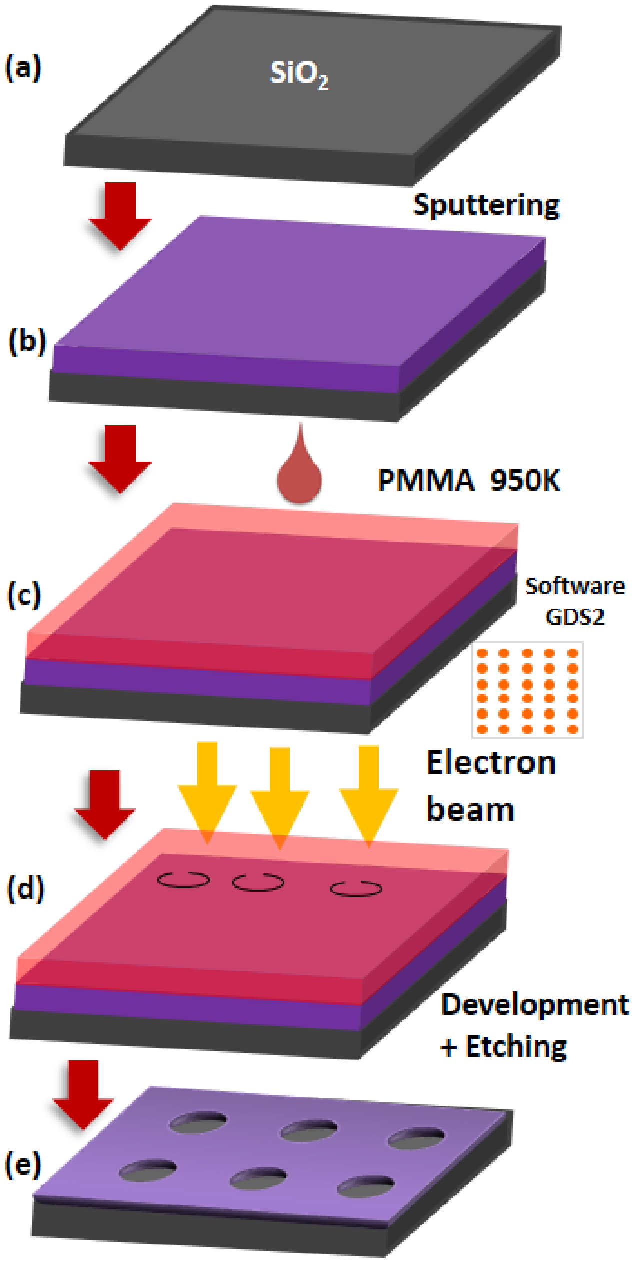

Figure 4.7: Electron beam lithography process: (a) Substrate cleaning (b) Deposition of thin film (c) Coating of the sample surface with resists (d) Exposure of the electron beam to the PMMA 950k resist (e) Development of resist and Plasma etching.

Fabrication of ellipse:

The steps used for the fabrication of ellipse are shown in the Fig. 4.8. The array of ellipses with different sizes and same aspect ratios were fabricated with lift-off technique.

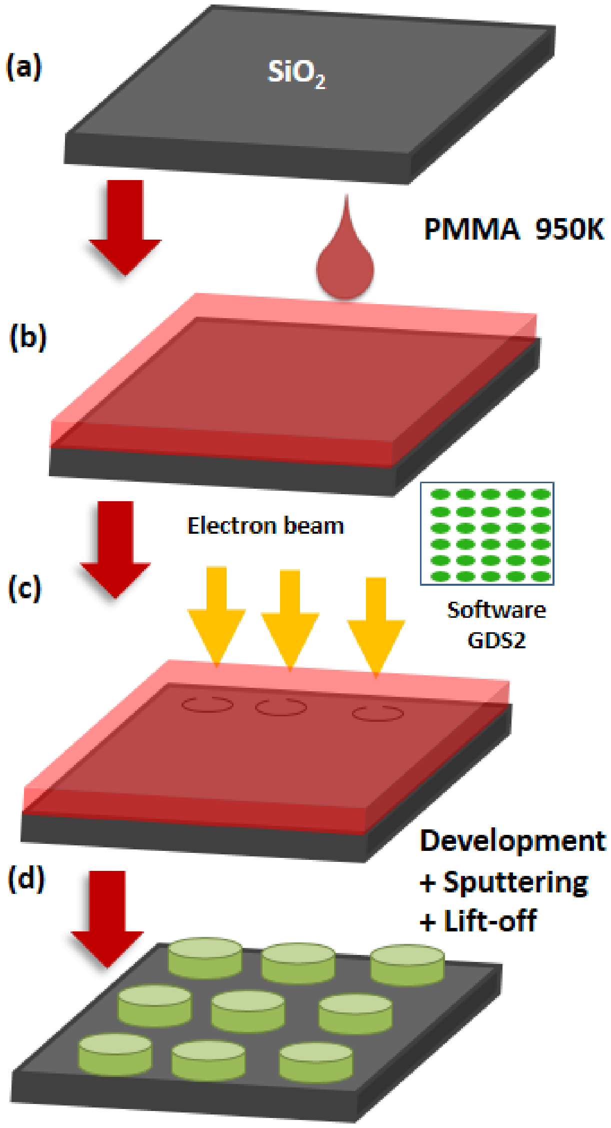

Figure 4.8: Electron beam lithography process: (a) Substrate cleaning (b) Coating of the sample surface with resists (c) Exposure of the electron beam to the PMMA 950k resist (d) Development of resist, sputtering and lift-off process(d).

4.1.3 Plasma Etching

This section describes the principles of plasma etching, i.e., of etching a material in a plasma. Plasma etching also known as reactive ion etching (RIE), and both expression will be used interchangeably in this Thesis. Plasma etching is often used for the fabrication of high-aspect-ratio structures. In a typical process, the pattern is first defined in a resist material, for example by electron-beam lithography.

The resist material is then used as a mask for etching into an underlying material. To etch into a material with high aspect ratios, a high selectivity, i.e., a high etch rate ratio between the material and the etch mask, is crucial. Since the etch resistance of resists is usually not very high, an intermediate hard mask layer with higher selectivity is often employed. The resist pattern is then first etched into this intermediate layer, and afterwards into the underlying material. Such a process is also called a trilayer process, and has been employed to fabricate antidots nanostructures in this thesis.

Etch mechanisms:

There are different etching principles that can be distinguished in plasma etching: for example chemical etching, sputtering etc. (see Fig. 4.9) [20, 105]. In chemical etching (see Fig. 4.9,a), the etching of the substrate material is purely chemical. This means that the purpose of the plasma is to supply reactive etchant atoms or molecules. Those etchants react at the substrate interface and form a volatile product which diffuses from the substrate, thereby removing material. This kind of etching can be highly material selective, as it is sensitive to differences in chemical bonds, and isotropic, i.e., non directional, except for some crystals with preferential etch directions. Sputtering (see Fig. 4.9,b), besides, removes substrate material by physical sputtering, i.e., by the ejection of substrate atoms by bombardment with energetic ions. This kind of etching has low selectivity, since it is sensitive only to difference in surface bond energies, which are small compared to the energy of the impinging ions [20], and anisotropic, as the etching direction depends on the angle of the incident ions.

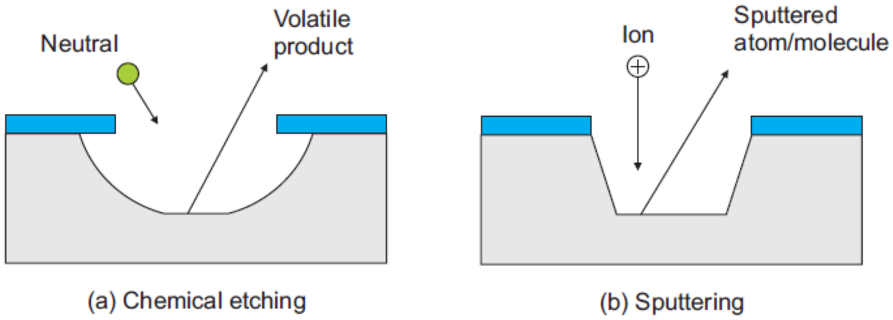

Figure 4.9: **RIE etch mechanisms**. Plasma etching basic principles: (a) chemical etching (b) sputtering. Adapted from Ref. [20].

RIE apparatus:

A schematic sketch of a typical RIE setup is shown in Fig. 4.10. A plasma is generated in a gas-filled chamber by applying a RF voltage between the lower electrode (called cathode, where the sample is placed), and the grounded chamber, which acts as the upper electrode. In this plasma, electrons, ions, and reactive neutrals are generated. The electrodes have a lower time-averaged potential than the plasma, and therefore, there is a DC potential drop in the regions close to the electrodes. This region is also called the sheath region, and in this region, the ions from the plasma are accelerated towards the sample at almost normal incidence. The energy of the bombarding ions is dependent on sheath potential, and therefore, on the applied RF voltage. It should be noted, however, that the RF power does not only determine ion energy, but also the plasma density. Therefore, an increase in RF power results in two effects: a higher plasma density, and therefore an increased production of reactive species, but also an increased energy of the substrate-bombarding ions [105].

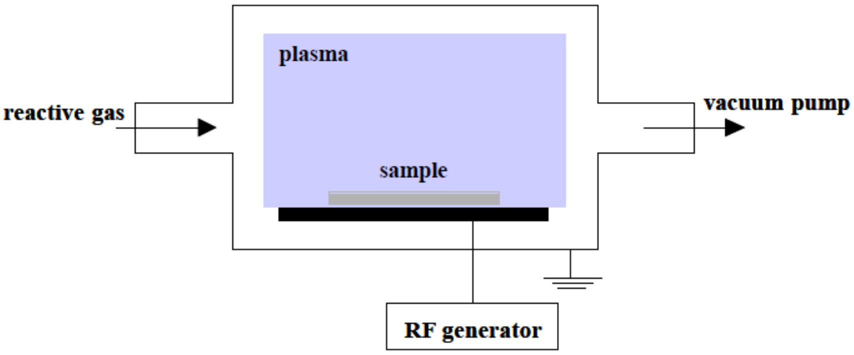

Figure 4.10: **Schematic sketch of a RIE chamber.** A plasma is generated in a gas filled chamber by applying a RF voltage between the cathode and the grounded chamber.

Process parameters:

For a suitable etch recipe, a variety of parameters have to be taken into account. The choice of the feed gas, e.g., CHF_3, Ar, or O_2, determine the reactive species that are generated in the plasma, and thereby the materials that can be etched in the plasma. In addition to that, the processing parameters, such as RF power, substrate temperature, cathode material, gas flow, and pressure, must be considered.

In general, a high RF power and a low pressure result in high-energy ions and promote sputtering. In contrast, a low RF power and high pressure favor chemical etching. The substrate temperature does not only affect the chemical reaction rate but also the condensation and sticking probabilities of gas species. Thus, the possibility to control substrate temperature is crucial for many RIE processes [105]. LABNANO/CBPF is equiped with Oxford PlasmaPro NGP80, where we have used differnt ectching recipes. The summary of these recipes are given in the Table below.

Table 4.2: Summary of the etching parameters.

Material	Etching parameters	Etch Rate	Etch Type
Ti	200 W, 100 mTorr,Ar: 50 sccm	1.0 nm/min	Sputtering
$Ni_{81}Fe_{19}$	200 W, 100 mTorr, Ar: 50 sccm	1.25 nm/min	Sputtering
Co	100 W, 50 mTorr, Ar: 50 sccm	1.3 nm/min	Sputtering
Ru	100 W, 50 mTorr, Ar: 50 sccm	2.3 nm/min	Sputtering
Au	100 W, 50 mTorr, Ar: 50 sccm	14.3 nm/min	Sputtering
SiO_2	200 W,100 mTorr,CHF_3+Ar: 12+38 sccm	25.0 nm/min	RIE
PMMA	200 W, 100 mTorr, Ar: 50 sccm	21.0 nm/min	Sputtering
PMMA	200 W, 100 mTorr, O_2:50 sccm	344 nm/min	Sputtering

4.1.4 Focused ion beam (FIB)

Focused Ion Beam (FIB) systems are identical to SEMs, except FIBs use a beam of ions instead of electrons. The source of ions is usually a Liquid Metal Ion Source (LMIS), gallium (Ga) being the most common. The heated Ga is brought in contact with a tungsten needle, and then flows to its sharp tip. Strong electric fields overcome the material work function and allows ion emission. The emitted ions are then accelerated by a potential difference of 1 kV to 50 kV and focused by electromagnetic lenses. Ion-specimen interactions may be used to form an image of the sample. Ions are heavier and more energetic than electrons, so specimen material is sputtered on impact. The process is referred to as ion milling. Relatively high ion current is required for milling. Ion-assisted deposition is also possible (e.g Pt protective layer). A thin needle brought very close to the sample surface is used to feed the source gas. The gas contains atoms to be deposited. Ions collide with gas molecules, strike out the target atoms, which are then deposited onto the sample surface. FIB is utilized for site-specific analysis. A combination of electron and ion columns is possible in dual beam instruments. LABNANO/CBPF has dual beam FIB (TESCAN LYRA3) which is extremely versatile. The electron column may be used for imaging of in-situ monitoring of the milling process. Precision cross-sectioning, circuit repair and modification, defect analysis etc. are among the uses of FIBs in semiconductor industry.

TEM sample preparation techniques

There are different methods for TEM sample preparation: conventional method [106], in-situ lift-out [107], and ex-situ lift-out [108]. In this thesis we used the in-situ lift-out method with FIB , which will be discussed briefly in the following.

In-situ lift-out: The in-situ lift-out technique does not require any sample preparation outside of the microscope. The sequence of steps is illustrated on Figure 4.11. A thin film and a TEM grid are placed inside a FIB. The milling of the film is mostly identical to that of a conventional method, except the film is partially released by FIB cuts along its perimeter. A built-in nanomanipultor is brought in close proximity to the lamella Figure 4.11, c). The film foil may be attached to the needle either via just electrostatic attraction or a supplementary layer of deposited metal (Figure 4.11, c and d). The thin section is then completely released, by further FIM milling or just broken out, and lifted out of the milling site (Figure 4.11, d). It is then transported onto a TEM grid and released The in-situ method is site specific and very fragile (Figure 4.11, e). Thin sections are milled and lifted out with high precision suitable for one-of-a-kind defects. Sample preparation takes about 2 hours, after which the specimen is on a TEM grid and ready for examination (Figure 4.11, f).

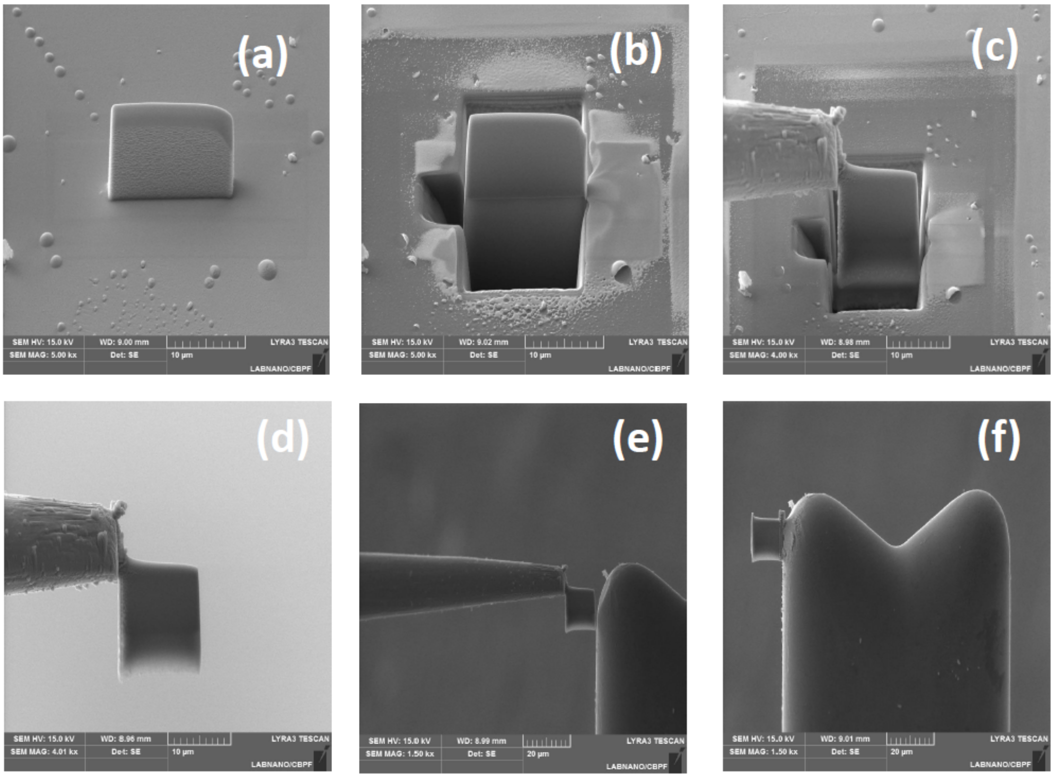

Figure 4.11: (a) Platinum deposition (b) Cross section (c) Fully cut sample (d) Sample lift out (e) Lamella attached to nanomanipulator (f) Lamella attached to TEM grid and final thinning of the sample.

4.2 Morphology and micro-structure characterization

Topographic characterization of the samples was realized using Atomic Force and Scanning Electron Microscopes (AFM and SEM). Moreover, the X-ray Diffraction (XRD) and Tansmission electron microscopy (TEM) were used for structural characterization. Here, in the following section the experimental techniques are described making special emphasis in those involving our most active work.

4.2.1 Scanning Electron Microscopy (SEM)

The surface morphological characterization of the magnetic nano structures has been carried out mainly by Scanning Electron Microscopy (SEM) (JEOL JSM-6490LV). This technique not only allows studying the micro and nano-structure of the samples, but also allows obtaining information on the chemical composition and homogeneity of the samples. The operation of the SEM is based on the interactions between the surface of the sample and the electron beam that runs through it in a sweeping/scanning mode (as seen in Figs. 4.12).

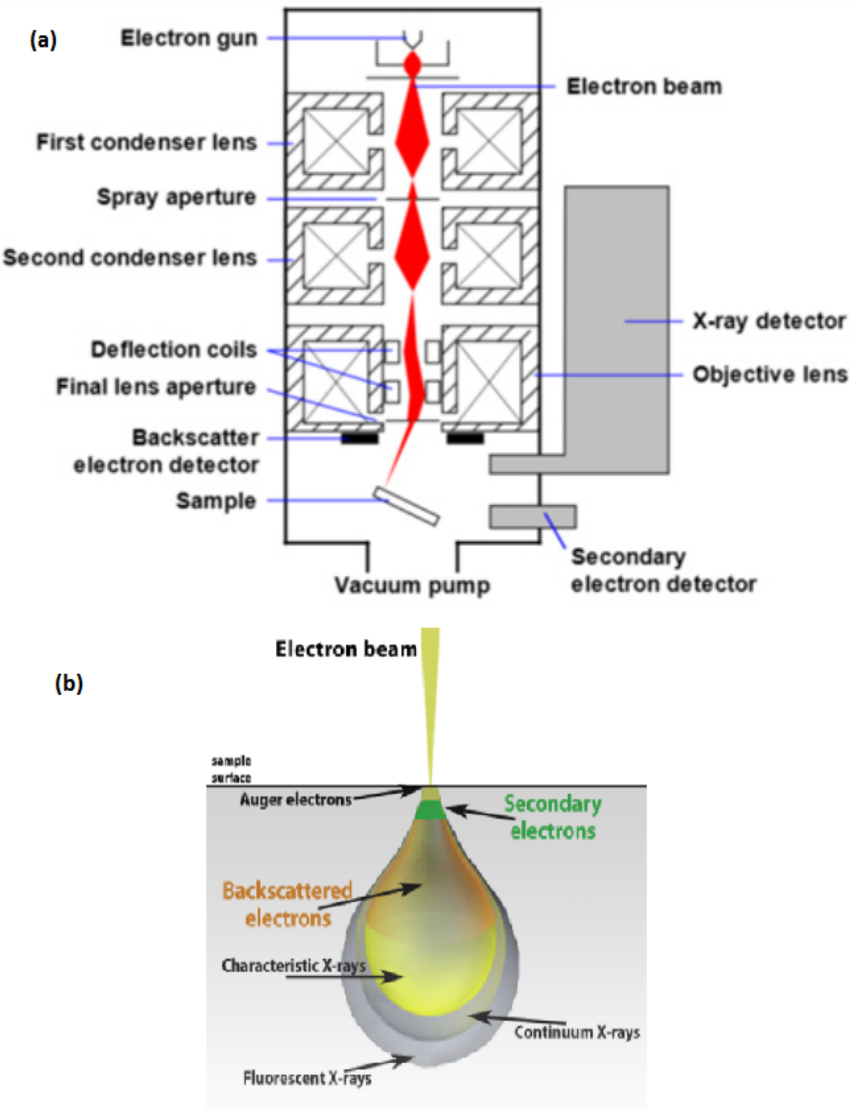

Figure 4.12: (a) Schematic of a Scanning Electron Microscope and (b) Schematic of electron beam interaction [21].

The SEM uses detection of the secondary electrons to produce the images. The generated secondary electrons depend on the energy of the incident beam, material and the surface of the sample. In the SEM images, the contrast is due to the morphology of the sample or due to a different compound in the sample. The resolution of the image could be obtained up to ~3 nm.

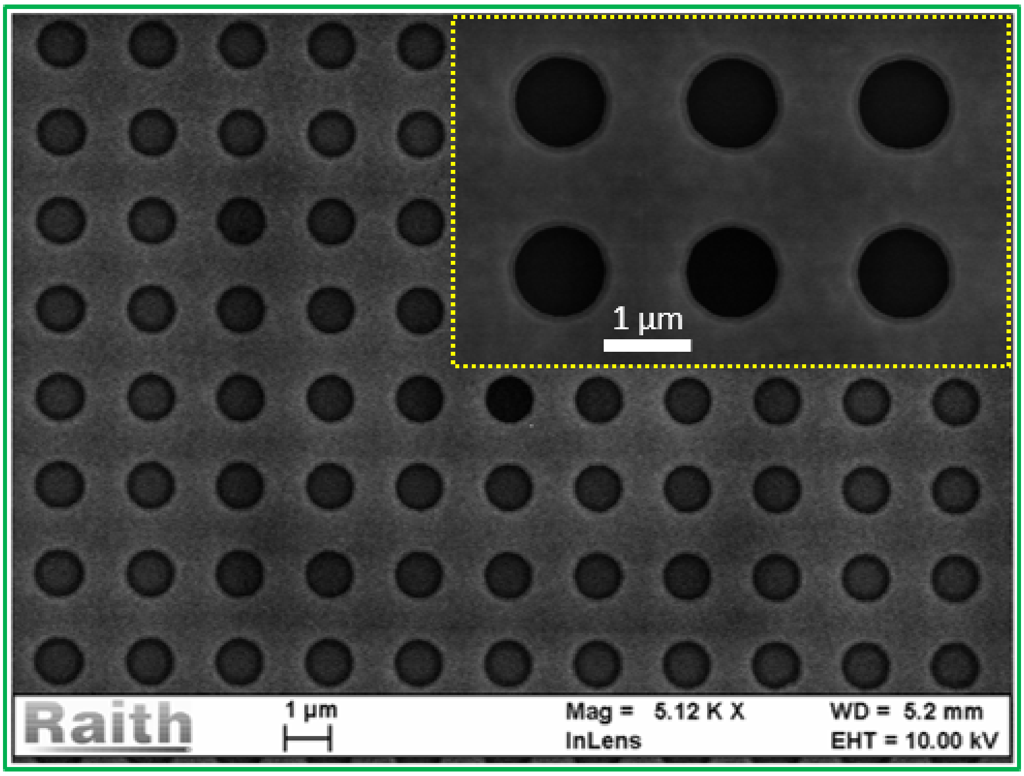

Figure 4.13: SEM-FEG images of antidots nano structures. Inset shows the zoomed image.

Figure. 4.13 shows an example of SEM images obtained with different magnification scale. In the specific case of the nano structure fabricated and presented in this thesis, its topographic and compositional characterization has been carried out using a commercial model of SEM, (JEOL JSM-6490LV) which is a facility of multi user lab. LABNANO/CBPF.

4.2.2 Energy Dispersive X-Ray Spectroscopy (EDS)

Chemical information of particular samples (as shown in the Fig. 4.14) was obtained by Energy Dispersive X-Ray Spectroscopy (EDS). Overall, the high energy of an incident beam ionizes the atoms then the X-ray photons are emitted; the energy of these photons is characteristic for each element (X-ray fluorescence). The EDS detector was embedded in a Field Emission Scanning Electron Microscopy and carried out using a commercial model of SEM, (JEOL JSM-6490LV)which is a facility of multi user lab. LABNANO/CBPF.

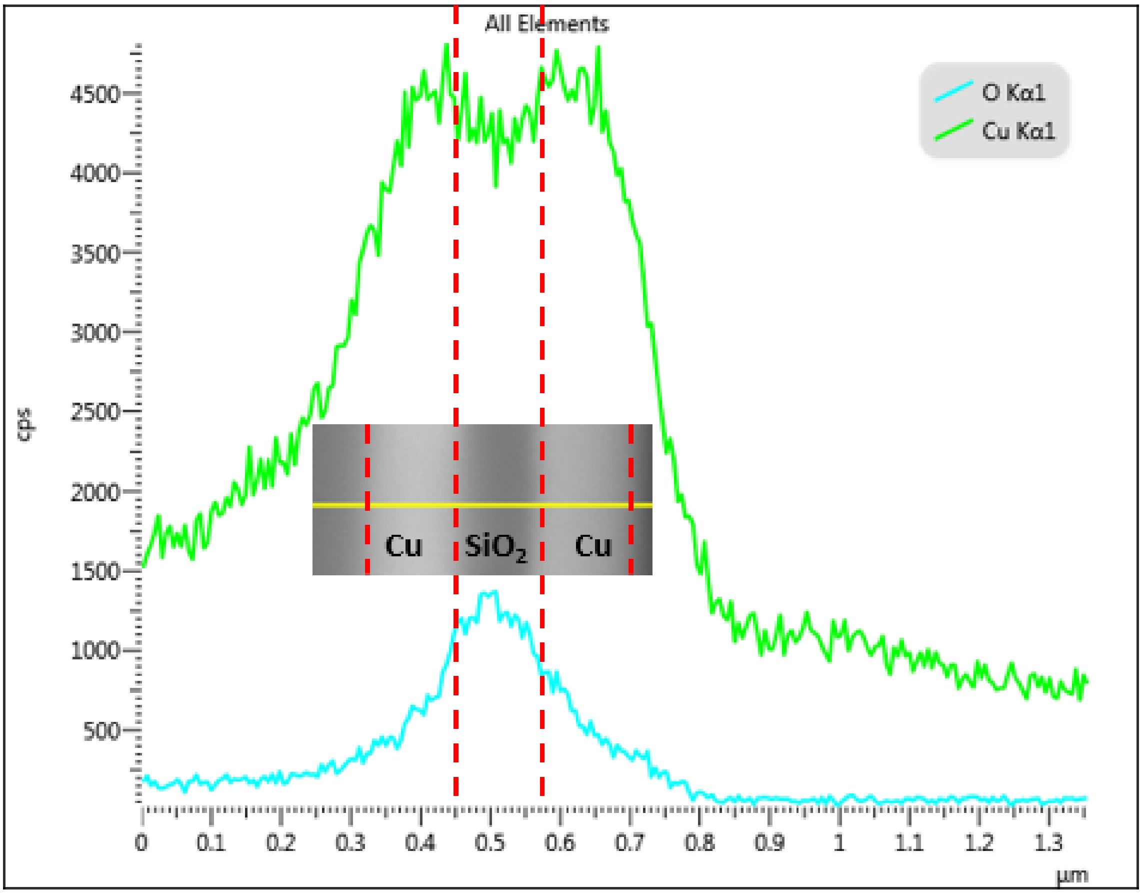

Figure 4.14: The EDS scan of SiO_2 with Cu (100 nm) on the top and bottom. Also the chemical information is presented for Cu and O.

4.2.3 Transmission Electron Microscopy (TEM)

The operating principle of the Transmission Electron Microscope, TEM, is similar to that of the transmission optical microscopes, but it uses electrons instead of photons to produce the image. The schematic representation of TEM operation is shown in Figure 4.15. Electrons are generated by an electron gun and accelerated by a high voltage (in the order of hundreds of kV).

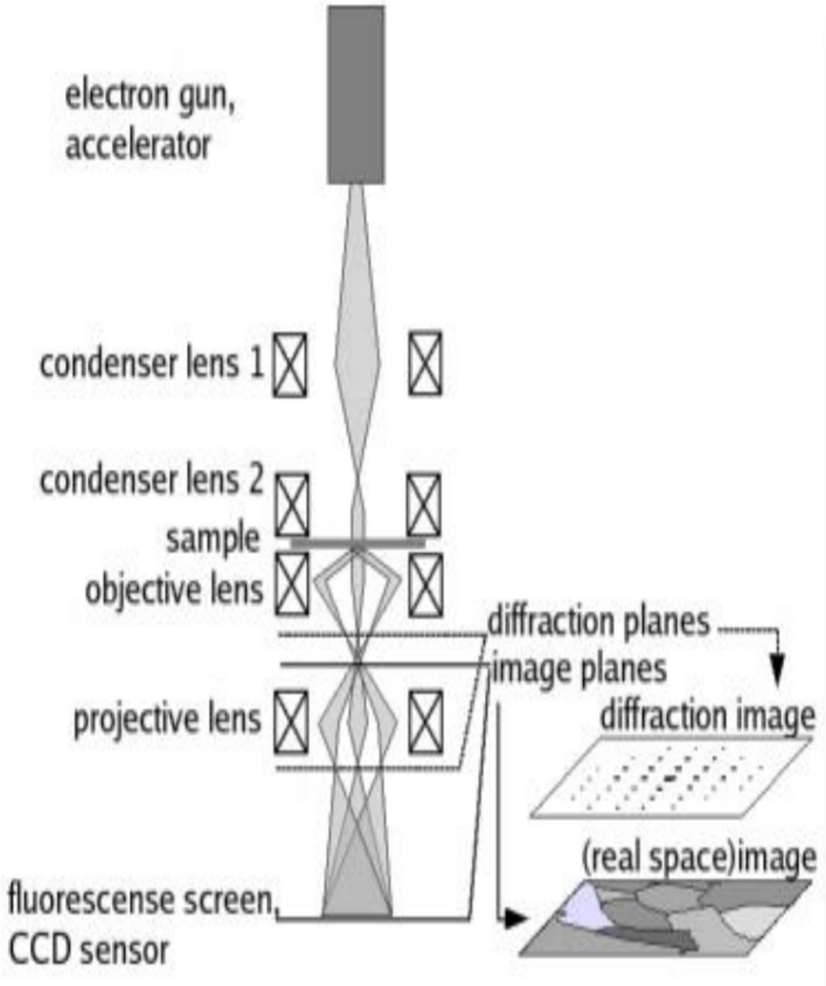

Figure 4.15: Diagram of a transmission electron microscope [22].

The basic difference between the SEM and TEM is that, in the case of TEM the electrons pass through the sample and are focused directly on a plate of a fluorescent material located at the base of the system as a screen. Moreover, TEM allows the obtaining of images in the reciprocal space (electron diffraction images, SAED) that provide information on the crystalline or amorphous structure of the samples.

Since in the TEM microscopes the image is obtained by transmission mode, the sample must be enough thin to allow to transmit through it an significant amount of electrons. The maximum allowed thickness of TEM sample is usually of the order of tens to hundreds of nanometers, which depends on the atomic number of the material being studied and the energy of the electrons. In order to solve this problem in our case, the thin foils of Co_2FeAl film were separated from the substrate with help of

Focused Ion Beam (FIB) technique (the details about it, are presented in the FIB section).

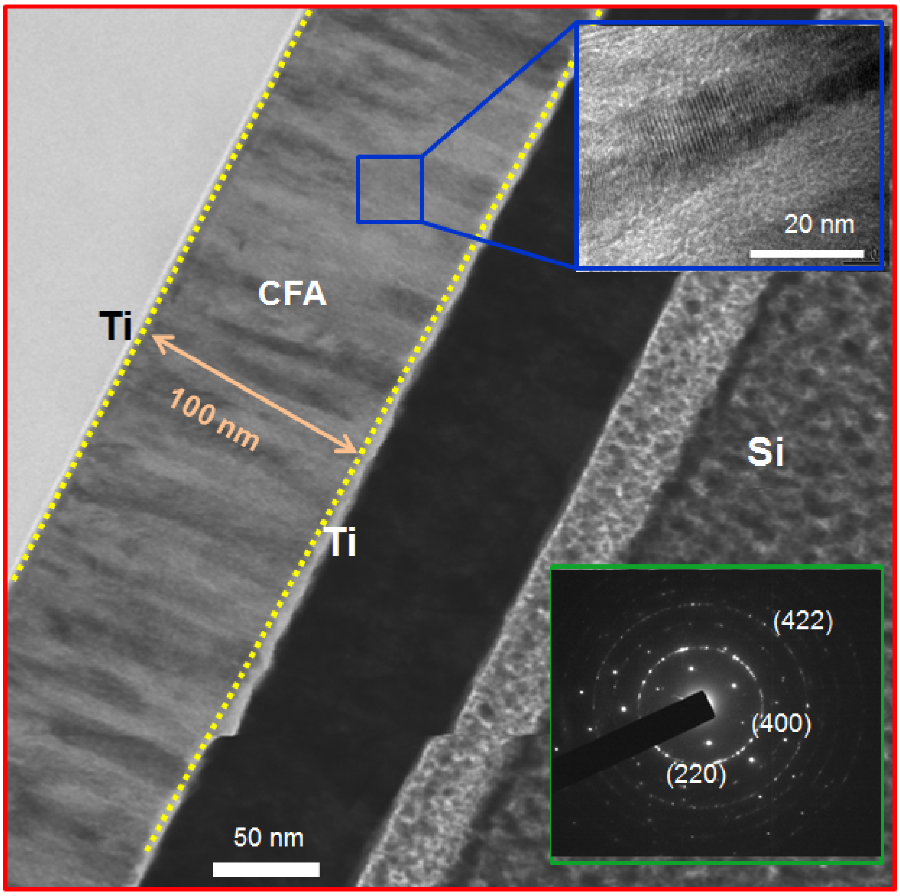

Figure 4.16: TEM image of 100 nm Co_2FeAl fims, while the lower inset shows the selected area electron diffraction pattern (SAED).

TEM micrograph of the Co_2FeAl film are shown in Figure 4.16, which demonstrates that the crystallographic nature of the sample. Also, the columnar grains growth in the sample. In addition, SAED spectrum, shown as the lower inset in Figure 4.16, indicates the crystal structure of the Co_2FeAl film. The morphological and structural studies performed by TEM presented in this thesis report have been carried out with TEM, (JEOL 2100F 200kV TEM.), belonging to the LABNANO/CBPF.

4.2.4 Atomic Force Microscope (AFM)

Atomic force microscopy is a powerful technique for probing the surface of the thin film layers and deducing information about its topological features, fast and accurately. AFM operates by scanning a very sharp and tiny tip attached to the end of a cantilever across the sample surface (Fig. 4.17). The tip approaches the surface of the sample and interacts with it via Van der Waals forces. The interaction translates in a cantilever deflection or a change in the cantilever's oscillating frequency, subject to the operational mode of the AFM: contact or tapping. The deflection or the frequency changes of the cantilever are detected by an optical system consisting of a laser beam, which is reflected on the cantilever. The vertical and the horizontal deflection are measured using a split photodiode detector that analyses the reflected beam. The displacement of the cantilever in the three directions is done with the help of a piezoelectric scanner, combining independently operated piezo-electrodes for X, Y and Z direction into a single tube. The two operating modes that have been used, contact – AFM and tapping – AFM, are described in more detail in the following.

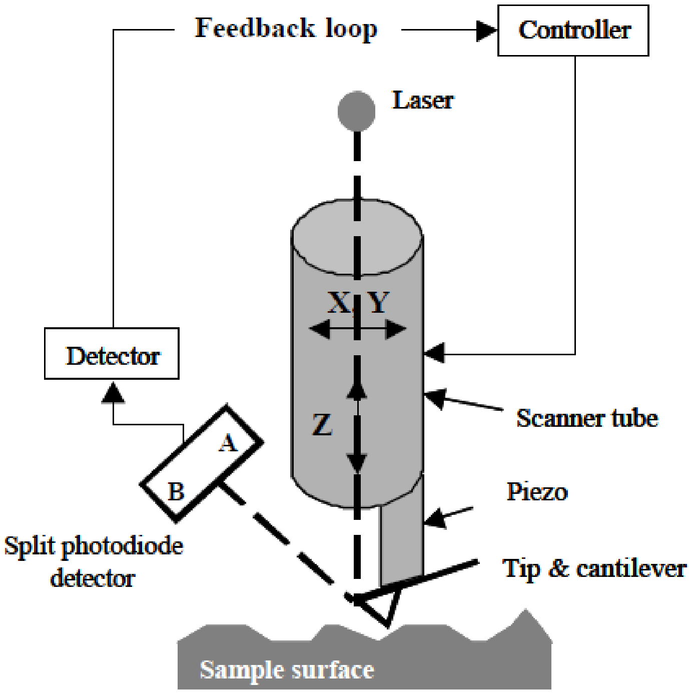

Figure 4.17: Schematic representation of Atomic Force Microscope [23].

Contact mode AFM:

In the case of contact mode the tip of probe is in constant physical contact with the sample surface. Although the tip scans along the surface, the sample topography induces a vertical deflection of the cantilever, which is mentioned with a split photodiode detector. A feedback loop maintains a constant deflection between the cantilever and the sample by vertically moving the scanner. By maintaining a constant cantilever deflection, the force between the tip and the sample remains constant. The force F is calculated from Hook's law: $\vec{F} = -k\vec{x}$, where k is the spring constant and x the deflection. The distance the scanner moves vertically at each point (x, y) is recorded by the computer to form the topographic image of the surface.

Tapping mode AFM:

In the tapping operational mode the cantilever is oscillated near its resonance frequency with the amplitude ranging typically from 20 to 100 nm. The tip lightly 'taps' the surface while scanning, contacting the surface at the bottom of its swing. The feedback loop maintains constant oscillation amplitude by maintaining a constant RMS of the oscillation signal acquired by the split photodiode detector. In order to maintain a constant oscillation amplitude the scanner has to move vertically at each point (x, y). The vertical position of the scanner is recorded by the computer, to form the topographic image of the sample surface.

4.3 Magnetic Characterization Techniques

This section is dedicated to the experimental techniques that are used for the magnetic characterization in this thesis. The group of Applied Magnetism Lab. has several magnetic characterization techniques, such as: VSM magnetometry at room temperture and low temperture (DynaCool), AGFM and VNA-FMR among other. Moreover, a qualitative study of the magnetic contrast in samples with in-plane anisotropy was realized using Magnetic Force Microscopy (MFM) measurements.

4.3.1 Static Magnetization Techniques (Curves MxH)

4.3.1.1 Alternating Gradient Field Magnetometer (AGFM)

The Alternating Gradient Field Magnetometer has as its working principle the vibration of a magnetic sample due to the force resulting from the interaction between its magnetic moment and an alternating magnetic field gradient applied on it. In addition to the field gradient, a static field is applied through a Helmholtz coil. The amplitude of vibration is amplified when the frequency of the field gradient approaches the resonance frequency of the rod that holds the sample. This vibration is transduced to a feedback signal, using a piezoelectric sensor, which is subsequently measured by a Lock-In *Stanford SR830 DSP*, and this signal is proportional to the magnetic moment of the sample in the direction of the static field. This system has a sensitivity of 10^{-7}emu, sufficient for measurements of the sample studied in this thesis. The schematic respresentation of the AGFM is given in the Fig.4.18).

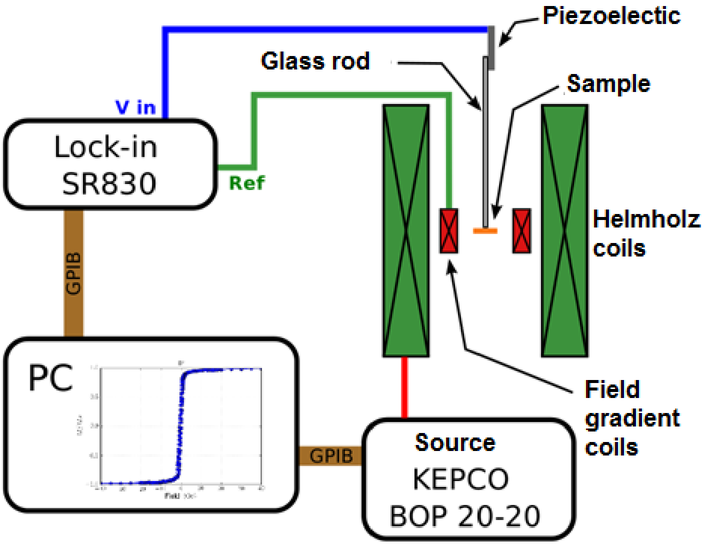

Figure 4.18: The experimental setup of AGFM.

4.3.2 Vibrating Sample Magnetometer (VSM)

The vibrating sample magnetometer is a magnetometer whose operation principle is based on Faraday's law of induction (a variable magnetic flux induces an electromotive force in a closely located conductor). The sample is attached to the end of a rod that vibrates with constant amplitude at a certain frequency. An external static magnetic field will excite the sample and, according to the intensity of the static field, the magnetization of the samples will vary, and with the signal captured by the sensing coils we can measure the magnetization of the sample. The system used operates between magnetic fields of ±300 Oe, supplied by a pair of high-resolution Helmholtz coils approximately 0.05 Oe in turn, powered by a bipolar source KEPCO BOP 20-20. The configuration of the VSM allows the angular investigation of magnetization curves with respect to the preferential axis of induced unidirectional anisotropy. The sensitivity of the VSM is of the order of 10^{-5} emu. A schematic representation of the system is shown in Fig.4.19.

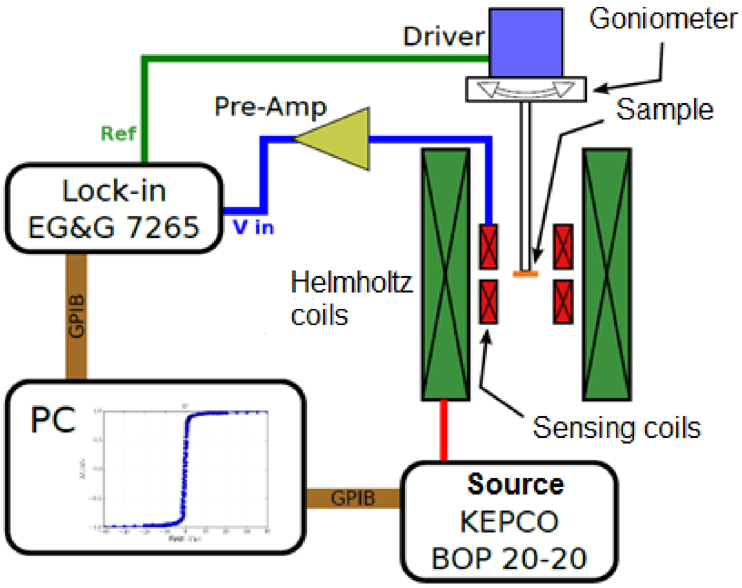

Figure 4.19: The experimental setup of VSM.

Fig. 4.20 shows the schematic representation of the Dynacool VSM system, which was also used in this thesis.

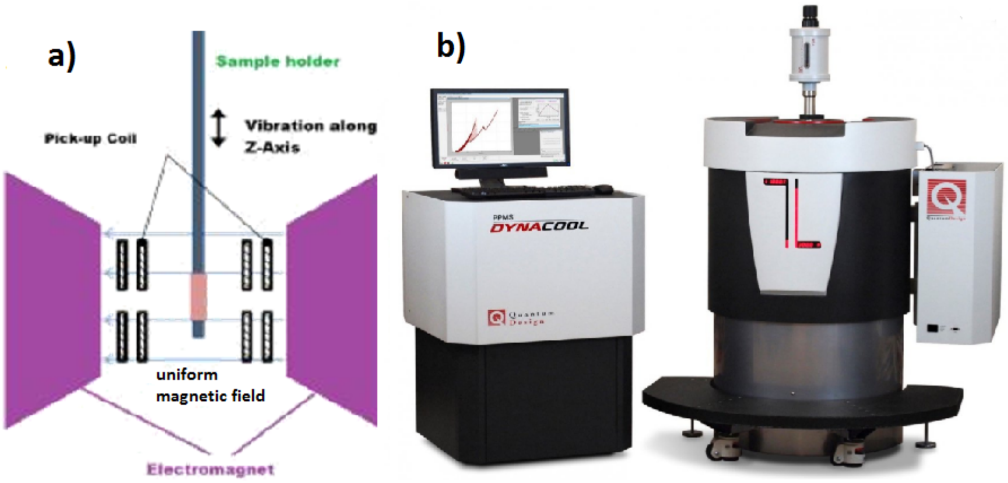

Figure 4.20: (a) The experimental setup of Dynacool VSM, (b) photograph of Dynacool VSM system.

4.3.3 Magnetic Force Microscope (MFM)

The magnetic force imaging is a feature provided by the atomic force microscope. In MFM we use a tapping mode cantilever equipped with a special magnetic tip (low moment).

Interleave mode: In this mode, first the tip is scanned over the sample in order to obtain the topographic information. After each scan line, the feedback is turned off and the tip is raised above the sample to a user-defined height (20-100 nm) to perform a second scan of the surface measuring any far field contribution, such as magnetic forces (at that height only long range forces can be detected while Van der Walls forces are negligible).

The topography data acquired during the first scan are used to maintain the tip at a constant height. The existence of magnetic forces shifts the resonant frequency of the cantilever by an amount proportional to vertical gradients in the magnetic forces on the tip. Resonant frequency shifts are very small (from 1 to 5 Hz for a resonant frequency of about 100 Hz) and can be detected either by phase detection mode or by amplitude detection mode. Phase detection measures the cantilever's oscillation phase relative to the piezo-drive, and amplitude detection measures the oscillation amplitude. In both cases, the measured signal is proportional to the second derivative of the stray field emanated from the sample. Phase detection is much superior than amplitude detection and has been used in this thesis to measure samples with magnetic vortices. The CBPF nanoscopy laboratory has an AFM/MFM equipment of Bruker shown in Fig.4.21.

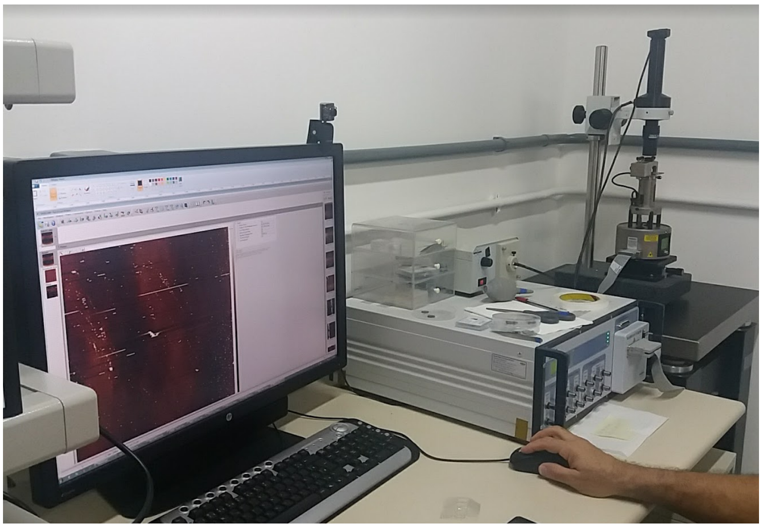

Figure 4.21: The photograph of AFM/MFM equipment of Bruker at Nanoscopy laboratory of CBPF.

4.4 Dynamic Magnetization Measurements

This section exclusively focuses on spin resonance in ferromagnetic materials (ferromagnetic resonance – FMR). We will discuss the different techniques for studying FMR in our systems.

In order to excite and detect the precession movement of magnetization there are servel experimental techniques developed. It is possible to generate the spin waves by external excitation with the means of waveguides [40, 109], microwave antennas [110, 35] resonant cavities and polarized light among other. It is also possible to generate excitations within devices such as, spin pumping or spin transfer torque. The methods are also varied, among them perturbative impedance methods in the microwave antennas as detectors, absorption in the resonant Kerr magneto optical (MOKE), Brillouin scattering (BLS) [109, 111, 112] and measurements of magneto impedance and others. One of the most established techniques to study spin waves in magnetic systems is vector network analyzer based technique which is commonly known as Broadband VNA-FMR. The vector network analyzer (VNA) is a test equipment that allows the characterization of radio frequency and microwave devices through the measurement of network scattering parameters, known as S parameters (as explained in Fig. 4.22 (b)). Such equipment is capable of carrying out extremely high precision measurements, and have several applications, for example, in industry, where they are used in the characterization of radio frequency components and devices. Since the beginning of the last decade, the investigation of the properties of electrical and magnetic materials in high frequency ranges, where the magneto-impedance effect and ferromagnetic resonance are evident, has been carried out using network vector analyzers. The main advantage of VNA over the traditional FMR technique, for example, is that it allows the investigation of the resonant dynamic response of magnetic materials by scanning over a wide range of frequencies.

The Applied Magnetism Lab. is equipped with A Rohde & Schwarz R& S ZVA 24 vector network analyzer with two ports, up to 24 GHz. This equipment allows you to excite a device and measure its response as a function of field, obtaining both the amplitude and phase of the response. The obtained data from the VNA-FMR used in this thesis is the calculation of the power absorbed by the sample due to the effect of ferromagnetic resonance on it. The relationship between the incident and absorbed power in the sample-waveguide set can be calculated using:

$$\frac{P_{Abs}}{P_{In}} = 1 - |S_{21}|^2 - |S_{11}|^2 . \tag{4.3}$$

The absorption in the waveguide is due to losses in the waveguide, losses in the dielectric material of the sample substrate, and magnetic losses in the studied films. For example, the losses of magnetic origin are due to the FMR processes within the sample. It is possible to calculate the non-magnetic losses by inhibiting these FMR processes, this is done by setting the magnetization of the sample in the same direction as the radio frequency (RF) field that excites it, as in the procedure for calculating the reference measure. The absorption due to the magnetic properties is then proportional to the U_{Abs} magnitude calculated by:

$$U_{Abs} = \left(1 - \left|S_{21}^{M}\right|^2 - \left|S_{21}^{M}\right|^2\right) - \left(1 - \left|S_{21}^{R}\right|^2 - \left|S_{21}^{R}\right|^2\right), \tag{4.4}$$

where S_{21}^{M} and S_{21}^{R} are the measured and reference scattering parameters. As U_{Abs} and a magnitude are calculated in arbitrary units, it should be normalized for later comparison with the absorbed power P calculated by theoretical models.

$$\frac{U_{Abs}}{MAX\left[U_{Abs}\right]} = \frac{P}{P_{Max}}. \tag{4.5}$$

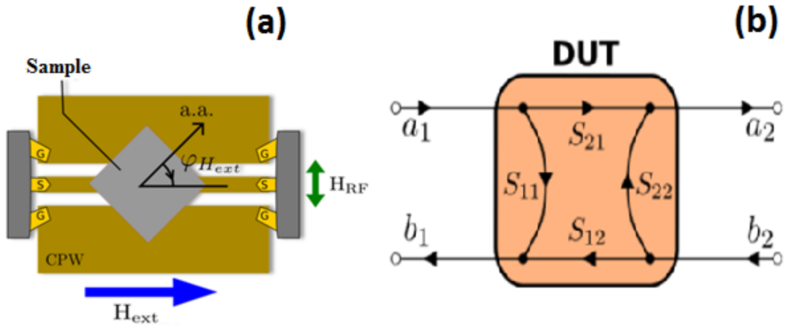

Figure 4.22: (a) The sample is placed over a coplanar waveguide connected to the two-ports VNA (b) Schematic illustration of the S-parameters definition for a 2-port measurements.

4.4.1 Coplanar Waveguide Methods

An advantage of this method is that a wide range of frequencies can be used. This means that resonance can be measured by holding the frequency constant and sweeping the external field H, similar to cavity FMR, or by fixing H and sweeping the frequency. A unique and useful representation of the data over a desired range of frequencies and H values can be constructed by fixing the frequency at the lowest desired value, sweeping the field, and recording the S_{21} parameter. The frequency is then changed to the next increment, and the process repeated. By plotting H values on the x-axis, frequency values on the y-axis, and S_{21} on the z-axis, as shown in the 4.26.

In this thesis we used Cascade Microtech coplanar wave guide (CPW) for some samples, with an operating frequency range up to 24 GHz, mounted on micro positioners, that allows to make contacts directly at the surface of the devices. In addition to coaxial cables and passive components usable in this frequency range, substrates, and reference standards required for equipment calibration.

Fig. 4.23 shows the experimental step-up of the Laboratory for high frequency Magnetometry, where the equipment mentioned above can be seen. With this equipment it is possible to carry out measurements of the magnetization response on the electrical properties of the devices in both frequency space and space temporal.

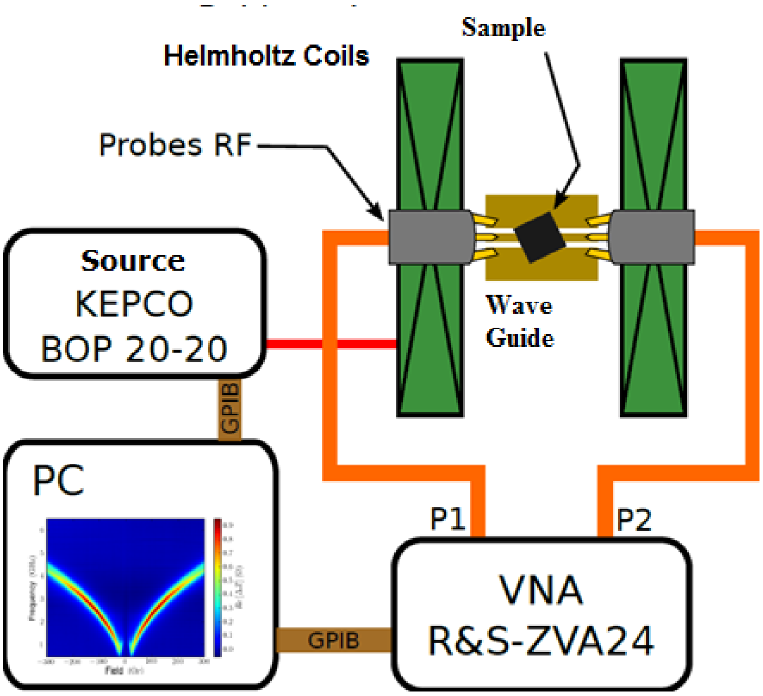

Figure 4.23: The experimental setup of VNA-FMR.

4.4.2 Microstrip Method

The VNA-FMR Differential measurements (dP/dH) were taken with help of Microstrip (MS) as shown in the figure 4.24. This setup has more accuracy for linewidth measurement, the setup described in the last subsection was modified in order to emulate a traditional dP/dH FMR measurement. In this case we used a microstrip line inside a solenoid which generate the external magnetic field H. At a given frequency f and H value, a small (± 1 Oe) software generated field sweep H_{sweep} is performed while the absorbed power is measured. The dP/dH is calculated by fitting the resulting P vs. H_{sweep} curve.

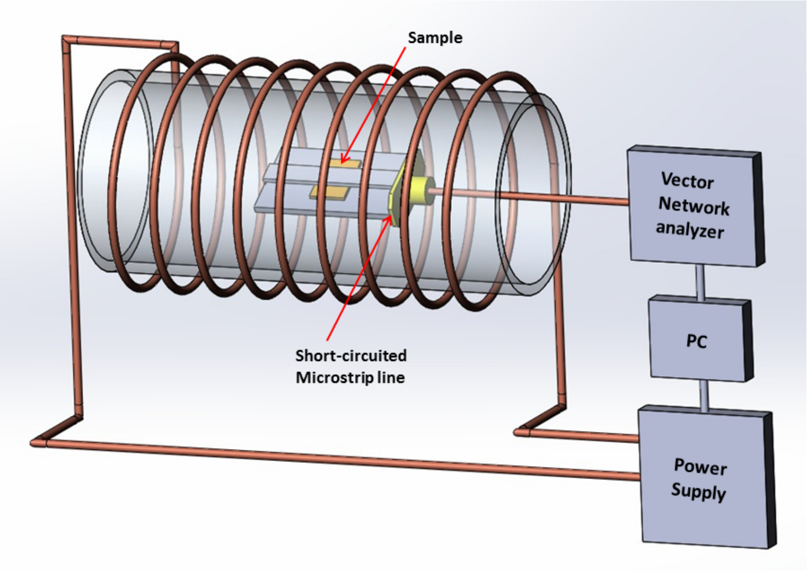

Figure 4.24: The experimental setup of Microstrip method for VNA-FMR differential measurements.

Here, in figure 4.25 dP/dH measurements are presented for 20 nm of Co_2FeAl sample sample at different frequencies, the results for linewidth and damping constant were obtained with the fits.

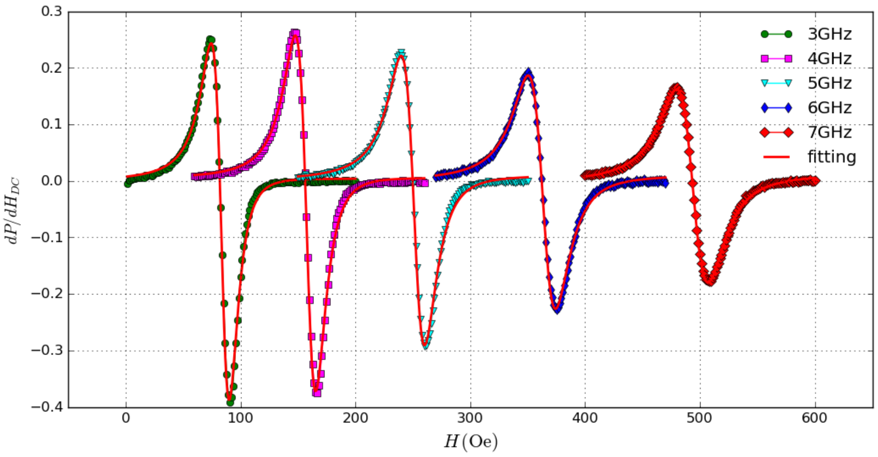

Figure 4.25: The dP/dH measurment at different frequencies with lorentz fitting for 20 nm Co_2FeAl sample.

4.4.3 Data analysis

The possible types of analysis of raw data vary in complexity and in the relevant physical information that can be obtained from them. The work of Bilzer et al. [113] performs a comparison of the different methods of analysis. Here, some of these methods are presented, including a new type of analysis that calculates a magnitude proportional to the absorbed power in the sample.

Color Map

The set of results obtained from the measurement of a 100 nm NiFe film is shown in figure 4.26. The set of values P/P_{max} vs. H vs. f is shown in the color map [Fig. 4.26 (a)] where the color scale denotes the intensity of P/P_{max}. The blue colors represent low or no absorption, while red colors indicate high absorption. In the color map two branches can be seen clearly, which vary in position in the field and frequency where absorption is maximum and the ferromagnetic resonance occurs. Making cuts in cross sections at a fixed frequency, it is possible to observe the amplitude of the resonance peaks as a function of the external field [Fig. 4.26 (b) and (c)]. The position of the peaks as a function of the field varies according to the measurement frequency. It is also possible to make cuts in cross sections for a fixed field [Fig. 4.26 (d) and (e)]. These graphs also show resonance peaks, where the maximum amplitude of the peak occurs at a certain resonance frequency f_r. When calculating f_r for each measured field, the dispersion relationship (f_r vs. H).

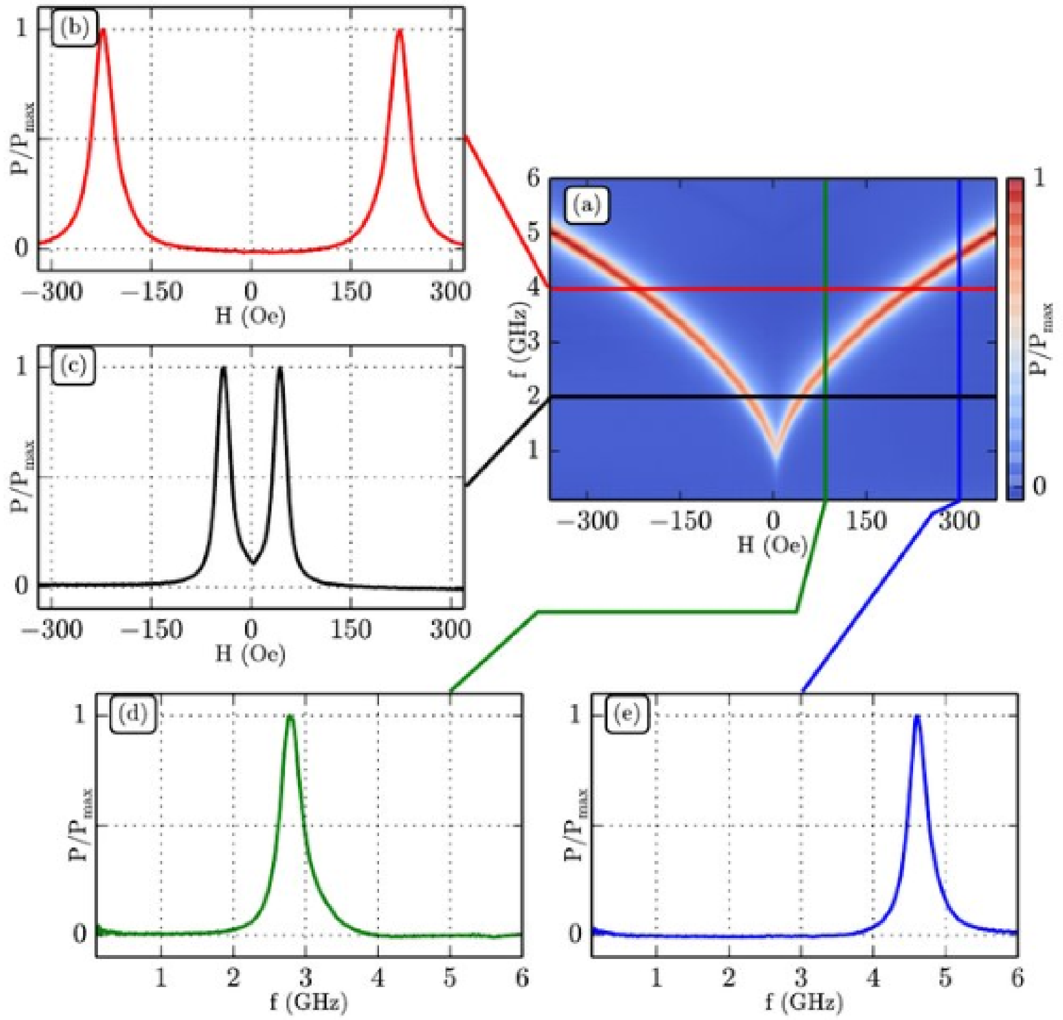

Figure 4.26: Ferromagnetic resonance measurement obtained by the VNA-FMR technique of a sample of Ta (5nm) / Py (100nm) / Ta (5nm) (GONZALEZ-CHAVEZ, 2013). (a) Color map related to the sample's resonance spectrum. Frequency cuts at (b) 4 GHz and (c) 2 GHz. (C) Field cuts at 100 Oe and (d) 300 Oe.

Chapter 5

Micromagnetic Simulations

This chapter is dedicated for the micromagnetic simulation, which is an important tool for studying the static and dynamic magnetization. In this thesis, the micromagnetic simulations were used to analyzed the experimental results for magnetic nanostructures. Moreover, we not only reproduced the experimental results, but also we investigated the detailed dynamics of the excited modes in each experimentally measured field and frequency. The micromagnetic simulation platform used the MuMax3 [114] and the specific softwares for analyzing the simulated data were developed by the Applied Magnetism Laboratory group. In this chapter first we discuss some information about the platform of MuMax3 and show the algorithm used in the simulations. Then, we describe how the absorbed power is obtained from the simulated results and take some considerations about the oscillations of the magnetization of the studied micro objects. Finally, we discuss an example of the oscillation modes obtained from the simulations.

5.1 Introduction

Micromagnetic simulation provides the means to describe and understand the magnetism of physically small magnetic objects. For many micromagnetic systems, the analytical solutions are not available, which makes numerical simulations necessary. Hence, micromagnetic simulators like, the Object Oriented Micro Magnetic Framework (OOMMF) [115], MAGPAR [116, 117], Nmag [118] has been widely used for this kind of simulations. Since all these simulators uses the CPU for calculation, the performance is greatly limited by the speed of the processor used. Many of the computations are highly parallelizable, and even though later versions of these program supports the parallellization processes.

On the other hand, the graphical processing units (GPUs) substantially increase the computational performance, due to a much larger number of parallel processing cores. This increase in performance means that simulations can run with fine discretizations, thereby improving the accuracy of the results [119].

5.1.1 Micromagnetic Simulation MuMax3

MuMax is a micromagnetic simulation program that works using graphics processing units (GPU). It was developed in Prof Van Waeyenberge's Dynamat group at the University of Ghent, Belgium and its code is written and maintained by Arne Vansteenkiste [114].

MuMax is an open source software released under the GNU General Public License (GPLv3) and can be freely used. The MuMax source code can be obtained via `https://github.com/mumax/3/releases`. MuMax3 works on Linux, Windows and Mac platforms, requiring an NVIDIA GPU video card. The MuMax resolution method is the finite difference (FD) method in which the volume of the magnetic system is discretized into cuboid cells. Magnetization is considered uniform within each cell and its evolution over time is given by the Landau-Lifshitz equation (LLE):

$$\frac{\partial M(\mathbf{r},t)}{\partial t} = -\frac{\gamma}{1+\alpha^2} M(\mathbf{r},t) \times H_{eff}(\mathbf{r},t) - \frac{\alpha\gamma}{M_s(1+\alpha^2)} M(\mathbf{r},t) \times (M(\mathbf{r},t) \times H_{eff}(\mathbf{r},t)) \tag{5.1}$$

where M_s is saturation magnetization, γ is the gyromagnetic ratio and α is the damping parameter. The H_{eff} is the effective field, which combines several field terms (one of them is the external magnetic field) with additional effects such as the possible anisotropy, thermal effects and the material parameters. The solutions of this equation can be obtained by integration method and the details can be found in the reference [114]. The samples are divided or discretized into a large number of cells and each cell is assigned with a single spin (equivalent to the average magnetization of the cell). The size of each cell is generally kept smaller than the exchange length (l_{ex}) of the material under consideration to take into account of the exchange interactions among the spins in addition to the magnetostatic interactions among them. For the case of Permalloy, in which we can disregard magneto crystalline anisotropy, the exchange length is ≈ 5.7 nm [120].

Moreover, MuMux3 solves the LLE numerically by discretizing the magnetic sample into cubiodal cells with a uniform magnetization, and then integrating the equation using a Runge-Kutta time stepping scheme. Since MuMax3 uses a method based on the fast fourier transform to calculate the magnetostatic field term, space has to be divided into equal cells on a regular grid, to solve each cell we used PBC (periodic boundary condition). Because of this, geometries other than perfect rectangles has to be approximated. However, smaller cell sizes can be used to improve this approximation. For more information on the theory behind MuMax3 we recommend reading the introductory article by Vansteenkiste and Van de Wiele [114]. Practical information and examples to get started using the program can be found on the official website [121].

In this thesis, we used Mumax3 using Go and Python languages for the simulation of the experimental results. Particularly, we simulated different geometries for example antidot and ellipse. The simulated results provide a better understanding of the micro magnetic behaviour in our samples.

5.1.2 Simulation Method

The micromagnetic simulations are used to reproduce the experimental results and obtain details about the dynamics of the excited modes for each field and frequency. Particularly, we obtain the temporal evolution of the magnetization of the system excited by an oscillating field at a given frequency. According to the algorithm used, the equilibrium position of the system is first reached for each static field value H_{dc}, through relaxation to the minimum energy state of the system (relax() command of MuMax). To simulate experimental results, we excite the magnetic system with oscillating magnetic fields of frequency in GHz range.

The interest is to analyze the magnetization response to the oscillating field. Once the system starts from the static equilibrium we expect that it reaches dynamic equilibrium allowing us to obtain a time series of its magnetization evolution. The radio frequency (RF) field used in the excitation is chosen to promote a relatively quick dynamic balance, so it has a time dependence defined as:

$$h^{rf}(t) = h_{rf}[1 - e^{-2\pi f(t-t_o)}] \times [2e^{-((t-t_o)f-1)^2}] \sin(2\pi f(t-t_o)), \tag{5.2}$$

where t_o is the time the simulation begins and $h_{rf} = 0.5$ Oe is the amplitude of the field $h^{\mathrm{rf}}(t)$ used in simulations. The first term corresponds to the exponential growth of the amplitude and avoids a peak with an initial amplitude, in the second term we have a Gaussian function, which makes the amplitude greater in the first oscillations. Finally, we have the harmonic oscillation term, being the only term that remains after some time. The $h^{\mathrm{rf}}(t)$ field is shown in Fig. 5.1, for a frequency of 6.0 GHz.

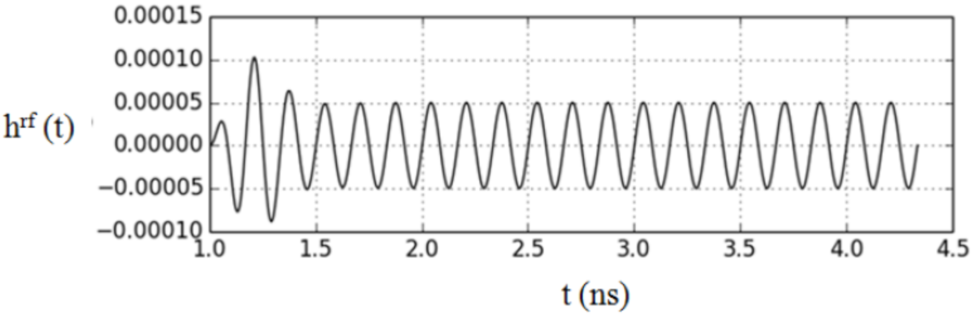

Figure 5.1: Evolution of the $h^{\mathrm{rf}}(t)$ field used for dynamic excitation in programs of micromagnetic simulation.

The magnetization response to the $h^{\mathrm{rf}}(t)$ field evolves in time, from the static equilibrium position to a harmonic oscillation of the same excitation frequency with well-defined amplitude and phase. Figure 5.2 shows the temporal evolution for magnetization m_x and m_y.

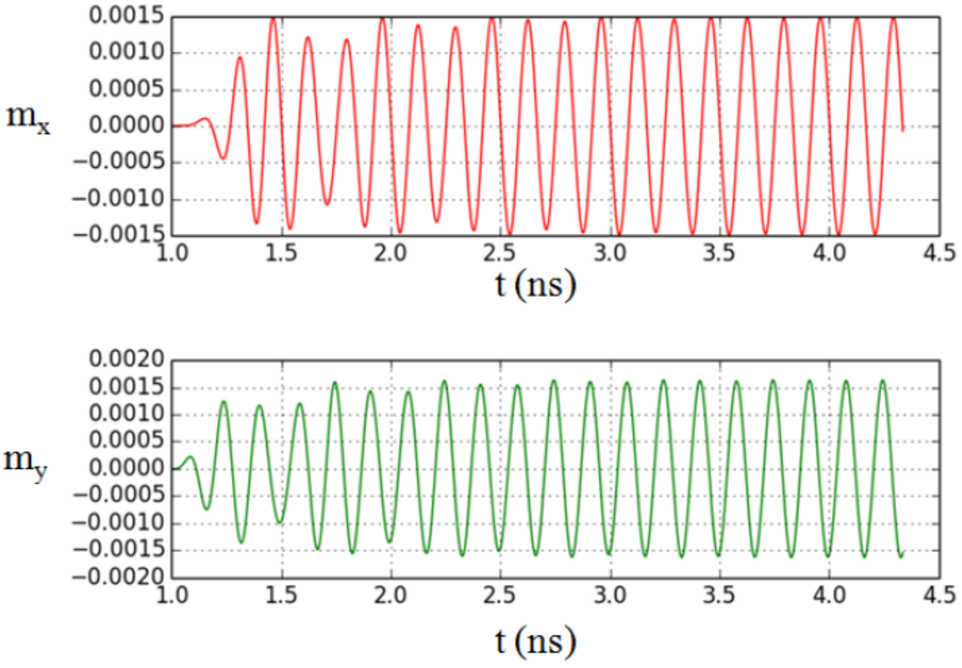

Figure 5.2: The temporal evolution of the dynamic components (m_x, m_y) of magnetization m for a disk of Permalloy with 1 μm of diameter and 50 nm thickness.

The dynamic response of the magnetization after stabilization is a harmonic oscillation, and it is only necessary to know its amplitude and phase to describe it.

For this, we obtain 20 temporal states during an oscillation period for each field and frequency, that is, we record states of the system at 20 particular time points (t). These snapshots are analyzed with the algorithm explained in the next section and thus we can obtain the amplitude and phase of the oscillation. The simulated data is organized in a table given in the appendix II. In the first column we have the times t used in the simulation. For each line in t we have the measured data values of the component m_x, m_y and m_z of the magnetization, as well as the components of the uniform excitation field such as h_x^{rf}, h_y^{rf} and h_z^{rf}. Parameters are also indexed in the table (n, h_i, f_i, c_i), which allows organizing the data for later analysis. In addition to the Table.txt file, we also obtain the simulation .ovf files which contain the magnitudes of m_x, m_y and m_z found for each field value and frequency.

5.1.3 Methods of Calculating Power and Phase

To understand the algorithm for calculating power and phase from our simulated data, we start with the simple harmonic function

$$m = A \sin(\omega t + \phi), \tag{5.3}$$

where A is the amplitude, ω is the angular frequency and ϕ is the phase. One can rewrite it as:

$$m = a_s \sin(\omega t) + a_c \cos(\omega t), \tag{5.4}$$

where the a_s and a_c are constants related to amplitude and phase by the following equations,

$$A = \sqrt{a_s^2 + a_c^2}\ , \ \tan\phi = \frac{a_s}{a_c}. \tag{5.5}$$

The values of a_s and a_c could be calculated as :

$$a_s = \frac{2}{T}\int_0^T m \sin(\omega t)\ , \ a_c = \frac{2}{T}\int_0^T m \cos(\omega t). \tag{5.6}$$

In our simulations the values of a_s and a_c are calculated by finding the average value of the time series for $\vec{m}$ (corresponding to an oscillation period) multiplied point by point with the reference ($\sin(\omega t)$) or ($\cos(\omega t)$) expressed as follows:

$$[m_0, m_1, ..., m_{20}] \times [\sin(\omega t_0), \sin(\omega t_1), ..., \sin(\omega t_{20})]\,. \tag{5.7}$$

In other words,

$$\frac{\sum_i^{20} m_i \sin(\omega t_i)}{20} \cong \frac{2}{T}\int_0^T m \sin(\omega t) = a_s. \tag{5.8}$$

Fig. 5.3 illustrates the 20 temporal values of the RF field and the average values of $< m_x >$ and $< m_y >$ obtained in a simulation for a disk from NiFe to $H = 0$ and $\omega_{RF} = 6$ GHz frequency.

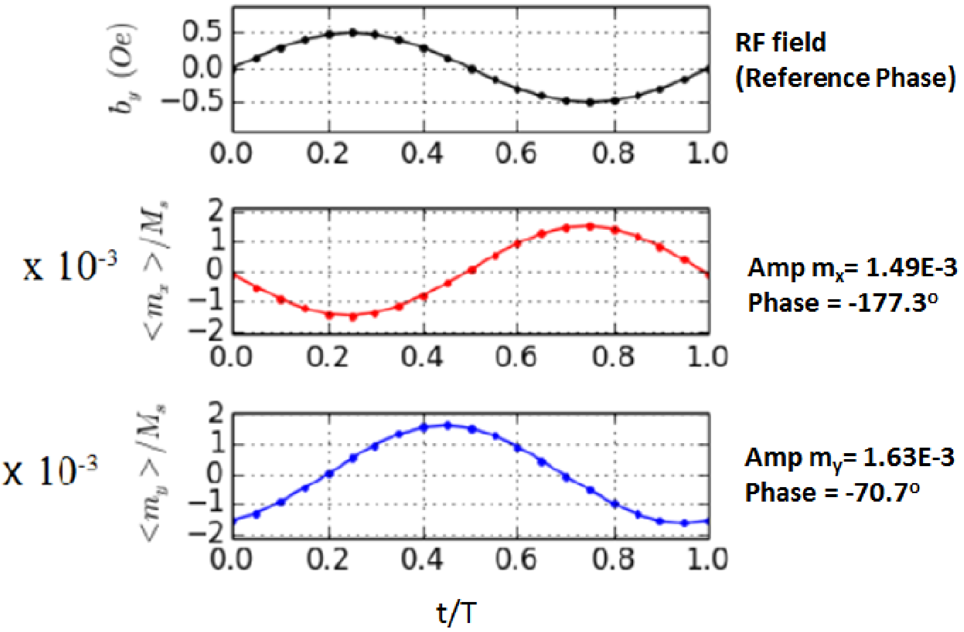

Figure 5.3: The RF field (reference Phase), Amplitude and Phase for the dynamic components (m_x, m_y) of magnetization $\vec{m}$.

5.2 Absorbed Power

The area under the magnetization curve $(M \times H)$, could be explained by the work done per unit volume of the magnetic material over a complete cycle of magnetization given by:

$$W = -\int \vec{M} \cdot d\vec{H}. \tag{5.9}$$

For a static field, a small magnetization cycle of period $T = \frac{2\pi}{\omega}$ is performed through the $\mathrm{h_{rf}}$ field that oscillates at a frequency ω. For a system comprising 20 elements, each of volume v_i and magnetization m^i_{osc}, the power dissipated during the magnetization cycle due to the h^{rf} field can be expressed as:

$$< P >= \frac{\omega}{2\pi} \int_{t=0}^{t=\frac{2\pi}{\omega}} \left(\sum_{i=0}^{20} v_i m^i_{osc} \right) \cdot \frac{dh^{rf}}{dt} dt. \tag{5.10}$$

The mean power $< P >$ will be proportional to the amplitudes, time phases and relative orientations of the applied h^{rf} field and the vector sum $\sum v_i m^i_{osc}$ of the oscillating parts of the magnetizations of each element of the system. The spherical coordinates of the magnetization vector in the mesh is given in the Fig. 5.4.

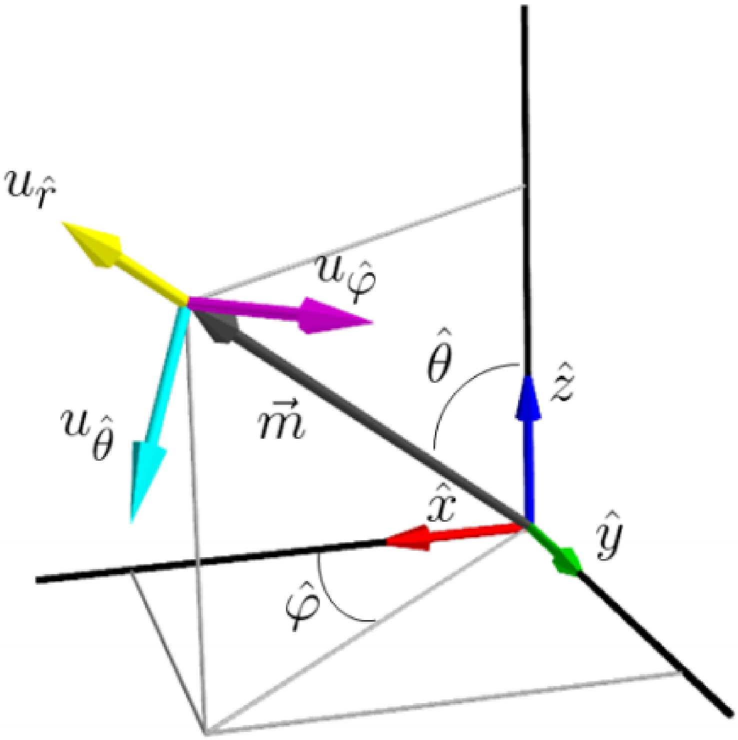

Figure 5.4: Graphical representation of the spin magnetization vector in the mesh in spherical coordinates.

5.2.1 Absorption Spectra - Color maps

The micromagnetic model was developed to simulate the broadband ferromagnetic resonance (FMR) experiment using parameters similar to those used in the VNA-FMR measurement. For this we calculate the average absorbed power by the simulated systems. The static components of the magnetization and the field do not contribute to the absorbed power, only the oscillatory ones. For a harmonic cycle, this power is determined by equation 5.10 according to which $< P >$ is proportional to the sum of the oscillating parts of the magnetization that are in the direction of the h_{rf} field. Since, magnetization and the h_{rf} field are harmonic, the $M \times H$ cycle has an elliptical shape, where the eccentricity depends on the phase between them. Observing the hysteresis cycles shown in Fig. 5.5 this relationship can be easily noticed. For a phase difference $\phi = 90°$ between the magnetization and the h_{rf} field, the $M \times H$ cycle displays an almost round shape and has the largest area (as shown in the middle of Figure 5.5). For $\phi = 0°$ or $\phi = 180°$ the ellipse turns into a line (as shown in the left and right of Fig. 5.5), which may have amplitude of oscillation and still not have significant absorption. Calculating the area inside the ellipse for each H field and each frequency f, we represent the absorption spectrum as color map we can compare it directly with the experimental result.

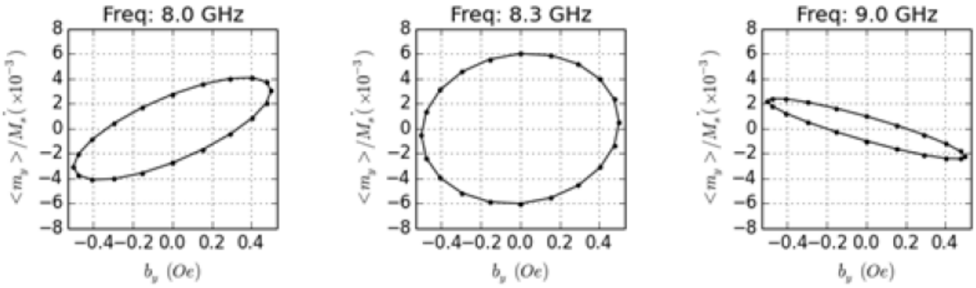

Figure 5.5: Cycles of Hysteresis $M \times H$ at different frequencies.

The flow chart of the simulation algorithm is given in the Fig. 5.6.

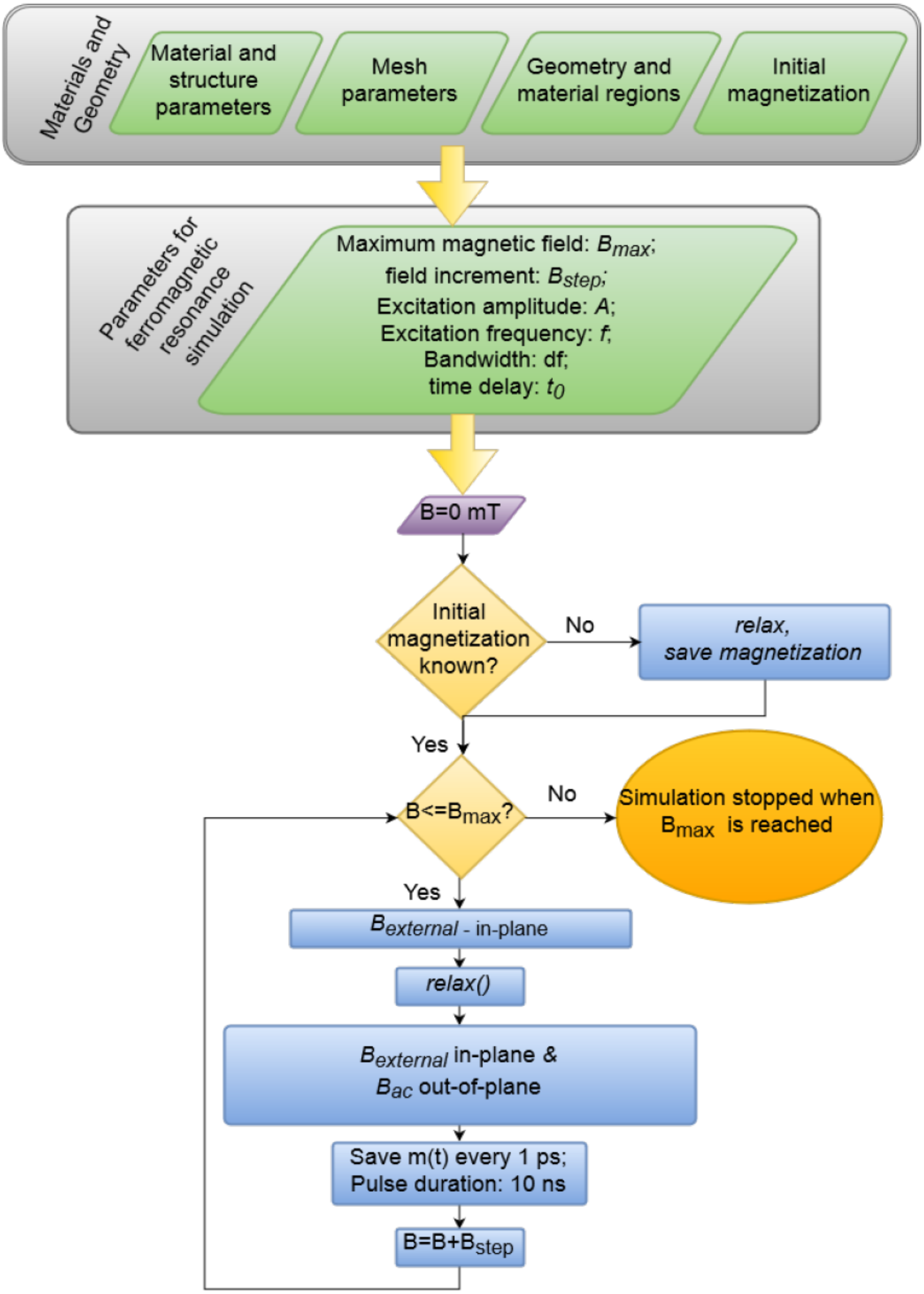

Figure 5.6: Algorithm for simulations of the FMR response.

5.3 Simulated Oscillation Modes in Permalloy Square

The oscillation modes presented in this thesis were described according to the spatial dependencies of the amplitude and the phase of $(\vec{m} \cdot \hat{u}_{\varphi i})$ (as shown in the Fig. 5.4). To show the types of oscillation modes that will be discussed throughout this thesis, we simulate a sample of Permalloy with dimensions 1 μm x 1 μm x 40 nm, saturated by $H = 2000$ Oe and excited by h_{rf} perpendicular to the H field.

In Fig. 5.7, a cross section is shown in the $H = 2000$ Oe field of the simulated absorbed power spectrum, where the magnetization is saturated in the direction of the field, along with the modes excited in this field at specific frequencies.

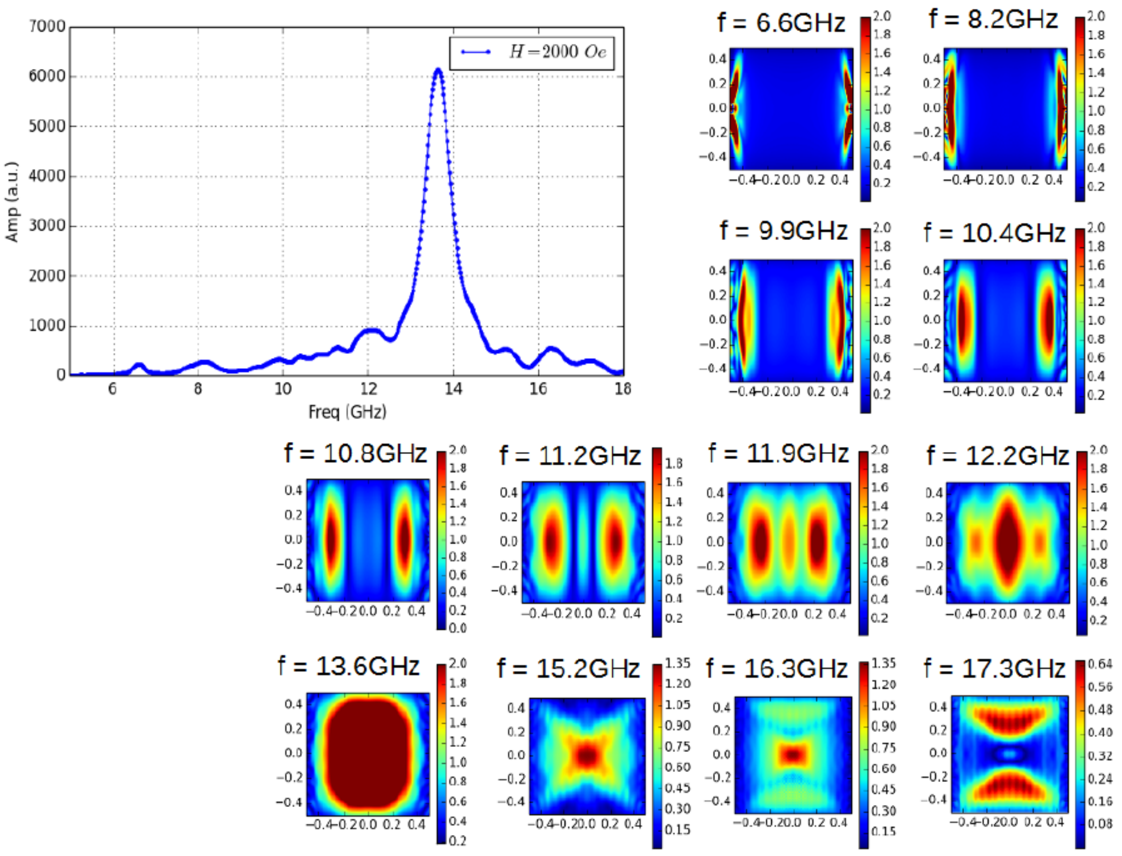

Figure 5.7: Simulated data from a 1 μm $\times$ 1 μm square with 50 nm thickness of Permalloy saturated by $H = 2000$ Oe and excited by h^{rf} perpendicular to the applied field H [18].

When the oscillations contained in the direction of the vector $\hat{u}_{\varphi i}$ have amplitude only in the regions of the edges and amplitude almost zero in the central region, we have the oscillation modes called edge mode (n-MB).

These modes appear at the lowest frequencies compared to the entire frequency range considered in the spectrum. In this case, we can see the edge modes at frequencies $f = 6.6$ GHz to 10.4 GHz. Oscillations can start to propagate along the central region in a nodal structure perpendicular to the direction of the applied magnetic field. This type of mode is known as volume volume (n-MVB) and begin to be excited in this case from the frequencies $f = 10.8$ GHz to 11.9 GHz.

In addition to the nodal pattern propagating perpendicular to the direction of the H field, nodal lines can also appear perpendicular to the direction of the H field, which is characteristic of the Damon-Eshbach mode (n-DE). In this case, the nodal lines can intertwine and form a mixed mode of (m-MVB n-DE), as in $f = 12.2$ GHz. When the spatial distribution of the oscillations contained in the direction of the vector $\hat{u}_{\varphi i}$ are in uniform phase (90) and uniform amplitude, as in the case of the oscillation mode shown at frequency $f = 13.6$ GHz we have the fundamental mode or uniform mode (MU). From $f = 12.9$ GHz the oscillations contained in the direction of the vector $\hat{u}_{\varphi i}$ have maximum amplitude in the direction parallel to the applied field and the static magnetization, having a typical (n-DE) mode.

These modes discussed above are excited modes when the magnetization is saturated by the applied field. In this thesis, the oscillation modes in the unsaturated state of magnetization are also investigated, such as in the ellipses with magnetic vortex (which will be explained in the last sections of the Ch. 6).

Chapter 6

Results and Discussions

This chapter presents the results from detailed investigations of the magnetization dynamics in continuous films and magnetic nanostructures in the form of antidots and ellipses. In the first part the structural, static and dynamic magnetic properties of Co-based Husler Alloys Co_2FeAl (CFA) films, deposited on Si(100) are presented and discussed. In the second part we discuss the static and dynamic magnetic properties in the trilayer system e.g $Co/Ni_{81}Fe_{19}/Co$ films. In the third part, we discuss the magnetization dynamics in permalloy ($Ni_{81}Fe_{19}$) based magnetic antidots. We analyzed the results with help of micromagnetic simulations. In the last part of the chapter the microwave response of permalloy ellipses with different diameters and a thickness of 50 nm is addressed. The ellipses were investigated using VNA-FMR techniques both in the remanent vortex state and as a function of an externally applied magnetic field. Micromagnetic simulations were employed to analyze the experimental results.

6.1 CoFeAl films

In this section the structural, static and dynamic magnetic properties of Co_2FeAl (CFA) films, deposited on Si(100) are presented and discussed. The focus is to study the evolution of the coercive field, anisotropies, damping constant and linewidth broadening as a function of CFA film thickness in the range 5 nm to 200 nm. We used the Vector Network Analyzer Ferromagnetic Resonance (VNA-FMR) for dynamic characterizations and AGFM for static characterizations.

We obtain coercive fields weakly dependent on thickness, with values in the range 4.2 Oe to 7.8 Oe. All samples show roughly constant in-plane magnetic anisotropy, and out-plane anisotropy originated from the CFA/Ti interfaces. With increasing thickness we observe the emergence of rotatable anisotropy. We found magnetic damping parameters α between 2.56×10^{-3} and 3.45×10^{-3}, and inhomogeneous linewidth ΔH_0 under 10.3 Oe for the whole range of CFA film thickness. These results of ΔH_0 are small when compared to the values reported for CFA in literature, specially for films with thickness above 100 nm. The present study contributes to a better understanding of the dynamic properties of magnetic CFA films, and open new potential applications in magneto-impedance sensors, RF shielding and others.

6.1.1 Co-based Husler Alloys

In recent decades, a great deal of attention have been paid to Co-based Heusler alloy films [122, 123, 124, 125, 126, 127, 128, 129] due to their large spin polarization up to 100% and high Curie temperature. These properties make them attractive for spintronic applications, dense magnetic storage and memory devices as well as applications in magnonic devices. An important property for these applications is the magnetic damping parameter α, which should be the lowest possible. There are different types of Co-based full Heusler alloys, represented by X_2YZ, e.g. Co_2FeSi [130], Co_2MnSi [131], Co_2MnAl [132, 133], Co_2MnGe [134, 135] and among them Co_2FeAl (CFA) which presents the lowest value for the damping constant α [136, 127, 137]. Depending on the type of substrate and deposition conditions, the CFA films may assume different phases [129, 138]: $L2_1$, $B2$ and $A2$, corresponding to the most ordered, partially disordered and disordered phase, respectively [139]. The $L2_1$ phase presents very small magnetic damping because of an efficient spin-flip process [140]. Unfortunately, to get this phase, special deposition conditions, substrates and heat treatment are needed. On the other hand, CFA films with B2 and A2 phase can also present low damping parameter, depending upon the deposition process [141, 127]. Some studies have been carried out on dynamic properties and damping parameter of CFA films with thickness of a few hundred nm [141, 126].

In the following investigation, we perform a detailed analysis of the structural and magnetic properties of CFA films, with thickness from 5 nm up to 200 nm, grown on Si(100) by magnetron sputtering. The structural properties were characterized by Grazing incidence X-ray diffraction GIXRD and high resolution transmission electron microscopy HR-TEM. The magnetic properties were studied with alternating gradient force magnetometry AGFM and broadband ferromagnetic resonance VNA-FMR. Our results indicate low damping, small inhomogeneous linewidth broadening and A2 structural phase for all samples, even the 200 nm thick film. This study provides further insight on the effect of thickness on the dynamic properties of CFA films.

6.1.2 Samples

Full-Heusler alloy Co_2FeAl films with thickness t_{CFA} = 5, 10, 20, 50, 100 and 200 nm, with 5 nm Ti buffer and capping layers, were deposited by using DC magnetron sputtering, at room temperature, on Si(100) substrates (as shown in the Fig. 6.1). The deposition rates are given in Table 4.1.

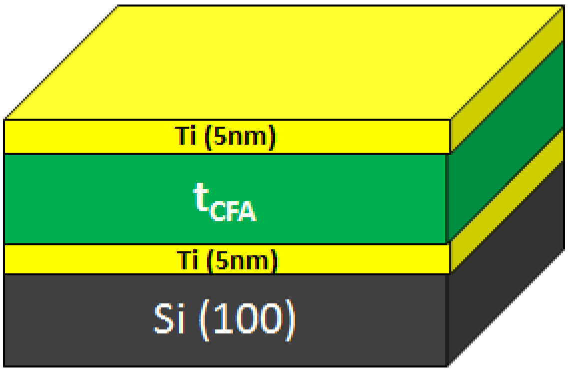

Figure 6.1: Illustration picture for the sample structure.

The base pressure was better than 5×10^{-8} torr, while the deposition was done under 5.0 mTorr/50 sccm Ar. All films were deposited using a commercial target with nominal mass composition $Co_{58.73}Fe_{27.83}Al_{13.44}$ and the target to substrate distance was kept to 10 cm. Deposition rates were calibrated by low angle X-ray reflectivity (XRR) measurements. During the growth process, an in-plane magnetic field of around 200 Oe was applied in order to induce an uniaxial anisotropy.

6.1.3 Structural Characterization

The crystalline nature of the as-deposited films was confirmed by Grazing incidence X-ray diffraction (GIXRD) using a Panalytical X'Pert Pro diffractometer with Cu-Kα radiation (λ = 1.54056 Å). Further structural analysis was carried out with high resolution transmission electron microscopy (HR-TEM). Samples were prepared with focused ion beam (FIB) (TESCAN LYRA3), for representative samples with thickness 5 nm and 100 nm. A protective layers of 50 nm gold and 2 μm paltanium were used. Bright-field images and selected area electron diffraction (SAED) patterns were obtained using a JEOL 2100F 200 kV TEM. Fast Fourier transform (FFT) analysis of the HR-TEM images, were performed by Gatan Digital Micrograph software. Moreover, energy dispersive X-ray spectroscopy (EDX) was used for elemental distribution analysis.

X-ray diffraction patterns for all CFA films are shown in Figure 6.2. For 50 nm thickness or more we observe the (220), (400) and (422) peaks, which clearly indicate an A2 crystalline structure [142, 143, 144]. We believe that films under 50 nm have the same A2 structure as the (220) peak is present. The other peaks, observed around $2\theta \approx 55°$, correspond to the Si substrate and the sample holder. The (220) peak full width at half maximum (FWHM) as function CFA thickness is shown in the inset of Fig. 6.2. Here we observe that the FWHM has small values above 50 nm thickness, this indicates that our samples have low structural stress/strain.

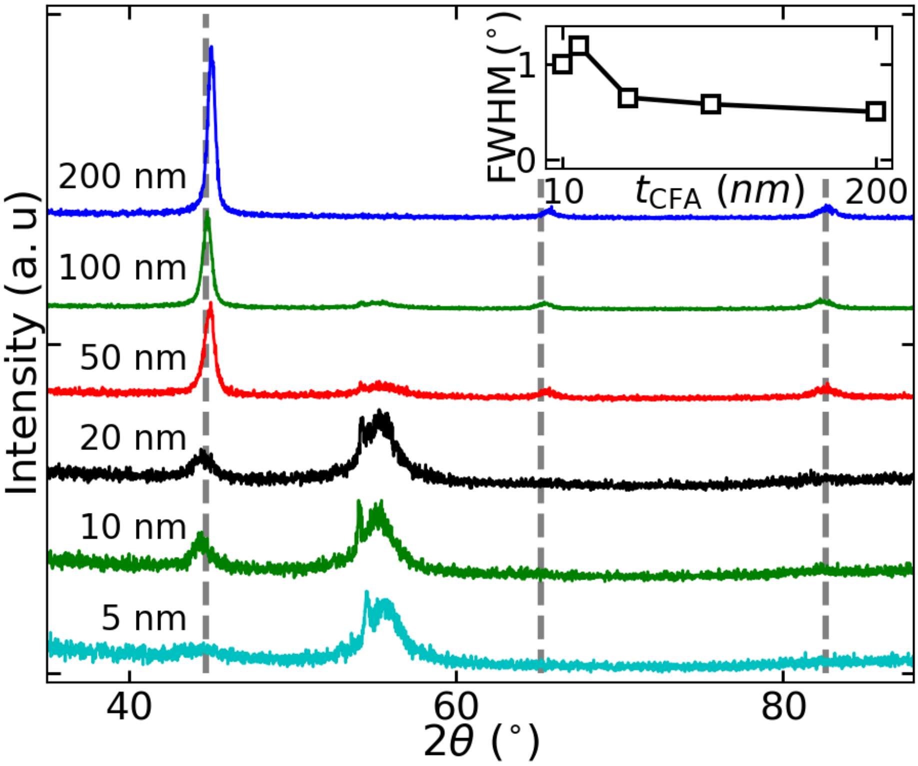

Figure 6.2: GIXRD pattern of the CFA films. The vertical lines indicate the crystalline planes (220) at $2\theta = 44.73°$, (400) at $2\theta = 65.20°$ and (422) at $2\theta = 82.60°$. The inset shows the calculated FWHM for (220) peak as function of CFA thickness (t_{CFA}).

High resolution transmission electron microscopy images for selected CFA samples (t_{CFA} = 5 nm and 100 nm) are shown in Figure 6.3. From these images we observe that our films have good interfaces and low surface roughness. We observe clear columnar growth for t_{CFA} = 100 nm (see Fig. 6.3(a)), while for t_{CFA} = 5 nm (Fig. 6.3(b)) polycrystaline grains are observed. SAED pattern for t_{CFA} = 100 nm (see inset in Fig 6.3(a)) indicates the presence of (220), (400) and (422) crystalline planes. For t_{CFA} = 5 nm the FFT analysis of the HR-TEM images is presented in the inset of Fig. 6.3(b) which shows a (220) diffraction pattern. Figure 6.4(b) shows the EDX elemental maps of Co, Fe, Al and Ti over the area indicated in Figure 6.4(a). It can be clearly seen that Co, Fe and Al are homogeneously distributed through the analyzed area, with no spurious precipitates of CoFe or Al. Considering these results observed in the structural characterization (HR-TEM, EDX and XRD) we are able to infer A2 structure in all samples studied in this work.

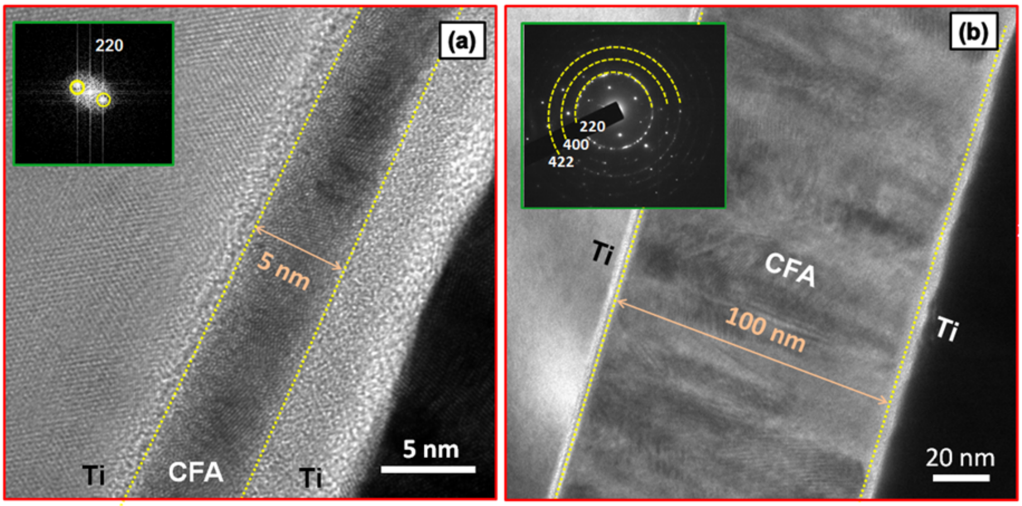

Figure 6.3: Cross-section HR-TEM images of CFA films: (a) t_{CFA} = 5 nm, (b) t_{CFA} = 100 nm. The insets show the FFT analysis for t_{CFA} = 5 nm and the selected area diffraction pattern (SAED) for t_{CFA} = 100 nm.

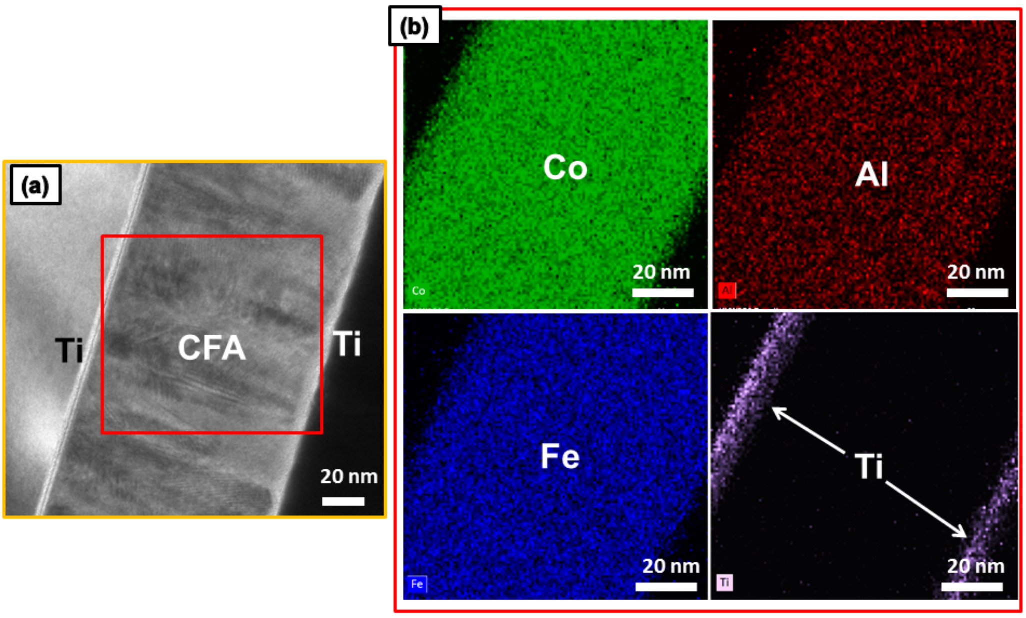

Figure 6.4: TEM/EDX analysis of $t_{CFA} = 100$ nm: (a) HR-TEM image depicting analyzed region, (b) EDX maps showing elemental distributions of Co, Fe and Al in the film thickness with Ti capping and buffer layers.

6.1.4 Static Characterization (MxH)

Room temperature magnetization curves (M vs. H) were obtained with an alternating gradient force magnetometer (AGFM). For all measurements, the magnetic field was applied in the film-plane, aligned with or perpendicular to the anisotropy axis direction induced during deposition.

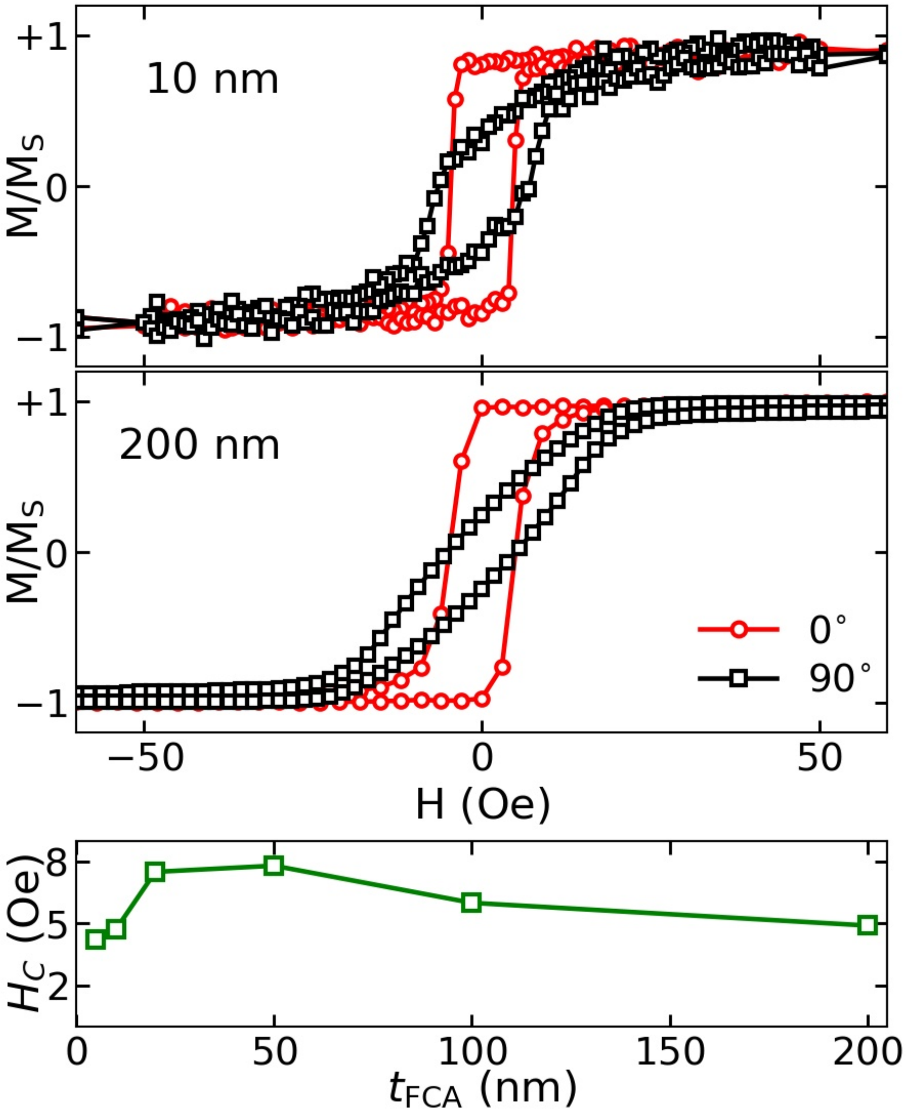

Figure 6.5: Upper panels: hysteresis loops for the easy (0°) and hard axis (90°) t_{CFA} = 10 and 200 nm films. Bottom panel: coercive field as a function of t_{CFA} measured for 0°.

In-plane static hysteresis loops (M vs. H) measured along (0°) and perpendicular (90°) with respect to the induced anisotropy axis, for t_{CFA} = 200 nm, and 10nm, are shown in Fig. 6.5. All M vs. H results clearly indicate an in-plane anisotropy as expected from the deposition conditions. Also, high squareness in all samples indicate low contribution of perpendicular anisotropy. Furthermore, the obtained coercive fields H_c with values from 4 Oe to 7 Oe exhibit a weak dependence with the

CFA thickness (see lower panel of Fig 6.5). We remark that the thicker films remain with low coercive fields: e.g. $H_c = 4.9$ Oe for $t_{\mathrm{CFA}} = 200$ nm and $H_c = 6.0$ Oe for $t_{\mathrm{CFA}} = 100$ nm.

6.1.5 Dynamic Characterization

Broadband ferromagnetic resonance measurements were performed for frequencies in the range 0.1 GHz to 10 GHz and fields in the range ± 800 Oe using the setup described in [145]. In order to improve line-width measurement accuracy, the setup described in Ref. [145] was modified in order to emulate a traditional dP/dH FMR measurement. In this case we used a micro-strip line inside a solenoid which generate the external magnetic field H. At a given frequency f and H value, a small (± 1 Oe) software generated field sweep H_{sweep} is performed while the absorbed power is measured. The dP/dH is calculated by fitting the resulting P vs H_{sweep} curve. For all magnetic measurements, the magnetic field was applied in the film plane, aligned with or perpendicular to the anisotropy axis direction induced during deposition.

Broadband FMR results and dispersion relation fittings are shown in figure 6.6 for selected samples. The color scale denotes the absorption amplitude, where blue corresponds to minimum and red corresponds to maximum absorption amplitude i.e. the resonance frequencies f_{R}. The effect of the induced in-plane anisotropy is clearly observed as the difference of measurements at 0° or 90°. At 0° both resonant branches close at the coercive field, while at 90° there is a field gap between them that is equal to twice the saturation field. It can be noticed that with increasing t_{CFA} the slope of the dispersion relations increases. This is a clear indication of an out-of-plane anisotropy. For thicker samples, an upward frequency shift in the dispersion relations is observed, which is the signature of rotatable anisotropy (RA), which refers to the reorientation of the easy axis of an uniaxial anisotropy towards the direction of the applied magnetic field [57, 58]. The RA was first observed in ferromagnetic films and was attributed to the ferromagnetic–antiferromagnetic exchange interaction with the expected NiO surface-oxide layer formed during the film deposition [59, 60]. It has been also observed in Ni–Fe films [61, 62, 64] and Heusler alloy films [63]. RA is attributed to the magnetic disorder, micro domains and the negative magnetostriction for films above a critical thickness.

By fitting the dispersion relations (f_{FMR} vs H) we are able to quantify the contributions of the anisotropy energies present in each sample in terms of anisotropy fields H_k, H_r and $H_\perp$ for in-plane, rotatable and out-of-plane anisotropies, respectively. The later is not calculated directly but through the effective magnetization

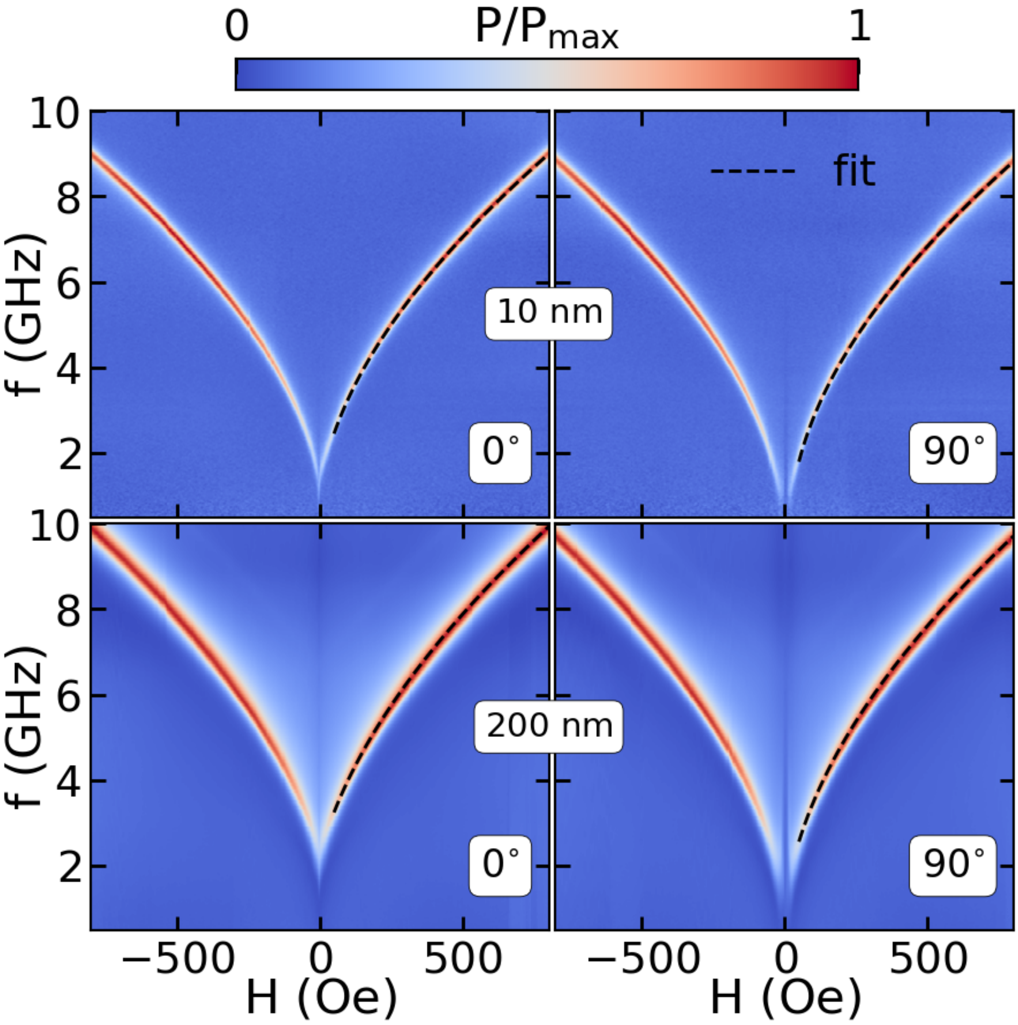

Figure 6.6: Broadband FMR spectra (color plots) and dispersion relation fits (dashed lines) for samples with t_{CFA} = 10 nm (Top panels) and t_{CFA} = 200 nm (bottom panels), measured along (0°) and perpendicular (90°) to the induced anisotropy axis.

$4\pi M_{\mathrm{eff}} = 4\pi M_s - H_\perp$. The fitting functions are

$$f_{\mathrm{FMR}} = \frac{\gamma}{2\pi}\sqrt{(4\pi M_s + H_\perp + H + H_k + H_r)(H + H_k + H_r)} \tag{6.1}$$

for external field H applied along the anisotropy axis, and

$$f_{\mathrm{FMR}} = \frac{\gamma}{2\pi}\sqrt{(4\pi M_s + H_\perp + H + H_r)(H - H_k + H_r)} \tag{6.2}$$

for H applied perpendicularly to the anisotropy axis. Here, we take the values γ = 18.32 MHz/Oe [141] and M_s = 1030 emu/cm^3 [146] for gyromagnetic ratio and saturation magnetization, respectively.

The results from the fits are summarized in Table 6.1. The value of the in-plane anisotropy remains almost constant for all samples, as expected from the M vs. H

curves as shown in Figure 6.5. We observe a monotonic increase in M_{eff} with larger t_{CFA} which could be attributed to the surface anisotropy effect between CFA and the Ti buffer and capping layers. From the linear fitting of M_{eff} vs $1/t_{\text{CFA}}$ [141] (not shown) for thickness up to 20 nm we calculate the out-of-plane surface anisotropy constant as $K_s = 0.54$ erg/cm^2. On the other hand, we observe that the rotatable anisotropy appears only for samples thicker than 50 nm and its value increases with CFA film thickness. This is expected as thicker films usually exhibit higher degrees of magnetic disorder.

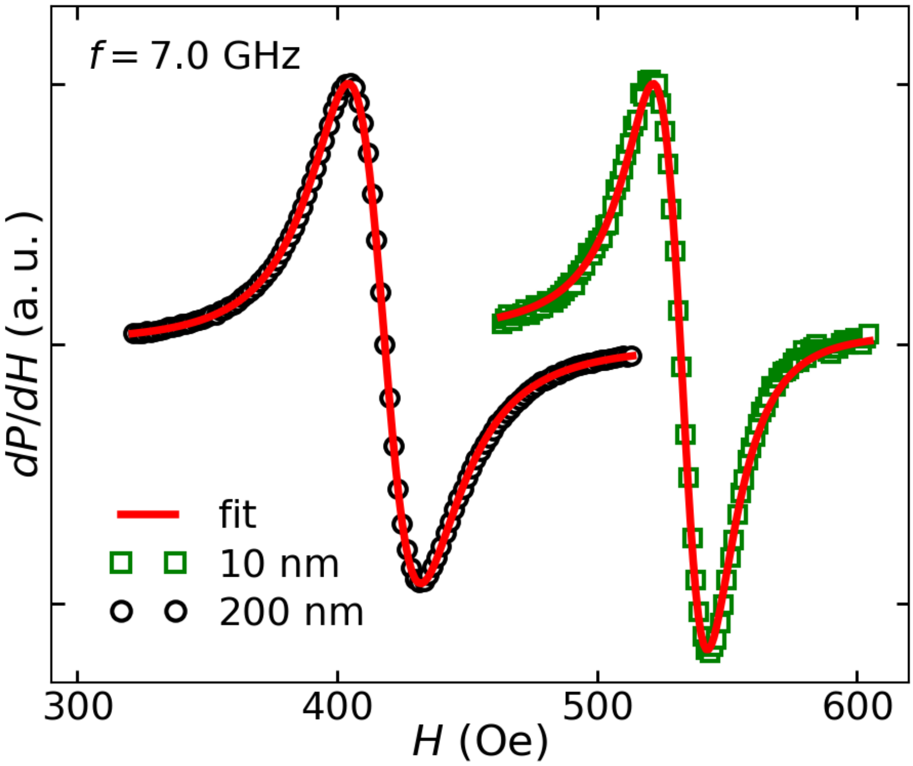

Figure 6.7: Derivative of the FMR absorption spectra for $t_{CFA} = 10$ and 200 nm films at (0°), measured at 7 GHz.

In Figure 6.7 we show the FMR absorption derivative dP/dH spectra for $t_{\text{CFA}} =$ 10 nm and 200 nm samples, measured at 7 GHz. In order to obtain the resonance field H_{FMR} and the linewidth ΔH we use a fitting function which takes into account the line asymmetry [147].

We obtain the Gilbert damping parameter α and the inhomogeneous linewidth parameter ΔH_0 from the ΔH vs f fittings performed using:

$$\Delta H = \Delta H_0 + \frac{4\pi\alpha f}{\gamma}. \tag{6.3}$$

Some of the ΔH vs f plots and respective fits are shown in Figure 6.8. Sample with $t_{\text{CFA}} = 200$ nm has the largest ΔH for all measured frequencies. Even so, for 8 GHz, ΔH is only 25.8 Oe for this particular sample, which is a remarkable small value for a thick film (t $>$ 100 nm). The obtained α and ΔH_0 values are presented in Table 6.1. It can be clearly seen from the table that the α values do not exhibit substantial changes with film thickness. On the other hand all samples present small ΔH_0 values. For samples thicker than 50 nm the small increase in ΔH_0 can be related to the degree of magnetic disorder, also observed on the above mentioned rotatable anisotropy. We believe that the relatively large ΔH_0 value for the 5 nm sample is related to the large out-of-plane anisotropy present in this sample.

It must be remarked that our thickest sample (200 nm) has $\alpha = 2.78 \times 10^{-3}$ and a small $\Delta H_0 = 10.3$ Oe, when compared to the values reported in literature [141, 125] where small α values were reported but with a large ΔH_0 which probably indicates damping mechanisms other than Gilbert damping.

This work of low damping and small ΔH_0 for thick ferromagnetic films provides new opportunities for applications such as spin-transfer-torque-induced switching, magnetoresistive devices and magnetic oscillations, because of their low energy loss and high sensitivity.

Table 6.1: Summary of results from static and dynamics magnetization analysis. Showing Coercive field H_c, Uniaxial anisotropy H_k, Rotatable anisotropy H_r, Effective saturation magnetization M_{eff}, Gilbert damping parameter α and Inhomogeneous linewidth ΔH_0 as function of sample thickness t_{CFA}.

t_{CFA} (nm)	H_c (Oe)	H_k (Oe)	H_r (Oe)	M_{eff}	α (10^{-3})	ΔH_0 (Oe)
5	4.2	15	0	690	3.12 ± 0.29	7.2 ± 0.6
10	4.7	15	0	860	2.56 ± 0.19	5.6 ± 0.6
20	7.5	15	0	940	3.66 ± 0.23	5.0 ± 0.8
50	7.8	13	5	960	3.45 ± 0.10	6.7 ± 0.3
100	6.0	10	20	1000	3.03 ± 0.12	6.9 ± 0.5
200	4.9	18	28	1020	2.78 ± 0.22	10.3 ± 0.7

6.1.6 Partial Conclusions

In summary, we have grown Co_2FeAl Heusler alloy thin films on Si(100) substrate at ambient temperature using magnetron sputtering technique. Based on the structural analysis with X-ray diffraction (XRD), transmission electron microscopy (TEM) and EDX, we found that these CFA films show the A2 ordered phase, good interface and

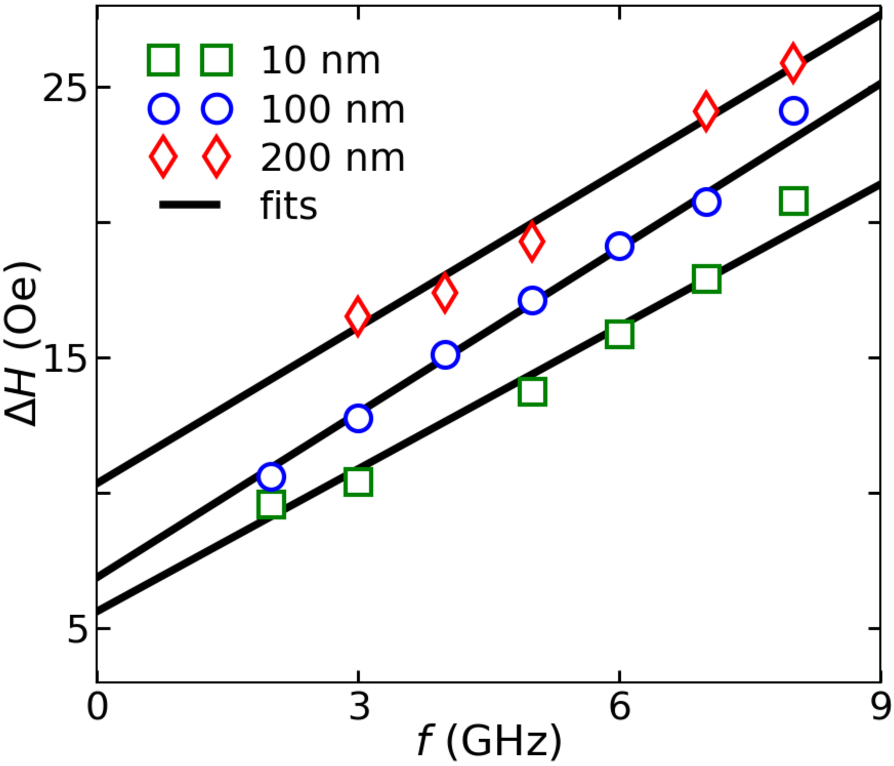

Figure 6.8: FMR linewidth (ΔH) as a function of resonance frequency (f_r) and corresponding linear fitting for selected samples.

low roughness. Static magnetization curves show the existence of in-plane magnetic anisotropy and coercive fields in the range 4.2 to 7.8 Oe. Dynamic magnetic properties were studied using broadband FMR. From the fittings of the dispersion relations we obtained the values of the in-plane, out-of-plane and rotatable anisotropies. The out-of-plane surface anisotropy constant for CFA/Ti interfaces was estimated as $K_s = 0.54$ erg/cm^2. We obtained damping constants as low as 2.56×10^{-3} for 10 nm CFA film, and 2.78×10^{-3} for 200 nm. It must be remarked that all ΔH_0 obtained values are small when compared to the values reported to CFA in literature. Moreover, there is a clear but yet small increase on ΔH_0 with increasing film thickness, which is probably correlated to the appearance of the rotatable anisotropy. Thick films of CFA with small FMR linewidth have potential for other applications than spintronics structures. This is the case of magneto-impedance sensors, RF shielding among others. The present study contributes to a better understanding of the effect of thickness on the dynamic properties of magnetic CFA films.

6.2 Co/NiFe/Co films

In the following section, we investigate the static and dynamic magnetic properties of trilayered systems consisting of Co(t_{Co})/Ni$_{81}$Fe$_{19}$(t_{NiFe})/Co(t_{Co}). Inside these synthetic layers, both uniform and perpendicular standing spin wave (PSSW) modes of ferromagnetic resonance do exist which are produced by the in-phase and out-of-phase precession of the spins in different layers. The Gilbert damping parameter is investigated as a function of thickness using broadband ferromagnetic resonance (VNA-FMR). We found that the magnetic damping constant α increases continuously with increasing the Co thickness $\mathrm{t_{Co}}$. Also, from fittings of the dispersion relations we were able to extract the values of H_k and M_{eff}. This work provide a deep understanding and control of anisotropies, effective magnetization, line width and magnetic damping in synthetic layered system, which could be used for potential applications.

6.2.1 Introduction

The magnetization dynamics of multilayered thin film structures with one or more magnetic layers has been extensively studied and plays an important role in investigating the properties of soft magnetic materials [148, 149, 150], the bases of most modern devices, widely used in many applications such as magnetoresistive devices[151], spintronics devices [152], information processing [153], ferromagnetic resonance imaging [154] and spin accumulation detection[155].

In the last few decades, the search for magnetic materials with high FMR frequencies become important advances of science and technology. In the FMR studies, the damping is an important parameter, as it controls the magnetization dynamics. Therefore its determination and control are critical for the performance increase of practical devices. Although many studies focus on the understanding of magnetic damping, there are yet several aspects concerning the damping parameter and magnetization dynamics in nanostructured materials that are not completely understood. The process of magnetic moment precession is described phenomenologically by the Landau-Lifshitz-Gilbert equation [156] (which is explained in section 3.1.1).

In most of the experimental work, the overall dynamic response is analyzed in the framework of the LLG equation using only one phenomenological parameter. However, a limited number of studies has addressed the microscopic origin of damping experimentally, by trying to distinguish different relaxation states, in which magnetization vector either has the transverse or the longitudinal components. In general, magnetic damping can be split into two different fundamental states: i) Gilbert type relaxation, in this case the energy is directly transferred to the lattice or to uncorrelated electron-hole pairs, such as in the spin-pumping mechanism, and ii) non-Gilbert-type damping, which takes the energy in the spin subsystem in the form of magnon scattering with nonzero wave vector ($\vec{k} \neq 0$) and is analogous to a phasing of the spin precession (transverse relaxation).

Gilbert type of relaxation is due to intrinsic damping of the magnetization vector, which results in a resonance linewidth which has linear relationship to the microwave frequency. However, experimentally, the linewidth is often found to have a linear frequency dependence with an extrapolated non-zero linewidth at zero frequency ΔH_0 [157]. Therefore, the measured linewidth versus frequency is often described using the simple relationship

$$\Delta H_{measured} = \Delta H_0 + \frac{4\pi\alpha f}{\gamma}, \tag{6.4}$$

where the linear term is assumed to be a measure of the intrinsic damping and the magnitude of ΔH_0 depends upon the purity of material as well as the thickness of FM layer and approaches zero for the impurity less samples. This implies that ΔH_0 is extrinsic, which may come from the non-uniform magnetization precession (non-Gilbert types of relaxation) [158, 70]. These types of relaxations could be changed, either due to any magnetic inhomogeneity, or surface anisotropy field, or dipolar coupling field between the magnetic moments within the sample or two magnon scattering.

Furthermore, in FMR experiments the external microwave field couples with uniform and nonuniform Spin Wave (SW) modes.The excitation of magnetostatic modes occurs when the dipole–dipole interaction dominates in the system and the wavevector ($\vec{q}$) lies in the film plane. On the other hand, the excitation of the modes with wavevector ($\vec{q}$) component perpendicular to the film surface is termed perpendicular standing spin waves (PSSW) modes and the quantization of these modes is due to the geometrical confinement [95].

It must be noticed that, in the confined structure the dispersion relation of SW is modified by the boundary conditions imposed by the lateral dimensions [90]. Especially, the SW finds a propagation channel [91] or form standing waves [159] in the distribution of 'potential wells' defined by the geometry of the structure. The formation of standing wave often leads to localized mode or quantized mode (with multiple quantization numbers) when the characteristic dimensions are of the order of the wavelength of the SW. In general, the number of SW modes increases and their properties strongly depend upon system geometry as well as on the orientation of the magnetic field.

In the following study, we have fabricated Co(t_{Co}) /Ni$_{81}$Fe$_{19}$(t_{NiFe}) /Co(t_{Co}) synthetic magnetic layers system with $2t_{\mathrm{Co}} + t_{\mathrm{NiFe}} = 110$ nm. The static magnetization curves ($M \times H$) were measured with AGFM, while Broadband spectra were measured by the means of VNA-FMR. By analyzing the dispersion relations we obtained anisotropies such as uniaxial, perpendicular and their variations in the synthetic layers. The Broadband spectra shows the typical uniform FMR and also PSSW modes. We investigated the influence of Co thickness on the magnetic damping and PSSW intensity. We observed that the measured damping increases with t_{Co}. The PSSW were analyzed by extracting the experimental dispersion relations and comparing them to the theoretical spin wave dispersion relation equation. For samples with larger t_{Co} we observed more and more intense PSSW modes.

6.2.2 Samples

We produced a series of Ru (5 nm)/Co(t_{Co})/Ni$_{81}$Fe$_{19}$(t_{NiFe})/Co(t_{Co})/Ru (5 nm) samples (as shown in Fig. 6.9) with cobalt thickness $t_{\mathrm{Co}} = 0$, 10, 20, and 30 nm and NiFe thickness $t_{\mathrm{NiFe}} = 120$, 90, 70 and 50 nm, such that $t_{\mathrm{NiFe}} + 2t_{\mathrm{Co}} = 110$ nm. The multilayer films were deposited by magnetron sputtering on Si(100) substrates at room temperature (RT) under a base pressure better than 5×10^{-8} torr. The deposition conditions were, working pressure 5 mTorr and 50 sccm Ar gas flow.

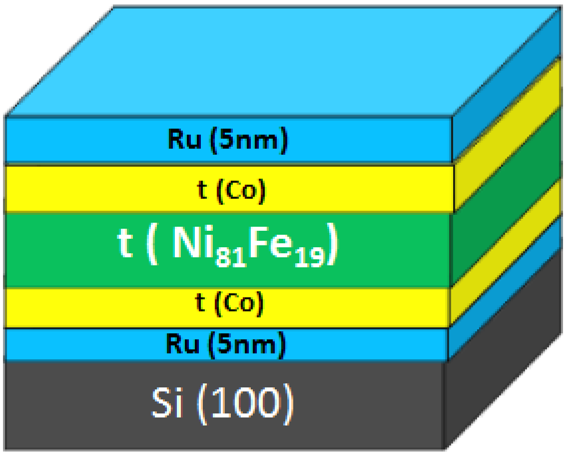

Figure 6.9: Illustration picture for the sample structure.

DC power sources were used for Co, NiFe, and Ru depositions. All deposition rates were calibrated by low angle x-ray reflectivity measurements. During the growth process, an in-plane magnetic field of about 200 Oe was applied in order to induce an unidirectional anisotropy. We performed static magnetic measurements (M vs. H) with an alternating gradient force magnetometer (AGFM) in the field range of $\pm$ 150 Oe. Dynamic magnetic measurements were performed by means of a broadband ferromagnetic resonance FMR technique using a Rhode and Shwarz ZVA24 VNA combined with a coplanar waveguide (CPW) by Cascade Microtech for frequencies in the range 0.1 GHz to 25 GHz and magnetic fields of $\pm$ 1000 Oe. For these measurements, each sample was placed on top of the coplanar wave guide and H was applied along the wave guide propagation direction. The absorption spectra were defined by measuring the S_{11} and S_{21} parameters as in equation 4.4 with respect to a reference spectrum obtained when the sample was saturated along the direction of the RF field; line width measurements were also done using the resonance frequencies as a function of H. All magnetic measurements were performed with H applied at angles of 0° and 90° with respect to the anisotropy axis ($A.A$) direction induced during deposition [145].

6.2.3 Static Characterization

The magnetization curves ($M \times H$) measured along the parallel (0° red curves) and transverse (90° black curves) directions of the samples are shown in Fig. 6.10. All curves are normalized for better comparison. All samples exhibit uniaxial induced anisotropy due to the applied magnetic field during the deposition. The coercive field H_c was modified from 3.5 Oe (shown Fig.6.10(a)) to 28 Oe (shown Fig.6.10(d)) for $2t_{\mathrm{Co}} = 0$ nm and 60 nm respectively (H_c values are summarized in Table 6.2).

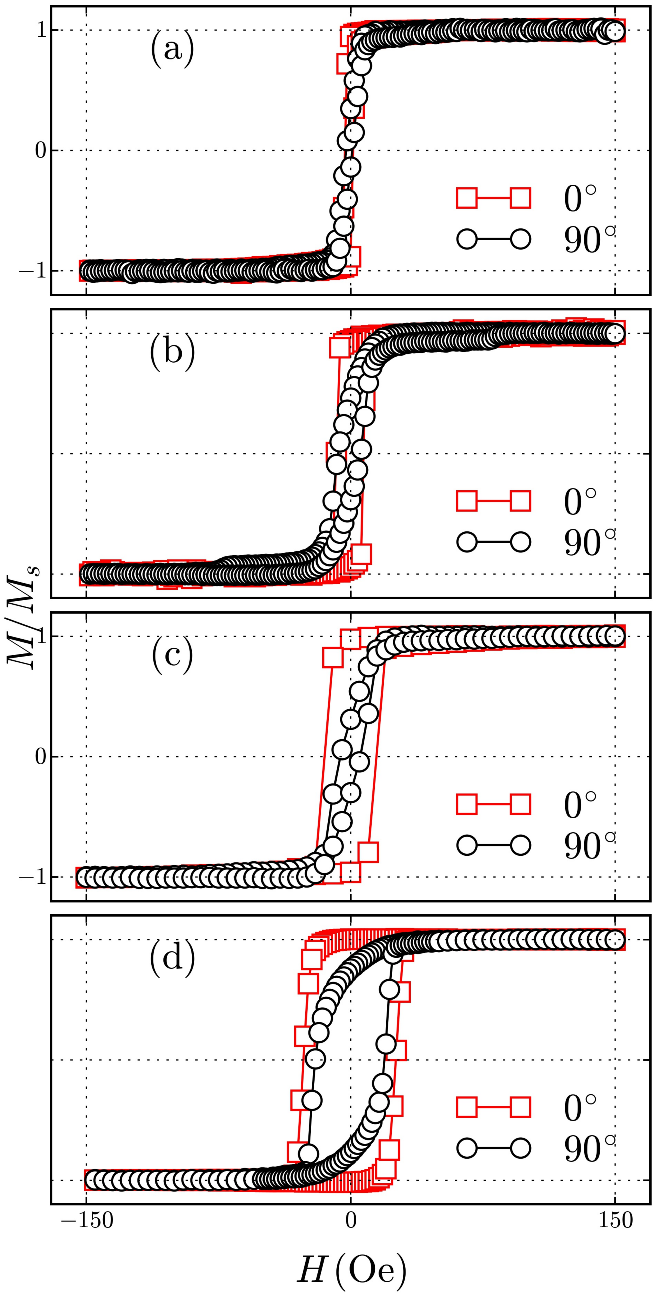

Figure 6.10: Hysteresis loops for the easy (0°) and hard axis (90°) Co(t_{Co})/$\text{Ni}_{81}\text{Fe}_{19}$($t_{\text{NiFe}}$)/Co($t_{\text{Co}}$) samples with cobalt thickness $t_{\text{Co}} = 0$ nm (a); 10 nm (b); 20 nm (c); and 30 nm (d); and NiFe thickness $t_{\text{NiFe}} = 120\,\text{nm} - 2t_{\text{Co}}$.

6.2.4 Dynamic Characterization

Broadband FMR results and dispersion relation fittings are shown in figure 6.11 for samples with Co(t_{Co})/$\text{Ni}_{81}\text{Fe}_{19}$($t_{\text{NiFe}}$)/Co($t_{\text{Co}}$). The color scale denotes the absorption amplitude, where blue corresponds to minimum and red corresponds to maximum absorption amplitude i.e. the resonance frequencies f_{FMR}. The effect of the induced in-plane anisotropy is clearly observed as the difference of measurements at 0° or 90°. At 0° both resonant branches close at the coercive field, while at 90° there is a field gap between them that is equal to twice the saturation field. It can be noticed that with increasing t_{co} the slope of the dispersion relations increases.

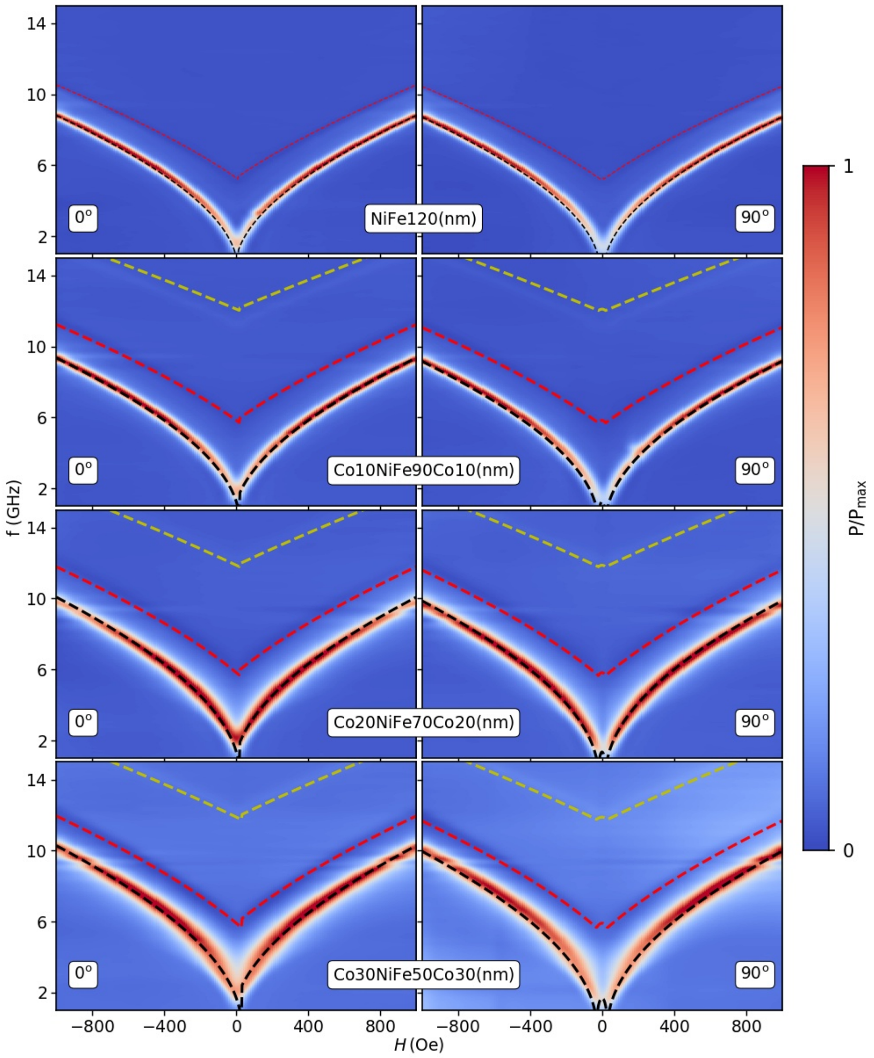

Figure 6.11: Broadband FMR spectra (color plots) and dispersion relation fits (dashed lines) for samples with Co(t_{Co})/Ni$_{81}$Fe$_{19}$(t_{NiFe})/Co(t_{Co}) with cobalt thickness $t_{\mathrm{Co}} =$ 0 nm (top); 10 nm (2nd row); 20 nm (3rd row); and 30 nm (bottom); and NiFe thickness $t_{\mathrm{NiFe}} = 120\,\mathrm{nm} - 2t_{\mathrm{Co}}$ measured along (0°) and perpendicular (90°) to the induced anisotropy axis.

By fitting the dispersion relations ($f_{\rm r}$ vs H) we were able to quantify the contributions of the anisotropy energies present in each sample in terms of anisotropy fields H_k and $M_{\rm eff}$ effective magnetization. The fitting functions is given as (the details about the fitting function are presented in section 3.5.1):

$$2\pi f_r = \gamma \left(H\cos(\phi_M - \phi_H) + H_k \cos 2(\phi_M - \phi_u) + \frac{2A_{\rm ex}}{M_s}(\frac{n\pi}{d})^2 \right)^{\frac{1}{2}}$$
$$\left(H\cos(\phi_M - \phi_H) + 4\pi M_{\rm eff} + H_k \cos^2(\phi_M - \phi_u) + \frac{2A_{\rm ex}}{M_s}(\frac{n\pi}{d})^2 \right)^{\frac{1}{2}}, \tag{6.5}$$

where d is the thickness of film, $H_k = \frac{2K_u}{M_s}$ where k_u is the unaxial anisotropy constant and M_s saturation magnetization, γ is the gyromagnetic ratio, A_{ex} is the effective exchange stiffness constant and n is the quantizied number for the PSSW along the thickness direction, $n = 0$ represents the uniform precession mode and the higher order modes (n = 1, 2, 3, ...) represent PSSW modes. We did the fitting using the parameters H_k and M_{eff}, to get more accuracy the fittings were done for 0° and 90° at same time. In the case of a single $\rm Ni_{81}Fe_{19}$ film we observed only the uniform FMR (n=0) and the 1$^{\rm st}$ PSSW modes. On the other hand when $2t_{\rm Co}$= 20, 40 and 60 nm we observed uniform the FMR mode (n= 0), as well as 1$^{\rm st}$ n= 1) and 2$^{\rm nd}$ (n= 2) PSSW. These higher order PSSW modes are excited in the trilayed system, because of the local oscillation magnetization profiles produced inside the synthetic layer. One of the component of wave number which lies perpendicular to the surface give raise to the PSSW modes. It was noted that the line width increases with $t_{\rm Co}$. The results from the fits are summarized in Table 6.2. We observe a monotonic increase in $M_{\rm eff}$ with larger $t_{\rm Co}$.

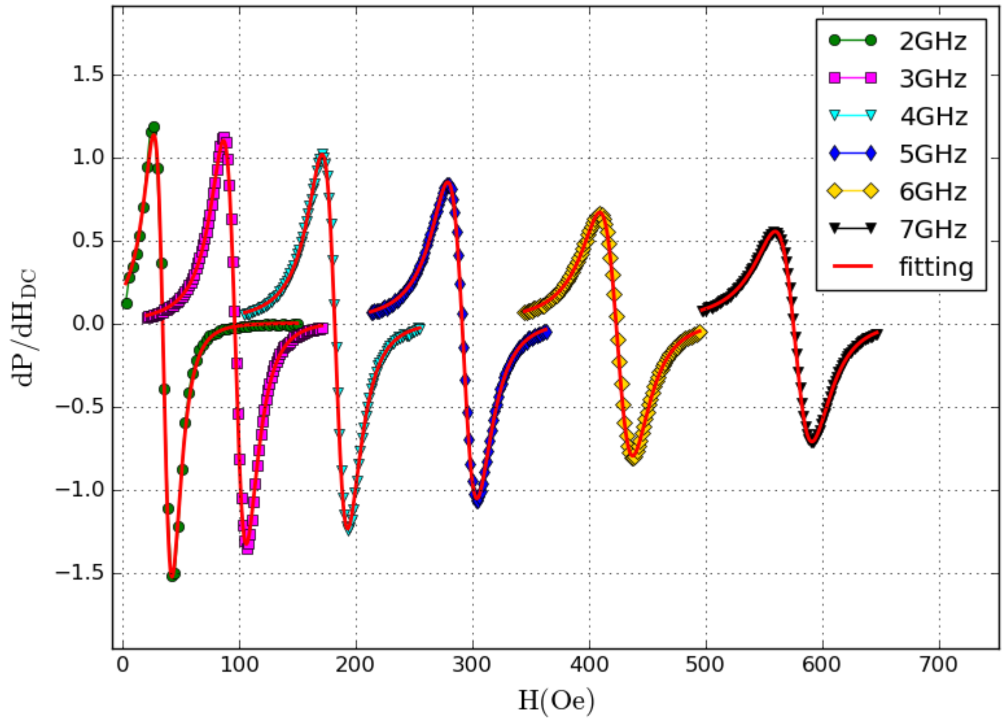

Figure 6.12: Derivative of the FMR absorption spectra for $Ni_{81}Fe_{19}$(120 nm) film at (0°), measured at different frequencies.

In Figure 6.12 we show the FMR absorption derivative dP/dH spectra for $Ni_{81}Fe_{19}$ (120 nm) samples, measured for frequencies from 2.0 GHz to 7.0 GHz. In order to obtain the resonance field H_{FMR} and the linewidth ΔH we use a fitting function which takes into account the line asymmetry [147]. We also obtain the Gilbert damping parameter α and the inhomogeneous linewidth parameter ΔH_0 from the ΔH vs f fittings performed using:

$$\Delta H = \Delta H_0 + \frac{4\pi\alpha f}{\gamma}, \tag{6.6}$$

where, α is the damping parameter and γ is the gyro-magnetic ratio.

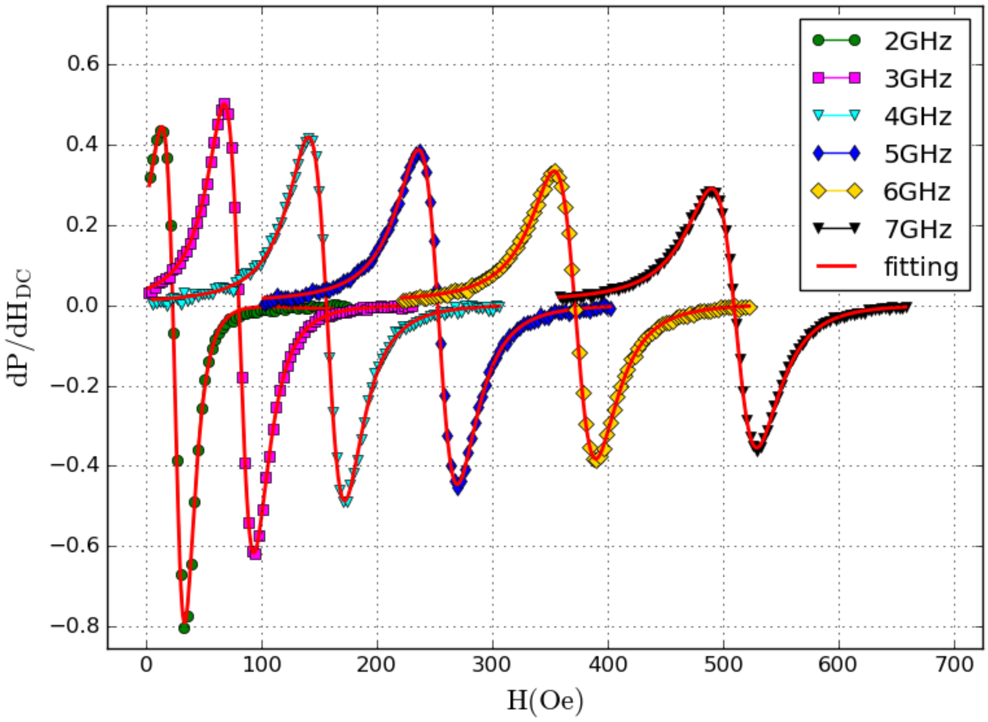

Figure 6.13: Derivative of the FMR absorption spectra for Co(10 nm)/$Ni_{81}Fe_{19}$(90 nm)/Co(10 nm) films at (0°), measured at different frequencies.

FMR absorption derivative dP/dH spectra for Co(10 nm)/$Ni_{81}Fe_{19}$(90 nm)/Co(10 nm) samples is given in Figure 6.13 measured for frequencies from 2.0 GHz to 7.0 GHz. The red line shows the fitting to the dP/dH spectra. We observe a single broad symmetric Lorentzian line in the entire frequency range, because we measured dP/dH spectra for the uniform mode only. It was noted that the value of H_{FMR} increases as we go to the higher frequencies, which corresponds to the FMR color maps in the figure 6.11.

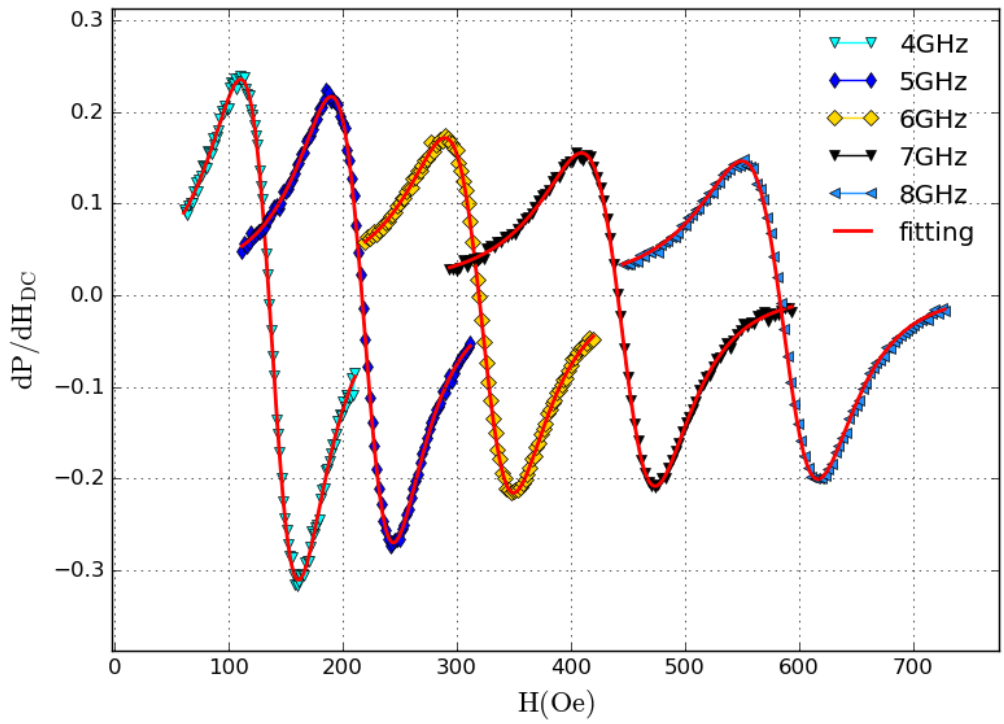

Figure 6.14: Derivative of the FMR absorption spectra for Co(20 nm) /Ni$_{81}$Fe$_{19}$(70 nm)/Co(20 nm) films at (0°), measured at different frequencies.

In Figure 6.13 we show the FMR absorption derivative dP/dH spectra for Co(20 nm)/ Ni$_{81}$Fe$_{19}$(70 nm)/Co(20 nm) samples, measured for 4.0 GHz to 8.0 GHz. The numerical fittings are with the red line in the figure 6.13. These values are summarized in in Table 6.2.

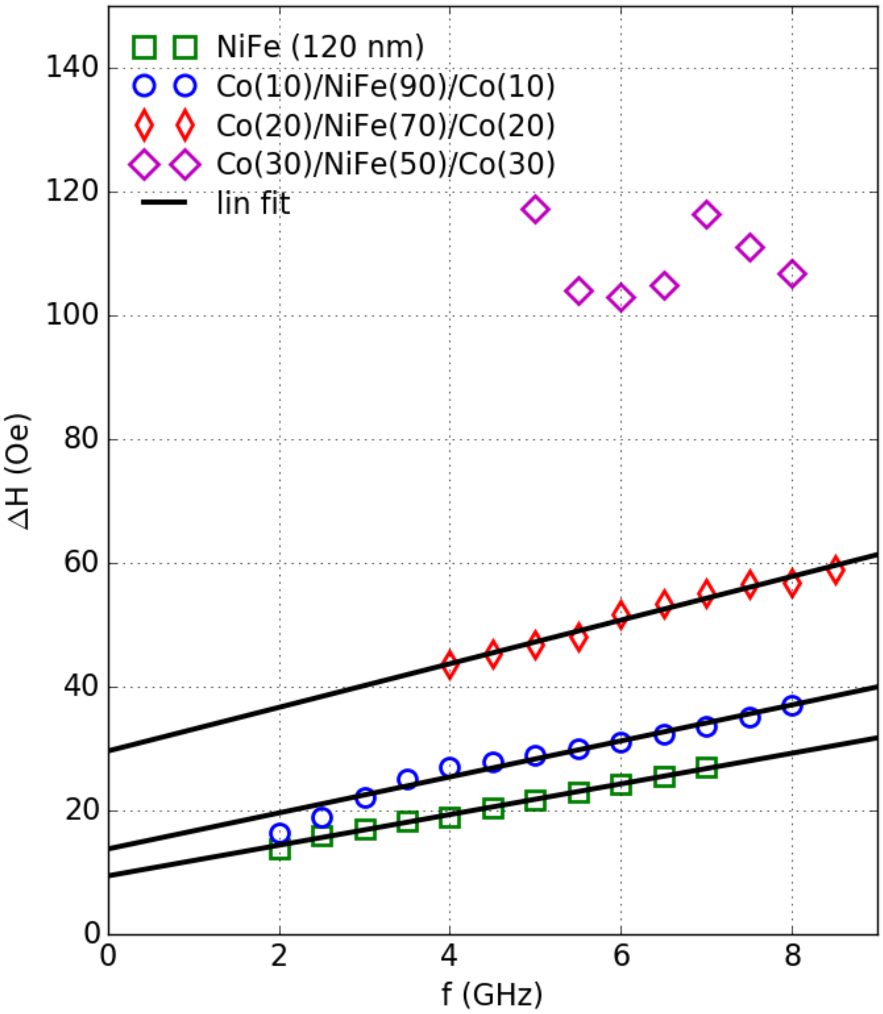

Figure 6.15: FMR linewidth (ΔH) as a function of resonance frequency (f_r) and corresponding linear fitting for selected samples.

Figure 6.15 shows the line widths $\mathit{\Delta H}$ as functions of resonance frequency (f_r) for different values of t_{Co}, and t_{NiFe}, where the applied field is at (0°) to the anisotropy axis. The black line shows the linear fittings according to equation 6.6. For the frequency range used in our measurements, we observe good linearity in all samples except for the case of Co(30)/NiFe(50)/Co(30), indicating that there are some other contributions in this sample, that requires further investigations.

It was noted that the damping constant (α) increases with increasing Co thickness, ranging from 3.47×10^{-3} to 4.94×10^{-3}. The summary of these results of $\mathit{\Delta H_0}$ and α for 0° are given in Table 6.2 for the whole series of sample. Moreover, we found that the effective properties of the synthetic layers are bounded between the properties of the pure Co and $Ni_{81}Fe_{19}$ layers, depending upon the Co to NiFe thickness fraction.

Table 6.2: Summary of results from static and dynamics magnetization analysis. Showing Coercive field H_c, Uniaxial anisotropy H_k, Effective saturation magnetization M_{eff}(emu/cm^3), Gilbert damping parameter α and Inhomogeneous linewidth ΔH_0 as function of sample thickness t_{NiFe} and t_{Co}.

Sample (nm)	H_c **(Oe)**	H_k **(Oe)**	M_{eff}	$\alpha(10^{-3})$	$\mathit{\Delta H_0(Oe)}$
NiFe(120)	3.5	10	700	3.47 ± 0.07	9.4 ± 0.3
Co(10)/NiFe(90)/Co(10)	8.5	15	780	4.08 ± 0.24	13.8 ± 0.9
Co(20)/NiFe(70)/Co(20)	14.5	20	920	4.94 ± 0.24	29 ± 1
Co(30)/NiFe(50)/Co(30)	28	35	960	-	-

6.2.5 Partial Conclusions

In conclusion, the trilayered samples of Co/Py/Co were fabricated on Si(100) substrate by using magnetron sputtering. The static magnetic measurements (M vs. H) were preformed with an alternating gradient force magnetometer (AGFM). The dynamic properties were done with the help of broadband FMR.

We observed coercive fields in the range 3.5 to 28 Oe. The results show that by incorporating t_{Co} we were able to excite the PSSW modes in synthetic layered system. We obtained the values of effective in-plane uniaxial anisotropy and effective saturation magnetization by using kittel fitting to the FMR dispersion relations. We were able to control the anisotropies and effective magnetization in the trilayered system. We also calculated the effective damping parameter α obtaining values that lies within 0.00347 to 0.00494 and also the inhomogeneous line width broading $\mathit{\Delta H_0}$ which lies in the range of 9.4 Oe to 29.6 Oe. We were able to manipulate the effective damping and inhomogeneous line width broadening ($\mathit{\Delta H_0}$) by playing with synthetic layer component. We found that the effective properties of the synthetic layers are bounded between the properties of the pure Co and NiFe layers, depending on the Co to NiFe thickness fraction.

Both the anisotropy and the effective magnetization depend upon the the thickness of the deposited Co layers, which demonstrates the possibility of controlling these properties in synthetic layer systems. The results of the this study are promising for spintronics or for sensors developments.

6.3 Antidot Lattices: Static and Dynamic Characterization

In this section we investigate ferromagnetic resonance modes of $Ni_{81}Fe_{19}$ film with a square lattice of antidots (pores in the film) using broadband ferromagnetic resonance measurements. We show that the antidots structures not only alter the coercive field and the remanent state but also the easy and hard-axis directions, when compared with continuous film. FMR experiments show a rich structure of modes in the resonance absorption spectra, with absorption peak amplitudes dependent on the direction of the external magnetic field. Micromagnetic simulations were preformed to analyse the experimental results. We show that the spin wave modes in the resonance spectrum are related to oscillation at different regions of the sample. This could be essential for working elements of magnonics.

6.3.1 Introduction

The magnetization dynamics and spin wave properties of ferromagnetic lattices of antidots (holes in the ferromagnetic film) are presently subject of intensive experimental and theoretical investigations. The patterning holes into ferromagnetic thin films is a simple and effective way to engineer magnetic properties [160, 161]. The antidot pattern modifies the static magnetization of the medium, creating regions with well-defined remanence which could be used for data storage [100, 15]. Extensive studies were carried out to investigate the spin wave dynamics and ferromagnetic resonance in antidot structures [162, 163, 164, 165, 166].

In this work, we discuss the broadband spin-wave spectra of a $Ni_{81}Fe_{19}$ antidots in square lattice with a lattice constant a of 2 μm and circular holes with a diameter d of 1 μm. We fond different prominent FMR and Spin Wave (SW) modes in our sample. They reflect an extended mode and localized modes. These modes are localized in a spin-wave well defined by the edges of antidots between either two nearest or next nearest neighborings and extended along the lattice. The results of the following study are important for spin wave propagation in a magnonic crystal.

The pattern morphology was analyzed by scanning electron microscopy with field emission gun (FEG-SEM), the static magnetic properties were studied using alternating gradient field magnetometer (AGFM) and Broadband ferromagnetic resonance (FMR) measurements were carried out at room temperature using a coplanar waveguide (CPW) connected to a vector network analyzer in the frequency range 0.5 GHz to 10.0 GHz. For all magnetic measurements, the in-plane magnetic field was applied, aligned to the lattice axis. In particular, 0° (along the 1st neighbors direction) and 45° (along the 2nd neighbors direction) were considered.

6.3.2 Sample Fabrication

The square array of antidot was fabricated from a permalloy film using magnetron sputtering, electron beam lithography and plasma etching processes. A stack of Ti(3)/$Ni_{81}Fe_{19}$(50)/Ti(3)/SiO_2(30) layers was deposited on Si(100) substrate by magnetron sputtering using DC power sources. The numbers in () indicates the layer thickness in nm. The deposition conditions were 5 mTorr pressure and 50 sccm Ar gas flow, after a 5×10^{-8} Torr base pressure has been attained in the whole chamber. A permanent magnet configuration that generates a field of ∼200 Oe in the direction parallel to the plane of the sample was used in the substrate holder. This field was used for the induction, during deposition, of the in-plane anisotropy in the sample.

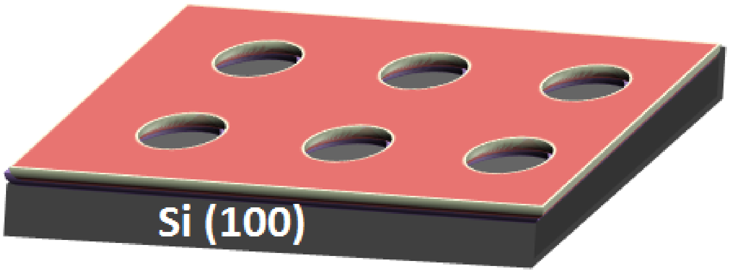

Figure 6.16: Illustration picture for the antidots nano structure on Si(100) substrate.

After preparing the stack, an array of dots was patterned, over an area of $2 \times 2\,\mathrm{mm}^2$, on a spin-coated layer of resist on the sample, using a Raith e_LINE e-beam lithography system. The illustration of antidot structure on Si(100) substare is shown in the Fig. 6.16.

Then, the antidot structure were defined by plasma etching process. As a result we got the structure with smooth surfaces and no defects at the edge. Several attempts were made for the production of this sample. In order to obtain sharp edges and a well defined antidots structures, it was necessary to use a hard mask. A 30 nm thick layer of SiO_2 was used as hard mask for etching process, further details about the process are discussed in the section (4.1.3). The final structure consists of antidot arrays of diameter $1\,\mu$m and the centre-to-centre spacing between nearest holes is

2 μm. The FEG-SEM image of the final structure with chosen coordinate system is given in Figure 6.17.

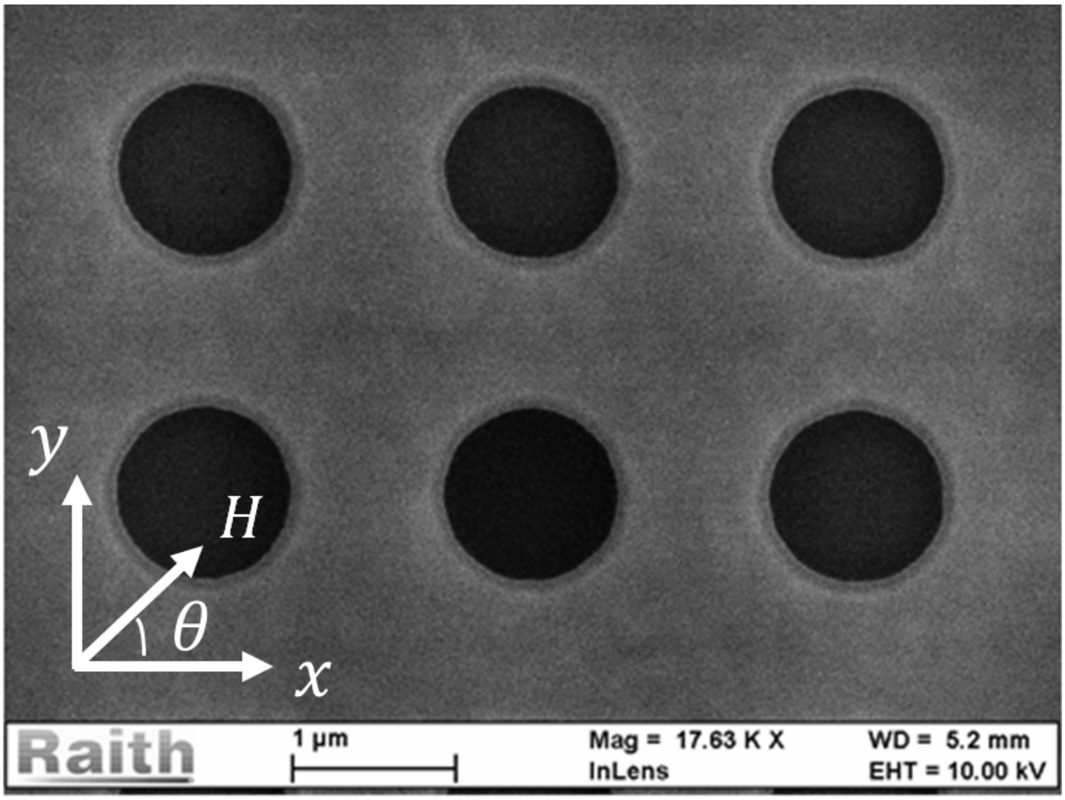

Figure 6.17: FEG-SEM images of the periodic arrangement of the antidots with diameter of 1 μm produced by electron beam lithography with chosen coordinate system.

After fabrication of the antidots nanostructures, morphological analysis of the sample was performed with AFM. We can see a well defined structure (upper panel of Fig.6.18). While the lower panel of Fig. 6.18 shows the horizontal cut of the AFM image, where we get the total depth of the antidot is equal to the thickness of the stack, which confirms that, the etching process was successful.

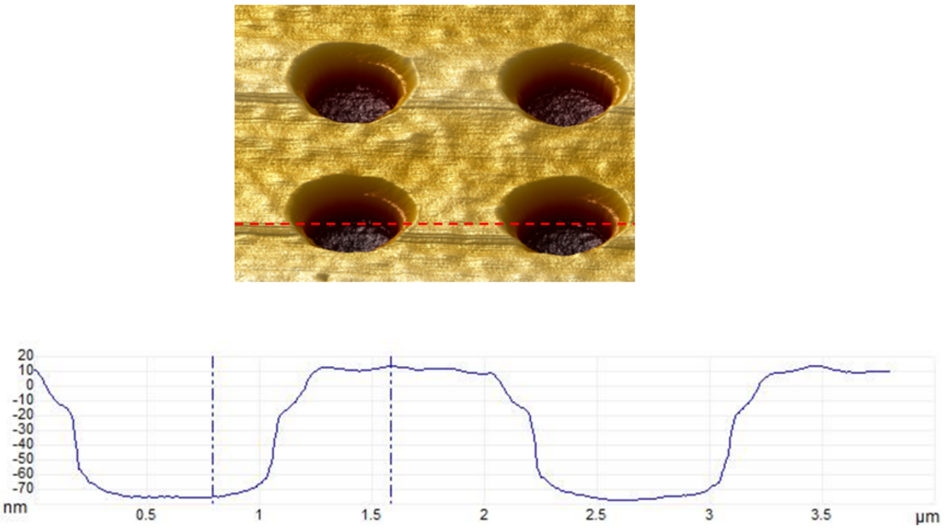

Figure 6.18: AFM image of the 1 μm antidots (upper panel), the size and depth of the antidots (lower panel).

6.3.3 Static Magnetization

The static magnetization curves (M vs. H) are shown in Fig. 6.19 for the unpatterned stack and antidots samples for H at $\theta = 0°$ and $\theta = 45°$. Due to the square symmetry in the lattice, the hysteresis loops shows a similar behavior when the external magnetic field is applied along the x ($\theta = 0°$) and y axis ($\theta = 90°$), and an easy magnetization axis at $\theta = 45°$. Moreover, in the case of antidots structures the shape anisotropy is stronger then the induced anisotropy. The coercive field was modified from 3.1 Oe to 4.6 Oe for unpatterned to antidots nanostructure.

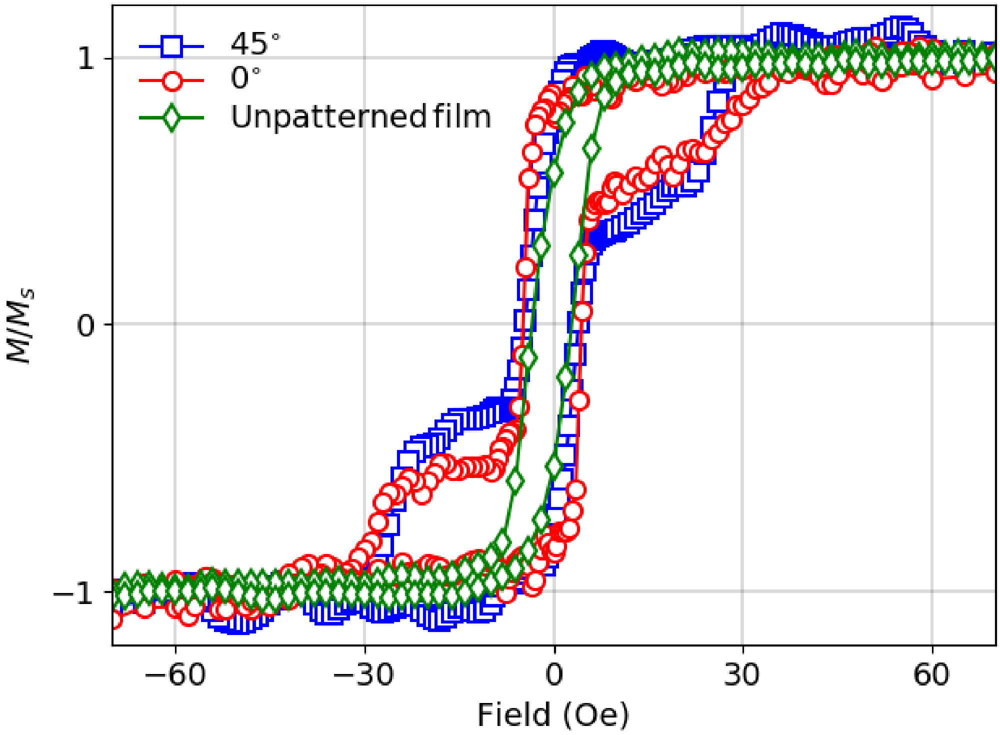

Figure 6.19: Hysteresis loops of the unpatterned stack and the antidots sample along the $\theta = 0°$ and $\theta = 45°$.

6.3.4 VNA-FMR study

We have used a broadband ferromagnetic resonance setup for the dynamic measurements, as described in section 4.4.3. In this experiment, a dc magnetic field H sweeping from -800 to +800 Oe was applied along the 0°, 45° and 90° axis direction. On the other hand, the radio-frequency probing fields h_{rf} of 0.5 Oe was applied perpendicular ($H \perp h_{rf}$) to the applied dc field.

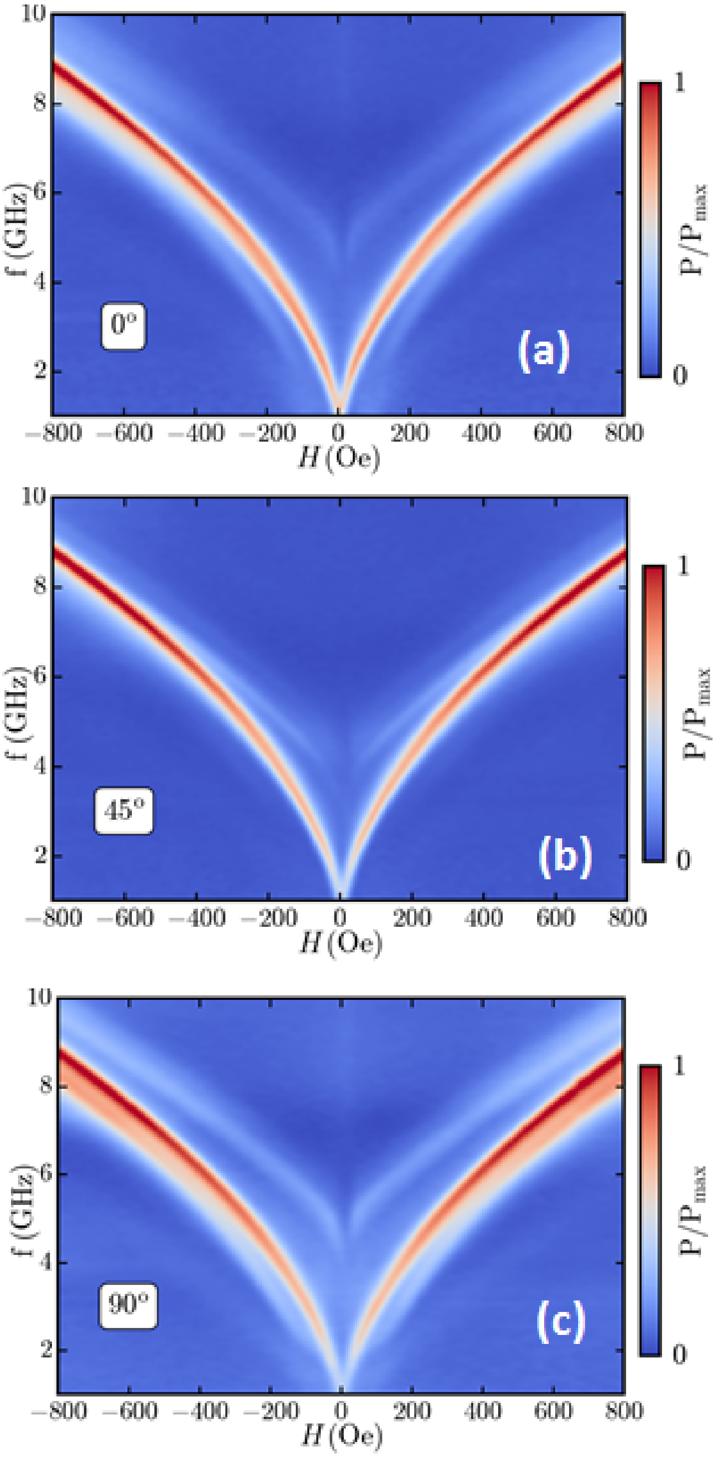

Figure 6.20: Broadband FMR spectra (color plots) for H applied along the 0° (a), 45° (b) and 90° (c) to the induced anisotropy axis.

Broadband FMR results are shown in figure 6.20 for antidots sample along the 0°, 45° and 90° to the array axis. The color scale denotes the absorption amplitude, where blue corresponds to minimum and red corresponds to maximum absorption amplitude i.e. the resonance frequencies f_{FMR}. The excitation of different modes is clearly observed as the difference of measurements at 0° or 45°. At 0° and 90° similar measurements were observed, at lower frequencies two modes and three modes at higher frequencies. While, in the case of 45° where at lower frequency values single mode was observed but at higher frequencies e.g above 4.0 GHz the second modes is also observed.

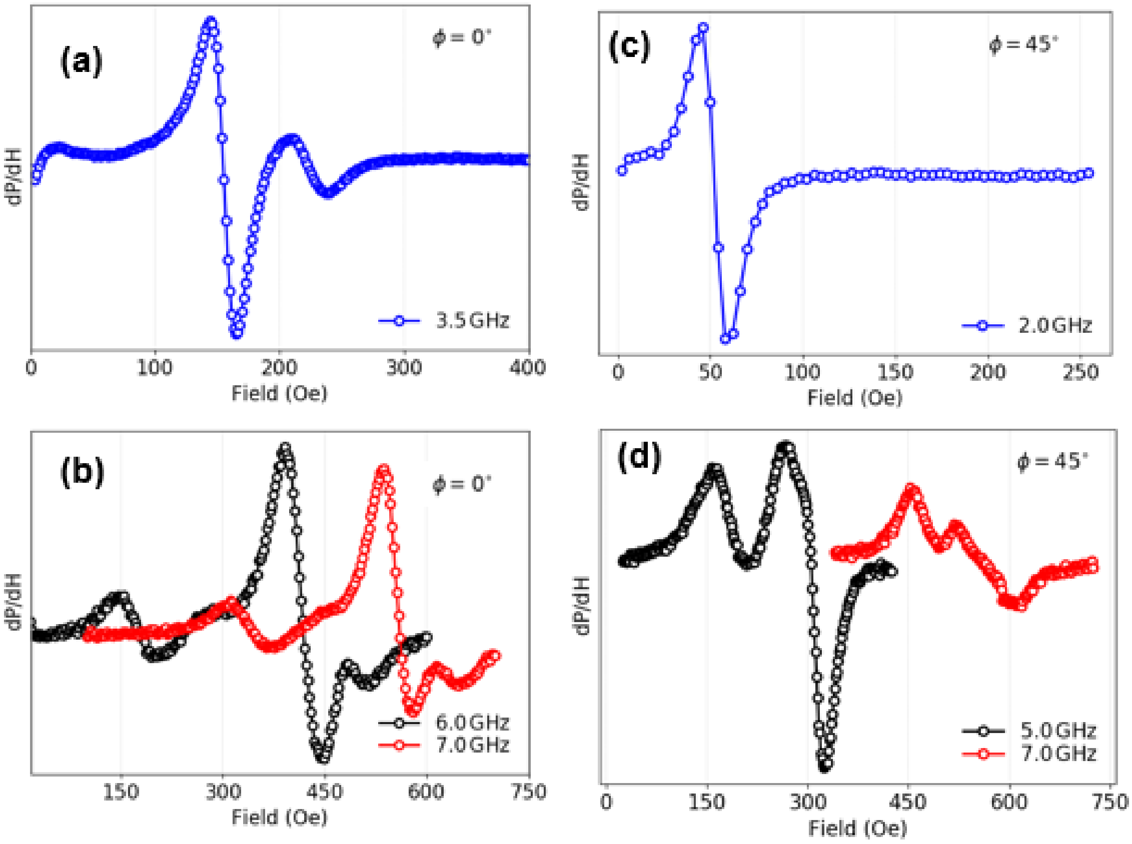

Figure 6.21: Derivative of the FMR absorption spectra for H applied along the 0°(a) & (b), and 45° (c) & (d) to the antidots array axis measured at different frequencies.

In Figure 6.21 we show the FMR absorption derivative dP/dH spectra for antidots samples. The dP/dH spectra for $\theta = 0°$ measured at 3.5 GHz shown in the figure 6.21 (a) shows the main excitation mode with $H_{FRM} = 154.5$ Oe and the 1st SW mode with $H_{FRM} = 223.5$ Oe. Fig. 6.21 (b) shows excitation modes for 6.0 GHz and 7.0 GHz, where we observe three different modes in both frequencies. The black curve in Fig. 6.21 (b) shows the modes for 6 GHz, and here the main mode is with $H_{FRM} = 419.5$ Oe, SW mode below it is with $H_{FRM} = 173$ Oe and the one above is with H_{FRM} = 499 Oe.

The red curve in Fig. 6.21 (b) shows the modes for 7.0 GHz, here the main mode is with H_{FRM} = 558 Oe, the SW mode below it is with H_{FRM} = 341 Oe and the one above is with H_{FRM} = 632.5 Oe. The case of $\theta = 45°$ measured at 2.0 GHz is shown in Fig. 6.21 (c). Here we observe only one mode with H_{FRM} = 52.5 Oe. While 5.0 GHz and 7.0 GHz measurements are shown in Fig. 6.21 (d), in both cases we observe just main and 1st SW modes. In the case of 5 GHz the main mode is with H_{FRM} = 296 Oe and the SW mode is with H_{FRM} = 185 Oe. On the other hand, in the case of 7.0 GHz the main mode is with H_{FRM} = 563 Oe and the SW mode is with H_{FRM} = 474 Oe.

6.3.5 Micromagnetic Simulation

In order to analyse the experimental results, we also performed the micromagnetic simulation with MuMax3 software [14]. To preform simulations for a magnetic antidot lattice we employ a discretized cell size $7.14 \times 7.14 \times 50\,\mathrm{nm}^3$ using a simulation box of $256 \times 256 \times 1$ cells. This corresponds to the shape and size of a single hole in the ferromagnetic film of our experimental sample. Moreover, we also used the periodic boundary conditions PBC (250, 250, 0).

The parameters used for the magnetic material were: saturation magnetization $M_s = 800 \times 10^3$ A/m, exchange constant $A = 1.3 \times 10^{-11}$ J/m and damping constant $\alpha = 0.02$. The simulations were carried on a field frequency (H, f), with H ranging from 1000 to 0 Oe, field steps of 5 Oe, f ranging from 0.5 GHz to 15.0 GHz, and frequency steps of 100 MHz.

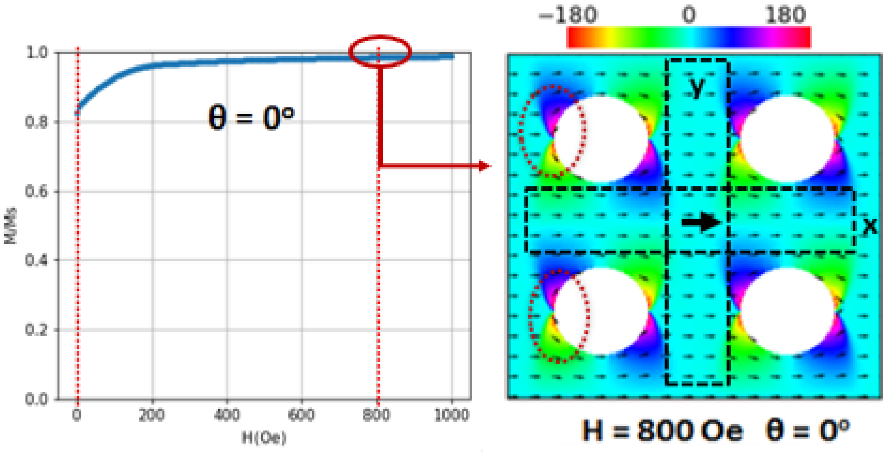

Figure 6.22: Saturated state simulated magnetization curve for antidots nanostructure for $\theta = 0°$ (left panel). Profile of simulated static magnetization distribution for $H = 800$ Oe (right panel).

Fig. 6.22 shows the simulated $M \times H$ curve of 1000 Oe to 0 Oe for antidots for ($\theta = 0°$), and the static magnetization configuration in the antidots at $H = 800$ Oe. In the case of 800 Oe M is almost saturated along the H direction, except for the edges of the antidots.

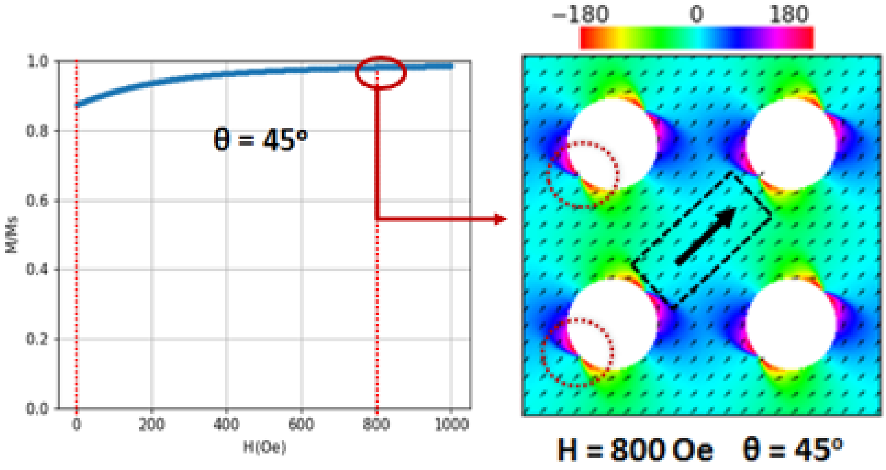

Figure 6.23: Saturated state simulated magnetization curve for antidots nanostructure for $\theta = 45°$ (left panel). Profile of simulated static magnetization distribution for $H = 800$ Oe (right panel).

Fig. 6.23 shows the simulated $M \times H$ curve of 1000 Oe to 0 Oe for antidots at ($\theta = 45°$), and the static magnetization distribution in the antidots at $H = 800$ Oe.

In the case of 800 Oe M is almost saturated along the H direction, except for the edges of the antidots, marked with dotted circle.

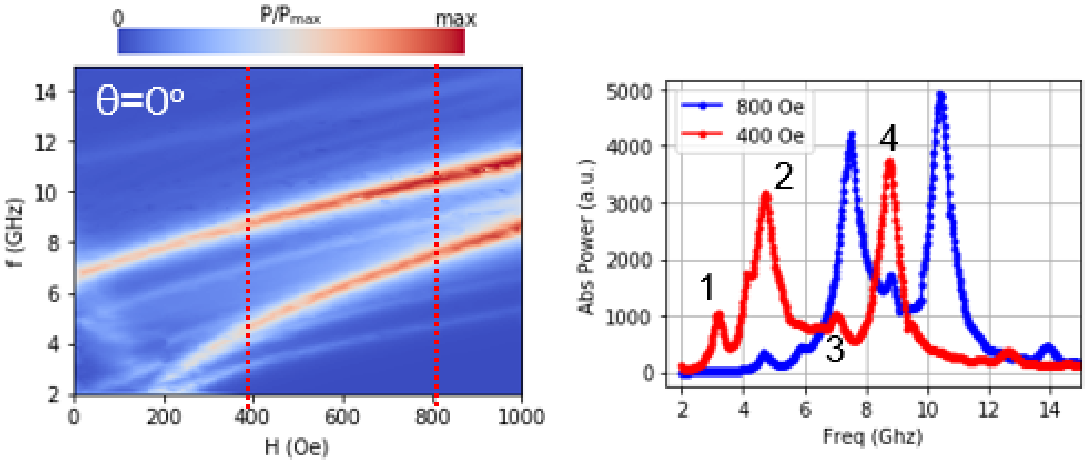

Figure 6.24: Micromagnetic simulation: the FMR spectra (color plots) of antidots nanostructure for $\theta = 0°$ (left panel). Simulated absorption spectra for $H = 400$ Oe and 800 Oe, where 1, 2, 3, 4 and 5 corresponds to modes M1, M2, M3, M4 and M5, for H= 400 Oe (right panel).

Figure 6.24 (left) shows the simulated FMR color maps for $\theta = 0°$. The color scale used maximizes the contrast in the presented H and f range. As seen from the figure, the main features of the experimental results are reproduced in the simulated spectra. The shapes and relative position of the absorption branches are well reproduced. However, the simulated absorption peaks occur at higher frequencies than their experimental counterparts. We expect these frequency variations due to magnetic anisotropies not taken into account in our simulations or they may be caused by our size of the mesh. Figure 6.24 (right) shows the simulated absorbed power spectra for $\theta = 0°$ for 400 Oe and 800 Oe (vertical cuts in the color map). Here 1, 2, 3, 4 and 5 shows the modes M1, M2, M3, M4 and M5, which are discussed in the Fig. 6.26.

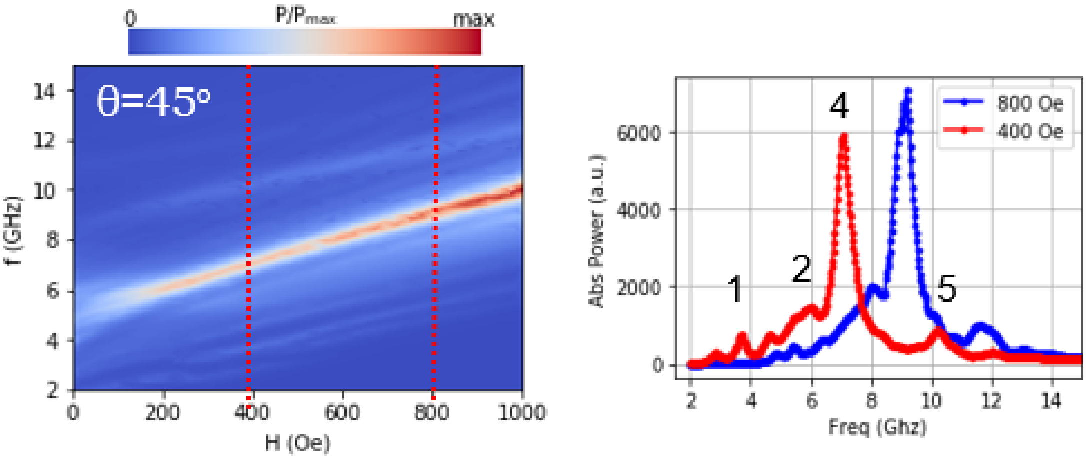

Figure 6.25: Micromagnetic simulation: the FMR spectra (color plots) of antidots nanostructure for $\theta = 45°$ (left panel). Simulated absorption spectra for $H = 400$ Oe and 800 Oe, where 1, 3, 4 and 5 corresponds to modes M1, M3, M4 and M5 for $H = 400$ Oe (right panel).

Figure 6.25 (left) shows the simulated FMR color maps for $\theta = 45°$. The color scale used maximizes the contrast in the presented H and f range. As seen from the figure, the main features of the experimental results are reproduced in the simulated spectra. The shapes and relative amplitudes of the absorption branches are well reproduced. We observed the main and first resonance modes. Figure 6.25 (right) shows the simulated absorbed power spectra for $\theta = 45°$ for 400 Oe and 800 Oe (vertical cuts in the color map). Here 1, 3, 4 and 5 shows the modes M1, M3, M4 and M5, which are discussed in the Fig. 6.27. It is worth mentioning that software developed by our research group is used to process the recorded data in order to obtain the absorbed power spectra comparable with experimental data and analyze the oscillation modes.

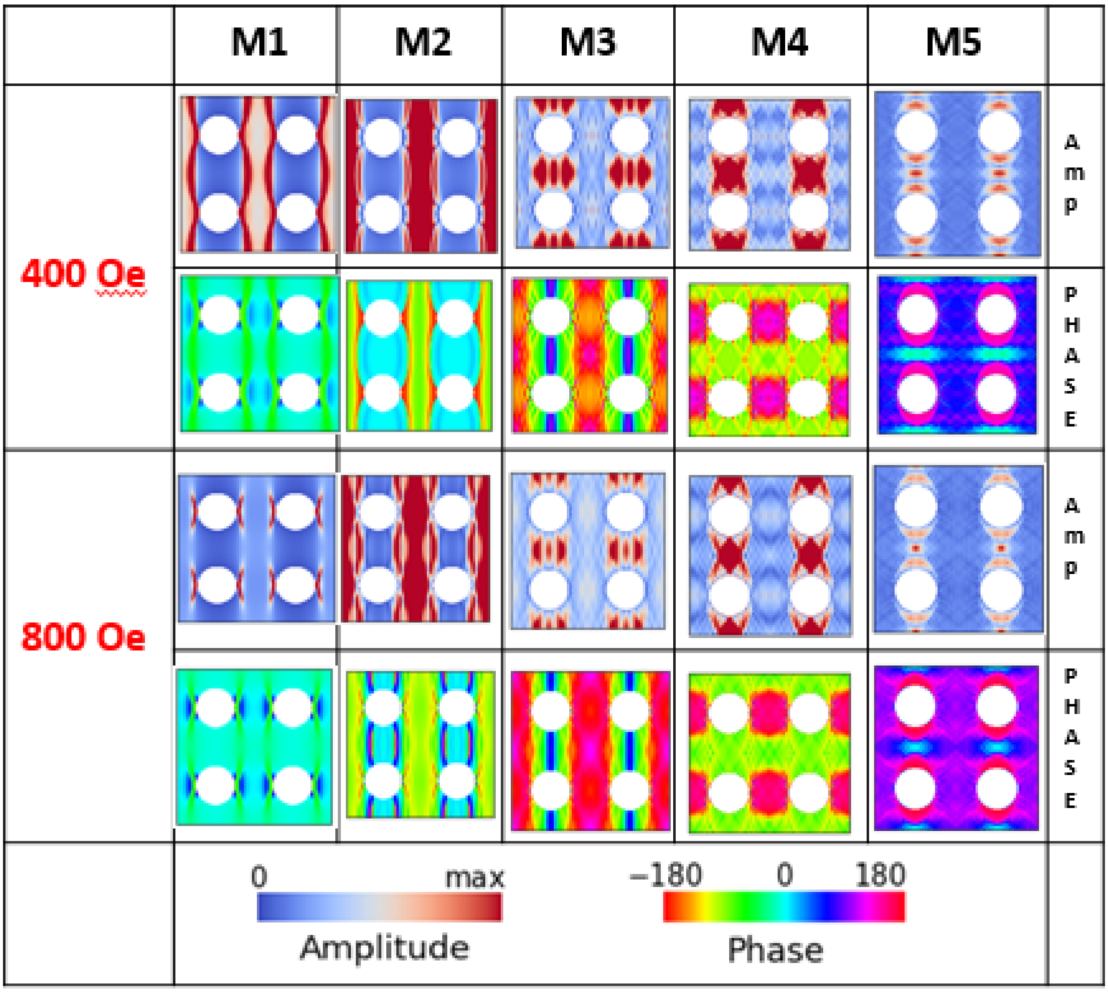

Figure 6.26: Simulated spin wave mode profiles (amplitude and phase maps) for the $Ni_{81}Fe_{19}$ antidots with square lattice symmetry in the case of H = 400 Oe and 800 Oe applied parallel ($\theta = 0°$) to the array axis. The color scales for the power and phase maps are shown at the bottom of the figure.

Figure 6.26 shows the simulated spin wave mode profiles (amplitude and phase maps) for the $Ni_{81}Fe_{19}$ antidots with square lattice symmetry in the case of H = 400 Oe and 800 Oe applied ($\theta = 0°$) to the array axis.

We found two prominent modes and three other modes with less intensity in our sample, they reflect two extended modes (M2 & M4), one edge mode (M1) and two standing spin wave modes (M3 & M5).

The M1 at 3.12 GHz is the edge mode which is extended along the lattice. Moreover, the M2 at 4.72 GHz and M4 at 7.0 GHz are extended modes, which are localized in a spin-wave well at the edges of the antidot. The M3 at 8.75 GHz and M5 at 12.60 GHz are standing SW modes localized centrally between either two nearest or next nearest neighboring antidot. All these mode frequencies correspond to the $H =$ 400 Oe configuration.

We note that the wave vector $\vec{k}$ associated with modes M1, M2, M3 and M4 is parallel to the applied field H_{ext}, which is known as backward volume modes (BV-like geometry). On the other hand, in the case of mode M5 ($k \perp H_{ext}$), which is called magnetostatic surface spin waves (MSSW) Damon Eshbach (DE) geometry.

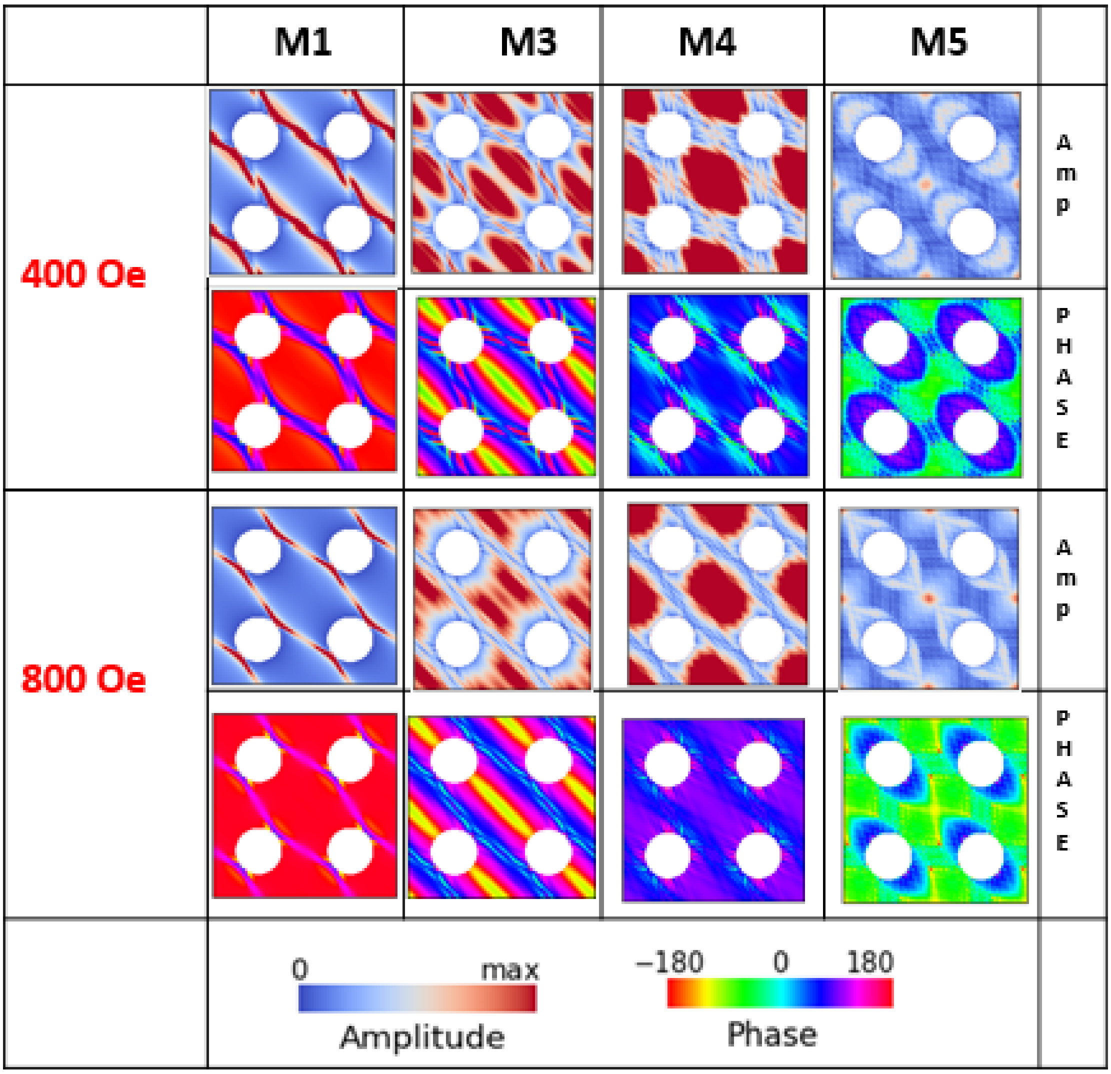

Figure 6.27: Simulated spin wave mode profiles (amplitude and phase maps) for the $Ni_{81}Fe_{19}$ antidots with square lattice symmetry in the case of $H = 400$ Oe and 800 Oe applied ($\theta = 45°$) to the array axis. The color scales for the power and phase maps are shown at the lower left of the figure.

Figure 6.27 shows the simulated spin wave mode profiles (amplitude and phase maps) for the $Ni_{81}Fe_{19}$ antidots with square lattice symmetry in the case of $H = 400$

Oe and 800 Oe applied ($\theta = 45°$) to the array axis. We find one prominent mode M4, and three other modes M1, M3 and M5 with low intensity in our sample. M2 mode not present in this configuration because there are no continuous channels of materials along the direction of the applied field, unlike the ($\theta = 0°$) configuration.

The M1 at 3.72 GHz is the edge mode which is extended along the lattice, and the mode frequency is higher ≈ 0.60 GHz when compared with the $\theta = 0°$ configuration. Moreover, M4 at 7.0 GHz represents a localized mode, located in a spin-wave well at the edges of the antidot; this mode is 1.75 GHz lower when compared with the ($\theta = 0°$).

The M3 at 5.80 GHz and M5 at 10.20 GHz are localized centrally between either two nearest or next nearest neighboring antidots. These modes are also at lower frequencies, when we compared with the $\theta = 0°$ configuration. In the case of M3 this difference is 1.20 GHz, while double for M5. All these mode frequencies corresponds to the $H = 400$ Oe configuration.

Furthermore, the modes M1, M3 and M4 are backward volume modes (BV-like geometry), while M5 corresponds to a magnetostatic surface spin waves MSSW with Damon Eshbach DE geometry.

It is worth mentioning that due to absence of either additional terms in our free energy or the chosen size of cell discretization in the mesh of our simulated samples, we were unable to obtain good agreement with the experimental samples.

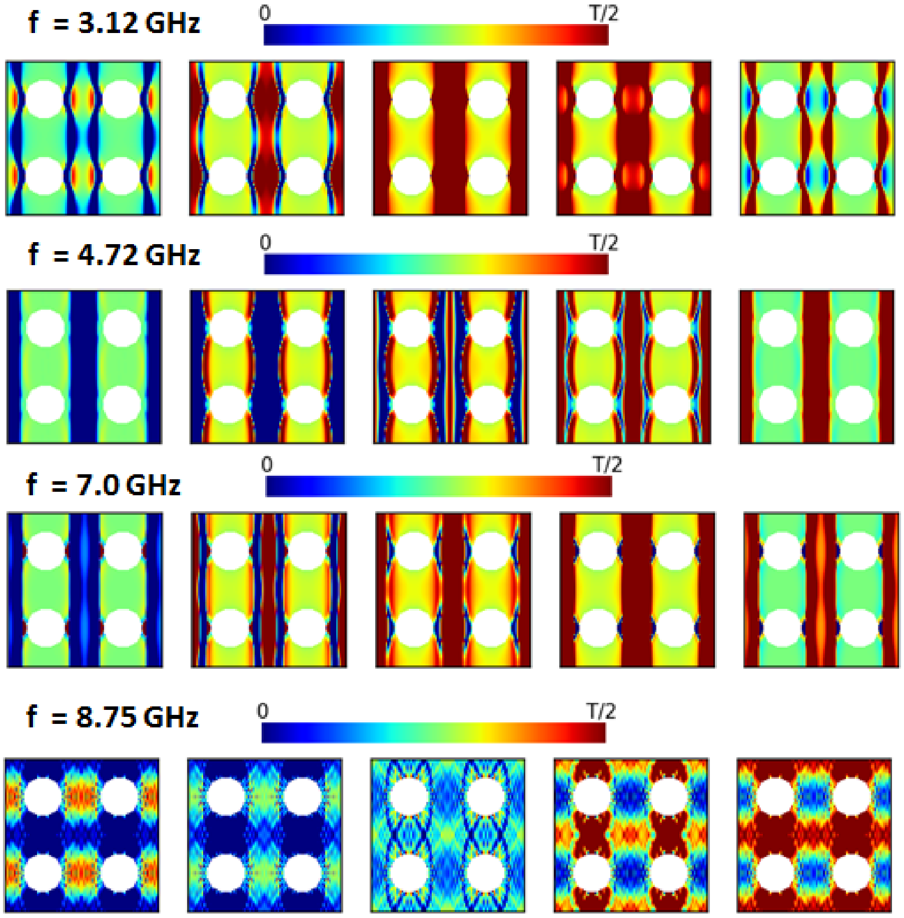

Figure 6.28: Temporal evolution of the spatial distribution of the magnetization $(\vec{m}.\hat{u}_{\varphi_i})$ of the excited modes at the given frequencies for $\theta = 0°$, $H = 400$ Oe.

The temporal evolution of the spatial distribution of the magnetization $(\vec{m}.\hat{u}_{\varphi_i})$ in antidot lattice is shown in Fig. 6.28, for an applied field $H = 400$ Oe and $\theta = 0°$. Fig. 6.28 shows the temporal propagation of the magnetization amplitude at five different intervals for M1 at 3.12 GHz, M2 at 4.72 GHz, M3 at 7.0 GHz and M4 at 8.75 GHz.

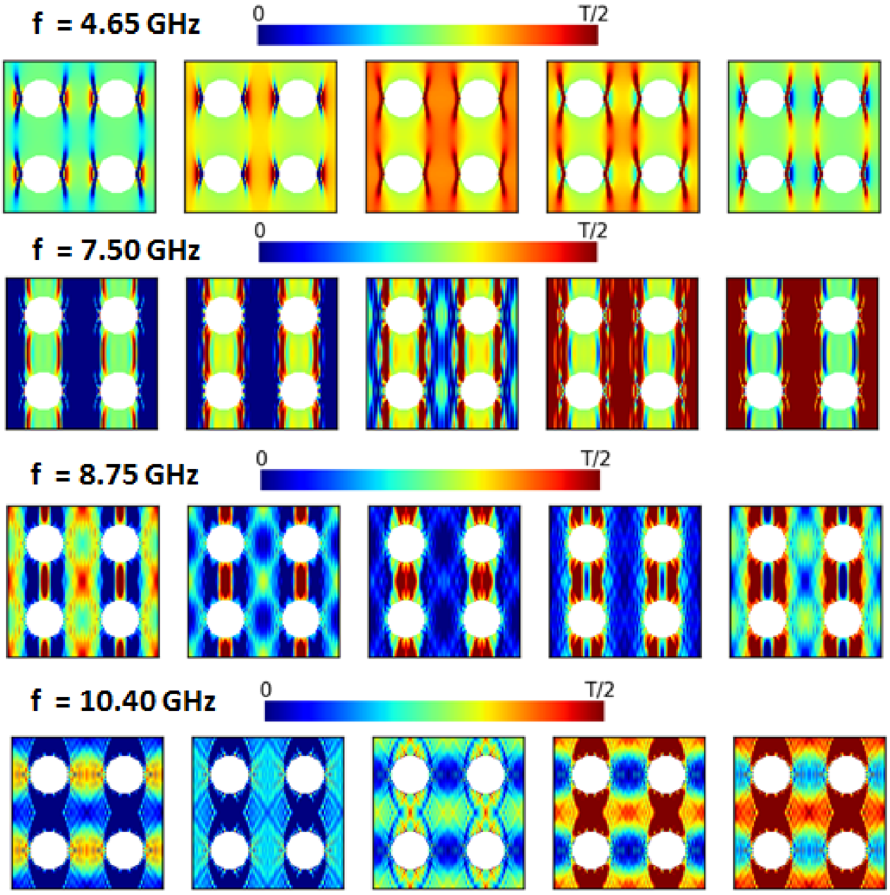

Figure 6.29: Temporal evolution of the spatial distribution of the magnetization $(\vec{m}.\hat{u}_{\varphi_i})$ of the excited modes at the given frequencies for $\theta = 0°$, $H = 800$ Oe.

The temporal evolution of the spatial distribution of the magnetization $(\vec{m}.\hat{u}_{\varphi_i})$ in antidot lattice is shown in Fig. 6.29, for an applied field $H = 800$ Oe and $\theta = 0°$. Fig. 6.29 shows the temporal propagation of the magnetization amplitude at five different intervals for M1 at 4.65 GHz, M2 at 7.50 GHz, M3 at 8.75 GHz and M4 at 10.40 GHz.

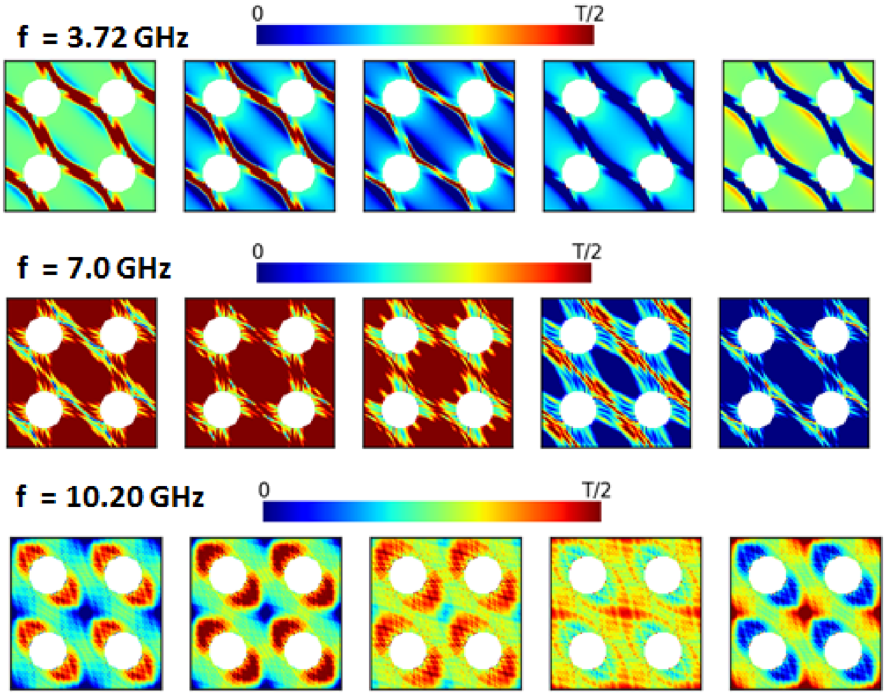

Figure 6.30: Temporal evolution of the spatial distribution of the magnetization ($\vec{m}.\hat{u}_{\varphi_i}$) of the excited modes at the given frequencies for $\theta = 45°$, $H = 400$ Oe.

The temporal evolution of the spatial distribution of the magnetization ($\vec{m}.\hat{u}_{\varphi_i}$) in antidot lattice is shown in Fig. 6.30, for an applied field $H = 400$ Oe and $\theta = 45°$. Fig. 6.30 shows the temporal propagation of the magnetization amplitude at five different intervals for M2 at 3.72 GHz, M3 at 7.0 GHz and M4 10.20 GHz.

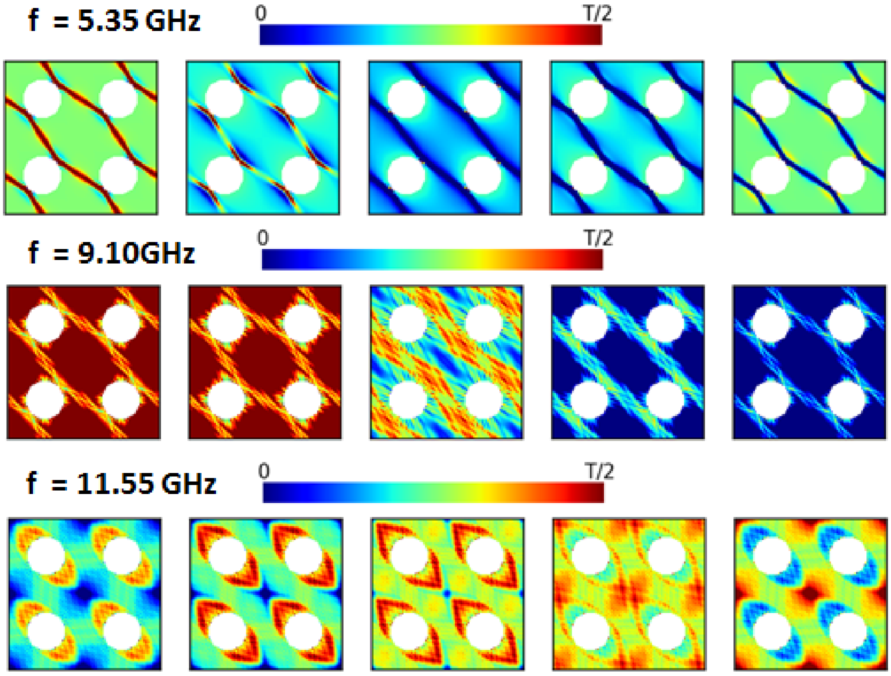

Figure 6.31: Temporal evolution of the spatial distribution of the magnetization ($\vec{m}.\hat{u}_{\varphi_i}$) of the excited modes at the given frequencies for $\theta = 45°$, $H = 800$ Oe.

The temporal evolution of the spatial distribution of the magnetization ($\vec{m}.\hat{u}_{\varphi_i}$) in antidot lattice is shown in Fig. 6.31, for an applied field $H = 800$ Oe and $\theta = 45°$. Fig. 6.31 shows the temporal propagation of the magnetization amplitude at five different intervals for M2 at 5.35 GHz, M3 at 9.10 GHz and M4 11.55 GHz.

6.3.6 Partial Conclusions

In conclusion, we have produced arrays of micron-sized $Ni_{81}Fe_{19}$ antidots with hard mask of SiO_2 by using magnetron sputtering, electron beam lithography and plasma etching processes. The static magnetic characterization (M vs. H) was measured with AGFM, which indicates that there is significant increase in the loop width (H_c) from 3.1 Oe to 4.6 Oe in the case of anti-dots structure. The dynamic properties were measured with broadband FMR. The results shows a rich structure of modes in the resonance absorption spectra, with absorption peak amplitudes dependent on the direction of the external magnetic field. We observed that the excited modes are affected by the direction of the applied field H. The micromagnetic simulations were preformed to analyse the experimental results. The modes along the 0° are known as the extended modes, while the modes along 45° are localized centrally between either two nearest or next nearest neighboring antidot.

The observation of such a wide mixture of extended and standing spin wave modes in the antidot lattice and their tunability by changing the applied field direction will enable the design of two-dimensional (2D) magnonic devices with a widely tunable magnonic band structures useful for applications in a wide range of devices.

6.4 Ellipse: Static and Dynamic Characterization

In this section we discuss the magnetization dynamics of a square array of nanometer-sized elliptical Permalloy elements with different sizes and same aspect ratios. They have been investigated using the broadband ferromagnetic resonance measurements (VNA-FMR) and analysed by micromagnetic simulations. We observed the vortex state and several other low-frequency spin wave modes in elliptical magnetic nanostructures. The high frequency modes were measured and simulated for different values of static external magnetic, in-plane rf fields applied perpendicular to the DC field. These systems dispaly a great diversity of results with increasing complexity. The relation of the spin waves with the symmetries of the nano-objects and the distribution of the free magnetic energy inside them is analyzed with special interest. Additionally, the boundary between the magneto-static waves governed by the dipole interaction and the spin waves where the exchange interaction is dominant are explored.

6.4.1 Introduction

Progress in magnetic recording lead to the development of patterned recording media. Growing demand for higher lateral density in magnetic recording and for higher speed of memory operation is attracting the attention of many researchers for the spin dynamics of patterned nanometers magnetic elements with controlled geometry [167, 168, 169, 170].

The magnetisation dynamics of nano and micron-sized circular and elliptical magnetic elements have been studied for saturated magnetization states. However, it is very important to understand the processes of excitation, propagation, and also interaction of spin waves in nanomagnetic elements, technologies for applications in electronics and spintronics.

The spin wave dynamics and high frequency modes in elliptical $Ni_{81}Fe_{19}$ elements have been studied by our group [171]. Here we shall explore excitations of dipole-exchange modes, which could be tuned by the geometry of the elliptical element. It was observed that when the geometry of the elliptical element is reduced, a competition between dipole and exchange interaction may take place, modifying the mode frequency significantly.

In the following project, we study the dipole-exchange modes of $Ni_{81}Fe_{19}$ ellipses in the magnetic field along the magnetization curve, including the vortex state, using broadband ferromagnetic resonance experiments and micromagnetic simulations. In Sec. II, we describe the experimental details and present the results. In Sec. III, we discuss the micromagnetic simulation approach, and compare our results with the experiment. In Sec. IV, we present the conclusions of this study.

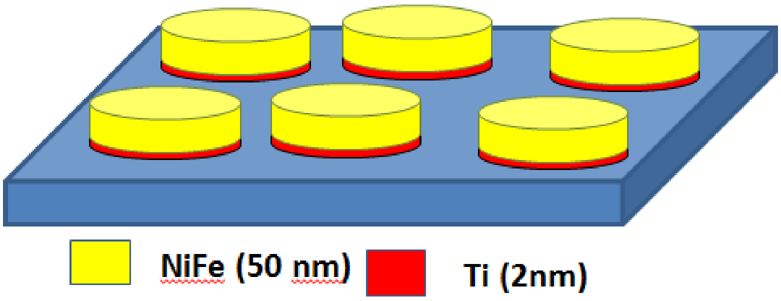

Figure 6.32: Illustration picture for the sample structure.

6.4.2 Sample

In our experiments, the periodic arrays of ellipses with different scale and same aspect ratios were fabricated using e-beam lithography, sputtering and lift-off processes. The array was patterned, over an area of $2 \times 2\,\mathrm{mm}^2$, on a spin-coated layer of resist on a SiO_2(100) substrate using a Raith e-beam lithography (EBL) system. A 50-nm-thick $Ni_{81}Fe_{19}$ layer with Ti (2 nm) buffer layer was deposited over the patterned substrate by magnetron sputtering using a rf power source (as shown in Fig. 6.32). The deposition conditions were 5 mTorr pressure and 50 sccm Ar gas flow, after a 5 × $10^{-}8$ Torr base pressure has been attained in the whole chamber. After lift-off, $2.4\,\mu\mathrm{m} \times 1.4\,\mu\mathrm{m}$, $2.0\,\mu\mathrm{m} \times 1.33\,\mu\mathrm{m}$, $1.5\,\mu\mathrm{m} \times 1.0\,\mu\mathrm{m}$ and $1.0\,\mu\mathrm{m} \times 0.67\,\mu\mathrm{m}$ elliptical elements with smooth surfaces and no defects at the edges were obtained (see Fig. 6.33). The spacing between the edges of the elliptical elements are, 730 nm and 640 nm along the major and minor axis directions for $2.4\,\mu\mathrm{m} \times 1.4\,\mu\mathrm{m}$ sample and the rest of them have 1 μm along the major and minor axis directions. For the dynamic measurements, we used a broadband ferromagnetic resonance setup described in Ref.[172].

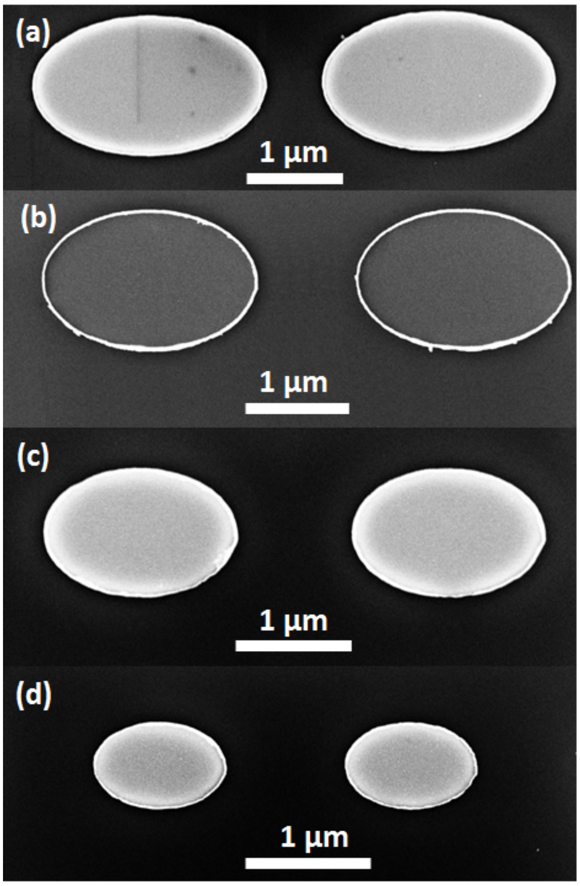

Figure 6.33: SEM images of the periodic arrangement of ellipses with different sizes and same aspect ratios, produced by EBL, $2.4\,\mu$m × $1.4\,\mu$m (a), $2.0\,\mu$m × $1.33\,\mu$m (b), $1.5\,\mu$m × $1.0\,\mu$m (c), $1.0\,\mu$m × $0.67\,\mu$m (d).

6.4.3 Static Magnetization

The magnetization curves $M \times H$ for the ellipses arrangements were made at room temperature using the AGFM, with an external magnetic field H applied along the major axis of the ellipses (easy axis) and along the minor axis (hard axis). Figure 6.34 shows the curves measured in both configurations.

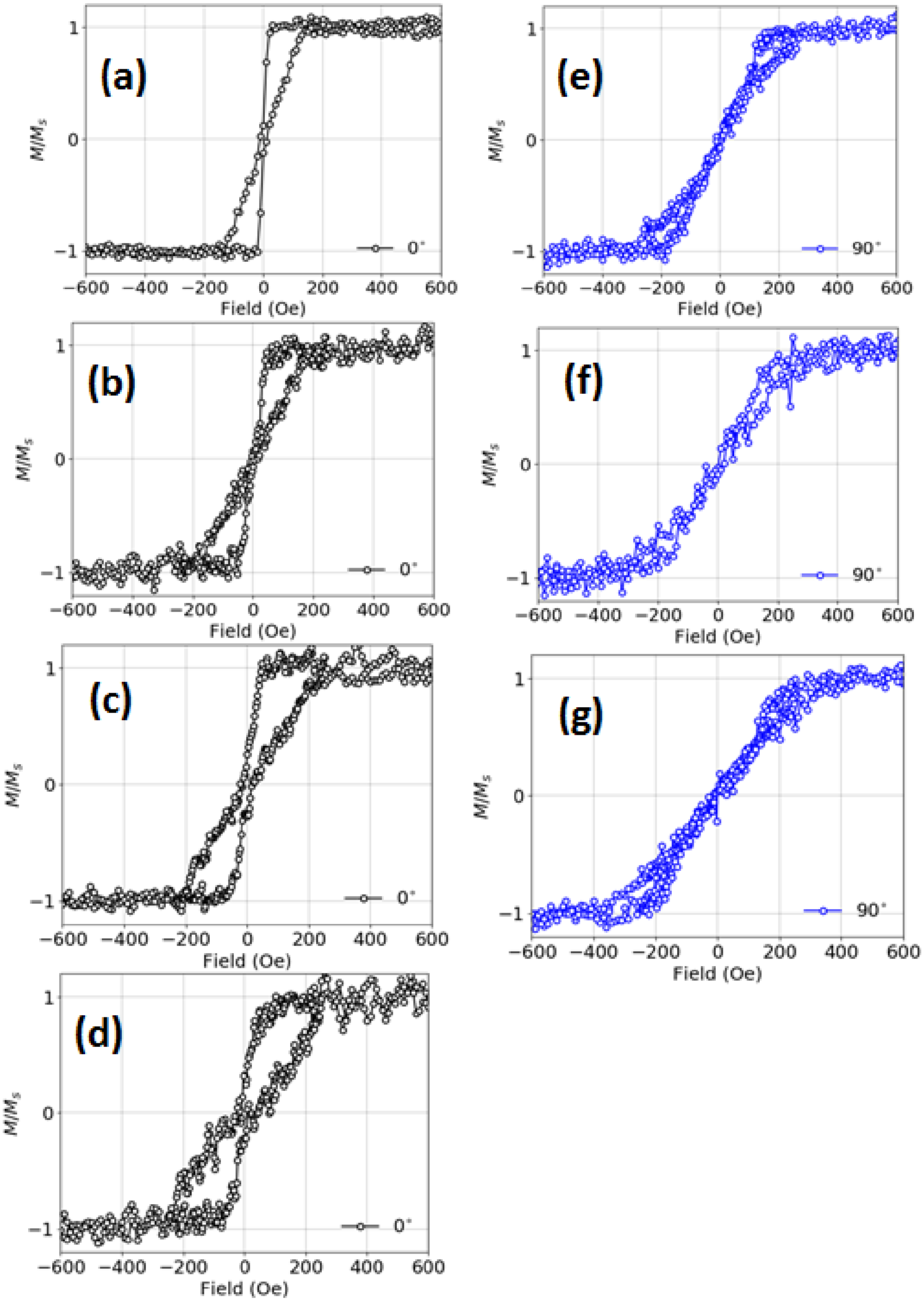

Figure 6.34: Hysteresis loops for external fields applied along $\theta = 0°$ and $\theta = 90°$ directions, measured for ellipse arrangements with different sizes and same aspect ratios (a)&(e) $2.4\,\mu\text{m} \times 1.4\,\mu\text{m}$ (b)&(f), $2.0\,\mu\text{m} \times 1.33\,\mu\text{m}$ (c)&(g), $1.5\,\mu\text{m} \times 1.0\,\mu\text{m}$ (d), $1.0\,\mu\text{m} \times 0.67\,\mu\text{m}$.

It is possible to observe qualitative differences between the curves for the two directions of applied field. Therefore, the reversal of magnetization occurs through different mechanisms. In according to the MFM images, when the external field is applied along the major axis of the ellipses, the remaining state is a magnetic state with a mixture of vortex states single and double vortexes most dominated by the latter (as shown in the Fig. 6.34 (a)-(d)). While applying the external field along the minor axis of the ellipses predominantly observed in the remnant magnetic state, only one vortex is (as shown in the Fig. 6.34 (e)-(g)).

6.4.4 Phenomenology of Magnetization Dynamics

6.4.5 VNA-FMR study

This subsection presents the broadband ferromagnetic resonance measurements of the ellipse arrays using the VNA-FMR technique with the external field H applied in the direction the longest and shortest axes of the ellipses. The absorption spectra (P vs. H vs. f) were obtained by varying the external DC field from H = +720 Oe to H = -720 Oe with steps of 2 Oe and sweeping the frequency from 0.5 to 10.0 GHz with frequency steps of 10 MHz. The samples were placed on the coplanar waveguide and dynamic measurements were performed with the radio frequency field h_{rf} applied in the sample plane and in the direction perpendicular to the external magnetic field H ($h_{\mathrm{rf}} \perp H$). Measurements were taken along the major and minor axes of the ellipses, as shown in Figure 6.35.

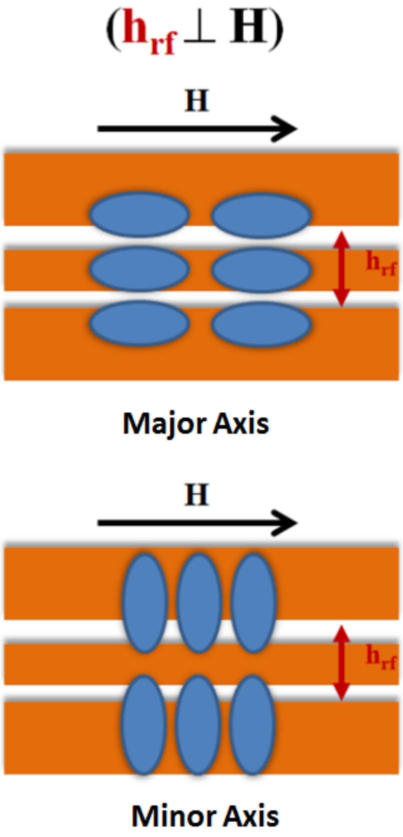

Figure 6.35: schematic representation of the sample on the top of CPW, with two different configurations.

Figure 6.36 shows the spectra (P vs. H vs. f) measured in the two distinct configurations with the H field along the minor and major axes of the ellipses. These spectra were obtained after saturating the ellipses along the major axis or minor axis, so they are associated with a magnetic configuration in the remainder of a pair of vortexes. The spectra shown in Figure 6.36 (a)-(d) were measured when the field H is applied in the major axis, where a single or two vortex in this configuration are expected. It was also noted that the evolution of the excited modes in the magnetic states within the ellipses, starting with the stable state with two of the vortex ($2V$) and abruptly passes to the saturated state (S) of the magnetization. In the saturated part of the magnetization, we have a well-defined branch of resonance associated with uniform precession and a mode at higher frequencies, in which it is more defined in the all samples. In addition, we observed that the nucleation field H_n is increased as we measured in the the smaller ellipses.

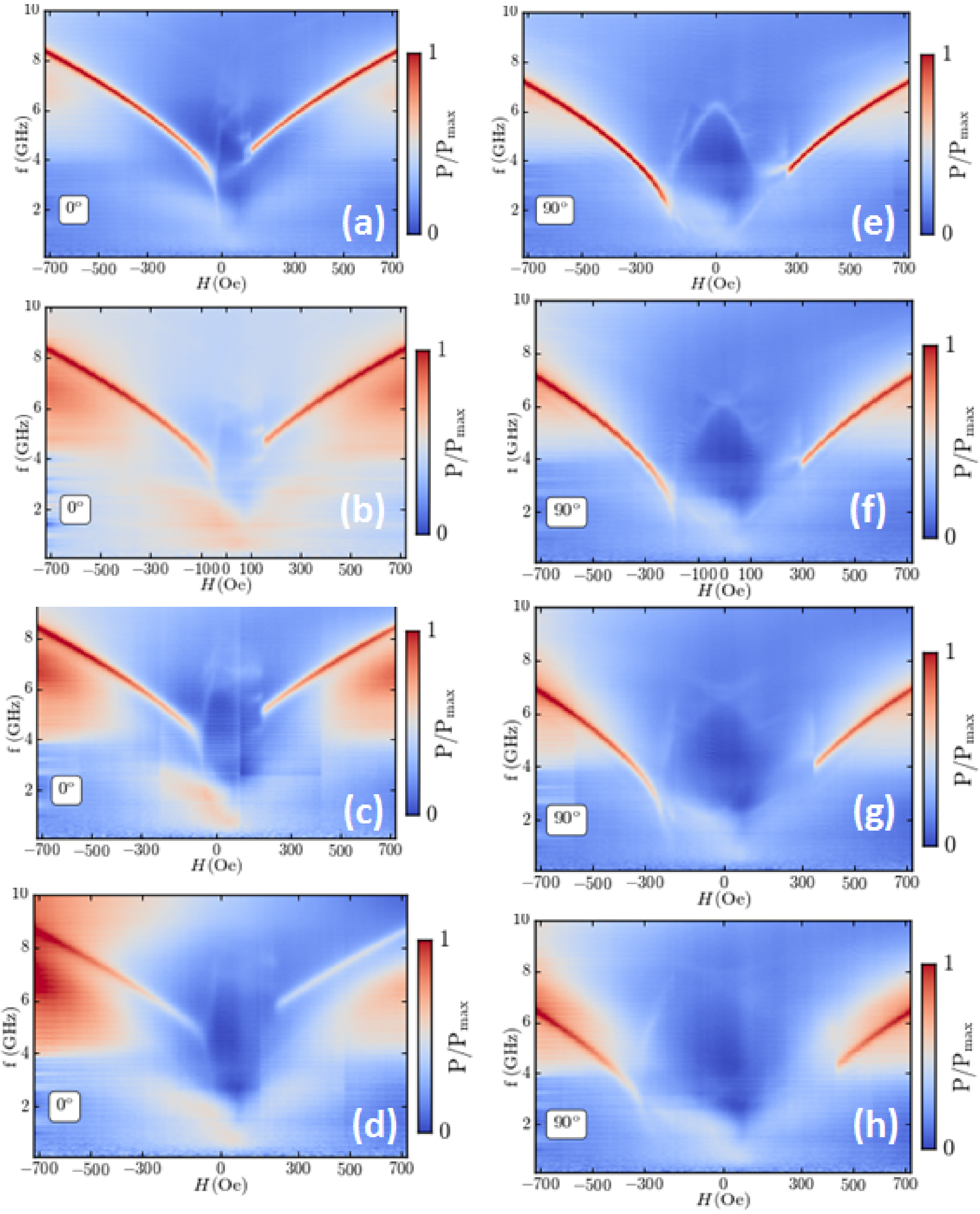

Figure 6.36: Broadband FMR spectra (color plots) ellipse arrangements with different sizes and same aspect ratios, (a)&(e) 2.4 μm × 1.4 μm (b)&(f), 2.0 μm × 1.33 μm (c)&(g), 1.5 μm × 1.0 μm (d)&(h), 1.0 μm × 0.67 μm. Panels (a)-(d) were measured with H applied along the major ellipse axis, and (e)-(h) when H is parallel to the minor axis.

Figure 6.36 (e)-(h) shows the (P vs. H vs. f) spectra of ellipses, measured when H field applied along the minor axis of the ellipses. These spectra were obtained after saturating the ellipses along the minor axis, so they are associated with a single vortex. The absorption peaks of the resonance modes excited in the field region between the H_n nucleation field and the H_{an} annihilation field, $H_n < H < H_{an}$ associated with the ground state with a vortex are relatively defined. The H_n increases as we go for the smaller ellipses. Also, the modes at zero field move to higher frequencies, as shown in the Fig. 6.37.

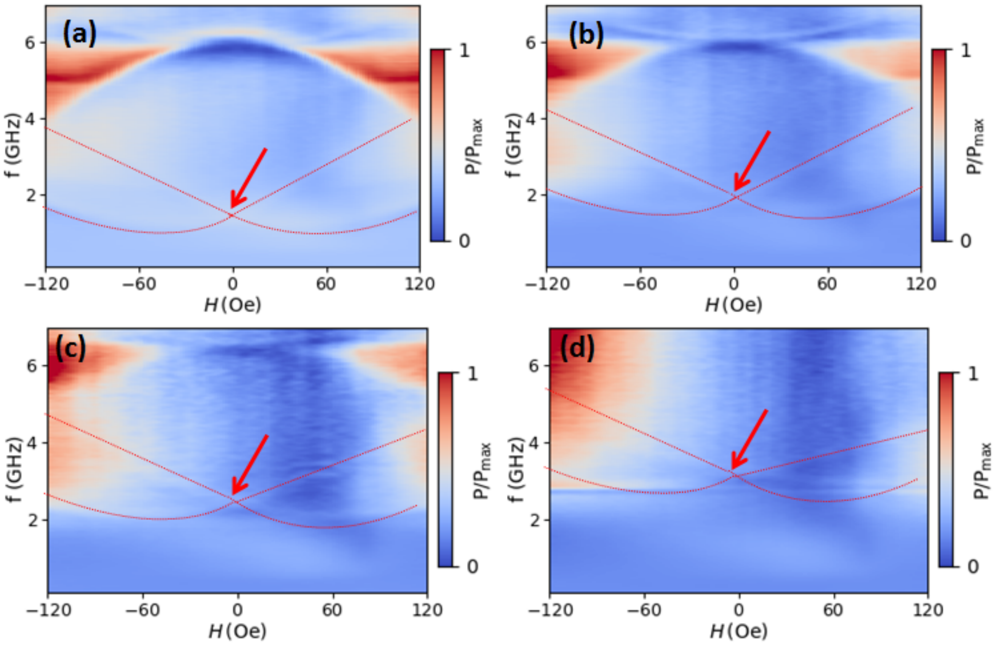

Figure 6.37: Zoomed broadband FMR spectra (color plots) of the ellipse with different sizes and same aspect ratios along the $\theta = 0°$ single vortex (a) $2.4\,\mu m \times 1.4\,\mu m$ (b), $2.0\,\mu m \times 1.33\,\mu m$ (c), $1.5\,\mu m \times 1.0\,\mu m$ (d), $1.0\,\mu m \times 0.67\,\mu m$. The red arrow indicates the mode at $H = 0$ Oe, while the red dotted lines are eye guidelines for the excited modes.

Figure 6.37 shows the zoomed (P vs. H vs. f) spectra of ellipses. These spectra were obtained after saturating the ellipses along the minor axis, so they are associated with a single vortex. Here, we show the absorption amplitudes for unsaturated state. The 1st mode at $H = 0$ Oe is observed at 1.25 GHz for sample $2.4\,\mu m \times 1.4\,\mu m$ as shown in the Figure 6.38(a). It moves to 1.82 GHz for sample $2.0\,\mu m \times 1.33\,\mu m$ as shown in the Figure 6.38(b), and 2.34 GHz Figure 6.38(c), in the case of $1.5\,\mu m \times 1.0\,\mu m$ sample . Finally, for the case of smallest sample $1.0\,\mu m \times 0.67\,\mu m$ this mode was observed at 3.10 GHz Fig. 6.38(d). Moreover, the shifitting of this mode towards higher frequencies is associated with the dipolar and exchange interactions inside the elliptical elements. These modes are known as dipole-exchange modes.

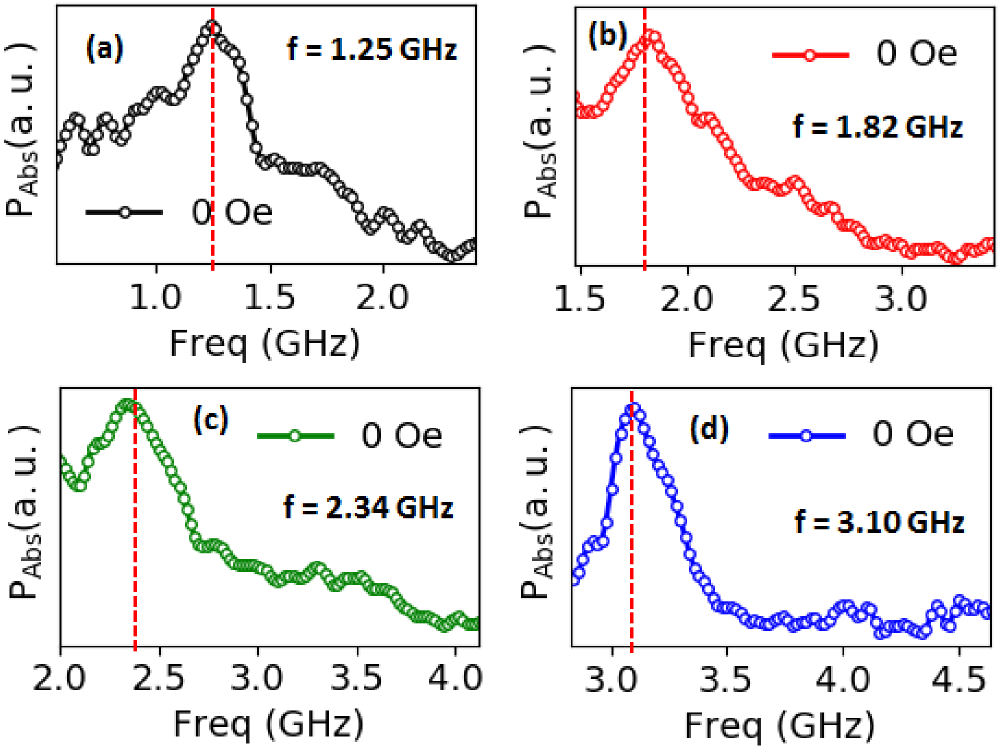

Figure 6.38: Experimental P_{Abs} as function of frequency for dipole-exchange mode of the ellipse with different sizes and same aspect ratios for $\theta = 0°$ single vortex (a) $2.4\,\mu\text{m} \times 1.4\,\mu\text{m}$ (b), $2.0\,\mu\text{m} \times 1.33\,\mu\text{m}$ (c), $1.5\,\mu\text{m} \times 1.0\,\mu\text{m}$ (d), $1.0\,\mu\text{m} \times 0.67\,\mu\text{m}$.

6.4.6 Micromagnetic Simulation

The micromagnetic simulations were performed using the Mumax3 code [173] to preform simulations of a magnetic ellipse lattice, discretized with cell size $7.14 \times 7.14 \times 50\,\text{nm}^3$ using a simulation box of $336 \times 196 \times 1$ cells. This corresponds to the shape and size of a single ellipse of our experimental sample. The parameters used for the magnetic material were: saturation magnetization M_s=800×10^3 A/m, exchange constant $A = 1.3 \times 10^{-11}$ J/m and damping constant $\alpha = 0.02$. The simulations were carried on a field/frequency (H, f) scheme, with H ranging from 0 to 800 Oe, with field steps of 5 Oe, and f ranging from 0.5 GHz to 10.0 GHz, with frequency steps of 100 MHz. The simulation routines for the dynamical response aim to reproduce the broadband ferromagnetic resonance experiment. For each H a fixed frequency h_{rf} is applied and the response is recorded after a stable harmonic oscillation is attained.

This procedure is repeated for all the frequencies to be measured. Finally, a software developed by our research group is used to process the recorded data in order to obtain absorbed power spectra comparable with experimental data and the oscillation modes.

Fig. 6.39(a) shows the simulated single vortex for the case when H is applied along the major axis. Panel(b) displays the MFM image of the single vortex at the remanence. The measurements were done with low moment probe of MFM. First we apply a field of several Oe and then measure the sample with interleave mode of MFM. Fig. 6.40 shows the vortex configuration at $H=0$ Oe with red curved arrows, while blue arrows illustrate the h_{rf} excitation. The vortex translation is shown in the right side of the Fig. 6.40 when $H > 0$.

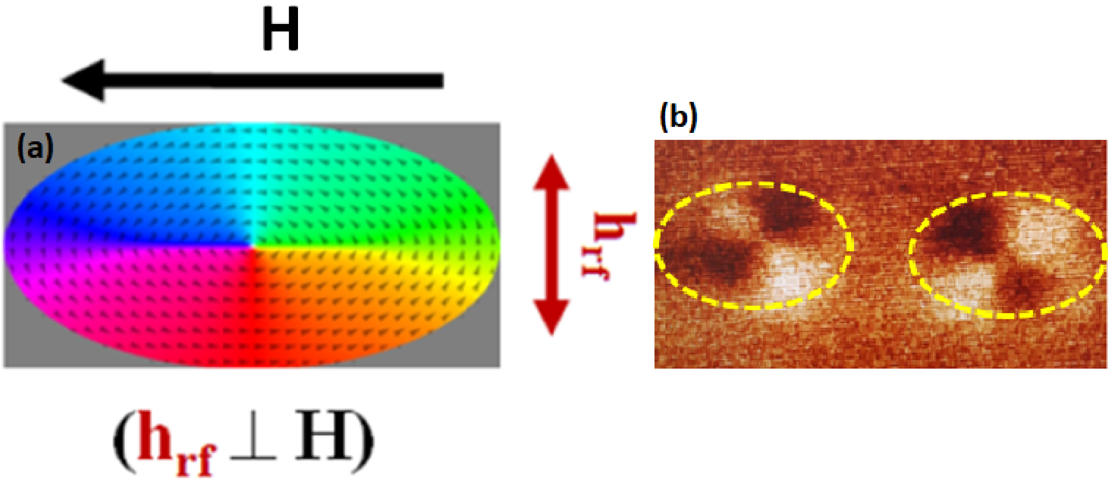

Figure 6.39: (a) Micromagnetic simulation: Single vortex at $H = 0$ Oe. (b) MFM image of the ellipse at remanence.

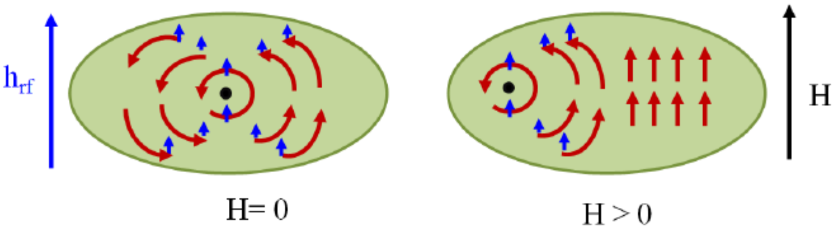

Figure 6.40: The red lines shows the single vortex configurations, while blue shows the applied RF field excitation at $H=0$ Oe and $H > 0$ Oe.

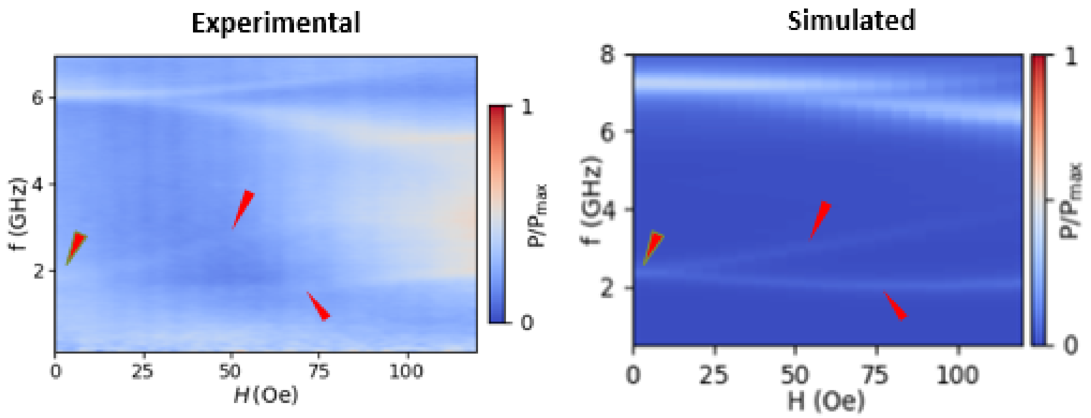

Figure 6.41: Broadband FMR spectra (left) and the micromagnetic simulated color polt (right) of the ellipse with size 2.0 μm × 1.33 μm and $\theta = 0°$.

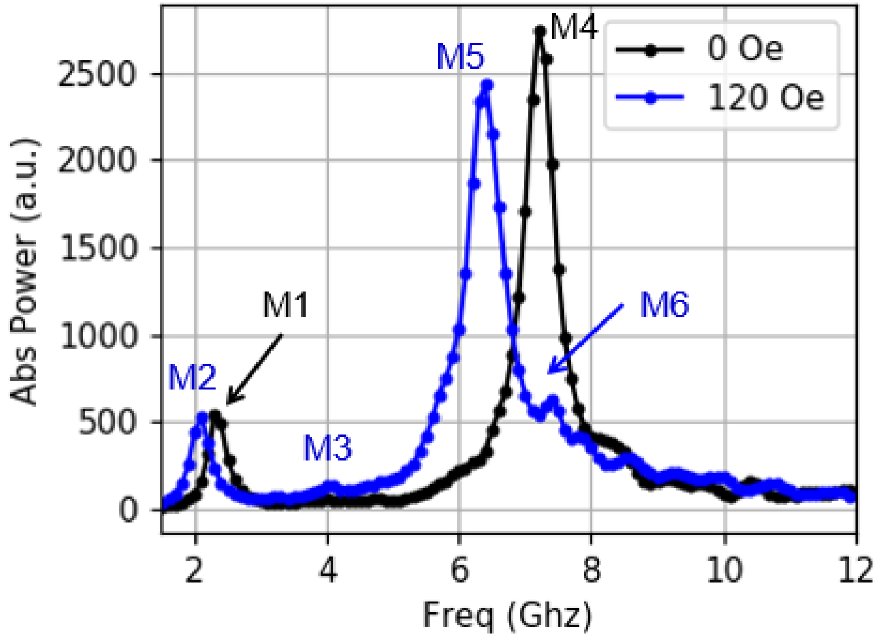

Figure 6.42: Simulated absorption spectra for H = 0 Oe and 120 Oe. Where M1, M2, M3, M4, M5 and M6 label the different modes.

Figure 6.41 shows the experimental and simulated FMR color maps for 2.0 μm × 1.33 μm sample. The color scale used maximizes the contrast in the presented H and f range. As seen from the figure, the main features of the experimental results are reproduced in the simulated spectra. The shapes and relative amplitudes of the absorption branches are well reproduced. We observed the mode at 2.30 GHz for $H = 0$ Oe.

Figure 6.42 shows the simulated absorbed power spectra of 2.0 μm × 1.33 μm sample for 0 Oe and 120 Oe (vertical cuts in the color map). The peaks are labeled with 1, 2, 3, 4, 5 and 6 which shows the modes M1, M2, M3, M4, M5 and M6, which are analyzed in Fig. 6.43.

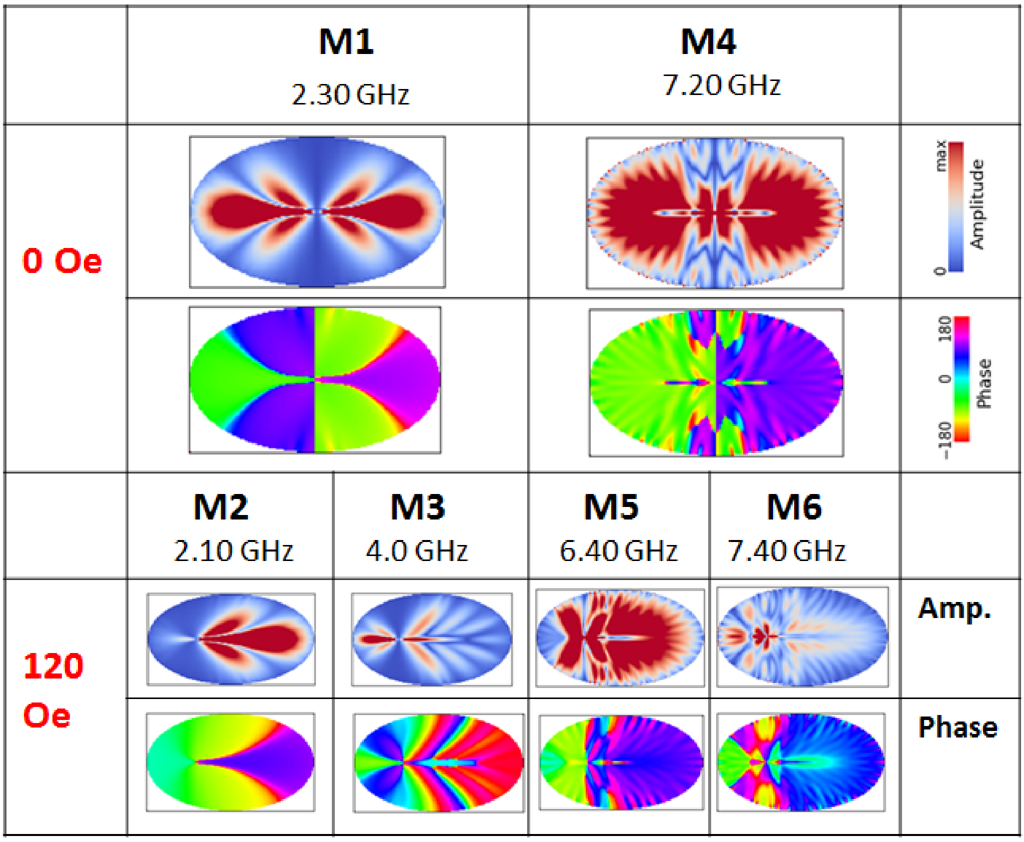

Figure 6.43: Simulated spin wave mode profiles (amplitude and phase maps) for the $Ni_{81}Fe_{19}$ ellipse with square lattice symmetry in the case of $H = 0$ Oe and 120 Oe applied parallel ($\theta = 0°$) to the array axis. The color scales for the power and phase maps are shown at the right side of the figure.

Figure 6.43 shows the simulated spin wave mode profiles (amplitude and phase maps) for the $Ni_{81}Fe_{19}$ ellipses of 2.0 μm × 1.33 μm with square lattice symmetry in the case of H =0 Oe and 120 Oe applied ($\theta = 90°$) to the array axis. We found two prominent modes when applied field $H = 0$ Oe at 2.30 GHz and 7.20 GHz, these modes are related to the vortex state modes, which are symmetric.

When $H = 120$ Oe we noticed that the M1 splits into M2 and M3, and this frequency splitting is related to symmetry breaking within the ellipse. Moreover, when $H > 0$ Oe fields are applied in the direction of the minor axis of the ellipse, the core of the vortex moves in the direction of the major axis of the sample, breaking the symmetry mode to the center of the ellipse (as shown in 6.40). As a result, we obtain a region close to the core of the vortex and another region with spins oriented towards the external field. These two regions now resonate at different frequencies.

In summary, when in equilibrium the two regions next to the vortex core oscillate under the same conditions, forming a single resonance peak for the same oscillation mode. However, when the nucleus is displaced, the resonances of each region occur at different frequencies, which is observed as an unfolding of the single peak of resonance. It was noticed that, the greater the asymmetry between the two regions, the greater the frequency difference as shown in Figure 6.43. On the other hand we also find that the M4 mode shows excitation at M5 and M6 when $H > 0$ Oe, this could be related with the effect of the confinement on the mode excitation frequencies.

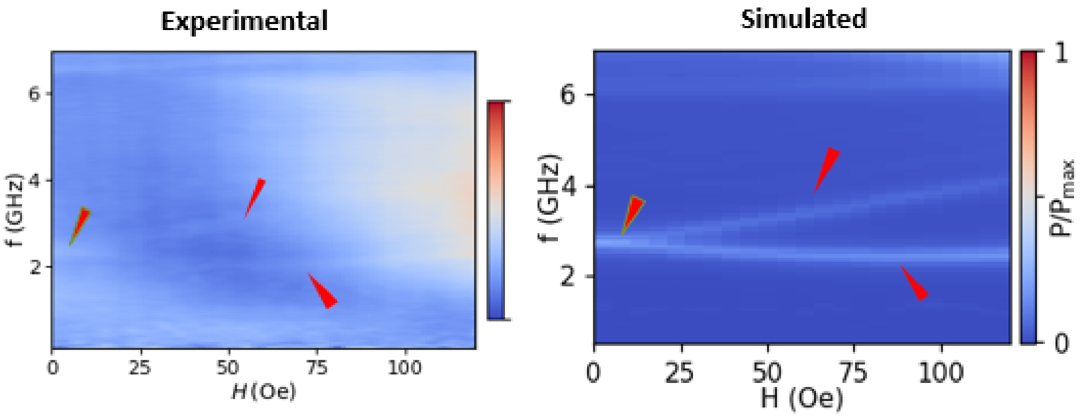

Figure 6.44: Broadband FMR spectra (left) and the micromagnetic simulated color polt (right) of the ellipse with size 1.5 μm × 1.0 μm and $\theta = 0°$.

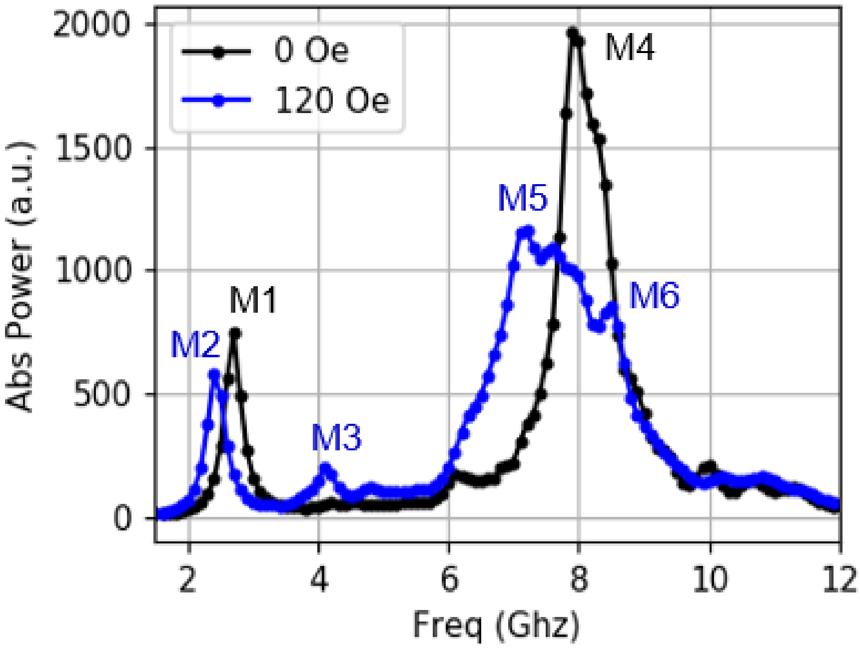

Figure 6.45: Simulated absorption spectra for $H = 0$ Oe and 120 Oe, where M1, M2, M3, M4, M5 and M6 symbolized different modes.

Figure 6.44 shows the experimental and simulated FMR color maps for $1.5\,\mu\text{m} \times 1.0\,\mu\text{m}$ sample. The color scale used maximizes the contrast in the presented H and f range. As seen from the figure, the main features of the experimental results are reproduced in the simulated spectra. The shapes and relative amplitudes of the absorption branches are well reproduced. We observed the mode at 2.70 GHz for $H = 0$ Oe.

Figure 6.45 shows the simulated absorbed power spectra of $1.5\,\mu\text{m} \times 1.0\,\mu\text{m}$ sample for 0 Oe and 120 Oe (vertical cuts in the color map). The peaks in this Fig. labeled 1, 2, 3, 4, 5 and 6 represent the modes M1, M2, M3, M4, M5 and M6, respectively, and are analyzed in Fig. 6.46.

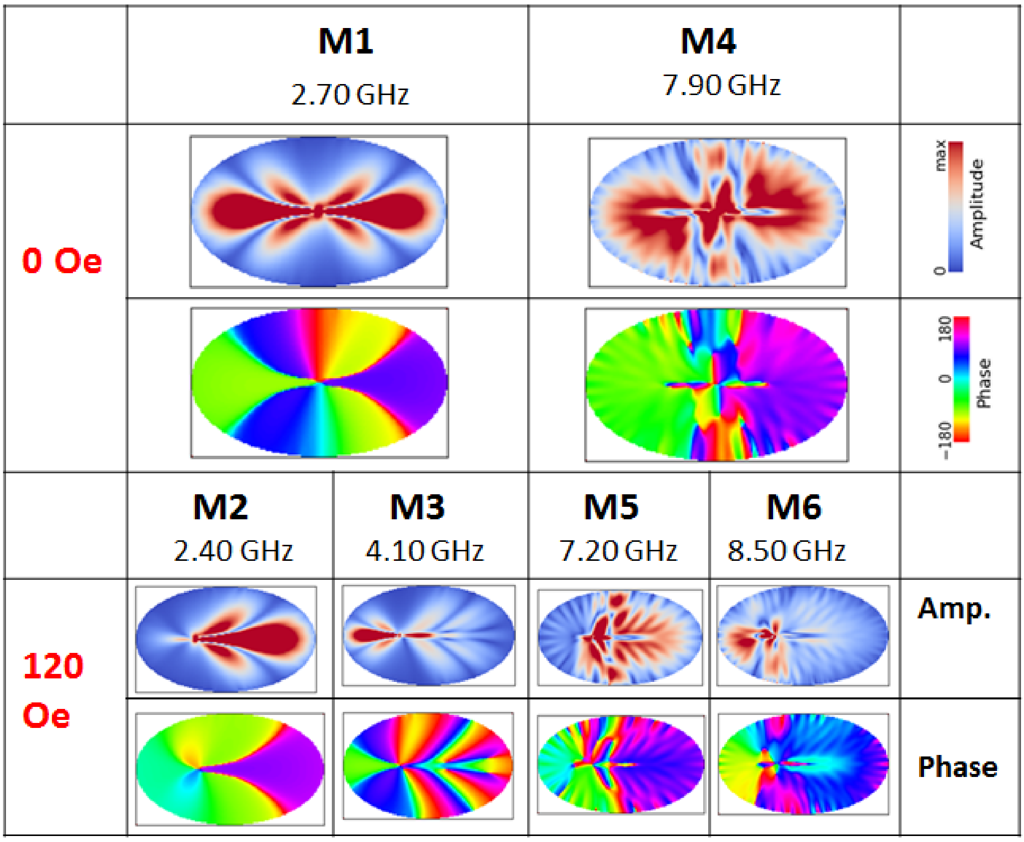

Figure 6.46: Simulated spin wave mode profiles (amplitude and phase maps) for the $Ni_{81}Fe_{19}$ ellipse with square lattice symmetry in the case of $H = 0$ Oe and 120 Oe applied parallel ($\theta = 0°$) to the array axis. The color scales for the power and phase maps are shown at the right side of the figure.

Figure 6.46 shows the simulated spin wave mode profiles (amplitude and phase maps) for the $Ni_{81}Fe_{19}$ ellipses of $1.5\,\mu m \times 1.0\,\mu m$ with square lattice symmetry in the case of $H = 0$ Oe and 120 Oe applied ($\theta = 90°$) to the array axis. For $H = 0$ Oe we found two prominent symmetric modes at 2.70 GHz and 7.50 GHz, and that are related to the vortex state. When $H = 120$ Oe we noticed that the M1 splits into M2 and M3, and this frequency splitting is related to the symmetry breaking within the ellipse. M4 also shows excitations at M5 and M6 when $H > 0$ Oe, which we suspect that, could be the effect of confinement.

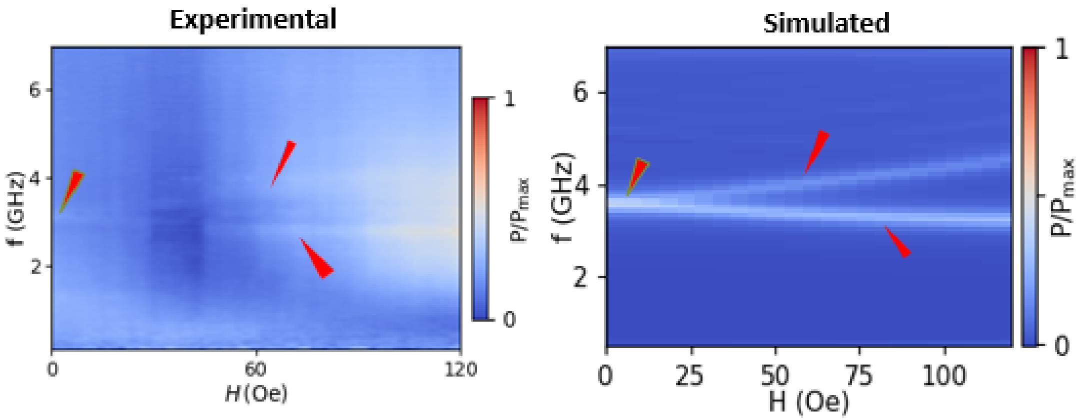

Figure 6.47: Broadband FMR spectra (left) and the micromagnetic simulated color plot (right) of the ellipse with size $1.0\,\mu\text{m} \times 0.67\,\mu\text{m}$ and $\theta = 0°$.

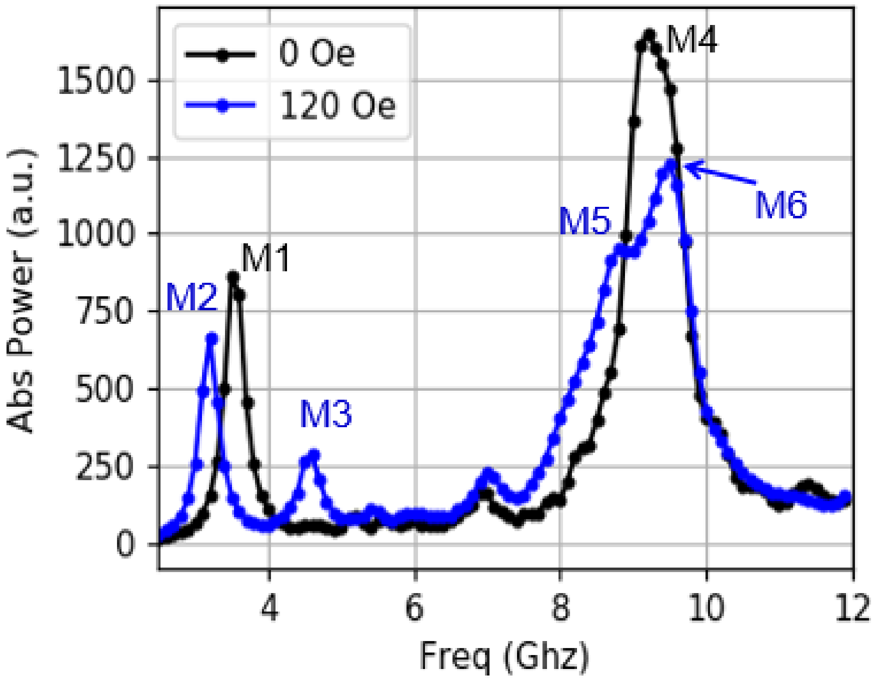

Figure 6.48: Simulated absorption spectra for $H = 0$ Oe and 120 Oe. Where M1, M2, M3, M4, M5 and M6 corresponds to different modes

Figure 6.47 shows the experimental and simulated FMR color maps for $1.0\,\mu\text{m} \times 0.67\,\mu\text{m}$ sample. The color scale used maximizes the contrast in the presented H and f ranges. As seen from the figure, the main features of the experimental results are reproduced in the simulated spectra. The shapes and relative amplitudes of the absorption branches are well reproduced. We observed the mode at 3.10 GHz for $H = 0$ Oe.

Figure 6.48 shows the simulated absorbed power spectra of 1.0 μm × 0.67 μm sample for 0 Oe and 120 Oe (vertical cuts in the color map). The peaks in Fig. are labeled with 1, 2, 3, 4, 5 and 6 which shows the modes M1, M2, M3, M4, M5 and M6, these are analyzed in the Fig. 6.49.

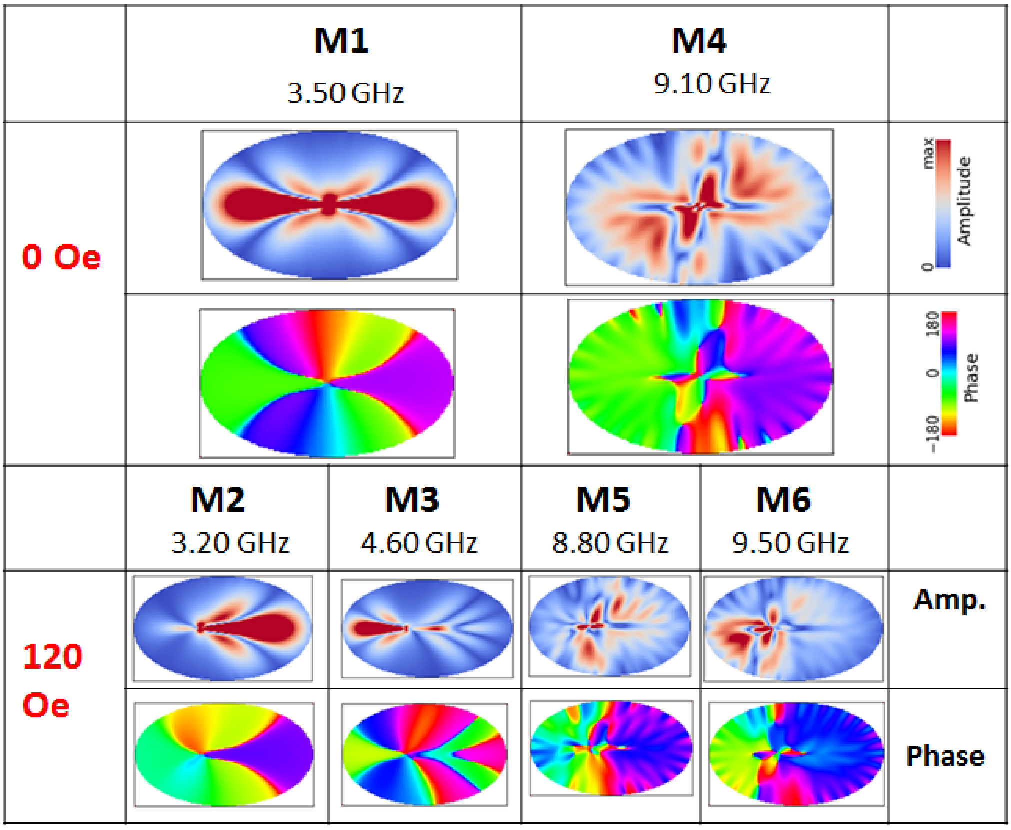

Figure 6.49: Simulated spin wave mode profiles (amplitude and phase maps) for the $Ni_{81}Fe_{19}$ ellipse with square lattice symmetry in the case of $H = 0$ Oe and 120 Oe applied parallel ($\theta = 0°$) to the array axis. The color scales for the power and phase maps are shown at the right side of the figure.

Figure 6.49 shows the simulated spin wave mode profiles (amplitude and phase maps) for the $Ni_{81}Fe_{19}$ ellipses of 1.0 μm × 0.67 μm with square lattice symmetry in the case of $H = 0$ Oe and 120 Oe applied ($\theta = 90°$) to the array axis. We find two prominent modes when applied field $H = 0$ Oe at 3.50 GHz and 9.10 GHz, these modes are related to the vortex state modes, which are symmetric. When $H = 120$ Oe we noticed that the M1 is split into M2 and M3, and this frequency splitting is related to the symmetry breaking within the ellipse. On the other hand, M4 also shows excitations at M5 and M6 when $H > 0$ Oe, this could be related with the effect of confinement.

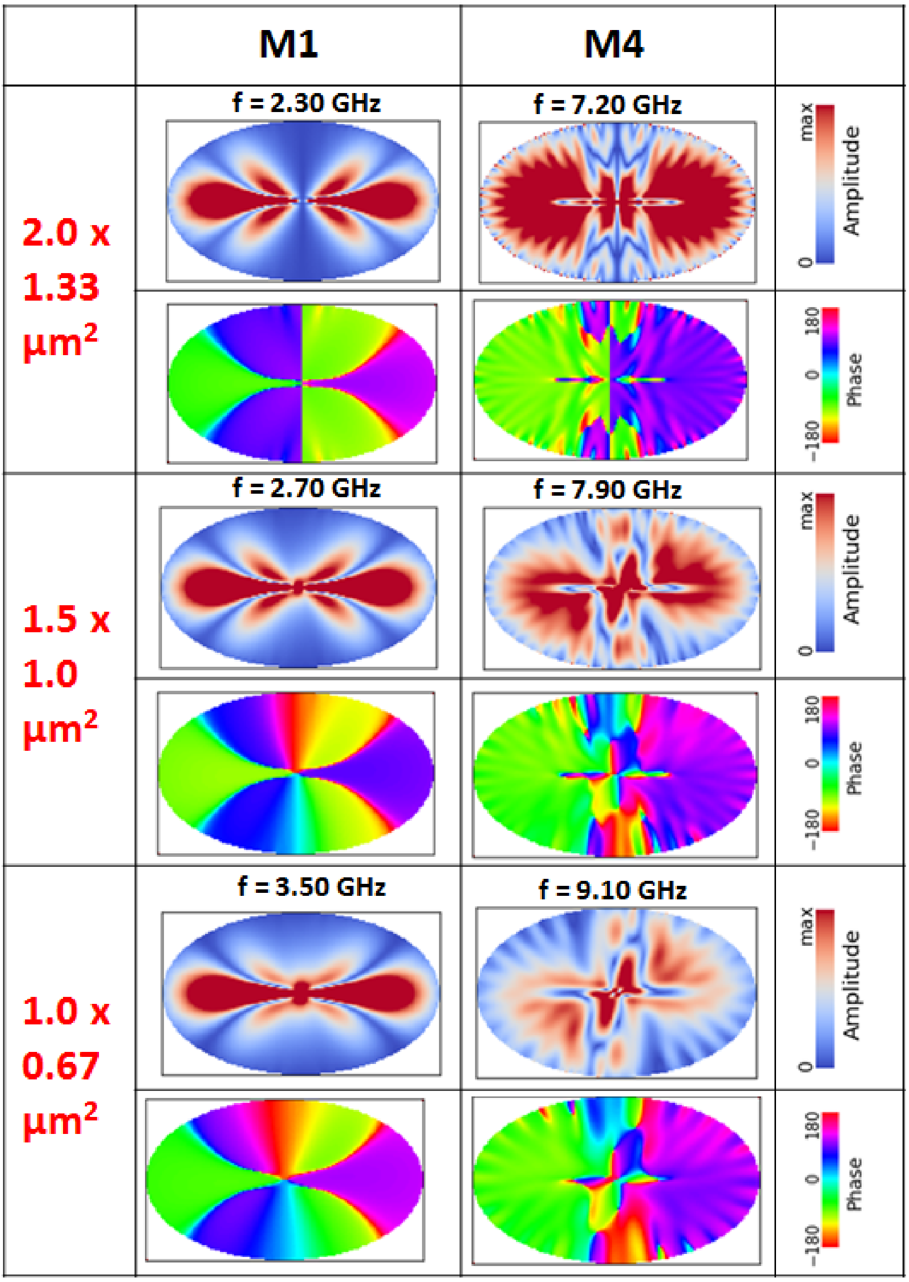

Figure 6.50: Simulated spin wave mode profiles (amplitude and phase maps) for the $Ni_{81}Fe_{19}$ ellipse with square lattice symmetry in the case of $H = 0$ Oe applied parallel ($\theta = 0°$) to the array axis. The color scales for the power and phase maps are shown at the right side of the figure, where M1 and M4 corresponds to the different modes.

Figure 6.50 shows the simulated spin wave mode profiles (amplitude and phase maps) for the $Ni_{81}Fe_{19}$ ellipses with square lattice symmetry at vortex state, field applied along the minor axis. In the case of sample with 2.0 μm × 1.33 μm we observed the modes at 2.30 GHz and 7.20 GHz. But in the case of sample with dimension 1.5 μm × 1.0 μm we observed these modes at 2.70 GHz and 7.90 GHz. Moreover, in the case of sample with size 1.0 μm × 0.67 μm we observed these modes, even at higher frequencies 3.50 GHz and 9.10 GHz. All these modes are observed when the sample is in vortex state, which could be seen from the symmetry of the modes from the core of the ellipses. It could be seen in Fig. 6.50 all the modes have same phase which indicates that the same mode is propagating towards higher frequencies when we measured the smaller ellipses. There is competition between dipole and exchange interaction within the ellipse within the ellipse, which is responsible for this shift in the mode frequency. The contribution of the dipolar field $\vec{H}_{eff}^{dip}$ and exchange field $\vec{H}_{eff}^{exch}$ to the effective dynamic field could be given as:

$$\vec{H}_{eff}^{dyn}(\vec{r}) = \vec{H}_{eff}^{dip}(\vec{r}) + \vec{H}_{exch}^{dyn}(\vec{r}) + h_{rf}. \tag{6.7}$$

With the help of micromagnetic simulations we are able to analyzed these contributions, the dipolar field which is relatively remains same, while the exchange field contribution is increased as we go for smaller sized ellipses. Hence, we were able to control the dipole and exchange interaction within the magnetic ellipses by tuning the geometry of the ellipses.

6.4.7 Partial Conclusions

In this project we have produced arrays of sub micron-sized $Ni_{81}Fe_{19}$ elliptical elements with four types of lateral dimensions, using e-beam lithography, sputtering and lift-off processes. The static (M vs. H) and dynamic magnetic characterizations indicates the typical vortex structures in all samples, when field applied along the minor axis. We observed single vortex state when field was applied along the minor axis and double vortex state when applied along the major axis. The micromagnetic simulation were preformed to reproduced the experimental results and analyse them. We observed that spin wave mode at lower frequencies for $H = 0$ Oe is moved to higher frequencies (1.25 GHz to 3.10 GHz) for for smaller sized elliptical elements, and this was related with the competition between exchange and dipolar modes, the dipolar contribution relatively remains same while exchange is increased. So, we were able to control the dipole and exchange interaction within the magnetic ellipses. We also analyzed two modes at vortex state ($H = 0$ Oe) both shows the frequency splitting due to an applied field, the first is related with exchange-dipolar competition and the second is due to geometrical confinement.

The results of this study will help to understand and provide insight into the magnetization dynamics in elliptical systems, opening new perspectives for the patterned high density media and devices.

Chapter 7

Conclusions and Perspectives

7.1 Conclusions

This thesis present the study of spin waves in confined nanostructures of single layered Co_2FeAl (CFA), trilayered $Co/Ni_{81}Fe_{19}/Co$ and in periodic arrays of $Ni_{81}Fe_{19}$ patterned elements in the form of antidots and ellipses. Continuous films were produced using the magnetron sputtering, while the periodic arrays were fabricated by combining electron beam lithography, magnetron sputtering, plasma etching and/or lift-off techniques. The dynamic properties of magnetization were measured with the broadband ferromagnetic resonance technique by vector network analyzer (VNA-FMR), while the static magnetization properties were characterized with an alternating gradient force magnetometer (AGFM).

For the case of CFA Heusler alloy films, the samples were grown on Si(100) substrate at ambient temperature. Based on the structural analysis with X-ray diffraction and transmission electron microscopy, we found that these CFA films show the A2 ordered phase, good interface and low roughness. Static magnetization curves show the existence of in-plane magnetic anisotropy and coercive fields in the range 4.2 to 7.8 Oe. From the fittings of the FMR dispersion relations we obtained the values of the in-plane, out-of-plane and rotatable anisotropies. The out-of-plane surface anisotropy constant for CFA/Ti interfaces was estimated as $K_s = 0.54$ erg/cm^2. We obtained damping constants as low as 2.56×10^{-3} for 10 nm CFA film, and 2.78×10^{-3} for 200 nm. It must be remarked that all ΔH_0 obtained values are small when compared to the values reported to CFA in literature. Moreover, there is a clear but yet small increase on ΔH_0 with increasing film thickness, which is probably correlated to the appearance of the rotatable anisotropy.

Another system of the continuous films, where a trilayered samples of Co/NiFe/Co were produced on Si(100) substrate. The results shows that, we were able to control the anisotropies and effective magnetization in a synthetic layer system. For the particular case of Co/NiFe/Co trilayers, the Co layers contributes with a large in-plane uniaxial magnetic anisotropy and increased saturation magnetization when compared to NiFe. But it also increases the effective damping parameter. We found that the effective properties of the synthetic layers are bounded between the properties of the pure Co and NiFe layers, depending on the Co to NiFe thickness fraction. The non uniform synthetic layer structure seems to enhance the PSSW absorption for high order modes due to the local oscillation magnetization profiles produced inside the synthetic layer. There is dependence of damping parameter and out of plane anisotropy on the deposition of Co layers, which demonstrates the possibility of controlling these properties within the synthetic layered system.

In the case of periodic arrays of $Ni_{81}Fe_{19}$ patterned elements, we have produced arrays of micron-sized antidots on SiO_2/Si substrate. We observed differences in the M vs. H curves for the antidots when compered with a continuous film. In particular we observe an increase in the coercive field. This is associated to the local demagnetizing field due to the anti-dots structures. The dynamic properties results show a rich structure of modes in the resonance absorption spectra, with absorption peak amplitudes dependent on the direction of the external magnetic field. We correlate this to the symmetries present in the antidot array. By using micromagnetic simulations we identify different standing spin waves excitations. Most of the spin waves are localized in the space between the antidots, and have wave vectors either perpendicular or parallel to the static magnetization direction. With the change of static field orientation the possible space where the spin waves can be accommodated changes. For 0° and 90°, the spin waves are localized in between nearest neighboring antidots. On the other hand, for 45° they are confined by antidots along the diagonals of the array.

Another system of periodic arrays of patterned elements, where an arrays of sub micron-sized $Ni_{81}Fe_{19}$ elliptical elements were produced with four types of lateral dimensions. Magnetization curves (M vs. H) indicates the typical vortex magnetization in all samples. We observed single vortex state when field was applied along the minor axis and double vortex state when applied along the major axis. Broadband FMR measurements show similar absorption peak profiles for all samples. The difference is that for smaller ellipses the resonances occurs at increased frequencies and fields. In particular, for zero field, the lower spin wave shifted for 1.25 GHz for an $2.4 \times 1.4\ \mu m^2$ ellipse to 3.10 GHz for an $1 \times 0.67\ \mu m^2$ ellipse. By using micromagnetic simulations we show that the lower spin wave in the vortex state is formed by both exchange and dipolar waves. We also showed that the most intense peak observed at zero field is divided into two peaks when a field is applied. This could be due the different imposed confinements at both sides of the vortex cores.

The results of this thesis will help to understand the spin waves in different confined nanostructures, starting with single layers of CFA, followed by trilayers of Co/$Ni_{81}Fe_{19}$/Co with vertical confinement and, finally, periodic arrays of $Ni_{81}Fe_{19}$ patterned elements in form of antidots and ellipses with lateral and vortex state confinements respectively.

It was observed that the confinement, symmetries and periodicity of the systems, enrich the spectrum of resonant frequencies measured by broadband FMR, therefore providing new insights on the magnetization dynamics and spin waves in these kind of systems. For example, in the case of CFA single layered system, where we were able to excite only FMR mode, while when in the case of Co/Py/Co system where a vertical confinement was imposed, we observed FMR mode as well as PSSW modes. Moreover, in the case of periodic arrays systems (e.g. antidots and ellipses), where we have four-fold symmetry. The lateral confinement in antidots give rise to SW modes, the boundaries of the antidots acts like a potential well. Also, the vortex state confinement in ellipses increases the complexity of the excitation modes. So, the confinement in these nanostructures plays an important role for the excitation of different modes.

Basically, in this thesis we have played with the competition between dipolar and exchange energies in different confined systems. For example in Co/Py/Co and antiodts systems, where the exchange and dipolar energies were controlled with vertical and lateral confinements. Moreover, in the case of ellipse the competition between exchange and dipolar interaction were studied as function of ellipse size. The micromagnetic simulation help us to understand this competition between exchange and dipolar interactions, we observed that with increasing the elliptical elements sizes, the dipolar contribution relatively remains same while exchange is increased. So, the confinements or geometries plays a crucial role for controlling the exchange and dipolar energies in magnetic nanostructures.

In this thesis we also preformed micromagnetic simulation for periodic arrays systems, these simulation were used to reproduce our experimental results. Furthermore, the simulated data was analyzed by means of algorithms developed by the Applied Magnetism Laboratory group, which allow to extract the spectral power absorbed as a function of applied field and frequency. In addition to the details about the power absorbed, we were able to analyze the excited resonant modes within each system.

We believe that, the results of this thesis will open further perspectives for tailoring spintronics, patterned high density media and magnonic devices.

7.2 Perspectives and future work

- In the project of Co-based Heusler alloy Co_2FeAl films, as we noted that there is relatively small magnetic damping for thick samples so in future we propose to use these films for magnetic nanostructures e.g. dots or ellipse. Its worth to mention that this propriety of small damping in thick films is not present in commonly used material like NiFe.

- In the project of periodic arrays of $Ni_{81}Fe_{19}$ patterned elements (antidots), we propose to work on different geometries and lattice structures. We also have plan to use these antidots structures to detect magnetic nanoparticles using nanoconfined system ferromagnetic resonance e.g. have many applications in magnetic biosensors.

- Integrate the magnetic nanostructures to the CPW, where we can fabricate sample sizes at even lower scale with greater sensitivity of the absorbed power in lower frequencies.

- In the project of patterned elements of ellipses based on $Ni_{81}Fe_{19}$, we intend to work on the control of the magnetic vortex with different magnetic layers separated by nonmagnetic spacer. We already produced some samples and have preliminary results.

- In the light of this thesis results and with the help of micromagnetic simulations we are working on the project of nanostructures with out-of-plane anisotropy, and use these structures for stabilizing vortex in the objects. In this regards, we produced samples in the form of magnetic rings with out-of-plane anisotropy and with second lithography we fabricated dots in the middle of the ring; this will be used to stabilized the magnetic vortex even at the the smaller size objects and thickness. The main challenges like lithography and lift-off are already dominated.

Bibliography

[1] Greg Parker. *Encyclopedia of materials: science and technology*. Elsevier, 2001.

[2] SSP Parkin and D Mauri. Spin engineering: Direct determination of the ruderman-kittel-kasuya-yosida far-field range function in ruthenium. *Physical Review B*, 44(13):7131, 1991.

[3] Albert Fert, Vincent Cros, and Joao Sampaio. Skyrmions on the track. *Nature nanotechnology*, 8(3):152–156, 2013.

[4] Safa O Kasap. *Principles of electronic materials and devices*, volume 2. McGraw-Hill New York, 2006.

[5] FJA Den Broeder, W Hoving, and PJH Bloemen. Magnetic anisotropy of multilayers. *Journal of magnetism and magnetic materials*, 93:562–570, 1991.

[6] Anjan Barman and Arabinda Haldar. Time-domain study of magnetization dynamics in magnetic thin films and micro-and nanostructures. In *Solid State Physics*, volume 65, pages 1–108. Elsevier, 2014.

[7] National Institute of Standards and Technology, USA. `https://www.nist.gov/image/landau-lifshitzjpg`. Accessed: 2020-04-13.

[8] Mingzhong Wu. Nonlinear spin waves in magnetic film feedback rings. In *Solid State Physics*, volume 62, pages 163–224. Elsevier, 2010.

[9] Sergej O Demokritov. *Spin wave confinement*. Pan Stanford Publishing, 2009.

[10] Orhan Yalçın. *Ferromagnetic Resonance: Theory and Applications*. BoD–Books on Demand, 2013.

[11] N David Mermin. The topological theory of defects in ordered media. *Reviews of Modern Physics*, 51(3):591, 1979.

[12] ERP Novais, P Landeros, AGS Barbosa, MD Martins, F Garcia, and AP Guimarães. Properties of magnetic nanodots with perpendicular anisotropy. *Journal of Applied Physics*, 110(5):053917, 2011.

[13] Ingo Neudecker. *Magnetization dynamics of confined ferromagnetic systems.* PhD thesis, der fakultät physik der universität regensburg, 2006.

[14] R Dutra, DE Gonzalez-Chavez, TL Marcondes, RL Sommer, SO Parreiras, and MD Martins. Spin wave dynamics in elliptical dots. *Physical Review B*, 99(1):014413, 2019.

[15] CC Wang, AO Adeyeye, and N Singh. Magnetic antidot nanostructures: effect of lattice geometry. *Nanotechnology*, 17(6):1629, 2006.

[16] CS Davies, AV Sadovnikov, SV Grishin, Yu P Sharaevskii, SA Nikitov, and VV Kruglyak. Generation of propagating spin waves from regions of increased dynamic demagnetising field near magnetic antidots. *Applied Physics Letters*, 107(16):162401, 2015.

[17] R Mandal, S Barman, S Saha, Y Otani, and A Barman. Tunable spin wave spectra in two-dimensional $Ni_{80}Fe_{20}$ antidot lattices with varying lattice symmetry. *Journal of Applied Physics*, 118(5):053910, 2015.

[18] Dutra Roberta. *Magnetization dynamics in Magnetic Multilayers and Magnetic Micro / Nanoobjects:.* PhD thesis, Centro Brasileiro de Pesquisas Físicas, 2014.

[19] Alongkorn Pimpin and Werayut Srituravanich. Review on micro-and nanolithography techniques and their applications. *Engineering Journal*, 16(1):37–56, 2012.

[20] Daniel L. Flamm and G. Kenneth Herb. Plasma etching technology—an overview. In *Plasma Etching Technology—An Overview.* Academic Press, Boston, 1989.

[21] Peter J Goodhew and John Humphreys. *Electron microscopy and analysis.* CRC Press, 2000.

[22] BARRY AUTOR CARTER, David Brian Williams, David Bernard Williams, and C Barry Carter. *Transmission Electron Microscopy: A Textbook for Materials Science. Diffraction. II*, volume 1. Springer Science & Business Media, 1996.

[23] Greg Haugstad. *Atomic force microscopy: understanding basic modes and advanced applications.* John Wiley & Sons, 2012.

[24] Alberto Passos Guimarães. From lodestone to supermagnets: understanding magnetic phenomena. *From Lodestone to Supermagnets: Understanding Magnetic Phenomena, by Alberto Passos Guimarães, pp. 248. ISBN 3-527-40557-7. Wiley-VCH, August 2005.*, page 248, 2005.

[25] Mario Norberto Baibich, Jean Marc Broto, Albert Fert, F Nguyen Van Dau, Frédéric Petroff, P Etienne, G Creuzet, A Friederich, and J Chazelas. Giant magnetoresistance of (001) Fe/(001) Cr magnetic superlattices. *Physical review letters*, 61(21):2472, 1988.

[26] Grünberg Binasch, Peter Grünberg, F Saurenbach, and W Zinn. Enhanced magnetoresistance in layered magnetic structures with antiferromagnetic interlayer exchange. *Physical review B*, 39(7):4828, 1989.

[27] Walter Barry. A broad-band, automated, stripline technique for the simultaneous measurement of complex permittivity and permeability. *IEEE Transactions on Microwave Theory and Techniques*, 34(1):80–84, 1986.

[28] Sangita S Kalarickal, Pavol Krivosik, Mingzhong Wu, Carl E Patton, Michael L Schneider, Pavel Kabos, TJ Silva, and John P Nibarger. Ferromagnetic resonance linewidth in metallic thin films: Comparison of measurement methods. *Journal of Applied Physics*, 99(9):093909, 2006.

[29] SA Wolf, DD Awschalom, RA Buhrman, JM Daughton, S Von Molnar, ML Roukes, A Yu Chtchelkanova, and DM Treger. Spintronics: a spin-based electronics vision for the future. *Science*, 294(5546):1488–1495, 2001.

[30] Igor Žutić, Jaroslav Fabian, and S Das Sarma. Spintronics: Fundamentals and applications. *Reviews of modern physics*, 76(2):323, 2004.

[31] Manh-Huong Phan and Hua-Xin Peng. Giant magnetoimpedance materials: Fundamentals and applications. *Progress in Materials Science*, 53(2):323–420, 2008.

[32] Subir Sachdev. *Handbook of magnetism and advanced magnetic materials.* Citeseer, 2006.

[33] Kasturi Chopra. *Thin film device applications.* Springer Science & Business Media, 2012.

[34] B Dieny. Giant magnetoresistance in spin-valve multilayers. *Journal of Magnetism and Magnetic Materials*, 136(3):335–359, 1994.

[35] AV Chumak, P Pirro, AA Serga, MP Kostylev, RL Stamps, H Schultheiss, K Vogt, SJ Hermsdoerfer, B Laegel, PA Beck, et al. Spin-wave propagation in a microstructured magnonic crystal. *Applied Physics Letters*, 95(26):262508, 2009.

[36] Jesco Topp, Detlef Heitmann, Mikhail P Kostylev, and Dirk Grundler. Making a reconfigurable artificial crystal by ordering bistable magnetic nanowires. *Physical review letters*, 104(20):207205, 2010.

[37] Mitsuteru Inoue, Alexander Baryshev, Hiroyuki Takagi, Pang Boey Lim, Kohei Hatafuku, Josho Noda, and Kenji Togo. Investigating the use of magnonic crystals as extremely sensitive magnetic field sensors at room temperature. *Applied Physics Letters*, 98(13):132511, 2011.

[38] Sebastian Neusser and Dirk Grundler. Magnonics: spin waves on the nanoscale. *Advanced Materials*, 21(28):2927–2932, 2009.

[39] AO Adeyeye and S Jain. Coupled periodic magnetic nanostructures. *Journal of Applied Physics*, 109(7):07B903, 2011.

[40] J Ding, M Kostylev, and AO Adeyeye. Broadband ferromagnetic resonance spectroscopy of permalloy triangular nanorings. *Applied Physics Letters*, 100(6):062401, 2012.

[41] J Ding and AO Adeyeye. $Ni_{80}Fe_{20}$/Ni binary nanomagnets for logic applications. *Applied Physics Letters*, 101(10):103117, 2012.

[42] David J Griffiths. Introduction to electrodynamics, 2005.

[43] John MD Coey. *Magnetism and magnetic materials.* Cambridge University Press, 2010.

[44] Soshin Chikazumi and Chad D Graham. *Physics of Ferromagnetism 2e.* Oxford University Press on Demand, 2009.

[45] Mathias Getzlaff. *Fundamentals of magnetism.* Springer Science & Business Media, 2007.

[46] Robert C O'handley. *Modern magnetic materials: principles and applications.* Wiley, 2000.

[47] Melvin A Ruderman and Charles Kittel. Indirect exchange coupling of nuclear magnetic moments by conduction electrons. *Physical Review*, 96(1):99, 1954.

[48] Tôru Moriya. Anisotropic Superexchange Interaction and Weak Ferromagnetism. *Phys. Rev.*, 120:91–98, Oct 1960.

[49] CD Hu. The dzyaloshinskii–moriya interaction in metals. *Journal of Physics: Condensed Matter*, 24(8):086001, 2012.

[50] Robert E. Camley and Robert L. Stamps. *Solid State Physics*, volume 62. Academic Press, 2010.

[51] Alex Hubert and Rudolf Schäfer. *Magnetic domains: the analysis of magnetic microstructures.* Springer Science & Business Media, 2008.

[52] Bernard Dennis Cullity and Chad D Graham. *Introduction to magnetic materials.* John Wiley & Sons, 2011.

[53] U Parlak, ME Akoz, S Tokdemir Ozturk, and M Erkovan. Thickness dependent magnetic properties of polycrystalline nickel thin films. *Acta Physica Polonica A*, 127(4):995–997, 2015.

[54] MT Johnson, PJH Bloemen, FJA Den Broeder, and JJ De Vries. Magnetic anisotropy in metallic multilayers. *Reports on Progress in Physics*, 59(11):1409, 1996.

[55] RJ Prosen, JO Holmen, and BE Gran. Rotatable anisotropy in thin permalloy films. *Journal of Applied Physics*, 32(3):S91–S92, 1961.

[56] R Dutra, DE Gonzalez-Chavez, TL Marcondes, AMH de Andrade, J Geshev, and RL Sommer. Rotatable anisotropy of $Ni_{81}Fe_{19}/Ir_{20}Mn_{80}$ films: A study using broadband ferromagnetic resonance. *Journal of Magnetism and Magnetic Materials*, 346:1–4, 2013.

[57] R. D. McMichael, M. D. Stiles, P. J. Chen, and W. F. Egelhoff. Ferromagnetic resonance studies of NiO-coupled thin films of $Ni_{80}Fe_{20}$. *Phys. Rev. B*, 58:8605–8612, Oct 1998.

[58] S. Nicolodi, L. G. Pereira, A. Harres, G. M. Azevedo, J. E. Schmidt, I. García-Aguilar, N. M. Souza-Neto, C. Deranlot, F. Petroff, and J. Geshev. Negative rotatable anisotropy in IrMn/Cr/Co thin films. *Phys. Rev. B*, 85:224438, Jun 2012.

[59] Donald O. Smith. Anisotropy in Permalloy Films. *Journal of Applied Physics*, 30(4):S264–S265, 1959.

[60] R. J. Prosen, J. O. Holmen, and B. E. Gran. Rotatable Anisotropy in Thin Permalloy Films. *Journal of Applied Physics*, 32(3):S91–S92, 1961.

[61] Sherwin S. Lehrer. Rotatable Anisotropy in Negative Magnetostriction Ni-Fe Films. *Journal of Applied Physics*, 34(4):1207–1208, 1963.

[62] H. Fujiwara, Y. Sugita, and N. Saito. MECHANISM OF ROTATABLE ANISOTROPY IN THIN MAGNETIC FILMS OF Ni, Fe, AND Ni–Fe. *Applied Physics Letters*, 4(12):199–200, 1964.

[63] S M Ryabchenko, V M Kalita, M M Kulik, A F Lozenko, V V Nevdacha, A N Pogorily, A F Kravets, D Y Podyalovskiy, A Ya Vovk, R P Borges, M Godinho, and V Korenivski. Rotatable magnetic anisotropy in $Si/SiO_2/(Co_2Fe)_xGe_{1-x}$ Heusler alloy films. *Journal of Physics: Condensed Matter*, 25(41):416003, sep 2013.

[64] J. Geshev, L. G. Pereira, J. E. Schmidt, L. C. C. M. Nagamine, E. B. Saitovitch, and F. Pelegrini. Frequency-dependent exchange bias in NiFe/NiO films. *Phys. Rev. B*, 67:132401, Apr 2003.

[65] LALE Landau and Evgeny Lifshitz. On the theory of the dispersion of magnetic permeability in ferromagnetic bodies. In *Perspectives in Theoretical Physics*, pages 51–65. Elsevier, 1992.

[66] Thomas L Gilbert. A phenomenological theory of damping in ferromagnetic materials. *IEEE Transactions on Magnetics*, 40(6):3443–3449, 2004.

[67] Burkard Hillebrands and Kamel Ounadjela. *Spin dynamics in confined magnetic structures I*, volume 83. Springer Science & Business Media, 2003.

[68] EA Turov. Ferromagnetic resonance. *Ed. SV Vonsovskii, Pergamon Press, Oxford*, 1966.

[69] J Jorzick, SO Demokritov, B Hillebrands, M Bailleul, C Fermon, K Yu Guslienko, AN Slavin, DV Berkov, and NL Gorn. Spin wave wells in nonellipsoidal micrometer size magnetic elements. *Physical review letters*, 88(4):047204, 2002.

[70] Rodrigo Arias and DL Mills. Extrinsic contributions to the ferromagnetic resonance response of ultrathin films. *Physical review B*, 60(10):7395, 1999.

[71] Marshall Sparks. *Ferromagnetic-relaxation theory*. McGraw-Hill, 1964.

[72] Harry Suhl. Theory of the magnetic damping constant. *IEEE Transactions on magnetics*, 34(4):1834–1838, 1998.

[73] K. Lenz, H. Wende, W. Kuch, K. Baberschke, K. Nagy, and A. Jánossy. Two-magnon scattering and viscous gilbert damping in ultrathin ferromagnets. *Phys. Rev. B*, 73:144424, Apr 2006.

[74] Charles Kittel. On the theory of ferromagnetic resonance absorption. *Phys. Rev.*, 73:155–161, Jan 1948.

[75] J Smit and HG Beljers. Ferromagnetic resonance absorption in $BaFe_{12}O_{19}$, a highly anisotropic crystal. *Philips Res. Rep*, 10(113):31, 1955.

[76] O Acher, S Queste, M Ledieu, K-U Barholz, and R Mattheis. Hysteretic behavior of the dynamic permeability on a Ni-Fe thin film. *Physical Review B*, 68(18):184414, 2003.

[77] Christoph Mathieu, Jörg Jorzick, Andre Frank, SO Demokritov, AN Slavin, B Hillebrands, B Bartenlian, C Chappert, D Decanini, F Rousseaux, et al. Lateral quantization of spin waves in micron size magnetic wires. *Physical review letters*, 81(18):3968, 1998.

[78] J Podbielski, F Giesen, and D Grundler. Spin-wave interference in microscopic rings. *Physical review letters*, 96(16):167207, 2006.

[79] Felix Bloch. Zur theorie des ferromagnetismus. *Zeitschrift für Physik*, 61(3-4):206–219, 1930.

[80] F Moussa, M Hennion, J Rodriguez-Carvajal, H Moudden, L Pinsard, and A Revcolevschi. Spin waves in the antiferromagnet perovskite LaMn O 3: A neutron-scattering study. *Physical Review B*, 54(21):15149, 1996.

[81] R Vollmer, M Etzkorn, PS Anil Kumar, H Ibach, and J Kirschner. Spin-polarized electron energy loss spectroscopy of high energy, large wave vector spin waves in ultrathin fcc Co films on Cu (001). *Physical review letters*, 91(14):147201, 2003.

[82] J Jorzick, SO Demokritov, C Mathieu, B Hillebrands, B Bartenlian, C Chappert, F Rousseaux, and AN Slavin. Brillouin light scattering from quantized spin waves in micron-size magnetic wires. *Physical Review B*, 60(22):15194, 1999.

[83] Sergej O Demokritov, Burkard Hillebrands, and Andrei N Slavin. Brillouin light scattering studies of confined spin waves: linear and nonlinear confinement. *Physics Reports*, 348(6):441–489, 2001.

[84] GT Rado and JR Weertman. Spin-wave resonance in a ferromagnetic metal. *Journal of Physics and chemistry of solids*, 11(3-4):315–333, 1959.

[85] Michael Farle. Ferromagnetic resonance of ultrathin metallic layers. *Reports on progress in physics*, 61(7):755, 1998.

[86] RF W Damon and JR Eshbach. Magnetostatic modes of a ferromagnet slab. *Journal of Physics and Chemistry of Solids*, 19(3-4):308–320, 1961.

[87] LR Walker. Resonant modes of ferromagnetic spheroids. *Journal of Applied Physics*, 29(3):318–323, 1958.

[88] Anil Prabhakar and Daniel D Stancil. *Spin waves: Theory and applications*, volume 5. Springer, 2009.

[89] BA Kalinikos and AN Slavin. Theory of dipole-exchange spin wave spectrum for ferromagnetic films with mixed exchange boundary conditions. *Journal of Physics C: Solid State Physics*, 19(35):7013, 1986.

[90] K Yu Guslienko and AN Slavin. Boundary conditions for magnetization in magnetic nanoelements. *Physical Review B*, 72(1):014463, 2005.

[91] Ruma Mandal, Susmita Saha, Dheeraj Kumar, Saswati Barman, Semanti Pal, Kaustuv Das, Arup Kumar Raychaudhuri, Yasuhiro Fukuma, YoshiChika Otani, and Anjan Barman. Optically induced tunable magnetization dynamics in nanoscale Co antidot lattices. *ACS nano*, 6(4):3397–3403, 2012.

[92] Gary Mankey. *Lateral Standing Spin Waves in Permalloy Antidot Arrays.* AIP Publishing, 2004.

[93] YS Gui, N Mecking, and C-M Hu. Quantized spin excitations in a ferromagnetic microstrip from microwave photovoltage measurements. *Physical review letters*, 98(21):217603, 2007.

[94] M Grimsditch, A Malozemoff, and A Brunsch. Standing spin waves observed by Brillouin scattering in amorphous metallic $Fe_{80}B_{20}$ films. *Physical Review Letters*, 43(10):711, 1979.

[95] B Samantaray, Akhilesh Kr Singh, Chandrima Banerjee, Anjan Barman, A Perumal, and P Mandal. Perpendicular standing spin wave and magnetic anisotropic study on amorphous FeTaC films. *IEEE Transactions on Magnetics*, 52(7):1–4, 2016.

[96] Kristen S Buchanan, Pierre E Roy, Marcos Grimsditch, Frank Y Fradin, Konstantin Yu Guslienko, Sam D Bader, and Valentyn Novosad. Soliton-pair dynamics in patterned ferromagnetic ellipses. *Nature Physics*, 1(3):172–176, 2005.

[97] RP Cowburn, AO Adeyeye, and JAC Bland. Magnetic domain formation in lithographically defined antidot permalloy arrays. *Applied physics letters*, 70(17):2309–2311, 1997.

[98] AO Adeyeye, JAC Bland, and C Daboo. Magnetic properties of arrays of "holes" in $Ni_{80}Fe_{20}$ films. *Applied physics letters*, 70(23):3164–3166, 1997.

[99] Joachim Gräfe, Markus Weigand, Nick Träger, Gisela Schütz, Eberhard J Goering, Maxim Skripnik, Ulrich Nowak, Felix Haering, Paul Ziemann, and Ulf Wiedwald. Geometric control of the magnetization reversal in antidot lattices with perpendicular magnetic anisotropy. *Physical Review B*, 93(10):104421, 2016.

[100] A Yu Toporov, RM Langford, and AK Petford-Long. Lorentz transmission electron microscopy of focused ion beam patterned magnetic antidot arrays. *Applied Physics Letters*, 77(19):3063–3065, 2000.

[101] S Michea, JL Palma, R Lavín, J Briones, J Escrig, JC Denardin, and RL Rodríguez-Suárez. Tailoring the magnetic properties of cobalt antidot arrays by varying the pore size and degree of disorder. *Journal of Physics D: Applied Physics*, 47(33):335001, 2014.

[102] Tobias Schneider, Manuel Langer, Julia Alekhina, Ewa Kowalska, Antje Oelschlägel, Anna Semisalova, Andreas Neudert, Kilian Lenz, Kay Potzger, Mikhail P Kostylev, et al. Programmability of co-antidot lattices of optimized geometry. *Scientific reports*, 7:41157, 2017.

[103] RV Stuart. Vacuum technologies, thin films and sputtering, 1983.

[104] AO Adeyeye and N Singh. Large area patterned magnetic nanostructures. *Journal of Physics D: Applied Physics*, 41(15):153001, 2008.

[105] SW Pang, RJ Shul, and SJ Pearton. Chapter 8, Surface Damage Induced by Dry Etching. Handbook of Advanced Plasma Processing Technologies, 2000.

[106] Lucille A Giannuzzi and Frederick A Stevie. A review of focused ion beam milling techniques for TEM specimen preparation. *Micron*, 30(3):197–204, 1999.

[107] Lucille A Giannuzzi, BW Kempshall, SM Schwarz, JK Lomness, BI Prenitzer, and FA Stevie. FIB lift-out specimen preparation techniques. In *Introduction to focused ion beams*, pages 201–228. Springer, 2005.

[108] LA Giannuzzi, JL Drown, SR Brown, RB Irwin, and FA Stevie. Focused ion beam milling and micromanipulation lift-out for site specific cross-section TEM specimen preparation. *MRS Online Proceedings Library Archive*, 480, 1997.

[109] S Neusser, G Duerr, S Tacchi, M Madami, ML Sokolovskyy, G Gubbiotti, Maciej Krawczyk, and D Grundler. Magnonic minibands in antidot lattices with large spin-wave propagation velocities. *Physical Review B*, 84(9):094454, 2011.

[110] VE Demidov, MP Kostylev, Karsten Rott, Jana Münchenberger, Günter Reiss, and SO Demokritov. Excitation of short-wavelength spin waves in magnonic waveguides. *Applied Physics Letters*, 99(8):082507, 2011.

[111] VL Zhang, HS Lim, CS Lin, ZK Wang, SC Ng, MH Kuok, S Jain, AO Adeyeye, and MG Cottam. Ferromagnetic and antiferromagnetic spin-wave dispersions in a dipole-exchange coupled bi-component magnonic crystal. *Applied Physics Letters*, 99(14):143118, 2011.

[112] G Gubbiotti, S Tacchi, M Madami, G Carlotti, AO Adeyeye, and M Kostylev. Brillouin light scattering studies of planar metallic magnonic crystals. *Journal of Physics D: Applied Physics*, 43(26):264003, 2010.

[113] C Bilzer, T Devolder, P Crozat, C Chappert, S Cardoso, and PP Freitas. Vector network analyzer ferromagnetic resonance of thin films on coplanar waveguides: Comparison of different evaluation methods. *Journal of applied physics*, 101(7):074505, 2007.

[114] A. Vansteenkiste and B. Van de Wiele. Mumax: A new high-performance micromagnetic simulation tool. *Journal of Magnetism and Magnetic Materials*, 323(21):2585 – 2591, 2011.

[115] M.J. Donahue and D.G. Porter. Oommf user's guide, version 1.0. *National Institute of Standards and Technology, Gaithersburg, MD*, 1999.

[116] Werner Scholz, Josef Fidler, Thomas Schrefl, Dieter Suess, Hermann Forster, Vassilios Tsiantos, et al. Scalable parallel micromagnetic solvers for magnetic nanostructures. *Computational Materials Science*, 28(2):366–383, 2003.

[117] Werner Scholz, Dieter Suess, Rok Dittrich, Thomas Schrefl, Vassilios Tsiantos, Hermann Forster, and Josef Fidler. Implementation of a high performance parallel finite element micromagnetics package. *Journal of magnetism and magnetic materials*, 272:693–694, 2004.

[118] Thomas Fischbacher, Matteo Franchin, Giuliano Bordignon, and Hans Fangohr. A systematic approach to multiphysics extensions of finite-element-based micromagnetic simulations: Nmag. *IEEE Transactions on Magnetics*, 43(6):2896–2898, 2007.

[119] L Lopez-Diaz, D Aurelio, L Torres, E Martinez, MA Hernandez-Lopez, J Gomez, O Alejos, M Carpentieri, G Finocchio, and G Consolo. Micromagnetic simulations using graphics processing units. *Journal of Physics D: Applied Physics*, 45(32):323001, 2012.

[120] AA Awad, GR Aranda, D Dieleman, KY Guslienko, GN Kakazei, BA Ivanov, and FG Aliev. Spin excitation frequencies in magnetostatically coupled arrays of vortex state circular permalloy dots. *Applied Physics Letters*, 97(13):132501, 2010.

[121] DyNaMat group. mumax3. *Ghent University - Belgium*, May 2014.

[122] S. Mizukami, D. Watanabe, M. Oogane, Y. Ando, Y. Miura, M. Shirai, and T. Miyazaki. Low damping constant for Co_2FeAl Heusler alloy films and its correlation with density of states. *Journal of Applied Physics*, 105(7):07D306, 2009.

[123] Zhaoqiang Bai, Lei Shen, Guchang Han, and Yuan Ping Feng. Data storage: review of Heusler compounds. In *Spin*, volume 2, page 1230006, 2012.

[124] M. Belmeguenai, H. Tuzcuoglu, M. S. Gabor, T. Petrisor, C. Tiusan, F. Zighem, S. M. Chérif, and P. Moch. Co_2FeAl Heusler thin films grown on Si and MgO substrates: Annealing temperature effect. *Journal of Applied Physics*, 115(4):043918, 2014.

[125] Q. L. Ma, X. M. Zhang, T. Miyazaki, and S. Mizukami. Artificially engineered Heusler ferrimagnetic superlattice exhibiting perpendicular magnetic anisotropy. *Scientific Reports*, 5:7863, 2015.

[126] Mohamed Belmeguenai, Hanife Tuzcuoglu, Mihai Gabor, Traian Petrisor, Coriolan Tiusan, Dominique Berling, Fatih Zighem, and Salim Mourad Cherif. Magnetic and structural properties of Co_2FeAl thin films grown on Si substrate. *Journal of Magnetism and Magnetic Materials*, 373:140 – 143, 2015. Recent Advances in Nanomagnetism and Spintronics.

[127] Sajid Husain, Serkan Akansel, Ankit Kumar, Peter Svedlindh, and Sujeet Chaudhary. Growth of Co_2FeAl Heusler alloy thin films on Si(100) having very small Gilbert damping by Ion beam sputtering. *Scientific Reports*, 6(1):28692, 2016.

[128] Sajid Husain, Ankit Kumar, Vineet Barwal, Nilamani Behera, Serkan Akansel, Peter Svedlindh, and Sujeet Chaudhary. Spin pumping in ion-beam sputtered Co_2FeAl/Mo bilayers: Interfacial Gilbert damping. *Phys. Rev. B*, 97:064420, Feb 2018.

[129] Jihong Liu and Shuang Qiao. Structure and magnetic research of the epitaxial Co_2FeAl films on the MgO substrates. *Journal of Alloys and Compounds*, 773:955 – 959, 2019.

[130] Mikihiko Oogane, Resul Yilgin, Masatsugu Shinano, Satoshi Yakata, Yuya Sakuraba, Yasuo Ando, and Terunobu Miyazaki. Magnetic damping constant of Co_2FeSi Heusler alloy thin film. *Journal of Applied Physics*, 101(9):09J501, 2007.

[131] Resul Yilgin, Yuya Sakuraba, Mikihiko Oogane, Shigemi Mizukami, Yasuo Ando, and Terunobu Miyazaki. Anisotropic Intrinsic Damping Constant of Epitaxial Co_2MnSi Heusler Alloy Films. *Japanese Journal of Applied Physics*, 46(No. 9):L205–L208, feb 2007.

[132] Y. Liu, L. R. Shelford, V. V. Kruglyak, R. J. Hicken, Y. Sakuraba, M. Oogane, Y. Ando, and T. Miyazaki. Ultrafast optical modification of magnetic anisotropy and stimulated precession in an epitaxial Co_2MnAl thin film. *Journal of Applied Physics*, 101(9):09C106, 2007.

[133] C. Guillemard, S. Petit-Watelot, L. Pasquier, D. Pierre, J. Ghanbaja, J-C. Rojas-Sánchez, A. Bataille, J. Rault, P. Le Fèvre, F. Bertran, and S. Andrieu. Ultralow Magnetic Damping in Co_2Mn-Based Heusler Compounds: Promising Materials for Spintronics. *Phys. Rev. Applied*, 11:064009, Jun 2019.

[134] M. Belmeguenai, F. Zighem, Y. Roussigné, S-M. Chérif, P. Moch, K. Westerholt, G. Woltersdorf, and G. Bayreuther. Microstrip line ferromagnetic resonance and Brillouin light scattering investigations of magnetic properties of Co_2MnGe Heusler thin films. *Phys. Rev. B*, 79:024419, Jan 2009.

[135] Justin M. Shaw, Erna K. Delczeg-Czirjak, Eric R. J. Edwards, Yaroslav Kvashnin, Danny Thonig, Martin A. W. Schoen, Matt Pufall, Michael L. Schneider, Thomas J. Silva, Olof Karis, Katherine P. Rice, Olle Eriksson, and Hans T. Nembach. Magnetic damping in sputter-deposited Co_2MnGe Heusler compounds with $A2, B2$, and $L2_1$ orders: Experiment and theory. *Phys. Rev. B*, 97:094420, Mar 2018.

[136] Ankit Kumar, Fan Pan, Sajid Husain, Serkan Akansel, Rimantas Brucas, Lars Bergqvist, Sujeet Chaudhary, and Peter Svedlindh. Temperature-dependent Gilbert damping of Co_2FeAl thin films with different degree of atomic order. *Phys. Rev. B*, 96:224425, Dec 2017.

[137] Serkan Akansel, Ankit Kumar, Nilamani Behera, Sajid Husain, Rimantas Brucas, Sujeet Chaudhary, and Peter Svedlindh. Thickness-dependent enhancement of damping in Co_2FeAl/β-Ta thin films. *Phys. Rev. B*, 97:134421, Apr 2018.

[138] Zhenni Zhan, Zhigao Hu, Kangkang Meng, Jianhua Zhao, and Junhao Chu. Temperature dependent phonon Raman scattering of Heusler alloy $Co_2Mn_xFe_{1-x}Al/GaAs$ films grown by molecular-beam epitaxy. *RSC Adv.*, 2:9899–9903, 2012.

[139] Peter J. Webster. Heusler alloys. *Contemporary Physics*, 10(6):559–577, 1969.

[140] Byong Sun Chun, Kyung-Ho Kim, Niklas Leibing, Santiago Serrano-Guisan, Hans-Werner Schumacher, Mohamed Abid, In Chang Chu, Oleg N. Mryasov, Do Kyun Kim, Han-Chun Wu, Chanyong Hwang, and Young Keun Kim. Structural and magnetic properties of epitaxial Co_2FeAl films grown on MgO substrates for different growth temperatures. *Acta Materialia*, 60(19):6714 – 6719, 2012.

[141] M. Belmeguenai, H. Tuzcuoglu, M. S. Gabor, T. Petrisor, C. Tiusan, D. Berling, F. Zighem, T. Chauveau, S. M. Chérif, and P. Moch. Co_2FeAl thin films grown on MgO substrates: Correlation between static, dynamic, and structural properties. *Phys. Rev. B*, 87:184431, May 2013.

[142] Rajendra P. Dulal, Bishnu R. Dahal, Andrew Forbes, Ian L. Pegg, and John Philip. Large magnetization and high Curie temperature in highly disordered nanoscale Fe_2CrAl thin films. *Journal of Magnetism and Magnetic Materials*, 423:314 – 317, 2017.

[143] N. Tezuka, N. Ikeda, A. Miyazaki, S. Sugimoto, M. Kikuchi, and K. Inomata. Tunnel magnetoresistance for junctions with epitaxial full-Heusler $Co_2FeAl_{0.5}Si_{0.5}$ electrodes with B2 and $L2_1$ structures. *Applied Physics Letters*, 89(11):112514, 2006.

[144] Shuang Qiao, Shuaihua Nie, Jianhua Zhao, and Xinhui Zhang. Growth temperature dependent structural and magnetic properties of epitaxial Co_2FeAl Heusler alloy films. *Journal of Applied Physics*, 113(23):233914, 2013.

[145] D. E. Gonzalez-Chavez, R. Dutra, W. O. Rosa, T. L. Marcondes, A. Mello, and R. L. Sommer. Interlayer coupling in spin valves studied by broadband ferromagnetic resonance. *Phys. Rev. B*, 88:104431, Sep 2013.

[146] Simon Trudel, Oksana Gaier, Jaroslav Hamrle, and Burkard Hillebrands. Magnetic anisotropy, exchange and damping in cobalt-based full-Heusler compounds: an experimental review. *Journal of Physics D: Applied Physics*, 43(19):193001, apr 2010.

[147] Luqiao Liu, Takahiro Moriyama, D. C. Ralph, and R. A. Buhrman. Spin-Torque Ferromagnetic Resonance Induced by the Spin Hall Effect. *Phys. Rev. Lett.*, 106:036601, Jan 2011.

[148] Arabinda Haldar, Chandrima Banerjee, Pinaki Laha, and Anjan Barman. Brillouin light scattering study of spin waves in NiFe/Co exchange spring bilayer films. *Journal of Applied Physics*, 115(13):133901, 2014.

[149] A Conca, S Keller, L Mihalceanu, T Kehagias, GP Dimitrakopulos, B Hillebrands, and E Th Papaioannou. Study of fully epitaxial Fe/Pt bilayers for spin pumping by ferromagnetic resonance spectroscopy. *Physical Review B*, 93(13):134405, 2016.

[150] Derang Cao, Xiaohong Cheng, Lining Pan, Hongmei Feng, Chenbo Zhao, Zengtai Zhu, Qiang Li, Jie Xu, Shandong Li, Qingfang Liu, et al. Tuning high frequency magnetic properties and damping of FeGa, FeGaN and FeGaB thin films. *AIP Advances*, 7(11):115009, 2017.

[151] Duy-Truong Quach, Quang-Hung Tran, Kristian Møhave, Dong-Hyun Kim, et al. Perpendicular magnetic anisotropy and the magnetization process in CoFeB/Pd multilayer films. *Journal of Physics D: Applied Physics*, 47(44):445001, 2014.

[152] Kyongmo An, Xin Ma, Chi-Feng Pai, Jusang Yang, Kevin S Olsson, James L Erskine, Daniel C Ralph, Robert A Buhrman, and Xiaoqin Li. Current control of magnetic anisotropy via stress in a ferromagnetic metal waveguide. *Physical Review B*, 93(14):140404, 2016.

[153] Vincent G Harris et al. Modern microwave ferrites. *IEEE Transactions on Magnetics*, 48(3):1075–1104, 2012.

[154] JH Hankiewicz, Z Celinski, KF Stupic, NR Anderson, and RE Camley. Ferromagnetic particles as magnetic resonance imaging temperature sensors. *Nature communications*, 7:12415, 2016.

[155] Changjiang Liu, Sahil J Patel, Timothy A Peterson, Chad C Geppert, Kevin D Christie, Gordon Stecklein, Chris J Palmstrøm, and Paul A Crowell. Dynamic detection of electron spin accumulation in ferromagnet–semiconductor devices by ferromagnetic resonance. *Nature communications*, 7:10296, 2016.

[156] Justin M Shaw, Thomas J Silva, Michael L Schneider, and Robert D McMichael. Spin dynamics and mode structure in nanomagnet arrays: Effects of size and thickness on linewidth and damping. *Physical Review B*, 79(18):184404, 2009.

[157] Z Celinski and B Heinrich. Ferromagnetic resonance linewidth of Fe ultrathin films grown on a bcc Cu substrate. *Journal of applied physics*, 70(10):5935–5937, 1991.

[158] MJ Hurben and CE Patton. Theory of two magnon scattering microwave relaxation and ferromagnetic resonance linewidth in magnetic thin films. *Journal of applied physics*, 83(8):4344–4365, 1998.

[159] Chengtao Yu, Michael J Pechan, Wesley A Burgei, and Gary J Mankey. Lateral standing spin waves in permalloy antidot arrays. *Journal of applied physics*, 95(11):6648–6650, 2004.

[160] Chengtao Yu, Michael J Pechan, and Gary J Mankey. Dipolar induced, spatially localized resonance in magnetic antidot arrays. *Applied physics letters*, 83(19):3948–3950, 2003.

[161] S McPhail, CM Gürtler, JM Shilton, NJ Curson, and JAC Bland. Coupling of spin-wave modes in extended ferromagnetic thin film antidot arrays. *Physical Review B*, 72(9):094414, 2005.

[162] Chengtao Yu, Michael J. Pechan, and Gary J. Mankey. Dipolar induced, spatially localized resonance in magnetic antidot arrays. *Applied Physics Letters*, 83(19):3948–3950, 2003.

[163] LJ Heyderman, F Nolting, and C Quitmann. X-ray photoemission electron microscopy investigation of magnetic thin film antidot arrays. *Applied physics letters*, 83(9):1797–1799, 2003.

[164] I Guedes, M Grimsditch, V Metlushko, P Vavassori, R Camley, B Ilic, P Neuzil, and R Kumar. Magnetization reversal in an Fe film with an array of elliptical holes on a square lattice. *Physical Review B*, 67(2):024428, 2003.

[165] I Ruiz-Feal, L Lopez-Diaz, A Hirohata, J Rothman, CM Guertler, JAC Bland, LM Garcia, JM Torres, J Bartolome, F Bartolome, et al. Geometric coercivity scaling in magnetic thin film antidot arrays. *Journal of magnetism and magnetic materials*, 242:597–600, 2002.

[166] AV Chumak, AA Serga, and B Hillebrands. Magnonic crystals for data processing. *Journal of Physics D: Applied Physics*, 50(24):244001, 2017.

[167] A O Adeyeye and N Singh. Large area patterned magnetic nanostructures. *Journal of Physics D: Applied Physics*, 41(15):153001, jul 2008.

[168] Gary A. Prinz. Magnetoelectronics. *Science*, 282(5394):1660–1663, 1998.

[169] R. P. Cowburn and M. E. Welland. Room temperature magnetic quantum cellular automata. *Science*, 287(5457):1466–1468, 2000.

[170] R. L. White, R. M. H. Newt, and R. F. W. Pease. Patterned media: a viable route to 50 gbit/in/sup 2/ and up for magnetic recording? *IEEE Transactions on Magnetics*, 33(1):990–995, Jan 1997.

[171] R. Dutra, D. E. Gonzalez-Chavez, T. L. Marcondes, R. L. Sommer, S. O. Parreiras, and M. D. Martins. Spin wave dynamics in elliptical dots. *Phys. Rev. B*, 99:014413, Jan 2019.

[172] D. E. Gonzalez-Chavez, R. Dutra, W. O. Rosa, T. L. Marcondes, A. Mello, and R. L. Sommer. Interlayer coupling in spin valves studied by broadband ferromagnetic resonance. *Phys. Rev. B*, 88:104431, Sep 2013.

[173] A. Vansteenkiste and B. Van de Wiele. Mumax: A new high-performance micromagnetic simulation tool. *J. Magn. Magn. Mater.*, 323(21):2585 – 2591, 2011.

Appendix I

This appendix describes the procedures and the recipes used for the preparation of the substrates and for the lithography processes.

Substrate Preparation

- Cleaning the substrate with acetone, isopropyl Alcohol (IPA) and deionized water.
- Heating for approximately 1 minute on hot plate at 150°C to evaporate any absorption.
- Leave the substrate at room temperature for approximately 5 minutes.
- PMMA 950K positive Resist (ARP-672.045): 4000rpm; @60sec; 250 nm; baking 150°C for 3 min
- Development: 30% deionized water + 70% isopropyl Alcohol (IPA) @60sec; post-baking 130°C for 1 min.
- Plasma Etching: 200 W; 100 mTorr; Ar: 50 sccm; Etching Rate for NiFe: 1.5 nm/min.
- Plasma Etching: 200 W; 100 mTorr; O_2: 50 sccm; Etching Rate for ARP-672.045 resist: 344 nm/min.

E-beam Quick Start Guide

- Open e-line & smart SEM software
- e-line ⇒ Gas injection ⇒ Initialized (if not initialized click HOME icon)
- Check the GUN status, compressed air, N_2 supply and Vacuum, main chamber: 10^{-6}; GUN: 10^{-9} (note these values)
- Sample loading/unloading: Navigation ⇒ via load lock ⇒ Follow the system instructions
- Turn ON (ETH)
- Stage control ⇒ Drive(x,y)⇒ 29 mm (Si); WD= 5.4 mm
- Select manu " file/Open Wafermap (Find the lower left corner of chip)
- Origin and angle Correction: Mark P2 and P1 at lower left and lower right of the chip (1000X; 20kV)
- Astigmatism and aperture correction: find the some dust particle use 30kX resolution (focus on it)
- Astigmatism and aperture correction: find the some edge of dust particle use 80kX resolution (focus on it); change the x, y of Astigmatism (check for no change in the shape); change the x, y of (Focus Wobble) lens alignments (check for motion along the x-axis and y-axis)
- Spot short: After doing SEM alignments make a spot shot or long near to the dust particle.
- Open new position: Drag and drop the design file on the chip
- 3 points: at the three edges of the chip mark P1, P2 and P3. Spot long (On) ⇒ Open (beam ON) ⇒ Spot long (OFF) ⇒ Get good focus/zoom ⇒ Put the crosshair in the center (Type the values with keyboard and press adjust). Similar for all points e.g P2, P3
- Writefield (WF) alignment: Scan manger ⇒ Manual ⇒ WF alignments ⇒ first 25 um ⇒ then 5 um and 1 um, respectively.

- Faraday Cup: Stage Control ⇒ Position ⇒ Faraday cup on USH ⇒ Go ⇒ Measure the current in (pA)
- Dose: positionList ⇒ right click ⇒ Properties ⇒ Put the conditions ⇒ put the dose valve and step size (0.02).
- RUN Scan: select all items in the position list ⇒ Right click ⇒ RUN
- **2nd lithography:** When doing the overlay patterning, Use the GDS layer markscans, Layer 63 and 61. When using these layers, these make the alignment to marks that were written during the first write, so you get the same “scaling” during the overlay write.

E-line lithography Recipes

AR-P 672.045 (+ve)

- Substrate cleaning with acetone, isopropyl Alcohol (IPA) and deionized water.
- Heating for approximately 3 minute on hot plate at $150°C$ to evaporate any absorption.
- Spin coating: 4000 rpm @ 60 sec; 0.230 μm
- Baking: 150°C @ 3 min (hot plate)
- Dose: 120 μC/cm^2
- Development: isopropyl Alcohol (IPA) + DI water (70%:30%) solution for 60 sec
- PostBaking: 130°C @ 1 min (hot plate)
- Lift-off: Acetone (until whole structure developed) + ultrasonic @ 10 sec.

AR-N 7700.18 (-ve)

- Substrate cleaning with acetone, isopropyl Alcohol (IPA) and deionized water.
- Heating for approximately 3 minute on hot plate at $150°C$ to evaporate any absorption.
- Spin coating: (i) 2000 rpm with 500 m/sec^2 @ 6 sec (ii) 4000 rpm with 4000 m/sec^2 @ 60 sec; 0.4 μm
- Baking: 85°C @ 60 sec (hot plate)
- Dose: 120 μC/cm^2
- Crosslinking : 105°C @ 2 min (hot plate)
- Development: AR300.47 pure solution for 60 sec (keep shaking)
- PostBaking (Optional): 120°C @ 1 min (hot plate)
- Lift-off: Acetone (until whole structure developed) + ultrasonic @ 10 sec.

LASER Writer Quick Start Guide

- Turn ON Power supply ⇒ Turn ON Vacuum pump ⇒ Turn ON PC
- Open the compressed air valve until 6 bar.
- Open the μP G 101 software ⇒ Show advance option
- Load CAD file of the design (unit 1000)
- Show control penal ⇒ Next ⇒ Load/unload sample ⇒ Put the sample ⇒ Click on move to center ⇒ Click on focus ⇒ Open Camera
- Tools ⇒ LASER off-set calibration X= 2000; Y= -7500
- Put the value of already calibrated DOSE ⇒ Find plate center ⇒ Next ⇒ Expose
- Unload sample ⇒ Yes
- Development with the specific developer solution and do Inspection.
- **2nd lithography:** When doing the overlay patterning, Use the find the extreme edges of the design and note the values of the Wafer coordinates (A, B)
- Open the CAD design and mark the CAD coordinates (A', B') at the same position.
- Save the Layer-2 of the design ⇒ Open the Layer-2 in CAD
- From the options of CAD software ⇒ Select All ⇒ Modify ⇒ Move/Copy ⇒ Delete Original
- Reference point (A') click on this point in CAD design.
- Translation: Target point (A) Type this value ⇒ Move ⇒ Delete Original
- Rotation: Rotation centre (A) type this value ⇒ Reference Point (B') click this point ⇒ Trget Point (B) type this value.

LASER Writer lithography Recipes

AZ-1505 (+ve)

- Substrate cleaning with acetone, isopropyl Alcohol (IPA) and deionized water.
- Heating for approximately 1 minute on hot plate at $150°C$ to evaporate any absorption.
- Spin coating: 4000 rpm @ 60 sec; 0.5 μm
- Baking: 100°C @ 60 sec (hot plate)
- Dose: 5 mW; 55 %
- Development: AZ 326MIF pure solution for 60 sec
- Lift-off: Acetone, until whole structure developed.

ARN4400.10 (-ve)

- Substrate cleaning with acetone, isopropyl Alcohol (IPA) and deionized water.
- Heating for approximately 1 minute on hot plate at $150°C$ to evaporate any absorption.
- Spin coating: (i) 400 rpm with 400 m/sec^2 @ 3 sec (ii) 1000 rpm with 1000 m/sec^2 @ 60 sec; 10 μm
- Baking: 93°C @ 10 min (hot plate)
- Dose: 30 mW; 60 % (invert 500 μm)
- Crosslinking: 80°C @ 10 min (hot plate)
- Development: AR300.47 pure solution for 8 min and 30 sec (keep shaking) + Deionized water @ 30 sec
- Lift-off: Acetone, until whole structure developed (ultrasonic if needed).

AR-P 3510 (+ve)

- Substrate cleaning with acetone, isopropyl Alcohol (IPA) and deionized water.
- Heating for approximately 3 minute on hot plate at 150°C to evaporate any absorption.
- Spin coating: 4000 rpm @ 60 sec; 2.0 μm
- Baking: 100°C @ 60 sec (hot plate)
- Dose: 30 mW; 60 %
- Development: AR300.26 + DI water (1:6) solution for 20 to 30 sec
- Lift-off: Acetone, until whole structure developed.